

CHEMICAL TRANSFORMATIONS OF NANOCRYSTALS: STRUCTURE,
SURFACE CHEMISTRY, AND DIFFUSION

A Dissertation

Presented to the Faculty of the Graduate School

of Cornell University

In Partial Fulfillment of the Requirements for the Degree of

Doctor of Philosophy

by

Andrew William Nelson

August 2019

© 2019 Andrew William Nelson

CHEMICAL TRANSFORMATIONS OF NANOCRYSTALS: STRUCTURE, SURFACE CHEMISTRY, AND DIFFUSION

Andrew William Nelson

Cornell University 2019

By selecting nanoparticle size, shape, and composition during synthesis, researchers have extraordinary control over the physical and chemical properties of nanostructures, giving rise to exciting properties such as high catalytic activities, enhanced charge extraction, and improved durability. Post-synthetic modification, or chemical transformation, of these nanomaterials has been shown to greatly expand the space of tunable parameters for designer nanoparticles. We examined chemical transformations of nanoparticles, specifically ligand exchange or displacement and ion exchange, as a route not only to produce materials for renewable energy applications but also to investigate the relation of nanocrystal subsurface structure to surface energy and to measure the rates of diffusion of ions at short length scales. An important technique in recent years is the process of ion exchange, by which cations or anions in nanocrystals of a parent binary compound are replaced with ions of a different type to produce an otherwise inaccessible structure. We find that anion exchange in oxides via introduction of sulfide can be used to optimize electrocatalytic activity of cobalt oxide for the hydrogen evolution reaction and show with first-principles calculations that this arises from tuning of adsorbate binding energies to favorable values. Using x-ray diffraction and spectroscopic techniques we explain the chemically selective dissolution of constituents of cation-exchanged nanocrystals in terms of an autocatalytic surface reaction by ostensibly protective surfactants, thereby

providing another route for controlling heterostructure morphology by material removal. This reaction entails the insertion and removal of ions to and from the lattice as dictated by the redox environment and local strain. Through in-situ x-ray diffraction of the cation exchange of lead sulfide to cadmium sulfide, we quantify the transport coefficients of ions through a nanoparticle shell and find that interdiffusion is accelerated by a factor of 10^4 or more during exchange relative to expectations from high-temperature data, even though the activation barrier to diffusion is similar. These results show the need for a more careful microscopic treatment of transport in the necessarily large chemical potentials found nanoparticle transformation processes far from equilibrium. Finally, we compare some important techniques for preparing clean and reproducible nanoparticle surfaces for electrochemical investigation and demonstrate in particular the effectiveness of ligand removal by alkylation, showing that it may be a useful and general technique for future investigations of well-defined nanocrystal electrocatalysts.

BIOGRAPHICAL SKETCH

Andrew Nelson was raised in Aurora, Illinois. Before entering university, he became interested in nanomaterials following a stint as a student intern at Argonne National Laboratory. He graduated with a Bachelors of Science in Materials Science and Engineering from the University of Illinois in Urbana-Champaign, where he was an undergraduate in the laboratory of Prof. Moonsub Shim working on electrical transport in carbon nanotube films. He then entered the PhD program at Cornell University, where he applied his appreciation of nanomaterials as a graduate research assistant working on nanoparticle synthesis, cation exchange, and electrocatalysis in the group of Prof. Richard Robinson.

To my family

ACKNOWLEDGMENTS

Many people made this work possible. Most prominently, I am indebted to Prof. Richard Robinson for his continual material and scientific support throughout my time at Cornell. Without his gentle and insistent prodding and encouragement, I would have been too timid to take many of the important opportunities available to me, including my first job after the program. Thank you, Rich, for keeping your eye on the goal when I did not.

I thank Prof. Jin Suntivich for service on my graduate committee and for his collaborative efforts. Jin was a wellspring of enthusiasm and encouragement whose tolerance for setbacks and appetite for scientific discovery I hope to live up to. Thanks are also due to Prof. Frank DiSalvo for his service as a committee member and for helpful comments.

My labmates and collaborators were indispensable to my scientific achievements. In particular I thank Don-Hyung Ha, my predecessor in the group, for granting me his technical skills and wisdom. I acknowledge gratefully the support from Matt Fayette, Curtis Williamson, Anuj Bhargava, Doug Nevers, Sanjaya Perera, Mahmut Aksit, Obafemi Otelaja, Kevin Fritz, Shreyas Honrao, Haitao Zhang, Robert Hovden, Matthew Ward, Stanislav Stoupin, Tobias Hanrath, and Richard Hennig, among countless others I regret I lack space to name.

This work was almost entirely supported financially by the National Science Foundation, the grants from which are enumerated in Chapters 2, 3, 4, and 5 and were provided through Prof. Robinson's tireless work.

And finally, most of all, I extend my heartfelt gratitude to my mother, father, and sister, who more than anyone have taught me what it means to be a scientist.

TABLE OF CONTENTS

BIOGRAPHICAL SKETCH	v
ACKNOWLEDGMENTS	vii
TABLE OF CONTENTS	viii
LIST OF FIGURES	xiii
LIST OF TABLES	xix
1 INTRODUCTION	1
1.1 Colloidal nanocrystals and their transformations	1
1.2 Outline	5
1.3 Areas of exploration	8
1.3.1 Examples of chemical transformations of nanoparticles	8
1.3.2 Chemical transformations of nanoparticles: ion exchange	10
1.3.3 Nanocrystal surface and interface science	13
1.3.4 Aspects of x-ray and electron diffraction and imaging	15
1.3.5 Electrochemistry with nanoparticles	20
1.3.6 Solid-state diffusion and mass transport in nanomaterials	23
1.A References	28
2 INCREASED ACTIVITY IN HYDROGEN EVOLUTION ELECTROCATALYSIS FOR PARTIAL ANIONIC SUBSTITUTION IN COBALT OXYSULFIDE NANOPARTICLES	43
2.1 Abstract	43
2.2 Introduction	44
2.3 Results and discussion	45
2.3.1 Structural characterization	46

2.3.2	Electrochemical properties	52
2.3.3	Enhancement mechanism from first principles	55
2.4	Conclusion	57
2.A	Appendix	59
2.A.1	Funding and acknowledgments	59
2.A.2	Materials and methods	59
2.A.3	Additional discussion	64
2.A.4	Supporting figures	73
2.B	References	78
3	SELECTIVE ETCHING OF COPPER SULFIDE NANOPARTICLES AND HETEROSTRUCTURES THROUGH SULFUR ABSTRACTION: PHASE TRANSFORMATIONS AND OPTICAL PROPERTIES	91
3.1	Abstract	91
3.2	Introduction	92
3.3	Results and discussion	94
3.3.1	Morphological and structural characterization	96
3.3.2	Optical characterization	107
3.3.3	Mechanism of etching	110
3.4	Conclusion	121
3.A	Appendix	123
3.A.1	Funding and acknowledgments	123
3.A.2	Materials and methods	123
3.A.3	Supporting figures	129
3.B	References	136
4	NANOCRYSTAL SYMMETRY BREAKING AND ACCELERATED SOLID-STATE DIFFUSION IN THE LEAD–CADMIUM SULFIDE	

CATION EXCHANGE SYSTEM	146
4.1 Abstract	146
4.2 Introduction	147
4.3 Results and Discussion	148
4.3.1 Phase relations by XRD intensity quantification	150
4.3.2 XRD peak shifts and symmetry breaking	154
4.3.3 Theoretical predictions: Debye scattering simulations	156
4.3.4 NC disorder and peak width	159
4.3.5 Density functional theory calculations of phase stability	162
4.3.6 Origins of apparent symmetry breaking: kinematical diffraction theory	163
4.3.7 Transmission electron microscopy and Raman spectroscopy	165
4.3.8 Kinetics: stages of cation exchange	169
4.3.9 Quantitation of cation exchange kinetics: stages A and B	170
4.3.10 Quantitation of cation exchange kinetics: stage C	173
4.3.11 Mechanisms of chemical diffusion: magnitude of \tilde{D}	176
4.3.12 Chemical diffusion in NCs: possible enhancement factors	179
4.3.13 Mechanism of diffusion: Arrhenius parameters	181
4.4 Conclusion	184
4.A Appendix	187
4.A.1 Funding and acknowledgments	187
4.A.2 Materials and methods	187
4.A.3 Computational and other results and procedures	195
4.A.4 Kinetic parameter determination	200
4.A.5 Supporting figures	208
4.B References	218

5	ASSESSMENT OF SOFT LIGAND REMOVAL STRATEGIES: ALKYLATION AS A PROMISING ALTERNATIVE TO HIGH- TEMPERATURE TREATMENTS FOR COLLOIDAL NANOPARTICLE SURFACES	229
5.1	Abstract	229
5.2	Introduction	230
5.3	Results and discussion	231
5.4	Conclusion	248
5.A	Appendix	250
	5.A.1 Funding and acknowledgments	250
	5.A.2 Materials and methods	250
	5.A.3 Supporting figures and tables	255
5.B	References	258
6	CONCLUSIONS AND OUTLOOK	265
6.1	Summary and concluding remarks	265
6.2	Future work	268
	6.2.1 High-resolution structural analysis by use of the pair distribution function	269
	6.2.2 Expansion of parameter space in metal oxysulfides and other anion-exchanged nanomaterials	275
	6.2.3 Physical electrochemistry and surface science of nanocrystals	280
	6.2.4 Direct identification of the defects and chemical gradients in nanoparticles	282
6.3	Preliminary study: x-ray diffraction and pair distribution function analysis of internally correlated nanomaterials	287

6.3.1	Motivation	288
6.3.2	Peak shape origin	292
6.3.3	Toy model of powder diffraction in nanowires and molecular aggregates	295
6.3.4	Limitations of the toy model and suggested experiments	302
6.A	References	309

LIST OF FIGURES

1.1	Size and surface chemical control of thermodynamic, electronic, and structural properties of materials	2
1.2	Examples of chemical transformations of nanomaterials	9
1.3	Cation exchange as a shape- and structure-preserving transformation of nanomaterials	11
1.4	The scattering of electromagnetic waves by a pair of electrons	17
1.5	Averaging of intensities of a section of reciprocal space (left) over all orientations (right)	19
1.6	Facet dependence of nanoparticle electrocatalytic activity in nanorods	22
1.7	Morphology and phase changes during transformation of nanoparticles depend on domain size, starting crystal structure, and mobility of different species	25
2.1	Schematic of the anionic substitution in CoO_x nanoparticles as a testbed for HER electrocatalysis	46
2.2	Schematic of the synthesis of cobalt oxysulfides via partial and “full” anion exchange	48
2.3	Cyclic voltammograms of carbon-supported thin-film electrocatalysts containing (samples not subjected to annealing) CoO_x (a), $\text{CoO}_x\text{S}_{0.18}$ (b), $\text{CoO}_x\text{S}_{1.03}$ (c), and $\text{CoO}_x\text{S}_{1.27}$ (d) nanoparticle electrocatalysts	53
2.4	Polarization curves of carbon-supported thin-film electrocatalysts containing cobalt oxide/oxysulfides (samples not subjected to annealing)	55
2.5	Calculated DFT adsorption energies of hydrogen and their correlation with experimental results for the activity of CoO_xS_y nanoparticle electrocatalysts	57
2.A.1	TEM characterization of structural transformations of CoO_xS_y nanoparticles	73
2.A.2	Cyclic voltammograms of carbon-supported thin-film electrocatalysts containing CoO (red line) and Co_3O_4 (blue line) nanopowders	74

2.A.3	Tafel plot comparing un-annealed $\text{CoO}_x\text{S}_{0.18}$ (blue curve) with annealed $\text{CoO}_x\text{S}_{0.17}$ (red curve)	74
2.A.4	DFT structural model showing the 2x2 unit cell $\text{CoO}(100)$ slab (c-direction)	75
2.A.5	Results from the DFT calculation of binding energies of H^* to various sites on the (modified) $\text{CoO}(100)$ surface	75
2.A.6	XRD patterns for Co_3O_4 (JCPDS 00-042-1467, blue line) and CoO (JCPDS 00-048-1719, red line) nanopowder reference samples	76
2.A.7	Structure and morphology of CoS_2 nanoparticles, as characterized by XRD (a) and TEM (b)	76
2.A.8	Tafel plots of the (a) specific activities and (b) mass activities of cobalt oxide (CoO_x), oxysulfide ($\text{CoO}_x\text{S}_{0.18}$) and sulfide (CoS_2)	77
3.1	Schematic of the etching process	96
3.2	Schematic and TEM images of the etching of Cu_{2-x}S pure nanocrystals (SC-NPs; a–c) and Cu_{2-x}S – ZnS heterostructures (H-NPs; d–i) by trialkylphosphines	98
3.3	X-ray diffraction analysis of structural changes in pure Cu_{2-x}S nanocrystals (SC-NPs) during etching	102
3.4	TEM images of heterostructured ZnS – Cu_{2-x}S nanoparticles (H-NPs) before (a, d) and after etching (b, e)	103
3.5	Optical properties of Cu_{2-x}S nanostructures after etching using tributylphosphine	108
3.6	Cu_{2-x}S oxidative etching into Cu- and S-containing species	113
3.7	Summary of proposed mechanism for etching of Cu_{2-x}S	115
3.8	Anisotropic etching in the presence of low concentrations of phosphine	118
3.9	Crossover from anisotropic to isotropic etching behavior in the presence of TOP	120

3.A.1	Exemplary TEM image of etched Cu_{2-x}S -ZnS heterostructures isolated from the cation-exchange reaction	129
3.A.2	High-resolution TEM image of initial Cu_{2-x}S nanocrystal	130
3.A.3	Closer view of isotropically etched Cu_{2-x}S nanocrystals showing small clusters that are believed to form by aggregation of Cu and S removed from the larger nanocrystals during etching	130
3.A.4	Effect of atmospheric exposure on the observed phase of Cu_{2-x}S in SC-NPs (a) and H-NPs (b,c)	131
3.A.5	Summary of the observed LSPR peak positions for nanoparticles in which the volume of the Cu_{2-x}S region was changed by etching	132
3.A.6	Preservation of heterostructure morphology in the presence of excess ligands of different types	132
3.A.7	TEM image of the heterostructured NPs after 1 hour of the etching reaction with TOP	133
3.A.8	TEM image of Cu_{2-x}S SC-NPs with faceting/hollowing and slightly reduced diameter due to etching by oleylamine (few mg/mL) in toluene	133
3.A.9	Purely isotropic etching behavior observed in “cross-over” experiment using ceric ammonium nitrate (CAN)	134
3.A.10	Titration of particle volume with $(\text{NH}_4)_2\text{Ce}(\text{NO}_3)_6$ (CAN), which may also be used as the oxidizing agent in the etching reaction	134
3.A.11	Anisotropic etching behavior observed by adding smaller amounts of TBP followed by allowing oxidation of the phosphine to run to completion over 8 hours in hexane	135
4.1	Schematic of isothermal transformation regimes observed with in situ XRD during the cation exchange of PbS NCs with Cd^{2+} at 100–200 °C	149
4.2	X-ray data (left) from the cation exchange of Cd^{2+} with PbS NCs at 200 °C	151

4.3	Intensity ratio I_{111}/I_{200} of the first two diffraction peaks (111) and (200) during cation exchange of PbS to CdS	153
4.4	Fitted (111), (200), and (220) peak positions from in situ XRD data for the cation exchange of 7 nm PbS NCs to CdS	155
4.5	Debye scattering equation simulations of the diffraction patterns for PbS@CdS core-shell NCs with increasing thickness of the CdS shell	158
4.6	Extracted peak widths for the cation exchange runs from Figure 3	161
4.7	High-resolution TEM imaging of PbS and PbS@CdS NCs	166
4.8	Raman spectra of PbS@CdS NCs, where the CdS shell was grown at the indicated temperature for 1 h	167
4.9	Typical single-exponential fits of the evolution of the (220) peak position for cation exchange at 120 and 150 °C (from Figure 4.4) at very short times	173
4.10	Arrhenius plots of interdiffusion coefficients, \tilde{D} , for ionic transport (Pb and Cd diffusion through shell) extracted from (220) data	176
4.A.1	PbS nanocrystals before cation exchange	208
4.A.2	Intensity ratio I_{111}/I_{200} of the first two diffraction peaks (111) and (200) during cation exchange of PbS to CdS (second experiment)	209
4.A.3	Fitted (111), (200), and (220) peak positions from in-situ XRD data for the cation exchange of 7 nm PbS NCs to CdS (second experiment)	210
4.A.4	From right to left: Contaminant position, intensity, and width from experiment 1 (top) and experiment 2 (bottom)	211
4.A.5	Results for the peak integrated intensity ratio, I_{111}/I_{200} , from fitting of Debye simulations of PbS@CdS core-shell NCs	211
4.A.6	Extracted peak widths for the cation exchange runs from experiment 2	212
4.A.7	Instrumental broadening increases the apparent width of PbS lines in experiment 1, which uses a 3.2 mm diameter capillary, versus experiment 2,	

which uses a 1.1 mm capillary	212
4.A.8 Results for peak width from fitting of Debye simulations of PbS@CdS core-shell NCs	213
4.A.9 Example of geometry used during DFT calculations for the (001) surface energy	213
4.A.10 Unit cells of PbS and CdS showing their crystallographic relationship	214
4.A.11 Raman spectrum of PbS NCs	214
4.A.12 Raman spectra of PbS@CdS nanocrystals in which the CdS shell was grown at 120° or 200°C for various times	215
4.A.13 Arrhenius representation of extracted rate constants from whole-curve fitting of the (220) peak position showing poor linearity	216
4.A.14 Shrinking core model values for experiment 1 (top) and experiment 2 (bottom)	217
5.1 Schematic of surface treatments to remove ligands from metal oxide surfaces for electrocatalysis	233
5.2 Transmission electron microscopy assessment of morphology and structure of Mn ₃ O ₄ nanocrystals subjected to various treatments	237
5.3 Surface chemistry of Mn ₃ O ₄ nanocrystals subject to various treatments	240
5.4 Thermogravimetric analysis in flowing air atmosphere of unsupported Mn ₃ O ₄ nanocrystals subjected to various treatments	247
5.A.1 BF-TEM observations (top) of Mn ₃ O ₄ etching in unsupported NCs subjected to ligand-removal treatment after deposition on a grid from colloidal solution	255
5.A.2 BF-TEM observations (top) of Mn ₃ O ₄ etching in unsupported NCs subjected to ligand-removal treatment in solution	256
6.1. High-resolution location of atomic bond lengths in real space through analysis of the pair distribution function obtained by x-ray total scattering	271

6.2	Example of pair distribution functions (PDFs) obtained from 7 nm PbS nanocrystals (top) and core-shell PbS@CdS nanoparticles (bottom)	273
6.3	Results of attempted anion exchange at 200 °C of Mn ₃ O ₄ to MnO _x S _y or MnS _z using ammonium sulfide, (NH ₄) ₂ S	276
6.4	Diagram of the gas-liquid phase sulfurization apparatus	279
6.5	Example of quantitative 3D structural characterization of a FePt nanoparticle	284
6.6	X-ray diffraction patterns of α-Cd ₃₇ S ₂₀ assemblies in various experimental configurations	289
6.7	Examples of asymmetrical lineshapes with heavy large-angle tails	292
6.8	Intensity distributions for one- and two-dimensional crystals in reciprocal space	293
6.9	Powder diffraction line shapes for a single reflection at location (hkl) = (600) determined by numerical integration of Equations 6.3 and 6.4	294
6.10	Assembly of a toy model of a molecular aggregate	296
6.11	Simulated reduced structure factors for molecular chains with different numbers of stacked benzene molecules	297
6.12	Smoothed pair distribution functions for molecular chains from transformation of the reduced structure factors	298
6.13	Effects of disorder types on reduced structure factors for flexural, spacing, and isotropic thermal disorder (a, b, and c, respectively)	300
6.14	Structures of some flat polycyclic aromatic hydrocarbons (a) and reduced structure factors for their aggregates (b)	304
6.15	Example of a one-dimensional “aggregate” structure in a metal-containing columnar liquid crystal with staggered M ₂ O ₈ centers	306
6.16	Example of an aggregate-forming dye, pseudoisocyanine (PIC)	307

LIST OF TABLES

2.A.1	Structural data extracted from the rotationally averaged SAED patterns of CoO _x S _y nanoparticles given in Figure 2.A.1	67
2.A.2	Results of the DFT calculations for the binding energy of H	71
4.A.1	Experimental parameters for in-situ x-ray diffraction at CHESS A1	191
4.A.2	Results of density functional theory calculations for surface energies, in meV Å ⁻² , of PbS slabs capped with varying numbers of CdS(rs) and CdS(zb) monolayers	198
4.A.3	Enthalpies of formation ΔH_f , in eV atom ⁻¹ , for neutral point defects in PbS, CdS(rs), and CdS(zb) calculated using DFT	199
4.A.4	Results of density functional theory calculations for diffusion barriers	199
4.A.5	Parameters for the double-exponential fit to the value of Q_{220} in Figures 4.4 and 4.A.3	200
4.A.6	Parameters for the second-order rate law fit to the value of Q_{220} in Figures 4.4 and 4.A.3	201
4.A.7	Exponential-fit parameters for the value of Q_{220} at short times in Figures 4.4 and 4.A.3	202
4.A.8	Arrhenius parameters for the rate constants of Table 4.A.7	202
4.A.9	Parameters from extraction of effective diffusion coefficients using Fick's second law	204
4.A.10	Shrinking core model parameters for determining the chemical diffusion coefficient	207
4.A.11	Reference data points for self-diffusion coefficients in materials given in Figure 4.10	207
4.A.12	Arrhenius parameters for the chemical diffusion coefficients of Tables 4.A.2,3	207

	208
5.1 Assignment of functional groups from infrared bands	241
5.2 Effectiveness of ligand removal procedures for various surface chemistry outcomes	249
5.A.1 Statistical comparison of nanoparticle size distributions	257
5.A.2 Specific charge derived from three independent CV measurements on nanoparticle-carbon composites for each ligand-removal method	257
6.1. Thermodynamic analysis for some anion exchange reactions of oxides to sulfides	277

CHAPTER 1

1 INTRODUCTION

1.1. COLLOIDAL NANOCRYSTALS AND THEIR TRANSFORMATIONS

The study of objects with dimensions on the order of one billionth of a meter, called nanoscience, now occupies a prominent place in the scientific consciousness. This work concerns nanoparticles that can be described as nanometer-size sections of bulk solids and details their surface and transport properties and how they change under chemical transformation. It extends prior work on the replacement of cations and anions in ionic nanocrystals and demonstrates the usefulness of such exchange reactions to provide insight into surface chemical reactions, improve the performance of energy conversion materials, and measure transport coefficients at short length scales. In each project described here, the integration of several complementary techniques, including x-ray and electron diffraction, optical spectroscopy, electrochemical analysis, and first-principles calculations provides a more complete picture of the underlying physicochemical principles governing the reactivity of colloidal nanoparticles.

Nanoparticles lie at an intermediate scale between bulk materials and molecules or atoms in terms of both length and physicochemical characteristics. The truncation of materials at the nm scale produces substantial changes in their properties: nearly all atoms in a nanoparticle are close to the surface. Some phenomena resulting from a reduction in the size of a solid domain are shown in **Figure 1.1**. Confinement of electronic wave functions and excited states in a semiconductor nanocrystal gives rise to the famous size-dependent absorption and emission spectra of quantum dots (QDs), which have drawn so much attention since the end of the last century.¹⁻⁴ Basic

thermodynamic properties change. For example, the phase transition temperatures such as the melting points of nanoparticles decrease with their size as a result of the competition of the energy of surface formation with the latent heat of the phase transition.⁵⁻⁷ Owing to the proximity of the solid surface, which can react with the external environment, the properties of nanoparticles can change depending on their surface environment as well. Trap states at surfaces strongly influence the photoluminescence quantum yield in colloidal semiconductors, which means that chemical intervention with passivating molecules or surface layers is required to preserve the unique advantages of QDs.^{4, 8, 9}

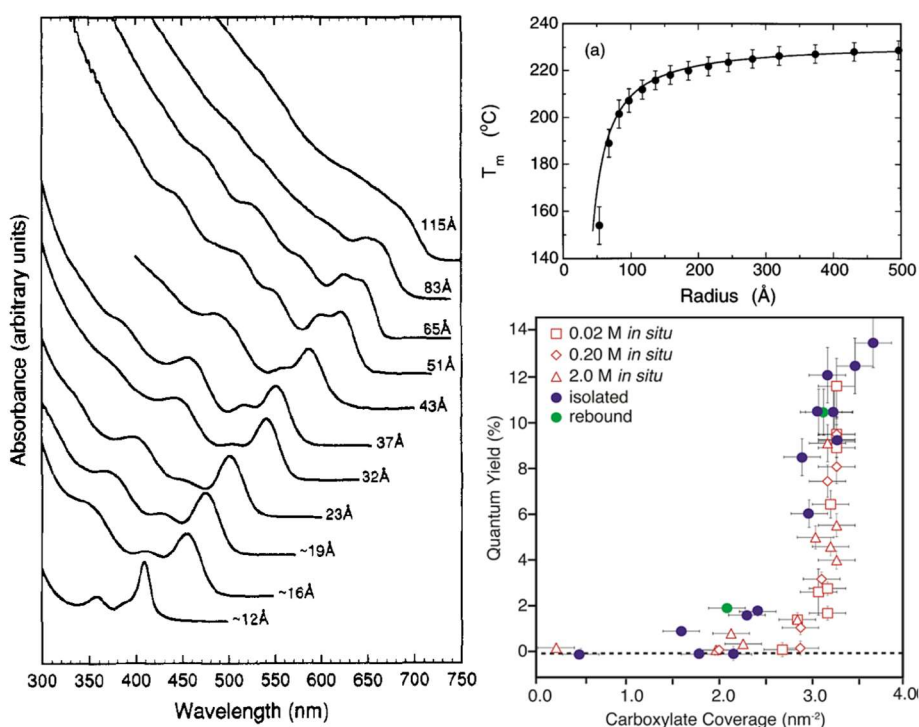


Figure 1.1. Size and surface chemical control of thermodynamic, electronic, and structural properties of materials. Left: size-dependent absorption spectra of CdSe nanocrystals. Reproduced from figure 3 of reference 1 by permission of the American Chemical Society. Upper right: size-dependent melting point of Sn nanocrystals. Reproduced from figure 2 of reference 5 by permission of the American Physical

Society. Lower right: Photoluminescence quantum yield versus ligand coverage for CdSe nanocrystals. Reproduced from figure 4 of reference 8 by permission of the American Chemical Society.

Colloidal systems are of great interest to scientists in many disparate areas due to the relative accessibility of solution-phase chemistry in both academic and industrial respects. In order to realize proposed low-cost solution processing schemes for future electronic, optical, and energy conversion applications, researchers have confronted the difficulties of surface science in two major stages. First, design principles for synthesizing nanoparticle building blocks had to be formulated. To ensure uniformity of the properties of an ensemble of colloidal particles, a desirable feature is a narrow (monodisperse) distribution of sizes about the mean particle diameter. Although the synthesis of monodisperse colloids with sizes below the resolving power of the human eye has a long history,¹⁰⁻¹² synthetic coverage of particle sizes in the nanometer range with near-monodispersity has been achieved only relatively recently.^{1, 2} Still, with an enormous investment of resources from a generation of chemists and physicists over the last few decades, techniques for the synthesis of monodisperse nanoparticles of many different compositions have reached a high degree of refinement.¹³⁻¹⁷

Work continues apace on extending newly developed synthetic methods to more complex systems,^{18, 19} but a fruitful second avenue of research has continued to build upon these foundational syntheses. With their high surface-area-to-volume ratio, colloidal nanoparticles react readily with their surroundings.²⁰ Like molecules, they undergo rearrangement, functionalization, and disproportionation based on those reactions. This has led to much work on the postsynthetic transformation of nanomaterials, developments in which have helped to begin solving important

problems.²¹ The properties of many useful engineered materials are not inherent to perfect crystalline solids in thermodynamic equilibrium but have been added by control over their processing history. Likewise, the “perfect” monodisperse building blocks of simple materials can be modified to achieve properties inaccessible by synthesis in one step. For example, an important problem following the synthesis of QDs for optical and electronic applications was how to achieve and maintain luminescence by suppressing trap formation at QD surfaces and “blinking.”⁴ This objective appeared not to be possible “out of the box” in one synthetic step, but appropriately applied chemical transformations, specifically the growth of a shell on the particle surface to form core-shell QDs,²²⁻²⁴ made possible the preparation of bright and stable light sources retaining all the advantages of QDs such as narrow emission linewidth. The approaches of surface modification and multistep growth have formed a large part of the literature on chemical transformations of nanoparticles.

This work uses chemical transformations to examine the properties of nanoparticles not just in terms of their surface modifications but also with regard to the internal mobility of the atomic constituents below the particle surface. A simplistic picture of nanoparticle surface as reflecting the simple attachment and detachment of functional groups and ions to a smooth face of a crystal lattice does not adequately reflect the actual atomic arrangements at a solid-liquid interface. The creation of a surface or interface entails a sharp change in the energy levels of nearby electrons as dangling bonds are created, and the relaxation of the surrounding atoms to bring the system into local equilibrium can give rise to significant reconstructions extending some distance into the underlying atomic layers.²⁵⁻²⁸ These changes in surface energy strongly affect nanoparticle stoichiometry, electronic properties, and phase stability, as shown above. Earlier work has left important aspects of nanoscale solid-state chemistry decidedly less well-explored than the (admittedly still important) area of

nanomaterials synthesis. These aspects discussed in the following chapters are all tied to the connection of the surface species to the underlying material.

- First, on an empirical basis the replacement of ions in binary nanocrystalline solids has been shown to greatly expand the accessible scope of useful materials when mixed-cation systems are constructed, but the possible benefits of anionic replacement are not as well-established.
- Second, highly nonstoichiometric, chemically “soft” materials react strongly to changes in surface properties, which should include changes in nanoparticle ligand shells, but the extent and uses of these changes are not well-characterized.
- Third, the actual rates at which atoms move when they are close to a free surface are difficult to measure, and chemical transformations of nanomaterials offer new ways in which to perform these measurements. Knowledge of the transport properties at short length scales will be critical for future nanoparticle devices, as the migration of atoms away from their designed positions becomes more detrimental to performance as the relevant dimensions of the material become smaller.
- Finally, the divergence of empirical approaches in the literature for surface treatments of nanoparticles has made “standardization” of the properties and structures of nanoparticle surfaces and subsurfaces difficult to establish. Actual comparative studies of the effects (and effectiveness) of different treatments are needed to address these uncertainties.

1.2. OUTLINE

This chapter introduces important concepts in the synthesis, transformation, and characterization of colloidal nanoparticles; elaborations on these themes are presented in the forthcoming material. Ion exchange in nanoparticulate solids is the

main experimental technique underlying the syntheses and modifications conducted in this work. The intended outcomes were threefold: 1) prepare more active metastable materials for future energy applications, especially electrocatalysis; 2) characterize the possible impact of surface treatments and reactions on underlying nanoparticle structure; and 3) perform accurate measurements of the rate of ionic transport at nanometer length scales. The main technique used in confirmation and description of the structural transformations was the diffraction of x-rays and electrons, with a secondary emphasis on spectroscopic and electrochemical methods.

- **Chapter 2** utilizes a previously developed technique of anion exchange in ionic nanocrystals to synthesize a metastable oxysulfide nanoparticle catalyst having optimized activity relative to either end-point composition in the cobalt oxide-cobalt sulfide system spanned by the achievable extent of anion exchange. The metastability of this oxysulfide can be shown by observing a lattice expansion upon doping hollow CoO particles with a small amount of sulfide anion, which disappears when the particles are annealed. Density functional theory calculations corroborate the trend observed electrochemically by showing that the hydrogen binding affinity to CoO surfaces, with O^{2-} replaced with increasing amounts of S^{2-} , reaches a value closest to that of an ideal catalyst, Pt, at a specific, small level of anion exchange.
- **Chapter 3** characterizes in more detail the lability of an emerging class of nanomaterials, the copper chalcogenides, by identifying a side reaction between a commonly used nanoparticle surfactant, trialkylphosphine, and the underlying nanocrystal core with its highly mobile cations. Under oxidizing conditions the phosphine acts to dissolve the redox-active chalcogenide material and change its structure and optical properties. The mechanism of this reaction involves coupling between the cation and anion oxidation states through reductive abstraction of the

anion enabled by oxidative dissolution of the cation. This reaction enables a new dimension of post-synthetic tuning of nanostructures by chemically selective etching.

- **Chapter 4** explores in detail the solid-state processes underlying the growth of core-shell semiconductor heterostructures by diffusive cation exchange. The case of PbS-core—CdS-shell (PbS@CdS) quantum dots is used as a model system for using synchrotron x-ray diffraction to identify the presence of metastable phases and quantify solid-state diffusion kinetics in nanoparticles. A more careful consideration of the kinematical theory of x-ray diffraction in epitaxially structured nanoparticles explains some observations of lattice distortion and symmetry breaking in nanoparticle structure. With these effects controlled for, detailed kinetic data allow separation of surface- and sub-surface-controlled processes and show that, likely due to the production of crystalline defects in a sharp chemical potential gradient, increase the rates of interdiffusion by factor of as much as 10^4 in nanocrystals.
- **Chapter 5** deals with a problem of lingering concern to the previous work, the need for a reproducible strategy to minimize or eliminate the role of colloidal nanoparticle ligands on their subsequent characterization or transformation. Because clean surfaces are desired in many applications, numerous groups working with colloidal nanoparticles have taken widely divergent approaches to remove the ligands which are crucial to the syntheses of well-defined nanoparticles. However, not as much attention has been given to identifying their relative effectiveness. **Chapter 5** thus compares some widely used methods for the postsynthetic cleaning of nanoparticles using an important redox-active electrocatalytic oxide material, Mn_3O_4 , as a test system, and shows that alkylation of surface ligands is a promising alternative to widely used high-temperature annealing processes that may destroy metastable nanoparticle structures.

- **Chapter 6** summarizes the results of **Chapters 2-5** and presents preliminary results from experiments following from the publications therein. Key among these are the generalization of the anion exchange reaction in **Chapter 2** and the expansion of the scope of the x-ray diffraction analysis through use of total scattering and pair distribution function analysis. Finally, **Chapter 6** discusses a more extensive preliminary investigation of the pair distribution function analysis of (what are called here) internally correlated nanomaterials, specifically aggregates of molecules or clusters with well-defined interparticle correlations. Some principles for interpreting unusual features of x-ray data are presented along with future experiments to confirm the theoretical analysis, which could be useful for determining intermolecular configurations in molecular aggregates or mesophases.

1.3. AREAS OF EXPLORATION

1.3.1. Examples of chemical transformations of nanoparticles

Presented here are studies of how these reactions, called chemical transformations of nanoparticles, change the properties of the material at and beneath the surface. Transformations may take place through adding, substituting, removing, or rearranging atoms in a nanostructure, all of which are considered in one way or the other in **Chapters 2-5**. The results of some representative chemical transformations of nanomaterials are shown in **Figure 1.2**.

A major class of transformations considered in this work is the process of cation or anion exchange, an example of which is at top in **Figure 1.2**. Here, Robinson et al.²⁹ produced nanorods where Cd atoms in CdS have been partially replaced with Ag, and the resulting Ag₂S domains spontaneously arranged themselves at regular intervals. In other words, a superlattice (a feature normally associated with complex

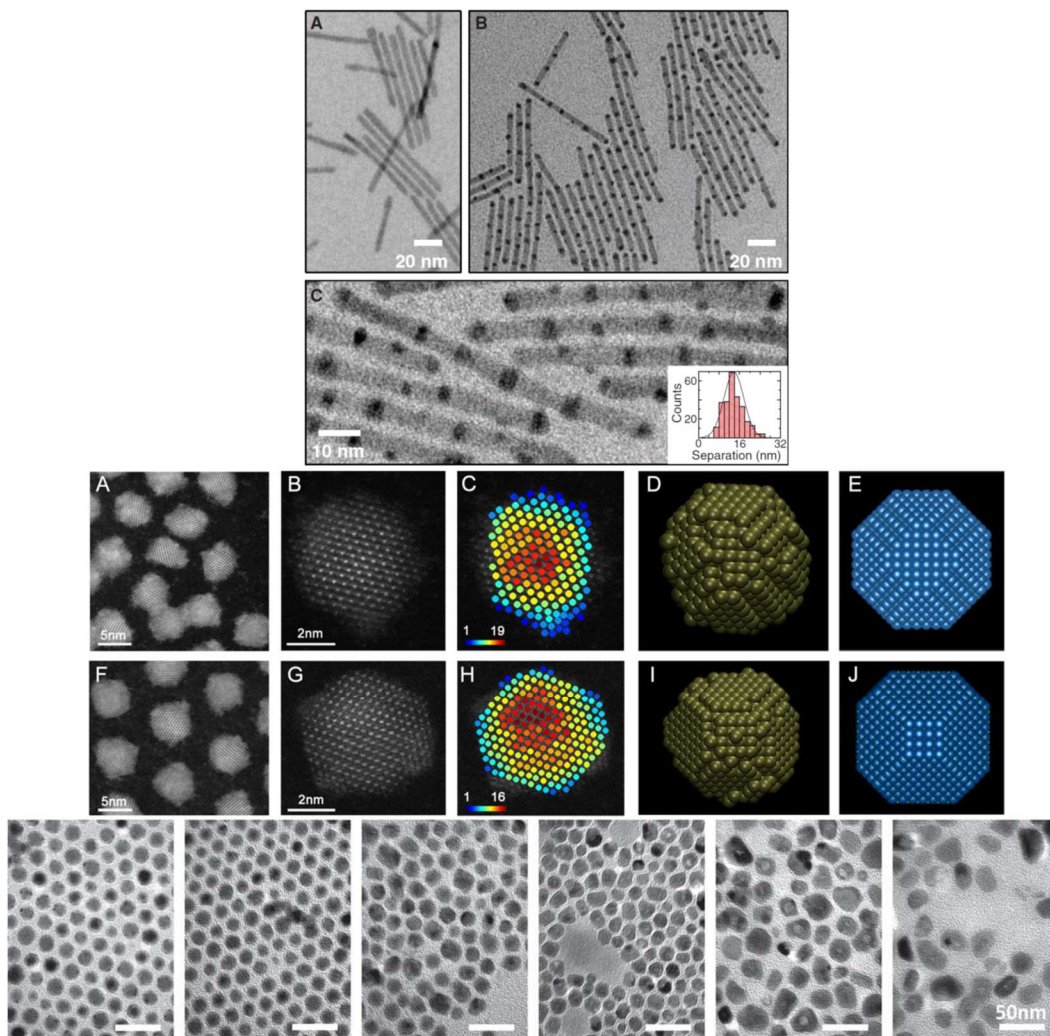


Figure 1.2. Examples of chemical transformations of nanomaterials. Top: partial cation replacement in CdS nanorods with Ag produces a spontaneously ordered linear superlattice of CdS and Ag₂S domains. Reproduced from figure 1 of reference 29 with permission of the American Association for the Advancement of Science. Middle: Ligand-induced reshaping of semiconductor nanocrystals. Reproduced from figure 4 of reference 31 under the CC-BY-NC-ND license. Bottom: phosphidization of cobalt metal nanocrystals produces core-shell cobalt-cobalt phosphide and eventually hollow cobalt phosphide nanoparticles. Reproduced from figure 2 of reference 30 with permission of the Royal Society of Chemistry.

and expensive vacuum deposition technologies) was formed within a nanorod through solution techniques alone. Below that, Peters et al. demonstrated a total redistribution of atoms around PbSe nanoparticles in the presence of excess capping ligands and ions in solution changed the chemical potential of each nanocrystal facet, thereby causing dissolution and reprecipitation of PbSe until facets had grown or shrunk in accordance with the altered surface energies. At bottom in **Figure 1.2**, another transformation is shown where the controlled phosphidization of Co metal nanoparticles by Ha et al.³⁰ produced metal-metal phosphide or metal phosphide nanoparticles of complex morphology and controlled phase. The process of phosphidization entailed the diffusion of P and Co in different directions as well as redistribution of atoms at the surface, and the greater mobility of Co relative to P resulted in the formation of an unusual hollow structure due to vacancy generation in the core.

1.3.2. Chemical transformations of nanoparticles: ion exchange

Chapters 2 and 4 of this work focus on the replacement of ions in binary ionic nanocrystals with a different type of ion to form new phases in the resulting nanoparticles. In wider industrial and scientific usage, ion exchange is understood as the charge-balanced displacement of cations or anions from an appropriate substrate (host), such as an ionic polymer, glass, or mineral, bearing outward-facing counterion moieties. Such materials are very useful in separation, extraction, and sequestration of ions in solution.³² However, ion exchange substrates are not limited to materials with comparatively “exposed” ion adsorption sites. In materials with relatively high ionic mobility, the sublattice with the slower-diffusing component (usually the anion) can serve as a rigid framework through which incoming and outgoing ions (usually cations) are redistributed between the solid and solution state in accordance with mass action and thermodynamics.³³⁻³⁵ This was brought to the attention of the wider

nanoparticle research community in a 2004 report³⁶ which demonstrated the highly reversible metathesis reaction of solvated Ag ions with colloidal nanocrystals of CdSe:



In this case, the observation of cation exchange was made possible by the high reactivity of nanoparticle surfaces and short diffusion lengths involved in replacing host cations. At room temperature, the movement of ions through NCs 4 nm in diameter is fast enough that Cd can be displaced quantitatively by incoming Ag in less than 1 s. An illustration of this process and its effects on CdSe nanocrystals is shown in **Figure 1.3**.

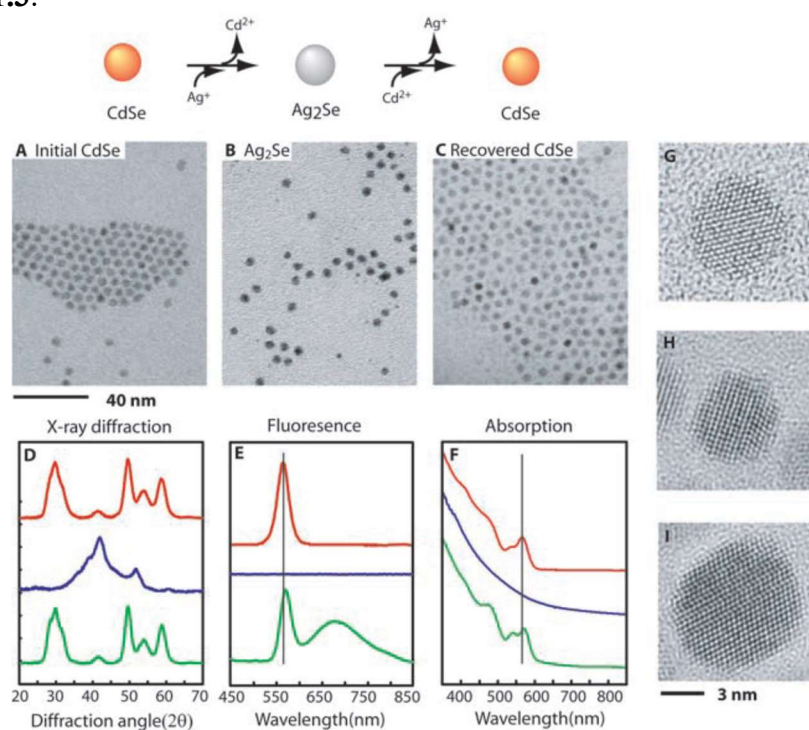


Figure 1.3. Cation exchange as a shape- and structure-preserving transformation of nanomaterials. Reproduced from figure 1 of reference 36 by permission of the American Association for the Advancement of Science.

With some caveats, the exchange reaction is shape-, size-, and structure-preserving. Spherical wurtzite CdSe NCs are converted to monoclinic Ag₂Se and

revert to wurtzite upon back-exchange without losing their sphericity (top). Quantum-confined electronic properties are also conserved, as indicated by the energies of CdSe fluorescence and absorption lines very nearly returning to their original positions (bottom). However, broad emission bands from trap luminescence, stacking faults, and agglomerates remain following reverse exchange (**Figure 1.3** lower center and right, respectively), indicating some involvement of anionic components in cation exchange as well. Additionally, the original report noted some size dependence of the reactivity, showing that very small nanorods had fully mobile anions and reverted to spherical shapes after cation exchange.³⁶ Despite those irregularities, further developments indicated that many complex morphologies in nanoparticles were stable over cycles of cation exchange, including high-aspect-ratio shapes like rods and tetrapods, core-shell structures, and dot-in-rod geometries.³⁷ For cation exchange in semiconductor nanocrystals, the assumption of a more or less rigid anion sublattice has generally been found to be acceptable for ionic nanostructures having a smallest dimension of more than a few nm, as validated by morphology conservation and specialized optical measurements.³⁸

Cation exchange is regarded as a promising tool for the transformation of nanoparticles to device-ready forms because features can be added post-synthetically that are impossible to accomplish by a direct synthesis.^{33,34} That is, cation exchange is usually possible at much lower temperatures than used in nanoparticle synthesis, and so metastable structures produced by controlled ionic substitution can be kinetically prevented from reverting to a more thermodynamically favorable form. Research has on numerous occasions demonstrated the kinetic trapping of nanocrystals with spontaneously formed superstructures^{29,39,40} and with phases not observed in the bulk.^{37,41,42} These techniques have been put to use in improving the performance of nanomaterials for energy applications, especially photovoltaics and emitters.⁴³⁻⁴⁵

Chapter 4 studies in detail the effects of cation exchange with Cd on PbS nanocrystals.

Ion exchange may also be carried out with anions. In semiconductors such as Cd chalcogenides and transition metal oxides, the size of the anion is usually much larger than that of the cation (hence the rigidity of the anion sublattice that allows cation exchange). However, under the appropriate conditions and with suitable sources of anion,⁴⁶⁻⁴⁸ transformations e.g. from oxides to chalcogenides can also be executed.

Chapter 2 discusses the transformation of cobalt oxide to cobalt sulfide and, by partial exchange, to cobalt oxysulfide. A particularly important utilization of anion exchange in the current literature is in the tuning of the lead halide perovskite nanocrystal properties,⁴⁹⁻⁵¹ which has seen a storm of work in recent years due to the defect tolerance and hence agreeable optoelectronic properties of these materials. In that system, the halide anions are instead smaller than the large Pb cations. The conclusions drawn in **Chapter 4** on cation exchange will be equally applicable to the charge-reversed case of anion exchange.

1.3.3. Nanocrystal surface and interface science

Because single-domain shape-controlled nanocrystals can be prepared using modern colloidal synthetic techniques with a high degree of crystallinity and uniformity, ensembles of nanocrystals produce a sample that is nearly entirely “interface,” greatly increasing the accessible sub-surface volume for probes that would otherwise be restricted by, for example, the very limited surface area of a large single crystal. The chemistry of solid-liquid interfaces is central to nanoparticle synthesis and transformation. Through post-synthetic modification, solid-solid interfaces or heterojunctions can also be formed in nanoparticles. Cation exchange has notably been put to that purpose.

Rather than being abrupt terminations of a solid domain, nanoparticle surfaces and phase or grain boundaries can lead to significant reconstruction of the atomic configuration in their vicinity. Reconstruction can be due to surface energy effects, as demonstrated in the center of **Figure 1.2**,³¹ or to strain imposed by a nearby solid phase boundary.³⁹ Solid-solution nanoparticle interfaces have been observed to cause ordering of nearby solvent molecules²⁵ as well as amorphization or “melting” of subsurface atoms in the particle,²⁶ phenomena which have previously been demonstrated in surfaces of bulk materials.^{27, 52}

Chapters 3 and 5 discuss the impact of surface chemistry on nanoparticle structure. An important theme is that the primary mode of tuning in nanoparticle synthesis, the use of surfactant ligands to control precursor conversion and monomer attachment, is ostensibly for size and shape control but remains a critical determining factor of all aspects of the final product, including crystal structure and stoichiometry.^{20, 53, 54} The effects are especially pronounced in chemically “soft” materials with many accessible phases. Many such materials are found in the family of metal chalcogenides,^{18, 19} which have been the primary targets of advanced nanoparticle syntheses. Far from being simple protecting groups to prevent nanocrystals from agglomerating, in many cases ligands react vigorously with nanoparticles.⁵⁵⁻⁵⁷

The same ligands are frequently also used for solvation of nanoparticle precursors, and an excess of ligands can accordingly lead to dissolution of the nanoparticles under the right circumstances. **Chapter 3** provides a striking example of such a reaction where an alkylphosphine ligand required for cation exchange in copper sulfide, Cu_{2-x}S , can also dissolve the material. The affinity of ligands for different components of a nanocrystal can lead to selective leaching or deposition of ions, as demonstrated for example in the extraction of anions or cations from various types of

transition metal chalcogenides. As mentioned previously, the redistribution of both cations and anions in PbSe in an excess of ligand³¹ suggests that many atoms below the surface of a nanoparticle exist in dynamic equilibrium with the solution in which the host nanocrystals are suspended.

In some cases, surface treatment can lead to intracrystal redistribution of atoms, without need for dissolution or reprecipitation. Phase changes in Cu chalcogenides upon treatment with reducing or oxidizing agents are proposed to reflect the migration of Cu to core or surface regions.⁵⁸⁻⁶⁰ The author has helped to demonstrate in a separate project⁶¹ that a change in the chemical potential boundary conditions at the surface of a semiconductor cluster can be used to reversibly switch its phase from zincblende- to wurtzite-like in a diffusionless phase transformation.

1.3.4. Aspects of x-ray and electron diffraction and imaging

A powerful structural characterization technique is required in providing one half of the structure-property relationship in chemically transformed nanomaterials. The diffraction of highly penetrating radiation, such as x-rays and high-energy electrons, from arrangements of atoms (both regular and irregular) has been utilized for material structure determination since Bragg's historic work.⁶² von Laue demonstrated that diffraction of waves from a regular array of points produced sharp maxima, or peaks, in the scattered wave intensity at specific angles relative to the array.⁶³⁻⁶⁵ X-rays have a wavelength, λ , on the order of 1 Å, comparable to the distances between atoms, and as a result elastically scattered (diffracted) x-rays are deflected at angles very accessible to experiment. This early work led to an understanding of diffraction from crystals as reflection of x-rays at Bragg angles, θ (measured as 2θ experimentally), from stacks of planes of atoms separated by an interplanar spacing d . This is summarized in what is now known as Bragg's law:

$$n\lambda = 2d \sin \theta \quad (1.1)$$

The integer n is a multiple of the wavelength (or fraction of the interplanar spacing). The interplanar spacings can be related to the true three-dimensional structure of the object by exploiting the symmetry of the crystal to determine “allowed” reflections, followed by location of the atoms through the calculation of a structure factor, F_{hkl} , determined by the scattering power of the atoms. This Bragg formalism is the basis of modern crystallography in the kinematical limit, where x-ray scattering is purely elastic and multiple reflections do not occur. To accommodate the imperfections of real experiments, numerous corrections have been added over time which rely on the shape, width, and intensity of Bragg reflections. Analysis of these parameters give information not only on the instrumental aberrations introduced but more importantly on defects in the crystal. One correction which is frequently applied to nanoparticles is for their finite domain size, d , which broadens the Bragg reflection into a Gaussian peak with a full width at half maximum (FWHM, β) approximately according to the Scherrer equation:

$$\beta = \frac{K\lambda}{d \cos \theta} \quad (1.2)$$

K is a geometrical parameter which is usually close to 1. In general, crystalline distortions contribute to the peak width as well. These include such factors as inhomogeneous strain, stacking faults, and other correlated atomic displacements.

Bragg diffraction arises as a limit in infinitely large crystals from coherent scattering of x-rays, neutrons, or electrons from the particles making up a crystal (largely electrons for incident x-rays and electrons, and nuclei for neutrons). **Figure 1.4** shows a representation of this effect. Rays with wavelength λ encounter a pair of particles with incident wavevector \mathbf{k} and are scattered along a different wavevector \mathbf{k}' . In Bragg diffraction \mathbf{k}' is a reflection of \mathbf{k} across a line perpendicular to the atomic

plane, with \mathbf{k}' forming an angle of 2θ relative to \mathbf{k} . The difference between wavevectors is equal to a momentum transfer $\mathbf{Q} = \mathbf{k}' - \mathbf{k}$, which is more general than 2θ because it is normalized for wavelength. The phase difference of the waves for \mathbf{k} and \mathbf{k}' is determined by the geometry of the interparticle distance vector, \mathbf{r} , and from this difference the intensity (amplitude squared) of the diffracted beam at that momentum transfer \mathbf{Q} can be calculated.^{64, 65}

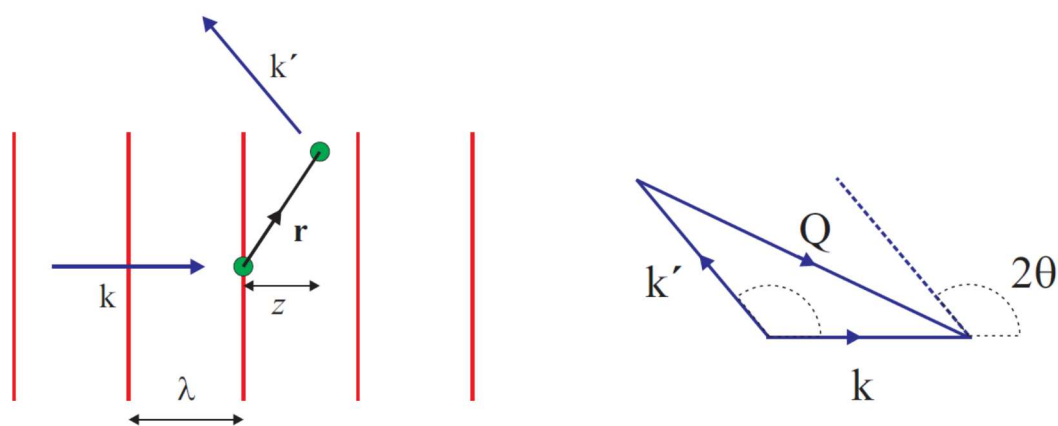


Figure 1.4. The scattering of electromagnetic waves by a pair of electrons.

Reproduced from figure 4.1 of reference 64 by permission of John Wiley and Sons.

An alternative approach to x-ray diffraction pattern analysis would thus be to calculate the scattered intensity directly from the collection of atoms from knowledge of the interaction between the incoming beam and each electron. Obviously, this is impractical for macroscopic objects which have an extremely large number (10^{21} - 10^{23}) of atoms per cm^3 , but this microscopic approach has become quite useful for diffraction calculations from nanoparticles. For particles less than 10 nm in diameter, calculating the scattering from all atoms (up to 10^4) is much more tractable with modern computing power.⁶⁶⁻⁶⁸ To perform calculations using atoms instead of electrons, for most purposes it suffices to use a pre-calculated atomic form factor f

(scattering power relative to a free electron) as a function of the momentum transfer Q .⁶⁹ As indicated in **Figure 1.4**, constructive and destructive interference arise from phase differences between beams scattered by pairs of particles. Therefore, the calculated intensity requires assessing this phase difference for every pair of atoms i and j (which have interatomic distance vector \mathbf{r}_{ij} and scatter the beam along some vector \mathbf{Q}_{ij}) in the nanoparticle. Summing each pair's contribution gives the overall intensity $I(\mathbf{Q})$ in three-dimensional reciprocal space.⁷⁰ A critical point here is that the sum of these intensities demonstrates that the intensity of the x-ray reflections, as a sum of periodic functions, is a Fourier transform of the interatomic vectors weighted by the atomic form factors:

$$I(\mathbf{Q}) = \sum_{i,j} f_i^* f_j \exp(i \cdot \mathbf{Q} \cdot \mathbf{r}_{ij}) \quad (1.3)$$

An asterisk indicates a complex conjugate for the form factor, which is usually not very important far from an x-ray absorption edge.⁶⁴ A convenient form of this sum for nanoparticle diffraction calculations was laid out by Debye in 1915.⁷¹ Averaging $I(\mathbf{Q})$ over all orientations allows the one-dimensional diffraction pattern $I(Q)$ to be calculated as a function of directionless interatomic distances r_{ij} .

$$I(Q) = \sum_{i,j} f_i^* f_j \frac{\sin Qr_{ij}}{Qr_{ij}} \quad (1.4)$$

Accordingly, this is referred to as the Debye scattering equation. The process of averaging is illustrated in **Figure 1.5**. Numerous programs have been written to very quickly evaluate this function for arbitrary collections of atoms. In **Chapter 4**, **Equation 1.4**, in combination with experimental data, provides great insight into how different parts of a nanoparticle structure contribute to the overall scattering pattern.

This orientational averaging is also generally assumed by default in XRD experiments on nanoparticles (and other finely divided materials) which are generally

not condensed into a single orientation when prepared for analysis. The resulting intensities measured therefore make up what is called a powder diffraction pattern.⁷² The use of powder diffraction data with Bragg's law to find a correspondence of the measured interplanar spacings to a database of crystal structures measured in bulk samples is the most common mode of nanoparticle structure determination.

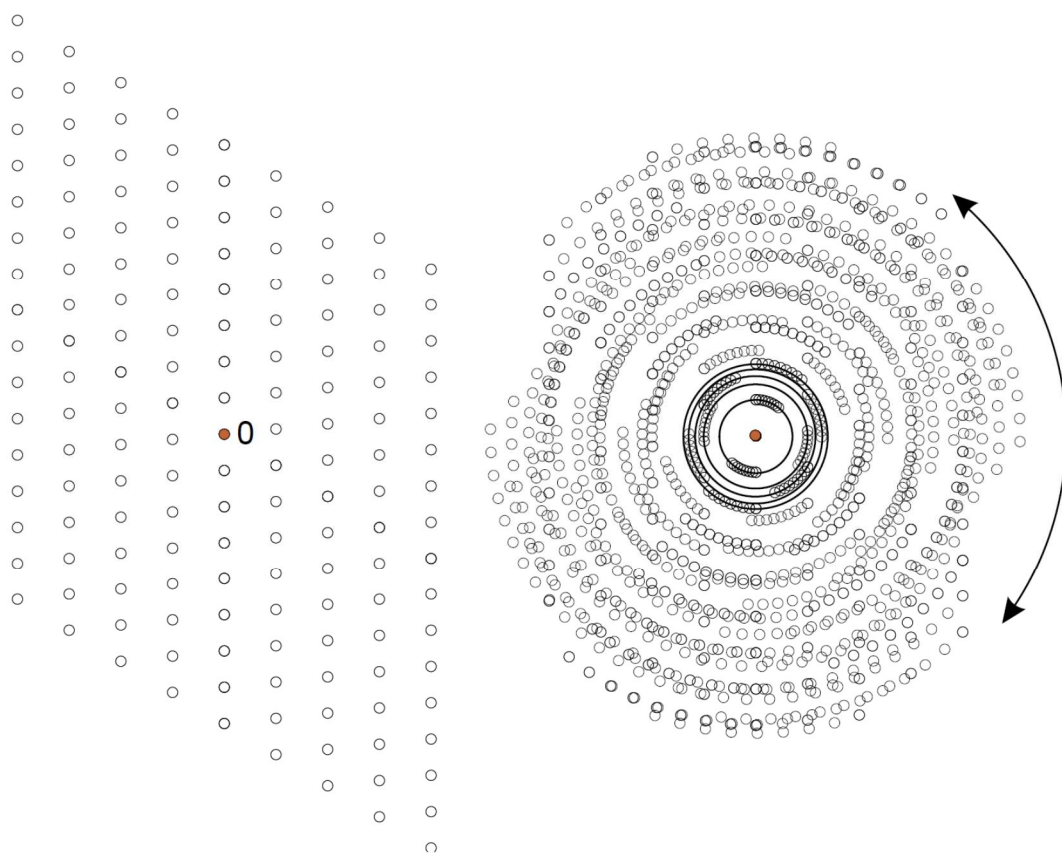


Figure 1.5. Averaging of intensities of a section of reciprocal space (left) over all orientations (right). This produces a powder diffraction pattern with rings instead of spots. Reproduced from figure 1.9 of reference 72 by permission of the Royal Society of Chemistry.

Electrons in a transmission electron microscope (TEM) are also used to form diffraction patterns.^{73, 74} Nearly all nanoparticle scientists, however, primarily use the TEM to image particles directly, since electrons can be focused like longer-wavelength light using electron optics. Because high-energy (100-200 keV) electrons have a much smaller effective wavelength (a few pm) than x-rays (0.1-1Å), the achievable resolution in the TEM can theoretically be far greater. Although modern resolution limits are still much greater than the electron wavelength due to the limitations of the optics, nanoparticle imaging is now routinely performed with resolving power on the order of 1 Å or less, where electron microscopy is generally referred to as high resolution TEM (HRTEM). At this scale lattice planes or fringes are resolvable. Although this approach is mostly not used in this work, a very important mode of operation in the TEM uses a scanned, tightly focused electron beam (hence scanning TEM, or STEM) to obtain images of atomic structure from the scattering of electrons at higher angles from columns of atoms along the incident beam axis. Because all scattered electrons collected by the optics originate from a specific point on the sample in STEM mode and contrast is largely only determined by the number of electrons in the path of the beam, STEM has become widely used also for chemically and electronically sensitive analysis of inelastically scattered electrons and x-rays produced by the beam-sample interaction.

1.3.5. Electrochemistry with nanoparticles

Chapters 2 and 5 of this work discuss the electrochemistry of chemically transformed nanoparticles. Nanoparticles have long been used in catalytic and surface chemical applications without special reference being made to their “nano” qualities.⁷⁵ Since major industrial processes depend on surface-bound catalytic reactions to proceed efficiently, the catalyst should naturally be as finely divided as possible to

maximize the surface-area-to-volume ratio. Better characterization methods have led to a better appreciation of the details of nanoparticle structure and a new interest in how size restriction effects might influence surface chemistry and other aspects of catalysis.⁷⁶⁻⁷⁸ Knowledge of these factors has become important since the need for optimization of catalytic technologies has steadily increased in urgency into the new millennium. In particular, electrocatalysis, where reactions involving charge transfer across interfaces are enabled by catalytic surfaces, will be a critical component in new renewable energy generation and storage technologies.^{79, 80} A major area of focus in electrocatalytic research is in the water oxidation and reduction, or water-splitting, reactions, where oxygen and hydrogen are produced from water or vice versa. Reactions involving the generation (evolution) or reduction of oxygen, termed the OER and ORR, respectively, are noted for being much too slow for widespread application in that much more energy is needed to achieve them electrochemically than indicated by the thermodynamic free energies of the reaction. Lowering this energy input or overpotential has been a major goal. Platinum has served as the electrocatalyst of choice in most hydrogen fuel cell technologies used today. Obviously, Pt is an expensive metal and non-precious metal alternatives are urgently desired. Research on non-precious-metal electrocatalysts has identified many promising candidates,⁸⁰⁻⁸⁵ but a major part of the work toward a platinum-free water-splitting electrode will lie in optimizing these candidates at the micro- and nanoscale levels so that they become viable both in performance and cost.

Of late, new uses have been found for the control that modern colloidal nanoparticle synthetic approaches afford. The size- and shape-selective synthesis of monodisperse nanocrystals allows electrochemists to thoroughly explore structure-property relationships in catalytic materials by determining the number and type of atoms exposed to the solution.^{86, 87} An example of such a test of shape-controlled

objects is shown in **Figure 1.6**.⁸⁸ Here, lithium cobalt oxide particles were prepared as nanorods with different sizes and aspect ratios, with the result that their apparent activity for oxygen reduction and evolution per surface area depended strongly on the proportion of crystal facets along the rod axis to those at the tip of the rod. The impact of surface termination and orientation has long been known in metals,^{89,90} and syntheses achieving these optimal orientations in nanoparticles^{91,92} should ultimately improve substantially the activity of electrocatalysts.

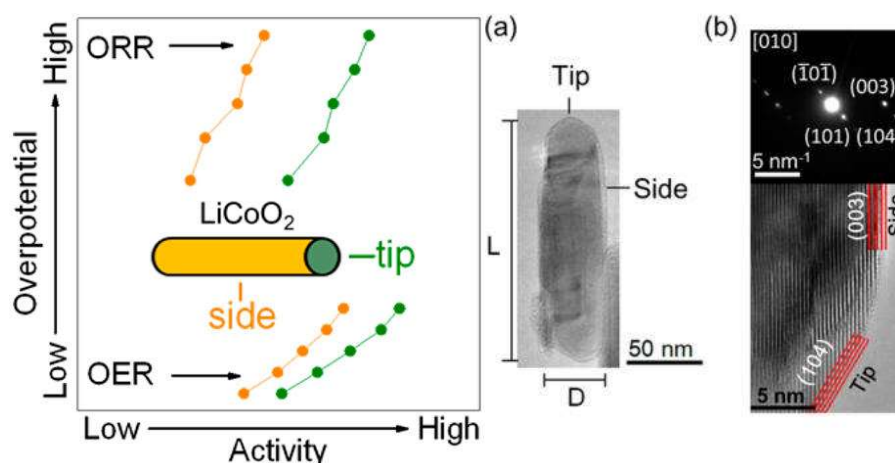


Figure 1.6. Facet dependence of nanoparticle electrocatalytic activity in nanorods. Right: side facets of LiCoO₂ are less active for oxygen evolution and reduction than tip facets. Left: TEM images of a LiCoO₂ nanorod showing different surface orientations and terminations. Reproduced from introductory figure and figure 1 from reference 88 by permission of the American Chemical Society.

The chemical transformations of colloidal nanomaterials add another option for activity maximization in electrocatalyst preparation.²¹ Metastable structures are accessible through relatively low-temperature modification that may not be accessible in the bulk or in larger particles. A number of groups have already reported

transformations in nanoparticles where removal or addition of atoms formed precisely tuned surface layers that, in combination with the underlying core, formed unusually active electrocatalysts.^{93, 94} Promising results in mixed-cation oxides are widespread.^{80, 81, 95, 96} Some are discussed in **Chapter 2**, but similar substitutions have been made for the anion sublattice in other nanosized materials,⁹⁷ which is the focus of that section.

Chapter 5 discusses one important concern in the utilization of colloidal nanoparticles in (electro)catalysis, specifically that components of nanomaterials, such as ligands, used for nanoparticle preparation must be considered as part of the system and may be utilized or need to be removed.^{98, 99} Work in nano-electrocatalysis generally proceeds with the assumption that surfactants must be removed with an appropriate procedure, but the relative impacts of these procedures on the residual surface after removal is not well-characterized.

1.3.6. Solid-state diffusion and mass transport in nanomaterials

Chemical transformations of nanocrystals in many cases take place via the diffusion of atoms through the particle lattice. This is logically necessary in order to explain the observations of morphology conservation mentioned in section **1.2** above. Atomic transport through solids is an area of great importance in physics and chemistry and has been widely studied for its applications in metallurgy, oxidation, and electronics, among many other areas. Beyond ion exchange,^{33, 36} another discovery in nanoparticle science generated great interest: the nanoscale Kirkendall effect, also popularized in 2004.¹⁰⁰ In this phenomenon, a binary compound (e.g. an oxide) at a nanoparticle surface requires the mixing or migration of two different atomic species. Where one species can move more rapidly than the other, voids can be generated where there are no additional sources of atoms to fill the space behind the diffusing atoms, i.e. in the center of a nanoparticle.^{101, 102} Fine points of nanocrystal structure,

such as size and crystal phase, can compound with solid-state diffusion to provide routes to very interesting structures,^{103, 104} as summarized in **Figure 1.7** for the example of cobalt colloids. Methods have been developed to prepare cobalt nanoparticles in an amorphous phase or three different crystalline structures: face-centered cubic (fcc), hexagonal close packed (hcp), or the more complex epsilon phase,¹⁰⁵ which appears only in nanoparticles. Oxidation of Co can lead to hollow polycrystalline nanoparticles, metal particles with an oxide shell of apparently self-limited thickness, solid polycrystalline or amorphous oxide particles, or even hollow oxide particles with a residual metal core. These different outcomes must arise from the particular rates of diffusion for oxygen and cobalt in the different metal and oxide phases. The nanoscale Kirkendall effect makes a significant contribution to the structure of the nanoparticle electrocatalysts studied in **Chapter 2**, and **Chapter 4** considers the impact of differences in component diffusion rates as well.

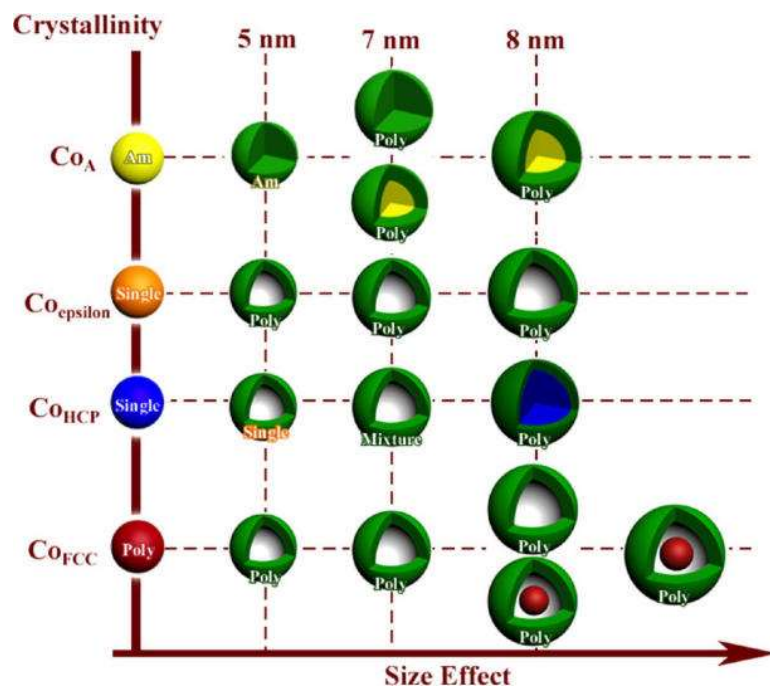


Figure 1.7. Morphology and phase changes during transformation of nanoparticles depend on domain size, starting crystal structure, and mobility of different species. Reproduced from figure 7 of reference 103 by permission of the American Chemical Society.

Because **Chapter 4** discusses the rates of diffusion in nanocrystals, this section describes some of the fundamental principles underlying a phenomenological or microscopic description of the transport of matter, especially in solids. Put most tersely, solid-state diffusion is the motion of atoms in response to a chemical potential gradient. In simple cases, this gradient is also equivalent to a gradient in concentration, (C) over some space coordinate (x). The flow of substance per unit area, J , in one dimension is given by what is known as Fick's first law:

$$J = -D \frac{dC}{dx} \quad (1.5)$$

D is known as the diffusion coefficient, and it is the property measured for Pb and Cd in PbS@CdS core-shell nanocrystals in **Chapter 4**. Because the flux is related

to the rate of change in concentration over time, t , **Equation 1.5** can be generalized to the similarly named Fick's second law:

$$\frac{dC}{dt} = D \frac{d^2C}{dx^2} \quad (1.6)$$

An important caveat exists, namely that D depends on many different factors, including the concentration of the substance itself. The phenomenological analysis of rates of diffusion¹⁰⁶ is thus largely based around applying **Equation 1.6** with the knowledge that D is really a function $D(C, t, \dots)$ and with the appropriate boundary conditions. Previous studies of diffusion in nanoparticles¹⁰⁷⁻¹¹¹ have most often measured D as a function of temperature T in order to obtain an activation energy E_a through the ostensible Arrhenius dependence of $D(T)$ based on rate theory. Although it is difficult to unambiguously determine microscopic mechanisms of diffusion from bulk kinetic experiments, E_a (or the lack of an Arrhenius dependence) could be taken as a valuable diagnostic. The central goal of diffusion experiments on nanoparticles in this work is to at least constrain the space of processes through which diffusion occurs. The target of interest is the identity of the point defect most responsible for mass transport, as discussed below.

In the solid state, it has been well-established that diffusion occurs through the motion of defects. In crystals, these can be effectively two-dimensional (grain boundaries and surfaces), one-dimensional (dislocations) or, most importantly for the purposes of this discussion, zero-dimensional (point defects).^{112, 113} The establishment of the existence of point defects, particularly vacancies, as the mediator for mass diffusion in crystalline solids by the work of Frenkel, Schottky, and Wagner among others^{112, 114} in ionic crystals and the experiments of Smigleskas and Kirkendall in metals¹¹⁵ was a major advance in solid-state physics. Point defects include gaps or missing points in the lattice (vacancies), atoms located off-lattice within the crystal

(interstitials), and replacements of one type of on-lattice atom with another (substitutional defects). The motion of these defects indicates a net displacement or flux of mass along the jump vector along which atoms move. Although a defective crystal is higher in energy than a perfect one, entropic considerations show that at any finite temperature a bulk crystal will always contain these point defects. This raises the interesting question of what happens when the crystal is finite or, in the case of nanocrystals, very small. It can be argued that since an arbitrary section of a solid is unlikely to enclose a point defect, nanocrystals must also be unlikely to contain them.^{116, 117} Somewhat sensationally, this has led to the description of nanocrystals as being pieces of perfect material with “nanoscale perfection”.¹¹⁸ Nonetheless, mass transport through solids occurs in nanocrystals as it does in the bulk. As the nanoscale Kirkendall effect¹⁰⁰ in **Figure 1.7** shows, this transport involves creation of defects. This has led to much work on introducing impurities or defects to nanocrystals and studying the effects of the presence of free surfaces on them.^{117, 119-121} Factors **Chapter 4** attempts to address through kinetic studies include whether the dominant type of defect might change in smaller domains, whether their populations or energies of formation are significantly different, how they couple to different types of surfaces or crystal facets, and whether this accelerates or slows down mass transport.

1.A. REFERENCES

1. Murray, C. B.; Norris, D. J.; Bawendi, M. G., Synthesis and Characterization of Nearly Monodisperse CdE (E = S, Se, Te) Semiconductor Nanocrystallites *Journal of the American Chemical Society* **1993**, 115, 8706-8715.
2. Murray, C. B.; Kagan, C. R.; Bawendi, M. G., Synthesis and Characterization of Monodisperse Nanocrystals and Close-Packed Nanocrystal Assemblies. *Annual Review of Materials Science* **2000**, 30, 545-610.
3. Rossetti, R.; Nakahara, S.; Brus, L. E., Quantum Size Effects in the Redox Potentials, Resonance Raman Spectra, and Electronic Spectra of CdS Crystallites in Aqueous Solution. *Journal of Chemical Physics* **1983**, 79, 1086-1088.
4. Owen, J.; Brus, L. E., Chemical Synthesis and Luminescence Applications of Colloidal Semiconductor Quantum Dots. *Journal of the American Chemical Society* **2017**, 139, 10939-10943.
5. Lai, S. L.; Guo, J. Y.; Petrova, V.; Ramanath, G.; Allen, L. H., Size-Dependent Melting Properties of Small Tin Particles: Nanocalorimetric Measurements. *Physical Review Letters* **1996**, 77, 99-102.
6. Goldstein, a. N.; Echer, C. M.; Alivisatos, A. P., Melting in Semiconductor Nanocrystals. *Science* **1992**, 256, 1425-1427.
7. Buffat, P.; Borel, J.-P., Size Effect on the Melting Temperature of Gold Particles. *Physical Review A* **1976**, 13, 2287-2298.
8. Anderson, N. C.; Hendricks, M. P.; Choi, J. J.; Owen, J. S., Ligand Exchange and the Stoichiometry of Metal Chalcogenide Nanocrystals: Spectroscopic Observation of Facile Metal-Carboxylate Displacement and Binding. *Journal of the American Chemical Society* **2013**, 135, 18536-18548.

9. Hohng, S.; Ha, T., Near-Complete Suppression of Quantum Dot Blinking in Ambient Conditions. *Journal of the American Chemical Society* **2004**, 126, 1324–1325.
10. LaMer, V.; Dinegar, R., Theory, Production and Mechanism of Formation of Monodispersed Hydrosols. *Journal of the American Chemical Society* **1950**, 72, 4847–4854.
11. Turkevich, J.; Stevenson, P. C.; Hillier, J., A Study of the Nucleation and Growth Processes in the Synthesis of Colloidal Gold. *Discussions of the Faraday Society* **1951**, 11, 55-75.
12. Sugimoto, T., Preparation of Monodispersed Colloidal Particles. *Advances in Colloid and Interface Science* **1987**, 28, 65-108.
13. Hendricks, M. P.; Campos, M. P.; Cleveland, G. T.; Jen-La Plante, I.; Owen, J. S., A Tunable Library of Substituted Thiourea Precursors to Metal Sulfide Nanocrystals. *Science* **2015**, 348, 1226-1230.
14. Peng, Z. A.; Peng, X., Formation of High-Quality CdTe, CdSe, and CdS Nanocrystals Using CdO as Precursor. *Journal of the American Chemical Society* **2001**, 123, 183–184.
15. Park, J.; An, K.; Hwang, Y.; Park, J.-G.; Noh, H.-J.; Kim, J.-Y.; Park, J.-H.; Hwang, N.-M.; Hyeon, T., Ultra-Large-Scale Syntheses of Monodisperse Nanocrystals. *Nature Materials* **2004**, 3, 891-895.
16. Zhou, J.; Pu, C.; Jiao, T.; Hou, X.; Peng, X., A Two-Step Synthetic Strategy toward Monodisperse Colloidal CdSe and CdSe/CdS Core/Shell Nanocrystals. *Journal of the American Chemical Society* **2016**, 138, 6475-6483.
17. Qiao, L.; Fu, Z.; Li, J.; Ghosen, J.; Zeng, M.; Stebbins, J.; Prasad, P. N.; Swihart, M. T., Standardizing Size- and Shape-Controlled Synthesis of Monodisperse

Magnetite (Fe₃O₄) Nanocrystals by Identifying and Exploiting Effects of Organic Impurities. *ACS Nano* **2017**, 11, 6370–6381.

18. Kovalenko, M. V.; Manna, L.; Cabot, A.; Hens, Z.; Talapin, D. V.; Kagan, C. R.; Klimov, V. I.; Rogach, A. L.; Reiss, P.; Milliron, D. J.; Guyot-Sionnest, P.; Konstantatos, G.; Parak, W. J.; Hyeon, T.; Korgel, B. a.; Murray, C. B.; Heiss, W., Prospects of Nanoscience with Nanocrystals. *ACS Nano* **2015**, 9, 1012-1057.

19. Coughlan, C.; Ibáñez, M.; Dobrozhan, O.; Singh, A.; Cabot, A.; Ryan, K. M., Compound Copper Chalcogenide Nanocrystals. *Chemical Reviews* **2017**, 117, 5865-6109.

20. Boles, M. A.; Ling, D.; Hyeon, T.; Talapin, D. V., The Surface Science of Nanocrystals. *Nature Materials* **2016**, 15, 141-153.

21. Fayette, M.; Robinson, R. D., Chemical Transformations of Nanomaterials for Energy Applications. *Journal of Materials Chemistry A* **2014**, 2, 5965-5978.

22. Chen, Y.; Vela, J.; Htoon, H.; Casson, J. L.; Werder, D. J.; Bussian, D. A.; Klimov, V. I.; Hollingsworth, J. A., “Giant” Multishell CdSe Nanocrystal Quantum Dots with Suppressed Blinking. *Journal of the American Chemical Society* **2008**, 130, 5026–5027.

23. Chen, O.; Zhao, J.; Chauhan, V. P.; Cui, J.; Wong, C.; Harris, D. K.; Wei, H.; Han, H.-S.; Fukumura, D.; Jain, R. K.; Bawendi, M. G., Compact High-Quality CdSe–CdS Core–Shell Nanocrystals with Narrow Emission Linewidths and Suppressed Blinking. *Nature Materials* **2013**, 12, 445–451.

24. Dabbousi, O.; Rodriguez-Viejo, J.; Mikulec, F. V.; Heine, J. R.; Mattoussi, H.; Ober, R.; Jensen, K. F.; Bawendi, M. G., (CdSe)ZnS Core–Shell Quantum Dots: Synthesis and Characterization of a Size Series of Highly Luminescent Nanocrystallites. *Journal of Physical Chemistry B* **1997**, 101, 9463–9475.

25. Zobel, M.; Neder, R. B.; Kimber, S. A. J., Universal Solvent Restructuring Induced by Colloidal Nanoparticles. *Science* **2015**, 347, 201-204.
26. Zhang, H.; Gilbert, B.; Huang, F.; Banfield, J. F., Water Driven Structure Transformation in Nanoparticles at Room Temperature. *Nature* **2003**, 424, 1025-1029.
27. Magnussen, O. M.; Ocko, B. M.; Regan, M. J.; Penanen, K.; Pershan, P. S.; Deutsch, M., X-Ray Reflectivity Measurements of Surface Layering in Liquid Mercury. *Physical Review Letters* **1995**, 74, 4444-4447.
28. Froyen, S.; Zunger, A., Surface-Induced Ordering in GaInP. *Physical Review Letters* **1991**, 66, 2132-2135.
29. Robinson, R. D.; Sadtler, B.; Demchenko, D. O.; Erdonmez, C. K.; Wang, L.-W.; Alivisatos, A. P., Spontaneous Superlattice Formation in Nanorods through Partial Cation Exchange. *Science* **2007**, 317, 355-358.
30. Ha, D.-H.; Moreau, L. M.; Bealing, C. R.; Zhang, H.; Hennig, R. G.; Robinson, R. D., The Structural Evolution and Diffusion During the Chemical Transformation from Cobalt to Cobalt Phosphide Nanoparticles. *Journal of Materials Chemistry* **2011**, 21, 11498-11510.
31. Peters, J. L.; van den Bos, K. H. W.; Van Aert, S.; Goris, B.; Bals, S.; Vanmaekelbergh, D., Ligand-Induced Shape Transformation of PbSe Nanocrystals. *Chemistry of Materials* **2017**, 29, 4122-4128.
32. Helfferich, F. G., *Ion Exchange*. McGraw-Hill: New York, 1962.
33. Beberwyck, B. J.; Surendranath, Y.; Alivisatos, A. P., Cation Exchange: A Versatile Tool for Nanomaterials Synthesis. *Journal of Physical Chemistry C* **2013**, 117, 19759-19770.
34. De Trizio, L.; Manna, L., Forging Colloidal Nanostructures via Cation Exchange Reactions. *Chemical Reviews* **2016**, 116, 10852-10887.

35. Wark, S. E.; Hsia, C.-H.; Son, D. H., Effects of Ion Solvation and Volume Change of Reaction on the Equilibrium and Morphology in Cation-Exchange Reaction of Nanocrystals. *Journal of the American Chemical Society* **2008**, 130, 9550-9555.
36. Son, D. H.; Hughes, S. M.; Yin, Y.; Paul Alivisatos, A., Cation Exchange Reactions in Ionic Nanocrystals. *Science* **2004**, 306, 1009-1012.
37. Li, H.; Zanella, M.; Genovese, A.; Povia, M.; Falqui, A.; Giannini, C.; Manna, L., Sequential Cation Exchange in Nanocrystals: Preservation of Crystal Phase and Formation of Metastable Phases. *Nano Letters* **2011**, 11, 4964–4970.
38. Meir, N.; Martín-García, B.; Moreels, I.; Oron, D., Revisiting the Anion Framework Conservation in Cation Exchange Processes. *Chemistry of Materials* **2016**, 28, 7872-7877.
39. Ha, D.-H.; Caldwell, A. H.; Ward, M. J.; Honrao, S.; Mathew, K.; Hovden, R.; Koker, M. K. A.; Muller, D. A.; Hennig, R. G.; Robinson, R. D., Solid–Solid Phase Transformations Induced through Cation Exchange and Strain in 2D Heterostructured Copper Sulfide Nanocrystals. *Nano Letters* **2014**, 14, 7090-7099.
40. Liu, Y.; Yin, D.; Swihart, M. T., Ag⁺-Induced Shape and Composition Evolution of Covellite CuS Nanoplatelets To Produce Plate–Satellite and Biconcave–Particle Heterostructures. *Chemistry of Materials* **2018**, 30, 8089–8098.
41. Fenton, J. L.; Steimle, B. C.; Schaak, R. E., Structure-Selective Synthesis of Wurtzite and Zinblende ZnS, CdS, and CuInS₂ Using Nanoparticle Cation Exchange Reactions. *Inorganic Chemistry* **2019**, 58, 672-678.
42. Fenton, J. L.; Steimle, B. C.; Schaak, R. E., Tunable Intraparticle Frameworks for Creating Complex Heterostructured Nanoparticle Libraries. *Science* **2018**, 360, 513-517.
43. Pietryga, J. M.; Werder, D. J.; Williams, D. J.; Casson, J. L.; Schaller, R. D.; Klimov, V. I.; Hollingsworth, J. A., Utilizing the Lability of Lead Selenide to Produce

Heterostructured Nanocrystals with Bright, Stable Infrared Emission. *Journal of the American Chemical Society* **2008**, 130, 4879-4885.

44. Kim, S.; Marshall, A. R.; Kroupa, D. M.; Miller, E. M.; Luther, J. M.; Jeong, S.; Beard, M. C., Air-Stable and Efficient PbSe Quantum-Dot Solar Cells Based upon ZnSe to PbSe Cation-Exchanged Quantum Dots. *ACS Nano* **2015**, 9, 8157–8164.

45. Wong, A. B.; Brittman, S.; Yu, Y.; Dasgupta, N. P.; Yang, P., Core–Shell CdS–Cu₂S Nanorod Array Solar Cells. *Nano Letters* **2015**, 15, 4096–4101.

46. Park, J.; Zheng, H.; Jun, Y.-w.; Alivisatos, A. P., Hetero-Epitaxial Anion Exchange Yields Single-Crystalline Hollow Nanoparticles. *Journal of the American Chemical Society* **2009**, 131, 13943–13945.

47. Zhang, H.; Solomon, L. V.; Ha, D.-H.; Honrao, S.; Hennig, R. G.; Robinson, R. D., (NH₄)₂S, a Highly Reactive Molecular Precursor for Low Temperature Anion Exchange Reactions in Nanoparticles. *Dalton Transactions* **2013**, 42, 12596-12599.

48. Anderson, B. D.; Tracy, J. B., Nanoparticle Conversion Chemistry: Kirkendall Effect, Galvanic Exchange, and Anion Exchange. *Nanoscale* **2014**, 6, 12195-12216.

49. Koscher, B. A.; Bronstein, N. D.; Olshansky, J. H.; Bekenstein, Y.; Alivisatos, A. P., Surface- vs Diffusion-Limited Mechanisms of Anion Exchange in CsPbBr₃ Nanocrystal Cubes Revealed through Kinetic Studies. *Journal of the American Chemical Society* **2016**, 138, 12065-12068.

50. Akkerman, Q. A.; D’Innocenzo, V.; Accornero, S.; Scarpellini, A.; Petrozza, A.; Prato, M.; Manna, L., Tuning the Optical Properties of Cesium Lead Halide Perovskite Nanocrystals by Anion Exchange Reactions. *Journal of the American Chemical Society* **2015**, 137, 10276–10281.

51. Nedelcu, G.; Protesescu, L.; Yakunin, S.; Bodnarchuk, M. I.; Grotevent, M. J.; Kovalenko, M. V., Fast Anion-Exchange in Highly Luminescent Nanocrystals of

- Cesium Lead Halide Perovskites (CsPbX_3 , X = Cl, Br, I). *Nano Letters* **2015**, 15, 5635–5640.
52. Frenken, J. W. M.; Veen, J. F. v. d., Observation of Surface Melting. *Physical Review Letters* **1985**, 54, 134-137.
53. Bealing, C. R.; Baumgardner, W. J.; Choi, J. J.; Hanrath, T.; Hennig, R. G., Predicting Nanocrystal Shape Through Consideration of Surface-Ligand Interactions. *ACS Nano* **2012**, 6, 2118-2127.
54. Manna, L.; Scher, E. C.; Alivisatos, A. P., Shape Control of Colloidal Semiconductor Nanocrystals. *Journal of Cluster Science* **2002**, 13, 521-532.
55. Sines, I. T.; Schaak, R. E., Phase-Selective Chemical Extraction of Selenium and Sulfur from Nanoscale Metal Chalcogenides: A General Strategy for Synthesis, Purification, and Phase Targeting. *Journal of the American Chemical Society* **2011**, 133, 1294-1297.
56. Moreau, L. M.; Ha, D.-H.; Bealing, C. R.; Zhang, H.; Hennig, R. G.; Robinson, R. D., Unintended Phosphorus Doping of Nickel Nanoparticles during Synthesis with TOP: A Discovery through Structural Analysis. *Nano Letters* **2012**, 12, 4530-4539.
57. Zhang, H.; Ha, D.-H.; Hovden, R.; Kourkoutis, L. F.; Robinson, R. D., Controlled Synthesis of Uniform Cobalt Phosphide Hyperbranched Nanocrystals Using Tri-n-octylphosphine Oxide as a Phosphorus Source. *Nano Letters* **2011**, 11, 188-197.
58. Kriegel, I.; Jiang, C.; Rodríguez-Fernández, J.; Schaller, R. D.; Talapin, D. V.; Como, E. d.; Feldmann, J., Tuning the Excitonic and Plasmonic Properties of Copper Chalcogenide Nanocrystals. *Journal of the American Chemical Society* **2012**, 134, 1583-1590.

59. Xie, Y.; Riedinger, A.; Prato, M.; Casu, A.; Genovese, A.; Guardia, P.; Sottini, S.; Sangregorio, C.; Miszta, K.; Ghosh, S.; Pellegrino, T.; Manna, L., Copper Sulfide Nanocrystals with Tunable Composition by Reduction of Covellite Nanocrystals with Cu^+ Ions. *Journal of the American Chemical Society* **2013**, 135, 17630-17637.
60. Dorfs, D.; Härtling, T.; Miszta, K.; Bigall, N. C.; Kim, M. R.; Genovese, A.; Falqui, A.; Povia, M.; Manna, L., Reversible Tunability of the Near-Infrared Valence Band Plasmon Resonance in Cu_{2-x}Se Nanocrystals. *Journal of the American Chemical Society* **2011**, 133, 11175-11180.
61. Williamson, C. B.; Nevers, D. R.; Nelson, A.; Hadar, I.; Banin, U.; Hanrath, T.; Robinson, R. D., Chemically Reversible Isomerization of Inorganic Clusters. *Science* **2019**, 363, 731-735.
62. Bragg, W. H.; Bragg, W. L., The Reflection of X-Rays by Crystals. *Proceedings of the Royal Society A: Mathematical, Physical and Engineering Sciences* **1913**, 88, 428-438.
63. Guinier, A., *X-Ray Diffraction in Crystals, Imperfect Crystals, and Amorphous Bodies*. Dover: Mineola, New York, 1994.
64. Als-Nielsen, J.; McMorrow, D., *Elements of Modern X-ray Physics*. 2nd ed.; John Wiley and Sons: West Sussex, UK, 2011.
65. Cullity, B. D., *Elements of X-Ray Diffraction*. Addison-Wesley: Reading, MA, 1956.
66. Hall, B. D.; Monot, R., Calculating the Debye–Scherrer Diffraction Pattern for Large Clusters. *Computers in Physics* **1991**, 5, 414-417.
67. Beyerlein, K. R., A Review of Debye Function Analysis. *Powder Diffraction* **2013**, 28, S2-S10.
68. Gelisio, L.; Scardi, P., 100 Years of Debye's Scattering Equation. *Acta Crystallographica A* **2016**, A72, 608–620.

69. Brown, P. J.; Fox, A. G.; Maslen, E. N.; O'Keefe, M. A.; Willis, B. T. M., Intensity of Diffracted Intensities. In *International Tables for Crystallography, Vol. C: Mathematical, Physical and Chemical Tables*, Prince, E., Ed. John Wiley and Sons: Weinheim, 2006.
70. Farrow, C. L.; Billinge, S. J. L., Relationship between the Atomic Pair Distribution Function and Small-Angle Scattering: Implications for Modeling of Nanoparticles. *Acta Crystallographica A* **2009**, 65, 232-239.
71. Debye, P., Zerstreuung von röntgenstrahlen. *Annalen der Physik* **1915**, 351, 809-823.
72. Dinnebier, R. E.; Billinge, S. J. L., *Powder Diffraction: Theory and Practice*. Royal Society of Chemistry: Cambridge, UK, 2008.
73. Fultz, B.; Howe, J., *Transmission Electron Microscopy and Diffractometry of Materials*. 4th ed.; Springer-Verlag: New York, 2013.
74. Williams, D. B.; Carter, C. B., *Transmission Electron Microscopy: A Textbook for Materials Science*. 2nd ed.; Springer Science+Business Media: New York, 2009.
75. Freund, H.-J.; Nilius, N.; Risse, T.; Schauer mann, S., A Fresh Look at an Old Nano-Technology: Catalysis. *Physical Chemistry Chemical Physics* **2014**, 16, 8148-8167.
76. Kinoshita, K., Particle Size Effects for Oxygen Reduction on Highly Dispersed Platinum in Acid Electrolytes. *Journal of the American Chemical Society* **1990**, 112, 845-848.
77. Sheng, W.; Chen, S.; Vescovo, E.; Shao-Horn, Y., Size Influence on the Oxygen Reduction Reaction Activity and Instability of Supported Pt Nanoparticles. *Journal of the Electrochemical Society* **2012**, 159, B96-B103.
78. Mayrhofer, K. J. J.; Blizanac, B. B.; Arenz, M.; Stamenkovic, V. R.; Ross, P. N.; Markovic, N. M., The Impact of Geometric and Surface Electronic Properties of

- Pt-Catalysts on the Particle Size Effect in Electrocatalysis. *Journal of Physical Chemistry B* **2005**, 109, 14433–14440.
79. Greeley, J.; Markovic, N. M., The Road from Animal Electricity to Green Energy: Combining Experiment and Theory in Electrocatalysis *Energy and Environmental Science* **2012**, 5, 9246-9256.
80. Hong, W. T.; Risch, M.; Stoerzinger, K. A.; Grimaud, A.; Suntivich, J.; Shao-Horn, Y., Toward the Rational Design of Non-Precious Transition Metal Oxides for Oxygen Electrocatalysis *Energy and Environmental Science* **2015**, 8, 1404-1427.
81. Suntivich, J.; May, K. J.; Gasteiger, H. A.; Goodenough, J. B.; Shao-Horn, Y., A Perovskite Oxide Optimized for Oxygen Evolution Catalysis from Molecular Orbital Principles. *Science* **2011**, 334, 1383-1385
82. Benck, J. D.; Hellstern, T. R.; Kibsgaard, J.; Chakthranont, P.; Jaramillo, T. F., Catalyzing the Hydrogen Evolution Reaction (HER) with Molybdenum Sulfide Nanomaterials. *ACS Catalysis* **2014**, 4, 3957-3971.
83. Bonde, J.; Moses, P. G.; Jaramillo, T. F.; Nørskov, J. K.; Chorkendorff, I., Hydrogen Evolution on Nano-Particulate Transition Metal Sulfides. *Faraday Discussions* **2009**, 140, 219-231.
84. Popczun, E. J.; McKone, J. R.; Read, C. G.; Biacchi, A. J.; Wiltrout, A. M.; Lewis, N. S.; Schaak, R. E., Nanostructured Nickel Phosphide as an Electrocatalyst for the Hydrogen Evolution Reaction. *Journal of the American Chemical Society* **2013**, 135, 9267-9270.
85. Cook, T. R.; Dogutan, D. K.; Reece, S. Y.; Surendranath, Y.; Teets, T. S.; Nocera, D. G., Solar Energy Supply and Storage for the Legacy and Nonlegacy Worlds. *Chemical Reviews* **2010**, 110, 6474-6502.
86. Cargnello, M., Colloidal Nanocrystals as Building Blocks for Well-Defined Heterogeneous Catalysts. *Chemistry of Materials* **2019**, 31, 576–596.

87. Cargnello, M.; Chen, C.; Diroll, B. T.; Doan-Nguyen, V. V. T.; Gorte, R. J.; Murray, C. B., Efficient Removal of Organic Ligands from Supported Nanocrystals by Fast Thermal Annealing Enables Catalytic Studies on Well-Defined Active Phases. *Journal of the American Chemical Society* **2015**, 137, 6906-6911.
88. Han, B.; Qian, D.; Risch, M.; Chen, H.; Chi, M.; Meng, Y. S.; Shao-Horn, Y., The Role of LiCoO₂ Surface Terminations in Oxygen Reduction and Evolution Kinetics. *Journal of Physical Chemistry Letters* **2015**, 6, 1357-1362.
89. Markovic, N. M.; Gasteiger, H. A.; Ross, P. N., Oxygen Reduction on Platinum Low-Index Single-Crystal Surfaces in Sulfuric Acid Solution: Rotating Ring-Pt(hkl) Disk Studies. *Journal of Physical Chemistry* **1995**, 99, 3411-3415.
90. Stamenković, V.; Schmidt, T. J.; Ross, P. N.; Marković, N. M., Surface Composition Effects in Electrocatalysis: Kinetics of Oxygen Reduction on Well-Defined Pt₃Ni and Pt₃Co Alloy Surfaces. *Journal of Physical Chemistry B* **2002**, 106, 11970–11979.
91. Chen, J.; Lim, B.; Lee, E. P.; Xia, Y., Shape-Controlled Synthesis of Platinum Nanocrystals for Catalytic and Electrocatalytic Applications. *Nano Today* **2009**, 4, 81-95.
92. Wang, C.; Daimon, H.; Onodera, T.; Koda, T.; Sun, S., A General Approach to the Size- and Shape-Controlled Synthesis of Platinum Nanoparticles and Their Catalytic Reduction of Oxygen. *Angewandte Chemie International Edition* **2008**, 47, 3588-3591.
93. Zhang, S.; Zhang, X.; Jiang, G.; Zhu, H.; Guo, S.; Su, D.; Lu, G.; Sun, S., Tuning Nanoparticle Structure and Surface Strain for Catalysis Optimization. *Journal of the American Chemical Society* **2014**, 136, 7734-7739.
94. Wang, D.; Xin, H. L.; Hovden, R.; Wang, H.; Yu, Y.; Muller, D. A.; DiSalvo, F. J.; Abruña, H. D., Structurally Ordered Intermetallic Platinum-Cobalt Core-Shell

Nanoparticles with Enhanced Activity and Stability as Oxygen Reduction

Electrocatalysts. *Nature Materials* **2013**, 12, 81-87.

95. Trotochaud, L.; Ranney, J. K.; Williams, K. N.; Boettcher, S. W., Solution-Cast Metal Oxide Thin Film Electrocatalysts for Oxygen Evolution. *Journal of the American Chemical Society* **2012**, 134, 17253–17261.

96. Zhu, H.; Zhang, S.; Huang, Y.-X.; Wu, L.; Sun, S., Monodisperse $M_xFe_{3-x}O_4$ (M = Fe, Cu, Co, Mn) Nanoparticles and Their Electrocatalysis for Oxygen Reduction Reaction. *Nano Letters* **2013**, 13, 2947-2951.

97. Liu, X.; Du, J.; Li, C.; Han, X.; Hu, X.; Cheng, F.; Chen, J., The Anion Effect on the Oxygen Reduction of MnX (X = O, S, and Se) Catalysts. *Journal of Materials Chemistry A* **2015**, 3, 3425-3431.

98. Li, D.; Wang, C.; Tripkovic, D.; Sun, S.; Markovic, N. M.; Stamenkovic, V. R., Surfactant Removal for Colloidal Nanoparticles from Solution Synthesis: The Effect on Catalytic Performance. *ACS Catalysis* **2012**, 2, 1358-1362.

99. Niu, Z.; Li, Y., Removal and Utilization of Capping Agents in Nanocatalysis. *Chemistry of Materials* **2014**, 26, 72-83.

100. Yin, Y.; Rioux, R. M.; Erdonmez, C. K.; Hughes, S.; Somorjai, G. A.; Alivisatos, A. P., Formation of Hollow Nanocrystals through the Nanoscale Kirkendall Effect. *Science* **2004**, 304, 711-714.

101. Ha, D.-H.; Moreau, L. M.; Honrao, S.; Hennig, R. G.; Robinson, R. D., The Oxidation of Cobalt Nanoparticles into Kirkendall-Hollowed CoO and Co_3O_4 : The Diffusion Mechanisms and Atomic Structural Transformations. *Journal of Physical Chemistry C* **2013**, 117, 14303-14312.

102. Cabot, A.; Puentes, V. F.; Shevchenko, E.; Yin, Y.; Balcells, L.; Marcus, M. A.; Hughes, S. M.; Alivisatos, A. P., Vacancy Coalescence during Oxidation of Iron Nanoparticles. *2007* **2007**, 129, 10358–10360.

103. Yang, Z.; Yang, N.; Pileni, M.-P., Nano Kirkendall Effect Related to Nanocrystallinity of Metal Nanocrystals: Influence of the Outward and Inward Atomic Diffusion on the Final Nanoparticle Structure. *Journal of Physical Chemistry C* **2015**, 119, 22249-22260.
104. Railsback, J. G.; Johnston-Peck, A. C.; Wang, J.; Tracy, J. B., Size-Dependent Nanoscale Kirkendall Effect During the Oxidation of Nickel Nanoparticles. *ACS Nano* **2010**, 4, 1913-1920.
105. Dinega, D. P.; Bawendi, M. G., A Solution-Phase Chemical Approach to a New Crystal Structure of Cobalt. *Angewandte Chemie International Edition* **1999**, 38, 1788-1791.
106. Crank, J., *The Mathematics of Diffusion*. 2nd ed.; Clarendon Press: Oxford, 1975.
107. Bothe, C.; Kornowski, A.; Tornatzky, H.; Schmidtke, C.; Lange, H.; Maultzsch, J.; Weller, H., Solid-State Chemistry on the Nanoscale: Ion Transport through Interstitial Sites or Vacancies? *Angewandte Chemie International Edition* **2015**, 54, 14183-14186.
108. Cabot, A.; Smith, R. K.; Yin, Y.; Zheng, H.; Reinhard, B. M.; Liu, H.; Alivisatos, A. P., Sulfidation of Cadmium at the Nanoscale. *ACS Nano* **2008**, 2, 1452-1458.
109. Tang, J.; Myers, M.; Bosnick, K. A.; Brus, L. E., Magnetite Fe₃O₄ Nanocrystals : Spectroscopic Observation of Aqueous Oxidation Kinetics. *Journal of Physical Chemistry B* **2003**, 107, 7501-7506.
110. Chakraborty, P.; Jin, Y.; Barrows, C. J.; Dunham, S. T.; Gamelin, D. R., Kinetics of Isovalent (Cd²⁺) and Aliovalent (In³⁺) Cation Exchange in Cd_{1-x}Mn_xSe Nanocrystals. *Journal of the American Chemical Society* **2016**, 138, 12885-12893.

111. Sung, Y.-M.; Lee, Y.-J.; Park, K.-S., Kinetic Analysis for Formation of $\text{Cd}_{1-x}\text{Zn}_x\text{Se}$ Solid-Solution Nanocrystals. *Journal of the American Chemical Society* **2006**, 128, 9002-9003.
112. Fine, M. E., Introduction to Chemical and Structural Defects in Crystalline Solids. In *Treatise on Solid State Chemistry, vol. 1: The Chemical Structure of Solids*, Hannay, N. B., Ed. Plenum: New York, 1974; Vol. 1, pp 283-333
113. Shewmon, P. G., *Diffusion in Solids*. 2nd ed.; Minerals, Metals, & Materials Society: Warrendale, Pa., 1989.
114. Mott, N. F.; Gurney, R. W., *Electronic Processes in Ionic Crystals*. 2nd ed.; Clarendon Press: Oxford, 1948.
115. Smigelskas, A. D.; Kirkendall, E. O., Zinc Diffusion in Alpha Brass. *Transactions of the American Institute of Mining and Metallurgical Engineers* **1947**, 171, 130-142.
116. Dalpian, G. M.; Chelikowsky, J. R., Self-Purification in Semiconductor Nanocrystals. *Physical Review Letters* **2006**, 96, 226802.
117. Norris, D. J.; Efros, A. L.; Erwin, S. C., Doped Nanocrystals. *Science* **2008**, 319, 1776-1779.
118. Buriak, J. M., Chemistry with Nanoscale Perfection. *Science* **2004**, 304, 692-693.
119. Erwin, S. C.; Zu, L.; Haftel, M. I.; Efros, A. L.; Kennedy, T. a.; Norris, D. J., Doping Semiconductor Nanocrystals. *Nature* **2005**, 436, 91-94.
120. Chan, T. L.; Zayak, A. T.; Dalpian, G. M.; Chelikowsky, J. R., Role of Confinement on Diffusion Barriers in Semiconductor Nanocrystals. *Physical Review Letters* **2009**, 102, 025901.

121. Srivastava, B. B.; Jana, S.; Pradhan, N., Doping Cu in Semiconductor Nanocrystals: Some Old and Some New Physical Insights. *Journal of the American Chemical Society* **2011**, 133, 1007-1015.

CHAPTER 2

2 INCREASED ACTIVITY IN HYDROGEN EVOLUTION ELECTROCATALYSIS FOR PARTIAL ANIONIC SUBSTITUTION IN COBALT OXYSULFIDE NANOPARTICLES *

2.1. ABSTRACT

The functionality of an electrocatalyst depends sensitively on the surface chemistry. In the case of transition-metal compounds, both the transition metal cation and the anion must be controlled to maximize the electrocatalytic activity. This realization has driven many efforts devoted to engineering the cation chemistry, producing many state-of-the-art electrocatalysts. Motivated by the critical role the cation plays in electrocatalysis, we seek to understand whether a similar effect can be achieved with the anion. Herein, we present a study on the effect of the anion substitution on the hydrogen evolution reaction (HER) electrocatalysis on cobalt oxysulfide nanoparticles. To control the sulfur substitution, we use ammonium sulfide to introduce sulfur to the cobalt oxide nanoparticles at low temperature without inducing secondary phase formation. We find that a lightly doped oxysulfide catalyst, which has the composition $\text{CoO}_x\text{S}_{0.18}$, exhibits a metastable, distorted S-substituted CoO phase and is 2–3 times more active for the HER than either end-member of the substitution series. Our first-principles calculations attribute the HER enhancement to the stronger surface H adsorption which is maximally favorable at a relatively low

* Originally published as: Nelson, A.; Fritz, K. E.; Honrao, S.; Hennig, R. G.; Robinson, R. D.; Suntivich, J. Increased Activity in Hydrogen Evolution Electrocatalysis for Partial Anionic Substitution in Cobalt Oxysulfide Nanoparticles. *J. Mater. Chem. A* **2016**, 4(8), 2842-2848. Reproduced by permission of the Royal Society of Chemistry.

doping level. Our work provides a protocol for synthesizing metastable mixed-anion materials and reveals the critical role of the anion on the surface physiochemical properties and the HER electrocatalysis.

2.2. INTRODUCTION

One of the largest factors limiting the commercialization of air-breathing electrochemical energy storage technologies lies in the requirement of rare, precious-metal catalysts.¹⁻¹⁰ Transition-metal-containing compounds such as oxides,¹⁰⁻¹⁵ chalcogenides,¹⁶⁻²¹ and pnictides²²⁻²⁴ exhibit high activities and are attractive alternatives to rare, precious metals. The pursuit of these transition-metal-containing electrocatalysts has driven many efforts^{11, 25, 26} in controlling physicochemical properties such as the surface–adsorbate interaction^{27, 28} to find the most electrocatalytically active surface.^{1, 2, 11} Thus far, approaches based on cationic substitutions have been highly successful in controlling the surface–adsorbate interaction for engineering the electrocatalytic activities.^{25, 29, 30} These investigations have produced many mixed-cation electrocatalysts that are considered the state-of-the-art.^{11, 13, 25, 29, 31, 32} Considering these positive results from cationic substitution, a natural question is whether a similar substitution of the anion can also benefit the activity of the transition-metal-containing electrocatalysts. Transition metal compounds with mixed anions have been explored for batteries,³³ transparent conducting oxides,³⁴ photocatalysts,^{35, 36} and electrocatalysts. In electrocatalysis, many works using mixed anionic compounds such as MoS₂–MoSe₂,³⁷ MoO_x–MoS₂,^{38, 39} sulfidized MoP,⁴⁰ phosphidized CoS₂,⁴¹ selenized Ni₂P,⁴² or amorphous Co–O–S⁴³ have established that mixed-anion materials can have superior performance. Still, it is not clear how the anion substitution affects the physicochemical and electrocatalytic

properties. This is partly because many of these studies have focused on compounds at the extremes of each compositional range or have used materials with poorly-defined morphologies, such as porous films or polydisperse nanoparticles.^{18, 44, 45} In view of the extensive literature on transition metal chalcogenides^{17, 21, 27, 46} and phosphides,^{22, 23, 47} knowledge of the role of the anion in controlling these physicochemical properties can help to rationalize future design strategies for optimizing electrocatalytic activity.

2.3. RESULTS AND DISCUSSION

In this work, we synthesize partially anion-exchanged nanoparticles (NPs) to determine how the anion substitution can affect electrocatalytic activity, using cobalt oxysulfide, CoO_xS_y , as a model system (**Figure 2.1a**). We focus on the hydrogen evolution reaction electrocatalysis (HER, $2\text{H}_2\text{O} + 2\text{e}^- \leftrightarrow \text{H}_2 + 2\text{OH}^-$ in alkaline), for which highly active electrocatalysts have been prepared utilizing cobalt sulfides^{43, 48-50} and other cobalt chalcogenides.⁵¹ We show that the HER activity depends sensitively on the anion chemistry, which can subsequently be optimized during catalyst synthesis. Specifically, we demonstrate that there is an optimum composition for the HER electrocatalysis at relatively small levels of sulfide doping (**Figure 2.1b**). We attribute the increased HER activity after anion exchange to the stronger hydrogen adsorption energy following the substitution of S^{2-} in place of O^{2-} in Co oxysulfide, effectively reducing the intermediate energy during the HER.

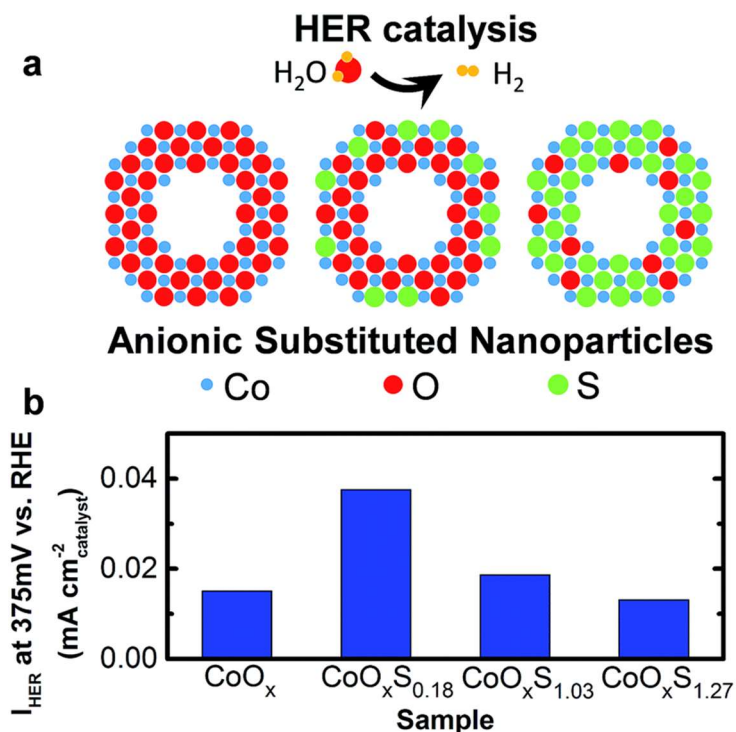


Figure 2.1. Schematic of the anionic substitution in CoO_x nanoparticles as a testbed for HER electrocatalysis (a). Results from this work indicate that the maximum HER activity occurs at low doping levels (e.g., $\text{CoO}_x\text{S}_{0.18}$), while at higher doping levels, activity decreases (b). The HER activity is normalized to the surface areas of the catalysts.

2.3.1. Structural characterization

To carry out the partial substitution of the anions, we use a protocol based on organic-phase colloidal synthesis. Colloidal NP synthesis offers many advantages, such as controlled nucleation and growth in solution, thereby producing particles with well-defined, highly-uniform size and shape.⁵²⁻⁵⁵ The monodispersity that is afforded by colloidal synthesis offers an unprecedented opportunity to establish and optimize structure-activity relationships.^{56, 57} Furthermore, the nanoscale nature of the produced materials can allow for non-conventional transformation kinetics, resulting in a metastable structure that is considered unobtainable according to the phase diagram.⁵⁸

A disadvantage of colloidal synthesis is the requirement of a surfactant to act as a stabilizer and particle growth regulator.⁵⁹⁻⁶¹ This requires a surface ligand removal step such as high-temperature annealing,⁵⁷ replacement of long-chain ligands with more volatile or soluble ones,^{62, 63} or, as used in this work, ligand displacement using highly reactive inorganic species.^{61, 64, 65} Our method to create the anion-substituted series is based on our previous finding that ammonium sulfide, $(\text{NH}_4)_2\text{S}$, can insert S into oxides under relatively mild conditions.⁶⁶ In this work, we achieve partial substitution by limiting the amount of added $(\text{NH}_4)_2\text{S}$ to control the diffusion of an isovalent anionic dopant, S^{2-} , into organosoluble cobalt oxide NPs, thereby producing S-substituted Co oxysulfide NPs (see schematic of this evolution **Figure 2.2a**). Briefly, we first oxidize cobalt NPs into CoO_x ⁶⁷ and then sulfidize them into CoO_xS_y NPs. The oxygen in the CoO_x is anion-exchanged for sulfur through the addition of $(\text{NH}_4)_2\text{S}$ dissolved in oleylamine to the CoO_x NP solution at 100 °C under N_2 atmosphere. We explore the nominal molar ratios of $(\text{NH}_4)_2\text{S}$ to Co at 3 : 10 (dilute doping), 1 : 1, and 3 : 1 (excess sulfur). We also investigate the effect of annealing by re-suspending the NPs following re-isolation in an organic solvent followed by a 200 °C heat-treatment under N_2 for 1 hour. These annealed NPs serve as a control to explore the phase stability of Co oxysulfides following the anion substitution.

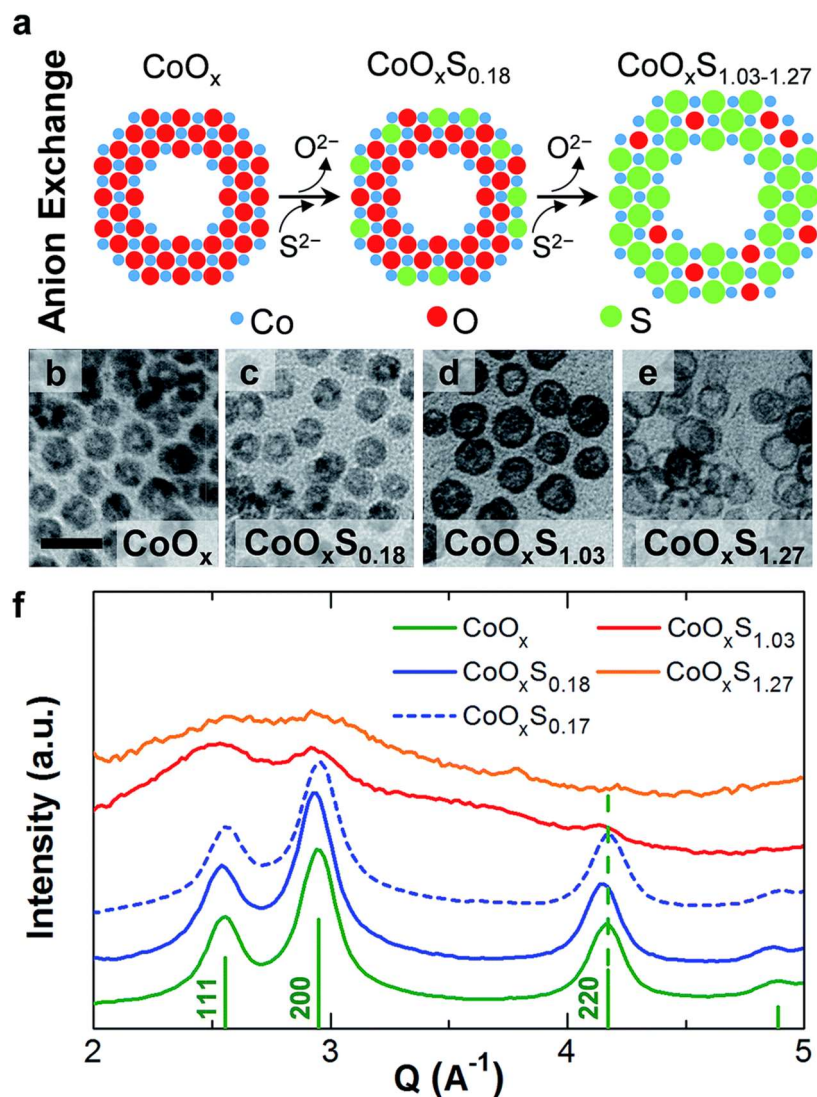


Figure 2.2. Schematic of the synthesis of cobalt oxysulfides via partial and “full” anion exchange (a). Transmission electron microscopy characterization of structural transformations of CoO_xS_y nanoparticles during anion exchange (a) of O^{2-} with S^{2-} ((b–e), scale bar 25 nm) and the rotationally averaged SAED patterns (f). The particle morphology and crystal structure of the CoO_x particles (b) are retained at low S^{2-} doping levels (c), but at higher doping levels the particles swell and become less crystalline (d and e). Reference lines are given in (f) for CoO (JCPDS 00-048-1719); the dashed vertical line identifies the (220) reflection, at which the shifts are most apparent.

To assess the stoichiometry of the Co oxysulfide particles, we apply inductively coupled plasma-optical emission spectrometry (ICP-OES). We find the approximate stoichiometries for the (non-annealed) doped samples to be $\text{CoO}_x\text{S}_{0.18}$, $\text{CoO}_x\text{S}_{1.03}$, and $\text{CoO}_x\text{S}_{1.27}$ for the $(\text{NH}_4)_2\text{S} : \text{Co}$ molar ratios of 3 : 10, 1 : 1, and 3 : 1, respectively. Annealing the sample did not significantly alter its stoichiometry (see **Section 2.A.3**). This elemental analysis confirms that significant amounts of S, in direct proportion to the amount of $(\text{NH}_4)_2\text{S}$ used, are incorporated into the NPs. As observed previously,⁶⁶ under our conditions the resulting S : Co ratio in the NPs will not exceed the stoichiometry of Co_3S_4 , even with a large excess of $(\text{NH}_4)_2\text{S}$.

The CoO_x NPs obtained after oxidation are hollow and polycrystalline, with a diameter of 13.0 ± 1.5 nm (**Figure 2.2b**). The most dilutely doped oxysulfide NPs ($\text{CoO}_x\text{S}_{0.18}$), created from the $(\text{NH}_4)_2\text{S} : \text{Co}$ ratio of 3 : 10, retain a morphology virtually identical to the initial pure oxide NPs (diameter 12.9 ± 1.4 nm) (**Figure 2.2c**). Annealing the most dilutely doped NPs does not change the morphology (**Figure 2.A.1**). For higher degrees of anion-exchange doping, the diameter increases ($\text{CoO}_x\text{S}_{1.03}$, 15.0 ± 1.7 nm, **Figure 2.2d**; $\text{CoO}_x\text{S}_{1.27}$, 14.5 ± 1.6 nm, **Figure 2.2e**). This increase is consistent with the previous report for cobalt oxide NPs fully anion-exchanged into cobalt sulfide NPs.⁶⁶ The increase in the particle size follows the growth of the cavity within the NPs as a result of the nanoscale Kirkendall effect.⁶⁷⁻⁶⁹

The structural changes in the sulfidized CoO_xS_y NPs are assessed using selected area electron diffraction (SAED) (**Figures 2.2f** and **2.A.1**), showing that the CoO_x and $\text{CoO}_x\text{S}_{0.18}$ NPs exhibit a rock-salt structure with broad reflections from the (111), (200), and (220) planes. Close examination of the rotationally averaged SAED patterns shows that the crystal structures for these NPs agrees well with the reference CoO structure; however, the $\text{CoO}_x\text{S}_{0.18}$ SAED pattern exhibits a small shift to lower scattering angles, indicating an expansion of the unit cell (vertical dashed line in

Figure 2.2f). Lattice expansion could be caused by the larger S anion occupying the O^{2-} lattice. Based on the magnitude of the shift, however, the calculated increase in unit cell size is, at most, 0.02 Å relative to the reference structure for CoO. Interestingly, this shift is an order of magnitude less than what one might expect based on the extrapolation of the Co–O/Co–S bond lengths from the Shannon radii⁷⁰ (see **Section 2.A.3**). We therefore anticipate that the S concentration at the surface may be higher than in the bulk.

To develop an intuition for this shift, we include the SAED pattern for an annealed Co oxysulfide sample that was prepared in the same way as $CoO_xS_{0.18}$ (using a 3 : 10 $(NH_4)_2S$: Co molar ratio, **Figure 2.2f**, blue dashed line). ICP-OES for this sample revealed a composition of $CoO_xS_{0.17}$, similar to that of the unannealed NPs. As shown in **Figure 2.2f**, the lattice spacing for the heat-treated $CoO_xS_{0.17}$ sample is more similar to the CoO reference than are the unannealed $CoO_xS_{0.18}$ NPs. We interpret this finding as an indication of phase separation in the annealed samples ($CoO_xS_{0.17}$) into CoO and either the Co_9S_8 or the Co_3S_4 phase. In contrast, we believe the data indicates the unannealed $CoO_xS_{0.18}$ sample has sulfur occupying the anion sites in the rock salt structure. We did not, however, observe reflections in the annealed $CoO_xS_{0.17}$ sample for the Co_9S_8 or Co_3S_4 phases. We hypothesize that these sulfides must have domain sizes too small to give observable reflections or that they form amorphous phases during the phase separation process (see **Section 2.A.3**). As we will show later in our first-principles calculations, phase separation is energetically favourable for the Co oxysulfide material.

We further increase sulfur substitution by using higher $(NH_4)_2S$: Co ratios (1 : 1 and 1 : 3) to increase the driving force for S incorporation. At these high S concentrations, the particles ($CoO_xS_{1.03}$ and $CoO_xS_{1.27}$) become partially crystalline or amorphous (**Figure 2.2d,e**). We observe weak peaks that could correspond to smaller

grains of CoO in the $\text{CoO}_x\text{S}_{1.03}$ samples (approximately 15 Å in size, compared to about 30 Å for CoO_x and dilutely doped samples as estimated by the Scherrer equation, **Equation 1.2**; see **Table 2.A.1**). With more sulfur addition, the primary rocksalt CoO reflections become very weak in $\text{CoO}_x\text{S}_{1.27}$. Annealing these Co oxysulfide NPs leads to a significant solid-state reconstruction within the NPs, which results in a phase separation into a structurally distorted oxide and sulfide (see **Section 2.A.3**). We note that this phase separation occurs without significantly changing the compositions. The annealed Co oxysulfides have stoichiometries of $\text{CoO}_x\text{S}_{0.88}$ and $\text{CoO}_x\text{S}_{1.26}$ for the $(\text{NH}_4)_2\text{S} : \text{Co}$ molar ratios 1 : 1 and 1 : 3, respectively, similar to those of the unannealed Co oxysulfides ($\text{CoO}_x\text{S}_{1.03}$ and $\text{CoO}_x\text{S}_{1.27}$). These annealed, higher sulfur-content NPs show a much less pronounced expansion in size relative to the starting NPs compared to their non-annealed analogues (see **Figures 2.A.1a–h**).

To better understand the substitution mechanism of S^{2-} for O^{2-} , we perform density-functional theory (DFT) calculations to study the energetics of the Co oxysulfide system (see **Section 2.A.3**). We find that although it is thermodynamically favorable for S^{2-} to reside in place of O^{2-} , the migration energy barrier for S^{2-} diffusion through CoO is significant (2.63 eV, as compared to 0.18 eV for Co), preventing rapid movement into the CoO_x NPs.⁶⁶ These observations support the possibility that S^{2-} substitutes in place of O^{2-} through under-coordinated surface and defect sites, as has been observed for sulfidized MoP.⁴⁰ Our calculations of the formation energies of different phases in the Co–O–S system suggest that mixtures of CoO and Co-sulfide phases (Co_9S_8 and Co_3S_4) are significantly lower in energy than the rocksalt CoO_xS_y structures. This DFT finding is consistent with the observed phase separation seen by SAED. We therefore propose that the unannealed Co oxysulfides are a metastable phase characterized by the substitution of sulfur onto the under-coordinated anion sites. With more introduced sulfide, the driving force for sulfidization becomes large

enough that Co rapidly diffuses outward,⁶⁶ forming an amorphous phase. Upon annealing, phase separation occurs, allowing the NPs to form Co-sulfide domains (Co_9S_8 and Co_3S_4). At the lowest $(\text{NH}_4)_2\text{S} : \text{Co}$ ratio, the resulting grains of Co-sulfide are likely too small to be observed.

2.3.2. Electrochemical properties

To understand how the anionic substitution affects the electrochemical properties, we conducted cyclic voltammetry (CV) experiments in Ar-saturated 0.1 M KOH. **Figure 2.3** shows the CV results of the NPs examined using a thin-film electrode prepared from a composite of the NPs, acetylene black, and K^+ -Nafion®.⁷¹ To ensure that the electrochemical response of these NPs is intrinsic to the surface chemistry, we treated the NPs with 0.1 M KOH in isopropanol under sonication for 30 minutes to strip off the ligands.^{64, 65} To ensure ligand removal, we compared the CV result of our CoO_x NPs to thin-film electrodes prepared in the same manner using nanopowders of known stoichiometry (CoO and Co_3O_4). The CoO reference showed a similar electrochemical response to our CoO_x NPs (see **Figure 2.A.2**), confirming the surface chemistry of our CoO_x NPs. We point out that the CV of our CoO_x NPs is distinct from that of the Co_3O_4 reference, supporting our conclusion that the CoO_x catalyst has a surface CoO crystal structure.

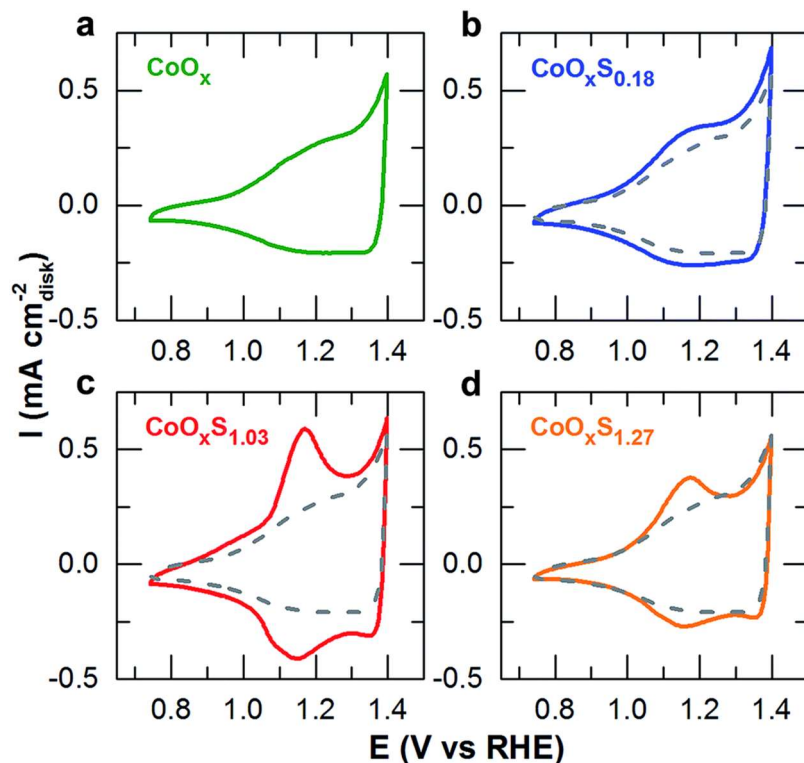


Figure 2.3. Cyclic voltammograms of carbon-supported thin-film electrocatalysts containing (samples not subjected to annealing) CoO_x (a), $\text{CoO}_x\text{S}_{0.18}$ (b), $\text{CoO}_x\text{S}_{1.03}$ (c), and $\text{CoO}_x\text{S}_{1.27}$ (d) nanoparticle electrocatalysts in Ar-saturated 0.1 M KOH at 50 mV s^{-1} scan rate. The grey dashed background CV in (b)–(d) shows a comparison to the CoO_x starting material.

Our CV results capture the evolution of the surface chemistry of the Co oxysulfide particles throughout the anion substitution process. Notably, although CoO_x and $\text{CoO}_x\text{S}_{0.18}$ share the same crystal structure (**Figure 2.2f**), their surface chemistries as revealed by the CV measurement are distinct. The starting CoO_x material shows a broad, shallow redox peak between ~ 1.0 and ~ 1.3 V vs. RHE, which is consistent with the $\text{Co}^{2+}/\text{Co}^{3+}$ redox couple in literature (**Figure 2.3a**).^{31, 72, 73} With the inclusion of more S^{2-} , a reversible peak in the region of 1.1 V vs. RHE grows (**Figure 2.3b–d**). This observation is consistent with previous reports on Co sulfides, which have

suggested that this redox couple can be attributed to the reaction(s) $\text{CoS} + \text{OH}^- \leftrightarrow \text{CoS} - \text{OH} + \text{H}_2\text{O} + \text{e}^-$ and/or $\text{CoS} - \text{OH} + \text{OH}^- \leftrightarrow \text{CoSO} + \text{H}_2\text{O} + \text{e}^-$.^{74, 75} This assignment is consistent with the growth of the ~ 1.1 V vs. RHE peak $\text{CoO}_x\text{S}_{1.03}$ sample with the addition of S^{2-} , but we caution that future work remains to be done to verify the nature of this redox couple. Interestingly, the peak height decreases for the $\text{CoO}_x\text{S}_{1.27}$ sample. At the moment, it is unclear what causes the peak height to decrease.

We characterize the HER activity on these partially-anion-substituted materials in an H_2 -saturated 0.1 M KOH electrolyte at 10 mV s^{-1} (**Figure 2.4a**). The polarization curves show that the addition of sulfur improves the HER activity beyond that of CoO_x . The improvement in the HER activity is most pronounced for the most dilute doping ($\text{CoO}_x\text{S}_{0.18}$). In comparison to the starting CoO_x material: the specific HER activity of $\text{CoO}_x\text{S}_{0.18}$ is $\sim 3\times$ more than the CoO_x starting material at -375 mV (vs. RHE). Further addition of S^{2-} does not sustain this increase in activity; the observed HER activity returns to a level close to that of CoO_x for samples with additional S^{2-} beyond $\text{CoO}_x\text{S}_{0.18}$. These results are summarized in the corresponding Tafel plots (**Figures 2.4b** and **2.A.3**). Interestingly, the CoO_x , $\text{CoO}_x\text{S}_{1.03}$, and $\text{CoO}_x\text{S}_{1.27}$ samples exhibit a large Tafel slope of 160–170 mV per decade, which corresponds to the phenomenological transfer coefficient (α) of $\sim 1/3$, while the $\text{CoO}_x\text{S}_{0.18}$ sample shows a Tafel slope of 200 mV per decade. These transfer coefficients are significantly larger than the reported Tafel slopes for metals^{76, 77} and other sulfide catalysts.^{16, 17, 51} Future work in understanding this rather high Tafel slope is essential to pinpoint the microscopic mechanism for the observed enhancement in the HER.

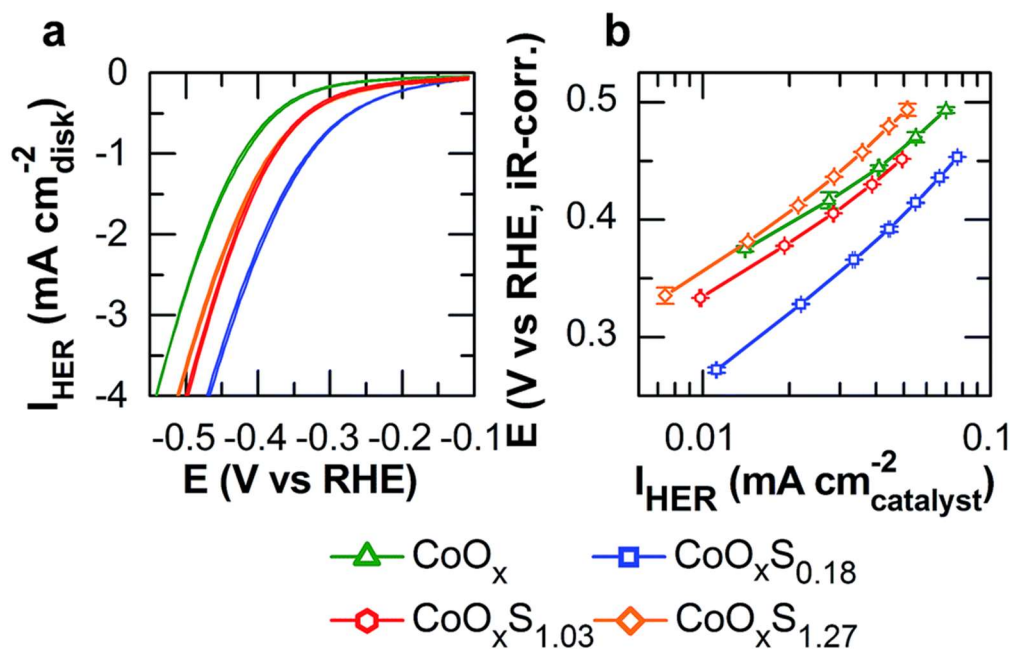


Figure 2.4. Polarization curves of carbon-supported thin-film electrocatalysts containing cobalt oxide/oxysulfides (samples not subjected to annealing). Geometric hydrogen evolution current densities (a) were measured in H₂-saturated 0.1 M KOH at 10 mV s⁻¹. A Tafel plot (b) is shown based on the known geometries of the particles. Error bars in (b) give the standard deviation from three independent measurements.

2.3.3. Enhancement mechanism from first principles

To understand the origin of the HER activity enhancement, which was experimentally observed to be most effective at low S concentration, we apply the activity descriptor approach pioneered by Parsons, Gerischer, and Nørskov.^{26, 78, 79} In this approach, the H adsorption energy estimates the surface's ability to form the HER intermediate.⁸⁰ We calculate the H adsorption energy on the CoO(100) surface, which is charge neutral and lowest in energy, as a function of the surface S composition using DFT (see **Figure 2.A.4**). In this framework, the most active HER electrocatalyst should have the H adsorption energy at a value that minimizes the energy difference

between the reactant, the intermediate (H^*), and the product. Generally, this value is found to be around the H adsorption energy on Pt.^{26, 80, 81}

We observe that H^* prefers to bind to a Co ion rather than an O or S ion. Further analysis shows that H^* develops a partial negative charge, explaining its tendency to sit above a positively charged Co ion. As we substitute more S onto the surface, the H^* adsorption energy first decreases, indicating stronger bonding between H^* and Co. Crucially, at an average of only 1 in 8 O^{2-} ions substituted with S^{2-} on a CoO(100) surface 2×2 unit cell, the adsorption energy of H approaches that of Pt(111), which we use as a benchmark for an “ideal” HER catalyst (**Figure 2.5**, blue plot). Also plotted are the experimentally determined values for HER current at 375 mV, as a function of S : Co ratio (**Figure 2.5**, red plot). As more O is displaced, the H binding energy returns to the initially high value. Assuming that the thermodynamic formation of the adsorbed H intermediate limits the HER kinetics,^{27, 80-82} our DFT calculations broadly agree with our experimental HER results. Specifically, the reduction in the H adsorption energy following the partial S^{2-} exchange increases HER activity initially; however, as more sulfur is incorporated, the formation of the H^* intermediate becomes more energetically intensive and consequently impedes the HER kinetics. We emphasize not just that isovalent anionic dopants may be used to tune the hydrogen adsorption free energy to optimize electrocatalytic activity but also that the composition of the doped electrocatalyst must be precisely tuned in order to exploit the surface's ability to facilitate an electrochemical reaction. To emphasize the importance of the anion control, we show through an additional HER measurement on sulfur-rich CoS_2 NPs that the HER is not catalyzed as efficiently on CoS_2 as it is on the Co oxysulfide NPs presented in this work (see **Figures 2.A.7** and **2.A.8**). Recent results from others reach a conclusion similar to ours, highlighting the need for precise control over anion chemistry.^{41, 42}

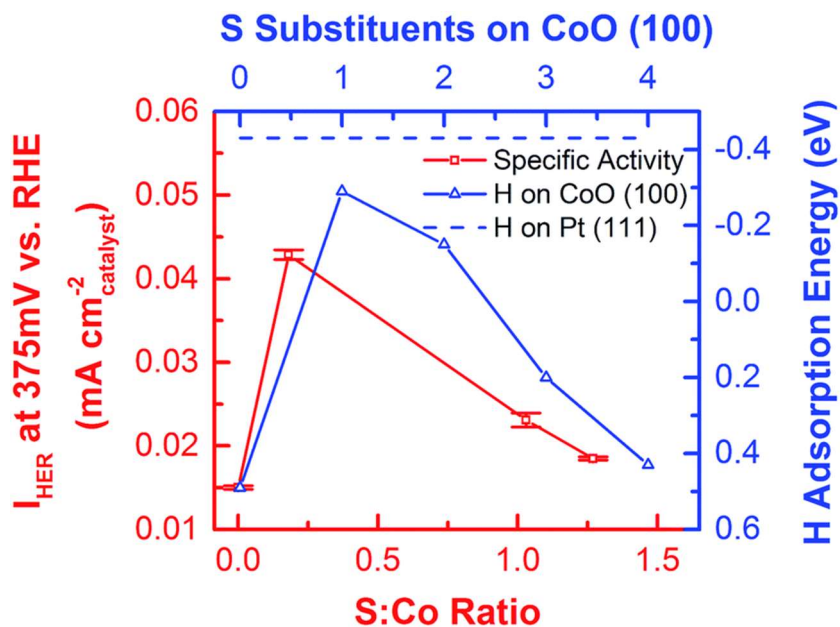


Figure 2.5. Calculated DFT adsorption energies of hydrogen and their correlation with experimental results for the activity of CoO_xS_y nanoparticle electrocatalysts (error bars give the standard deviation based on three independent measurements). At low doping levels (e.g., $\text{CoO}_x\text{S}_{0.18}$) the experimentally-determined HER specific activity of the particles substantially increases (red curve) while at higher doping levels, activity decreases. This activity change is a result of S^{2-} strengthening the H adsorption energy on the CoO surface (blue curve), bringing it closer to the H adsorption energy on Pt(111) (blue dashed curve) at low S^{2-} doping levels.

2.4. CONCLUSION

In summary, we report the critical role of an isovalent anionic substitution in controlling the electrocatalytic activity of a transition-metal-containing electrocatalyst. As shown in the cobalt oxysulfide system, anionic substitution can positively affect the HER activity; however, the substitution process must be tightly controlled to

obtain the desired enhancement. In our cobalt oxysulfide nanoparticles, we accomplish this control by engineering the anion-exchange driving force by adjusting the amount of the highly reactive S^{2-} precursor. Using this protocol, we produce a series of cobalt oxysulfide nanoparticles with different amounts of S^{2-} , which allow us to establish the trend between the HER activity and the sulfide content. We find a small amount of S is best for enhancing the HER; further sulfur addition disrupts the H^* intermediate energy and also alters the phase of the oxysulfides. We attribute the activity enhancement at low S^{2-} concentration to a ‘dopant’ effect, whereby the presence of the S^{2-} in the surface layer modifies the hydrogen adsorption on the oxysulfide electrocatalyst. Our results highlight an opportunity to control the anionic composition as a strategy for not just clarifying the role of the anions but also for further increasing the activity of electrocatalysts.

2.A. APPENDIX

2.A.1. Funding

This work was supported in part by the National Science Foundation (NSF) under award numbers CHE-1152922, CMMI-1344562, CHE-1507753, DMR-1149036, and ACI-1440547. This work made use of the Cornell Center for Materials Research Shared Facilities, which are supported through the NSF MRSEC program (DMR-1120296). This research used computational resources provided by the Texas Advanced Computing Center under Contract No. TG-DMR050028N and the Extreme Science and Engineering Discovery Environment (XSEDE), which is supported by National Science Foundation grant number ACI-1053575. We also thank Gregg McElwee of the Cornell Geochemistry Laboratory for analytical measurements.

2.A.2. Materials and methods

Trioctylphosphine oxide (99%), ammonium sulfide (40-48 wt% solution in water), oleic acid (99%), 1,2-dichlorobenzene (DCB, 99.8%, anhydrous), oleylamine (70%), 1-octadecene (90%), dicobalt octacarbonyl (>90%), Nafion 117 solution (~5% mixture of lower aliphatic alcohols and water), N,N-dimethylformamide (99.8%, anhydrous), pentane (>99%, anhydrous), nitric acid (70%), potassium hydroxide (99.99%), lead (II) nitrate (>99.99%), cobalt (II,III) oxide (nanopowder, 99.5%), 1-butanol (99.8%, anhydrous), and thiourea (>99%) were obtained from Sigma Aldrich and used as received except as noted. The sulfide content of commercially available $(\text{NH}_4)_2\text{S}$ was checked by gravimetric analysis of precipitated lead sulfide formed by adding the sulfide solution to an aqueous solution containing excess $\text{Pb}(\text{NO}_3)_2$.⁶⁶ Oleic acid and DCB were stored under inert atmosphere in a glove box. $\text{Co}_2(\text{CO})_8$ was recrystallized from cold pentane immediately before use. Acetylene black (AB, Alfa

Aesar, 99.9+%) was treated in nitric acid at 80°C for several hours, then filtered and dried at 100°C overnight. Other chemicals were used as received: isopropyl alcohol (99%) and hexanes (>98.5%) from BDH; cobalt (II) oxide (nanopowder, 99.7%) from US Research Nanomaterials, Inc; ethyl ether (>99%, anhydrous, stabilized with BHT) from Fisher Scientific; cobalt (II) nitrate hexahydrate (99%) from Acros Organics; and ethanol (200 proof) from KOPTEC. Molecular sieves (Fluka, UOP type 3 Å) were activated at 300°C under vacuum for at least 3 hours before use. All aqueous solutions were prepared using 18.2 MΩ water from a Direct-Q system (Millipore).

Nanoparticle synthesis

CoO nanoparticles were synthesized by oxidation of monodisperse cobalt nanoparticles.⁶⁷ Standard Schlenk line techniques were used. In a typical experiment, a three-necked, round-bottom flask was loaded with TOPO (0.1 g), sealed, and purged with nitrogen by three evacuation and backfilling cycles. 12 mL of 1,2-dichlorobenzene containing 0.1 mL dissolved oleic acid was added, followed by degassing the solution with three additional evacuation and backfilling cycles. Subsequently, the solution was heated to reflux (180-183°C), and 0.54 g of Co₂(CO)₈ dissolved in 3 mL of DCB was quickly injected via syringe. After 10 minutes, growth was stopped by quenching the vessel in a water bath. Ethanol was added (1:1 by volume) to precipitate out the nanoparticles, which were separated by centrifugation, re-suspended in hexane, and precipitated once more with ethanol (2:1 hexane:ethanol) to remove very small particles which remained in the supernatant. The purified nanoparticles were redissolved in DCB; after this solution was heated to 180°C, a gentle stream of air was blown through the solution for 4 hours to quantitatively oxidize the particles to CoO. The particles were then precipitated with ethanol (1:1 DCB:ethanol) followed by centrifugation.

Sulfur-doped cobalt oxides were synthesized by anion exchange according to our previous report.⁶⁶ The degree of anion exchange was controlled by varying the amount of added $(\text{NH}_4)_2\text{S}$. Three different exchange ratios were examined based on the nominal molar ratio of cobalt (assuming particles were 100% CoO) to introduce sulfide: 10:3, 1:1, and 1:3. In a typical experiment, approximately 30 mg of CoO nanoparticles were dissolved in 3.5 mL of mixed octadecene and oleylamine (1:1 by volume). This solution, in a sealed three-neck flask, was degassed by three evacuation/backfill cycles with nitrogen on a Schlenk line, then heated to 100°C. A solution of $(\text{NH}_4)_2\text{S}$ in oleylamine was prepared by dissolving an appropriate amount of aqueous $(\text{NH}_4)_2\text{S}$ (~56, ~189, or ~589 μL of solution for each ratio above, with an aqueous $(\text{NH}_4)_2\text{S}$ concentration of 41.7 wt%) in 10 mL of oleylamine followed by drying for about 20 minutes with molecular sieves. 3.5 mL of this solution was injected into the hot solution of CoO_x NPs, after which the temperature was set to 70°C. The color of the solution immediately changed from dark brown to black. The reaction was allowed to proceed for five minutes following injection, then the flask was cooled in a water bath. The anion-exchanged nanoparticles were recovered by precipitation with ethanol/centrifugation and were washed once more by resuspension in hexane followed by precipitation with ethanol/centrifugation.

Annealed NPs were synthesized according to an adaptation of our previous procedure.⁶⁶ Approximately 40 mg of NPs of any composition were dissolved in a mixed solvent of 4.4 mL of octadecene and 1.1 mL of OLA in a three-neck flask. After degassing by three evacuation/backfill cycles on a Schlenk line, the solution was heated to 200°C and kept at that temperature for 1 hour, after which it was cooled by removing the heating mantle. The annealed NPs were recovered by precipitation with ethanol/centrifugation and washed once more by resuspension in hexane followed by precipitation with ethanol/centrifugation.

Post-synthetic characterization

Transmission electron microscopy (TEM) and selected area electron diffraction (SAED) images were obtained using an FEI Tecnai T12 at an accelerating voltage of 120 kV. SAED pattern analysis and calibration were done using D.R.G. Mitchell's script for circular Hough transform analysis⁸³ in Gatan DigitalMicrograph 2.32. Power law background from the forward-scattered beam was subtracted by fitting a portion of the background before the reflections to an equation of the form $y = a \cdot x^b$,⁸⁴ and all peaks were fit to Lorentzian distributions. The camera length for each SAED image was calibrated against an evaporated Al foil standard (Electron Microscopy Sciences). The stoichiometry of the products was also checked using an energy-dispersive x-ray spectrometer (EDX) on the same instrument, but without a calibration standard; in general the oxygen content of the samples was found to vary widely from point to point (15-30%) and the S content somewhat less (5-10%).

The ratio of Co:S in a set of nanoparticle samples was quantified using inductively coupled plasma-optical emission spectroscopy (ICP-OES) at the Cornell Geochemistry Laboratory, Cornell University, Ithaca, New York. Samples were digested with hot aqua regia and diluted with a 2% nitric acid matrix for analysis using a Spectroblue ICP-OES spectrometer equipped with an argon torch. Co and S were standardized against concentrations from 2mg/L to 20 mg/L in 2% nitric acid. Sc was used as an internal standard. Relevant emission lines were: Co, 228.616 nm; S, 180.731 nm; and Sc, 361.384 nm. Relevant operating parameters were: RF power 1450 W, coolant flow 12 L/min, auxiliary flow 0.9 L/min, and nebulizer flow 0.77 L/min.

The particular set of samples shown in **Figure 2.1a-d** was found to have the compositions $\text{CoO}_{1.6}$, $\text{CoO}_{1.6}\text{S}_{0.11}$, $\text{CoO}_{0.5}\text{S}_{0.97}$ and $\text{CoO}_{0.5}\text{S}_{1.08}$ by EDX. The respective Co:S stoichiometries as found by ICP-OES were CoO_x , $\text{CoO}_x\text{S}_{0.18}$, $\text{CoO}_x\text{S}_{1.03}$, and

CoO_xS_{1.27}. In general this EDX analysis underestimated the amount of S present in the NP samples, especially when the samples were only slightly sulfidized. Given the limitations of EDX as an analytical technique in this case with less than optimal samples and insufficient calibration,⁸⁵ these numbers are of only qualitative importance compared to those found by ICP-OES. The phase purity of the CoO, Co₃O₄, and CoS₂ nanopowders used as reference materials was checked by x-ray powder diffraction using a Scintag θ -2 θ diffractometer with Cu K-alpha radiation. The materials were found to be free of secondary phases (**Figure 2.A.6**).

Catalyst ink preparation

Purified particles were dried overnight under vacuum. A 1 mg/mL solution of the nanoparticles in hexane was prepared by re-dispersing the powder using a horn sonicator (Branson Digital Sonifier 450D). A 1 mg/mL solution of AB in N,N-dimethylformamide was prepared similarly. Subsequently, the two immiscible solutions were mixed with the sonicator, causing the carbon to transfer to the hexane phase and uniformly mix with the nanoparticles.

The mixture was precipitated by adding ethanol (1:1 by volume) followed by centrifugation. To remove the long-chain hydrocarbon ligands, the material was re-dispersed with 0.1 M KOH in isopropanol and sonicated for 30 minutes. The catalyst was then precipitated with ethanol, centrifuged, and dried under vacuum overnight, yielding a powder of nanoparticles dispersed on acetylene black.

Electrochemical testing

Catalyst inks were prepared using isopropanol/water (1:4 by volume) as a solvent; the concentration of catalyst used was 1 mg/mL. Nafion solution was neutralized by addition of 0.1M aqueous KOH (approx. 2:1 KOH:Nafion solutions by

volume), then added to the ink (3.4 μ L per mL) as a binder before mixing by sonication. 10 μ L of this catalyst ink, containing 5 μ g each of neutralized Nafion, AB, and cobalt oxide/sulfide/oxysulfide nanoparticles was dropcast onto a glassy carbon electrode and allowed to dry under ambient atmosphere. A three-electrode electrochemical cell (Pine) was utilized for all electrochemical measurements and the potential applied to the cell was controlled using a Bio-Logic SP-300 potentiostat. 0.1M KOH was used as the supporting electrolyte. A platinum wire was used as a counter electrode and an Ag/AgCl electrode (Pine) was used as a reference electrode. The potential of this reference electrode was calibrated against the reversible hydrogen electrode (RHE) by measuring the hydrogen evolution/oxidation currents on a polycrystalline Pt disk (Pine) in 0.1M KOH saturated with hydrogen (Airgas, ultra-high purity) and taking the voltage at which the current was zero as 0 V vs. RHE. We measured 0 V vs. RHE to be 0.943 ± 0.005 V vs. Ag/AgCl. All the potentials in this study were referenced to the RHE potential scale and correspond to the applied potentials, E_{applied} , unless they are stated to be iR -corrected potentials, $E_{iR\text{-corrected}}$, calculated with $E_{iR\text{-corrected}} = E_{\text{applied}} - iR$ where i is the current and R is the uncompensated ohmic electrolyte resistance. R was taken as the AC impedance at high frequency of the three-electrode system as measured by the same potentiostat.

Cyclic voltammetry measurements were taken by saturating the electrolyte with argon (Airgas, ultra-high purity) prior to measurements and HER measurements were taken after saturating the electrolyte with hydrogen (Airgas, ultra-high purity).

2.A.3. Additional discussion

Further remarks on TEM micrographs and SAED structural data

A second population of cobalt oxide NPs was synthesized to produce the annealed $\text{CoO}_x\text{S}_{0.17}$ sample (**Figure 2.2f**, dashed line); which had an as-synthesized

diameter of 11.5 ± 1.2 nm immediately after oxidation (micrograph not shown). Samples of annealed CoO_x and annealed $\text{CoO}_x\text{S}_{0.17}$, $\text{CoO}_x\text{S}_{0.88}$, and $\text{CoO}_x\text{S}_{1.26}$ were all prepared from this population, and they had diameters of 10.8 ± 1.4 , 10.1 ± 1.5 , 10.5 ± 1.5 , and 11.6 ± 1.6 nm respectively (**Figure 2.A.1e-h**).

In the $\text{CoO}_x\text{S}_{0.88}$ (annealed) sample, one of the phases is consistent with a rocksalt CoO ; however, a shift to smaller diffraction angles indicates that the CoO structure is distorted. The second observed phase does not match to either spinel Co_3S_4 or rocksalt Co_9S_8 , but matches to Co_9S_8 , suggesting the presence of a Co-sulfide phase which is deficient in Co, thus explaining the larger diffraction angles observed. Thus, it appears that there now is sufficient S to form both Co-sulfide domains and substituted oxides. It is unclear whether phase separation occurs within NPs or if they separate into two populations, as we observe that some particles more closely resemble the original oxide particles and some are more similar to the larger, less well-crystallized $\text{CoO}_x\text{S}_{1.26}$ NPs (see **Figure 2.A.1f**). This observation of phase separation in our annealed oxysulfide NPs may also explain the discrepancy between the observed stoichiometries of the samples reacted at $(\text{NH}_4)_2\text{S} : \text{Co}$ ratios 1:1 for the non-annealed ($\text{CoO}_x\text{S}_{1.03}$) and annealed ($\text{CoO}_x\text{S}_{0.88}$) samples. The free energies of formation of the individual phases, in particular the stable sulfides (see below), could provide sufficient driving force not only to cause recrystallization of the particles but also to eject excess S under the reducing conditions of the annealing experiment.

The lattice parameter, a , of the cubic unit cell was determined by averaging the lattice parameter found by applying the following equation to the (111), (200), and (220) principal reflections:

$$\frac{1}{d_{hkl}^2} = \frac{h^2 + k^2 + l^2}{a^2} \quad (2.1)$$

Where d_{hkl} is the interplanar spacing and h, k, and l are the Miller indices. The Debye-Scherrer formula was also used to find the domain size t with a shape factor of 0.9:

$$t = \frac{0.9 \cdot \lambda}{B \cdot \cos \theta_B} \quad (2.2)$$

λ , the de Broglie wavelength of 120 keV electrons, is 0.0354 Å; B is the full width at half maximum of the Lorentzian fitted peak in radians; and θ_B is the Bragg diffraction angle in radians. No instrumental correction was used. The extracted lattice parameters and crystallite sizes are given in **Table 2.A.1**.

Vegard's law calculation

The crystal radii (ionic radii will give an identical result) r_X of 6-fold coordinated Co^{2+} (high spin⁸⁶), S^{2-} , and O^{2-} are taken as 0.885 Å, 1.70 Å, and 1.26 Å respectively, as given by Shannon.⁷⁰ Using these radii, the calculated lattice parameter a_{CoO} of rocksalt CoO is 4.29 Å, which compares favorably with the measured value of 4.2612 Å (JCPDS 00-048-1719). We assume that the hypothetical ionic compound CoS has a lattice parameter of 5.17 Å using the Shannon radii. For comparison, $\frac{1}{2}$ of the parameter for Co_9S_8 is 4.9644 Å (JCPDS 00-056-0002). Using Vegard's law to adjust the lattice parameter for the increased radius of S^{2-} to a_{CoOS} :

$$a_{\text{CoOS}} = 2 \cdot r_{\text{Co}^{2+}} + 2 \cdot X_{\text{CoO}} \cdot r_{\text{O}^{2-}} + 2 \cdot X_{\text{CoS}} \cdot r_{\text{S}^{2-}} \quad (2.3)$$

With the fraction of CoO given by X_{CoO} and of CoS given by X_{CoS} . We find that the lattice parameter should increase by 0.158 Å (relative to the calculated radius of 4.29 Å) assuming perfect substitution of S^{2-} for O^{2-} in rocksalt CoO for a composition $\text{CoO}_{0.82}\text{S}_{0.18}$. The deviation found for $\text{CoO}_x\text{S}_{0.18}$ is +0.021 Å relative to the reference structure, +0.016 Å relative to the un-annealed CoO_x , and +0.027 Å relative to the annealed CoO_x and annealed $\text{CoO}_x\text{S}_{0.17}$ samples (see above). These deviations are thus nearly an order of magnitude lower than that anticipated by Vegard's law.

Table 2.A.1. Structural data extracted from the rotationally averaged SAED patterns of CoO_xS_y nanoparticles given in **Figure 2.A.1**. Measurements are given based on the average of the values fitted from the (111), (200), and (220) CoO rocksalt structure reflections unless noted.

Sample composition	CoO lattice	CoS _x lattice	Crystallite size,
	parameter, Å [std. deviation]	parameter, Å [std. deviation]	Å [std. deviation]
CoO _x	4.267 [0.005]		31.2 [2.2]
CoO _x (annealed)	4.256 [0.003]		28.8 [4.4]
CoO _x S _{0.18}	4.284 [0.001]		29.2 [4.0]
CoO _x S _{0.17} (annealed)	4.256 [0.003]		30.4 [5.6]
CoO _x S _{1.03}	4.309 [0.055]		14.7 [7.3] ^a
CoO _x S _{0.88} (annealed)	4.262 [0.031]		24.0 [4.3]
		9.653 [0.180] ^b	13.0 [9.0] ^b
CoO _x S _{1.27}	4.247 [0.063] ^c		9.8 [0.2] ^c
CoO _x S _{1.26} (annealed)		9.673 [0.160] ^d	9.3 [7.7] ^d

^a Crystallite size based on the (111) and (200) reflections. If the much weaker reflection (220) is included, measurement increases to 26.1 (20.5) Å.

^b Based on the reflections (311) near 2.2 Å⁻¹, (511) near 3.3 Å⁻¹, and (440) near 3.7 Å⁻¹.

^c Based on the (111) and (200) reflections. Very weak signal.

^d Based on the reflections (511) near 3.3 Å⁻¹ and (440) near 3.7 Å⁻¹.

Calculation of the cobalt sulfide content of an oxysulfide NP

In this section, we consider the set of NPs used to generate the annealed sample $\text{CoO}_x\text{S}_{0.17}$. The average particle size of the cobalt NPs (epsilon phase) used for this sample set as measured by TEM was 9.5 ± 1.2 nm, and the calculated crystallographic density of ϵ -Co is 8.635 as given by Dinega and Bawendi.⁸⁷ Using the average particle size we estimate based on this density that there are on average 39,610 atoms/particle. Assuming this number of Co atoms does not change as the particle is oxidized to CoO and this material is then anion-exchanged with S^{2-} , there are therefore ca. 6,734 S atoms/particle available to form Co-sulfide domains in $\text{CoO}_x\text{S}_{0.17}$. As there are 32 S atoms in each unit cell (for Co_9S_8 $a = 9.9287$ Å, $Z = 4$ per JCPDS 00-056-0002; for Co_3S_4 $a = 9.4232$ Å, $Z = 8$ per JCPDS 00-047-1738), enough Co_9S_8 or Co_3S_4 should be formed to produce a single domain of diameter 7.3 nm to 7.0 nm, respectively. Such crystalline domains are not observed in the SAED for $\text{CoO}_x\text{S}_{0.17}$, indicating that phase segregation is incomplete, likely due to the overall low mobility of S. Where measurable domains of CoS_x are observed, their size as measured by the Scherrer equation is much less than 7 nm (see above, **Table 2.A.1**).

Calculation of the catalyst active area

Particle and void diameters d_{particle} and d_{void} were measured from TEM images using at least 250 measurements. From these measurements the geometric surface area of each particle A_s was calculated assuming that only the outer surface contributed to the area:

$$A_s \approx \frac{\sum 4 \cdot \pi \cdot r_{\text{particle}}^2}{\sum \left(\frac{4}{3}\right) \cdot \rho \cdot \pi \cdot (r_{\text{particle}}^3 - r_{\text{void}}^3)} = \frac{6}{\rho} \cdot \frac{\sum d_{\text{particle}}^2}{\sum (d_{\text{particle}}^3 - d_{\text{void}}^3)} \quad (2.4)$$

Because the material density ρ is not known with certainty, it was estimated by taking a weighted average of bulk densities. For the catalysts based on CoO_x , $\text{CoO}_x\text{S}_{0.18}$, and

CoO_xS_{0.17}, which are all isostructural, the weighted average of the densities of cobalt (ii) oxide⁸⁸ (6.44 g/cm³) and cobalt (ii) sulfide⁸⁸ (5.45 g/cm³) were used based on the hypothetical compound CoO_{1-y}S_y, where y is the measured S:Co ratio. For the amorphized catalysts CoO_xS_{1.03} and CoO_xS_{1.27}, the density was estimated by taking a weighted average of the bulk densities of CoO and Co₃S₄ (4.843 g/cm³, JCPDS 00-047-1738) based on the hypothetical compound (CoO)_{1-3y/4}(Co₃S₄)_{3y/4}, again where y is equal to the measured S:Co ratio.

Density functional theory calculations

Density-functional theory (DFT) calculations were performed with the Vienna Ab-initio Software Package (VASP)⁸⁹⁻⁹² using the PBE exchange-correlation functional⁹³ and the projector augmented wave method.^{94, 95} The Brillouin zone integration was performed using a Monkhorst and Pack k-point mesh.⁹⁶ 3×3×1 k-point meshes were employed for structural relaxations and energy calculations for the slabs. The energy cutoff for the plane wave basis was set to 400 eV and the corresponding cutoff energies for the augmentation functions were set to 650 eV for all our calculations. We did not employ the DFT+U method here for the reason that the results depend sensitively on the Hubbard U value. Furthermore, it is expected that U should depend on the local environment of the Co atoms, resulting in a different value required in the bulk, on the surface, and as a function of the S composition. To avoid this complication and resulting arbitrariness, we performed our calculations of the H adsorption energies on the S substituted CoO surfaces using the PBE approximation.

We used a 64-atom CoO(100) slab to calculate the adsorption and formation energies, since CoO is the most stable Co oxide phase under our experimental conditions; furthermore, the (100) surface is used because it has the lowest energy and is charge neutral. A vacuum spacing of 12 Å was used to ensure that the surface does

not interact with its periodic image. Only the top two layers of the slab are allowed to relax. We first determine whether a substitutional S atom prefers to sit on a surface site or in the bulk. For just a single S, it was 0.65 eV more expensive for S to replace a surface O atom compared to one sitting in the second layer. However, as we added more S atoms, the energy required to sit on the bulk site started going up; the surface was now a better site for these S atoms. We attribute this increase in energy to the fact that the S anion is considerably larger than the O anion, starting to cause strain inside the slab. Furthermore, the migration barrier for S to diffuse into the CoO slab is quite high at 2.63eV, preventing inward diffusion.⁶⁶ This supports our conclusion that most of the sulfur in our experiment must be present on the surface. Our formation energy calculations combined with the Co-O-S phase diagram from the Materials Project website^{97, 98} suggest that a mixture of cobalt oxides and sulfides will be lower in energy than the rocksalt CoO_xS_y phase. Based on calculated energies for bulk CoO and Co_3S_4 phase, we estimate that the rocksalt CoO_xS_y structure with all surface O atoms replaced by S would be at least 0.17 eV/atom more unstable than a phase separated mixture of CoO and Co_3S_4 . We calculated the adsorption energies of H^* for the same size slab. Starting with the pure CoO slab, we successively replaced O atoms on the surface with S until all the surface anion sites (8) were occupied by S. Placing a single H atom on top of Co, O and S sites, we calculated adsorption energies for each case. All possible configurations of the surface were considered, and we picked the one with the lowest energy as it indicates strongest binding. Reference values for H-adsorption energy on platinum were obtained using a 64-atom Pt(111) slab. A schematic of the CoO slab is shown in **Figure 2.A.4**. The results are shown in **Figure 2.A.5**; the results of every calculation are shown in **Table 2.A.2**.

Table 2.A.2. Results of the DFT calculations for the binding energy of H. Bold numbers indicate that the energy is the minimum calculated for the species that H sits on for each S substitution.

# of S on surface	Location of H	Species H sits on	Defect Formation Energy (eV)
0	edge	Co	0.49
0	center	O	1.23
1	edge	Co	1.03
1	inside	Co	-0.29
1	corner	O	6.38
1	octahedral	O	5.63
1	tetrahedral	O	1.97
1	center	S	6.23
2	inside	Co	-0.14
2	edge	Co	-0.15
2	tetrahedral	O	2.22
2	octahedral	O	2.21
2	center	S	1.97
2	corner	S	1.90
3	edge	Co	0.48
3	inside	Co	0.20
3	tetrahedral	O	2.71
3	corner	O	2.13
3	octahedral	S	1.78
3	center	S	1.43
4	edge	Co	0.43
4	inside	Co	0.43
4	tetrahedral	O	1.64
4	corner	S	2.36
4	center	S	1.55
4	octahedral	S	1.27
8	edge	Co	0.65
8	center	S	0.78

CoS₂ nanoparticle electrochemical testing

We use cobalt disulfide as a reference HER activity for an active sulfide-rich cobalt disulfide phase.⁴⁸ We synthesized phase-pure CoS₂ nanopowder via the thermal decomposition of Co[SC(NH₂)₂]₄(NO₃)₂ at 400 °C under N₂ for 2 h, as described previously.⁹⁹ The CoS₂ phase was confirmed with XRD (**Figure 2.A.7**, left) and the particle size was characterized with TEM (**Figure 2.A.7**, right), shown below. Based on TEM analysis, the particle size is 13.0 nm ± 4.3 nm, in agreement with the crystallite size extracted from XRD using the Scherrer equation (13.7 ± 1.5 nm, from 8 strongest reflections).

We characterize the HER activity of the CoS₂ nanoparticles using the same electrode protocol that was used to characterize the Co oxysulfide. We find that CoS₂ has a lower specific activity and mass activity than CoO_x as well as CoO_xS_{0.18}, as seen in the Tafel plots below (**Figure 2.A.8**). Further, the CoS₂ showed significant activity degradation after only five cycles. Therefore, we can conclude on the basis of this preliminary characterization that the improved activity seen in the mixed anion compounds does not result from a possible sulfide-rich CoS₂-like phase on the Co-oxysulfide surface.

2.A.4. Supporting figures

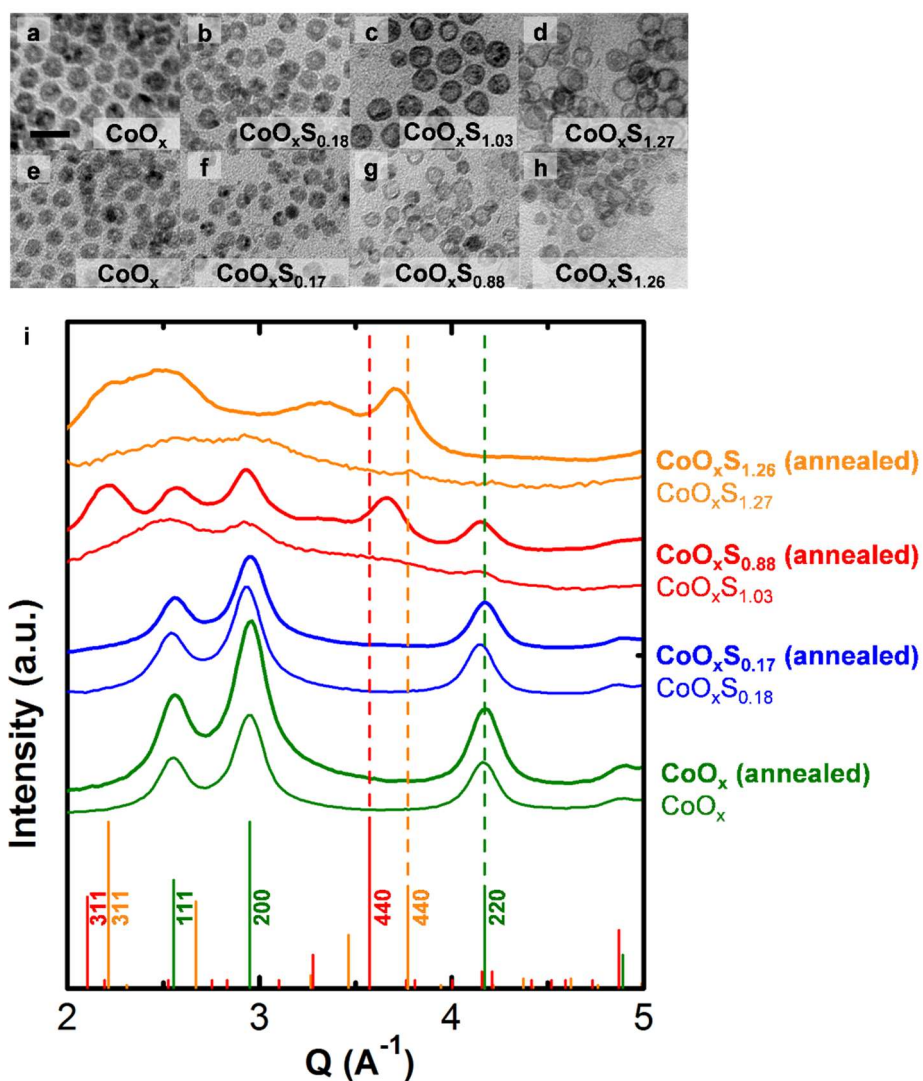


Figure 2.A.1. TEM characterization of structural transformations of CoO_xS_y nanoparticles. Both as-exchanged (a-d, same as **Figure 2.1.a-d**) and annealed (e-h) samples are shown. Scale bar is 25 nm. Also shown (i) is an overall summary for the rotationally averaged SAED patterns of the NPs, with reflections from rocksalt CoO (brown, JCPDS 00-048-1719), rocksalt Co_9S_8 (red, JCPDS 00-056-0002), and spinel Co_3S_4 (green, JCPDS 00-047-1738) indicated with Miller indices for prominent lines.

Dashed lines are drawn for key reflections as a guide to the eye.

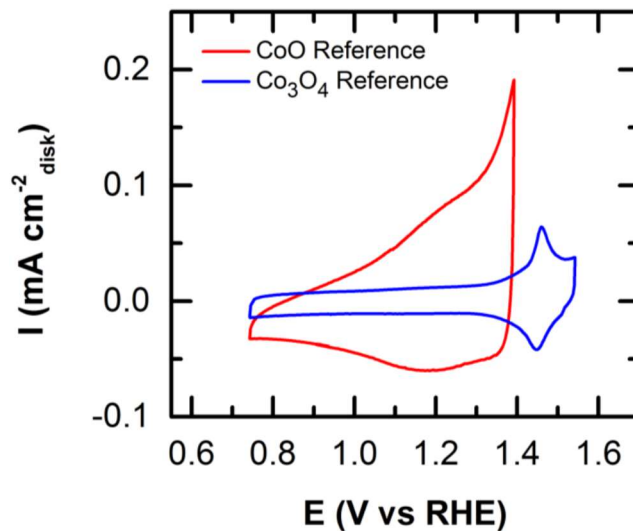


Figure 2.A.2. Cyclic voltammograms of carbon-supported thin-film electrocatalysts containing CoO (red line) and Co₃O₄ (blue line) nanopowders in Ar-saturated 0.1 M KOH at 50 mV/s scan rate.

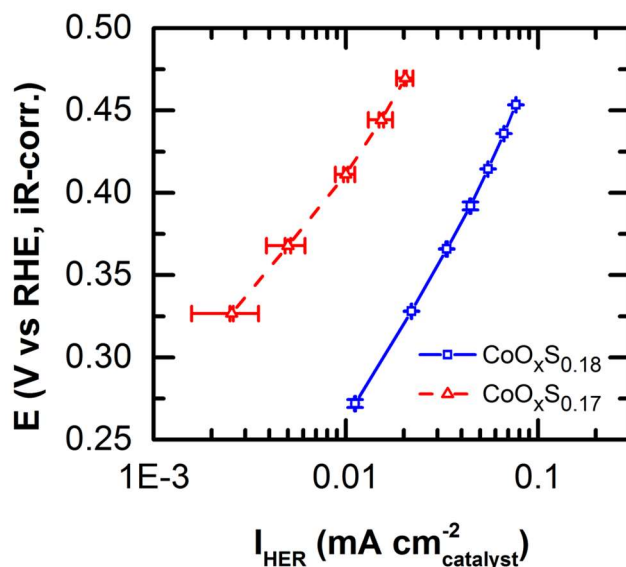


Figure 2.A.3. Tafel plot comparing un-annealed CoO_xS_{0.18} (blue curve) with annealed CoO_xS_{0.17} (red curve) is shown based on the known geometries of the particles. It is seen that the activity of the annealed catalyst at 375 mV vs. RHE is lower than that of the un-annealed one by nearly an order of magnitude. Error bars give the standard deviation from three independent measurements.

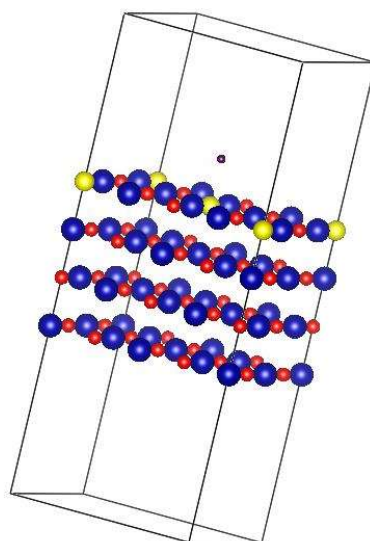


Figure 2.A.4. DFT structural model showing the 2x2 unit cell CoO(100) slab (c-direction). Red: Co atoms; blue: O atoms; yellow: S atoms. Small red atom is an H atom.

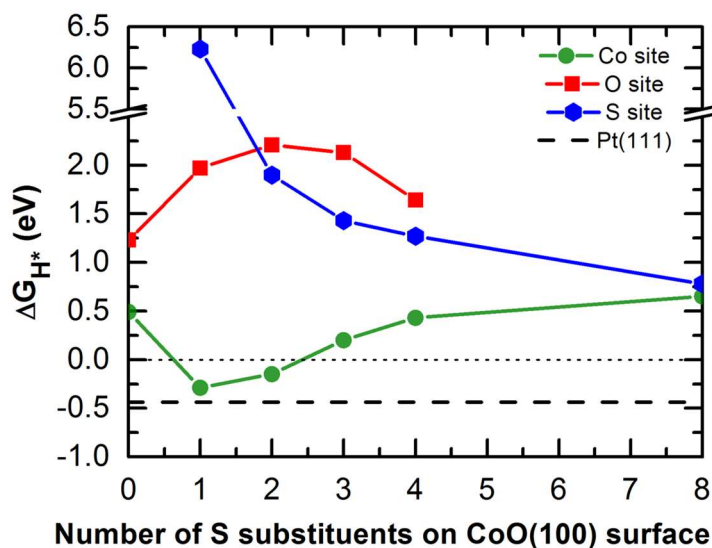


Figure 2.A.5. Results from the DFT calculation of binding energies of H* to various sites on the (modified) CoO(100) surface. Adsorption of H is always favored on Co; only at very high levels of S substitution at the surface does binding to S become comparatively favorable. At only 1 anion site in 8 replaced with S, the adsorption energy approaches that of the highly active Pt(111).

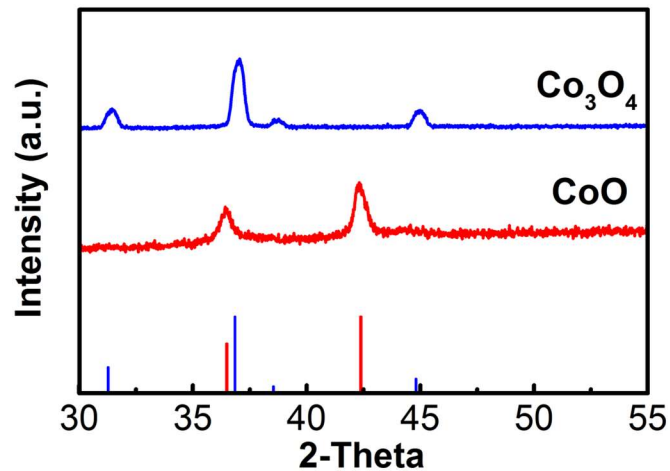


Figure 2.A.6. XRD patterns for Co_3O_4 (JCPDS 00-042-1467, blue line) and CoO (JCPDS 00-048-1719, red line) nanopowder reference samples.

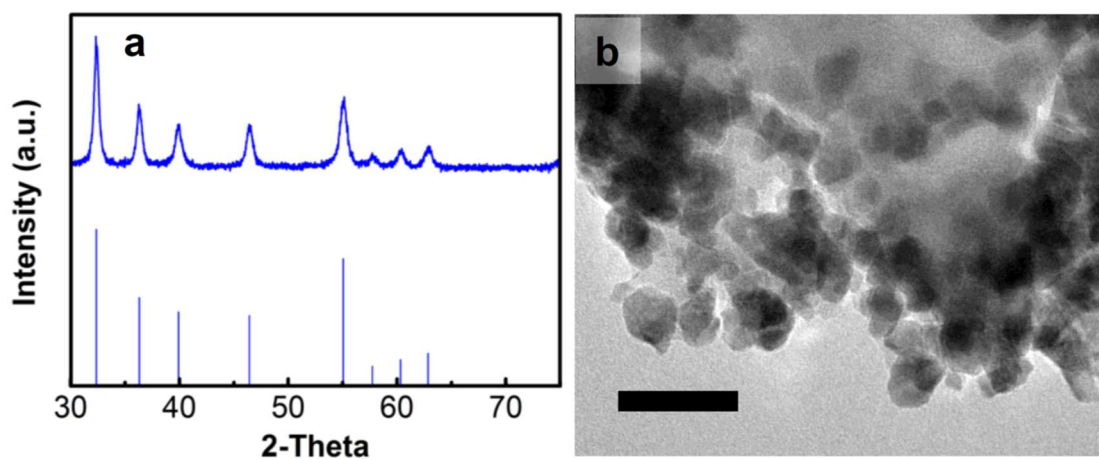


Figure 2.A.7. Structure and morphology of CoS_2 nanoparticles, as characterized by XRD (a) and TEM (b). All peaks can be indexed to the CoS_2 structure (JCPDS 01-070-2865). Scale bar is 50 nm.

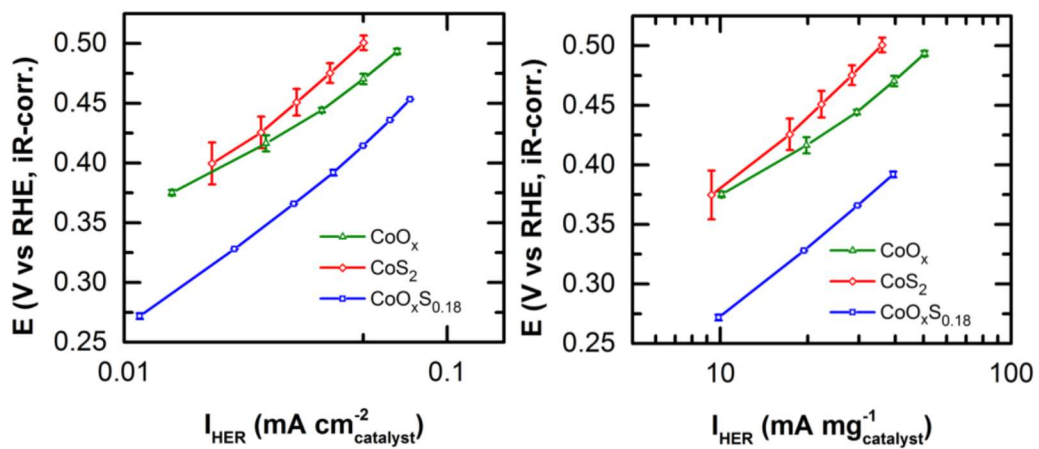


Figure 2.A.8. Tafel plots of the (a) specific activities and (b) mass activities of cobalt oxide (CoO_x), oxysulfide ($\text{CoO}_x\text{S}_{0.18}$) and sulfide (CoS_2). The activity of CoS_2 is $\sim 4x$ lower than that of the Co oxysulfide.

2.B. REFERENCES

1. Greeley, J.; Markovic, N. M., The Road from Animal Electricity to Green Energy: Combining Experiment and Theory in Electrocatalysis *Energy and Environmental Science* **2012**, 5, 9246-9256.
2. Greeley, J.; Stephens, I. E. L.; Bondarenko, A. S.; Johansson, T. P.; Hansen, H. A.; Jaramillo, T. F.; Rossmeisl, J.; Chorkendorff, I.; Nørskov, J. K., Alloys of Platinum and Early Transition Metals as Oxygen Reduction Electrocatalysts. *Nature Chemistry* **2009**, 1, 552-556.
3. Stephens, I. E. L.; Bondarenko, A. S.; Grønbjerg, U.; Rossmeisl, J.; Chorkendorff, I., Understanding the Electrocatalysis of Oxygen Reduction on Platinum and Its Alloys. *Energy and Environmental Science* **2012**, 5, 6744-6762.
4. Sheng, W.; Bivens, A. P.; Myint, M.; Zhuang, Z.; Forest, R. V.; Fang, Q.; Chen, J. G.; Yan, Y., Non-Precious Metal Electrocatalysts with High Activity for Hydrogen Oxidation Reaction in Alkaline Electrolytes. *Energy and Environmental Science* **2014**, 7, 1719-1724.
5. Esposito, D. V.; Hunt, S. T.; Kimmel, Y. C.; Chen, J. G., A New Class of Electrocatalysts for Hydrogen Production from Water Electrolysis: Metal Monolayers Supported on Low-Cost Transition Metal Carbides. *Journal of the American Chemical Society* **2012**, 134, 3025-3033.
6. Han, Z.; Qiu, F.; Eisenberg, R.; Holland, P. L.; Krauss, T. D., Robust Photogeneration of H₂ in Water Using Semiconductor Nanocrystals and a Nickel Catalyst *Science* **2012**, 338, 1321-1324
7. Ma, T. Y.; Ran, J.; Dai, S.; Jaroniec, M.; Qiao, S. Z., Phosphorus-Doped Graphitic Carbon Nitrides Grown In Situ on Carbon-Fiber Paper: Flexible and

Reversible Oxygen Electrodes. *Angewandte Chemie International Edition* **2014**, *54*, 4646–4650.

8. Zhou, W.; Zhou, Y.; Yang, L.; Huang, J.; Ke, Y.; Zhou, K.; Li, L.; Chen, S., N-Doped Carbon-Coated Cobalt Nanorod Arrays Supported on a Titanium Mesh as Highly Active Electrocatalysts for the Hydrogen Evolution Reaction. *Journal of Materials Chemistry A* **2015**, *3*, 1915-1919.

9. Zhou, W.; Zhou, J.; Zhou, Y.; Lu, J.; Zhou, K.; Yang, L.; Tang, Z.; Li, L.; Chen, S., N-Doped Carbon-Wrapped Cobalt Nanoparticles on N-Doped Graphene Nanosheets for High-Efficiency Hydrogen Production. *Chemistry of Materials* **2015**, *27*, 2026–2032.

10. Ma, T. Y.; Dai, S.; Jaroniec, M.; Qiao, S. Z., Metal–Organic Framework Derived Hybrid Co_3O_4 -Carbon Porous Nanowire Arrays as Reversible Oxygen Evolution Electrodes. *Journal of the American Chemical Society* **2014**, *136*, 13925–13931.

11. Hong, W. T.; Risch, M.; Stoerzinger, K. A.; Grimaud, A.; Suntivich, J.; Shao-Horn, Y., Toward the Rational Design of Non-Precious Transition Metal Oxides for Oxygen Electrocatalysis *Energy and Environmental Science* **2015**, *8*, 1404-1427.

12. Cook, T. R.; Dogutan, D. K.; Reece, S. Y.; Surendranath, Y.; Teets, T. S.; Nocera, D. G., Solar Energy Supply and Storage for the Legacy and Nonlegacy Worlds. *Chemical Reviews* **2010**, *110*, 6474-6502.

13. Maiyalagan, T.; Jarvis, K. A.; Therese, S.; Ferreira, P. J.; Manthiram, A., Spinel-Type Lithium Cobalt Oxide as a Bifunctional Electrocatalyst for the Oxygen Evolution and Oxygen Reduction Reactions. *Nature Communications* **2014**, *5*, 1-8.

14. Robinson, D. M.; Go, Y. B.; Mui, M.; Gardner, G.; Zhang, Z.; Mastrogiovanni, D.; Garfunkel, E.; Li, J.; Greenblatt, M.; Dismukes, G. C., Photochemical Water

Oxidation by Crystalline Polymorphs of Manganese Oxides: Structural Requirements for Catalysis. *Journal of the American Chemical Society* **2013**, 135, 3494-3501.

15. Cheng, H.; Su, Y.-Z.; Kuang, P.-Y.; Chen, G.-F.; Liu, Z.-Q., Hierarchical NiCo₂O₄ Nanosheet-Decorated Carbon Nanotubes Towards Highly Efficient Electrocatalyst for Water Oxidation. *Journal of Materials Chemistry A* **2015**, 3, 19314-19321.

16. Falkowski, J. M.; Concannon, N. M.; Yan, B.; Surendranath, Y., Heazlewoodite, Ni₃S₂: A Potent Catalyst for Oxygen Reduction to Water under Benign Conditions. *Journal of the American Chemical Society* **2015**, 137, 7978–7981.

17. Benck, J. D.; Hellstern, T. R.; Kibsgaard, J.; Chakthranont, P.; Jaramillo, T. F., Catalyzing the Hydrogen Evolution Reaction (HER) with Molybdenum Sulfide Nanomaterials. *ACS Catalysis* **2014**, 4, 3957-3971.

18. Liu, X.; Du, J.; Li, C.; Han, X.; Hu, X.; Cheng, F.; Chen, J., The Anion Effect on the Oxygen Reduction of MnX (X = O, S, and Se) Catalysts. *Journal of Materials Chemistry A* **2015**, 3, 3425-3431.

19. Xu, Y.-F.; Gao, M.-R.; Zheng, Y.-R.; Jiang, J.; Yu, S.-H., Nickel/Nickel(II) Oxide Nanoparticles Anchored onto Cobalt(IV) Diselenide Nanobelts for the Electrochemical Production of Hydrogen. *Angewandte Chemie International Edition* **2013**, 52, 8546-8550.

20. Huang, J.; Hou, D.; Zhou, Y.; Zhou, W.; Li, G.; Tang, Z.; Li, L.; Chen, S., MoS₂ Nanosheet-Coated CoS₂ Nanowire Arrays on Carbon Cloth as Three-Dimensional Electrodes for Efficient Electrocatalytic Hydrogen Evolution *Journal of Materials Chemistry A* **2015**, 3, 22886-22891.

21. Zhou, W.; Wu, X.-J.; Cao, X.; Huang, X.; Tan, C.; Tian, J.; Liu, H.; Wang, J.; Zhang, H., Ni₃S₂ Nanorods/Ni Foam Composite Electrode with Low Overpotential for

- Electrocatalytic Oxygen Evolution *Energy and Environmental Science* **2013**, 6, 2921-2924.
22. Tian, J.; Liu, Q.; Asiri, A. M.; Sun, X., Self-Supported Nanoporous Cobalt Phosphide Nanowire Arrays: An Efficient 3D Hydrogen-Evolving Cathode over the Wide Range of pH 0–14. *Journal of the American Chemical Society* **2014**, 136, 7587-7590.
23. Popczun, E. J.; McKone, J. R.; Read, C. G.; Biacchi, A. J.; Wiltrout, A. M.; Lewis, N. S.; Schaak, R. E., Nanostructured Nickel Phosphide as an Electrocatalyst for the Hydrogen Evolution Reaction. *Journal of the American Chemical Society* **2013**, 135, 9267-9270.
24. Feng, L.; Vrubel, H.; Bensimon, M.; Hu, X., Easily-Prepared Dinickel Phosphide (Ni₂P) Nanoparticles as an Efficient and Robust Electrocatalyst for Hydrogen Evolution. *Physical Chemistry Chemical Physics* **2014**, 16, 5917-5921.
25. Suntivich, J.; May, K. J.; Gasteiger, H. A.; Goodenough, J. B.; Shao-Horn, Y., A Perovskite Oxide Optimized for Oxygen Evolution Catalysis from Molecular Orbital Principles. *Science* **2011**, 334, 1383-1385
26. Nørskov, J. K.; Bligaard, T.; A. Logadottir; Kitchin, J. R.; Chen, J. G.; Pandelov, S.; Stimming, U., Trends in the Exchange Current for Hydrogen Evolution. *Journal of the Electrochemical Society* **2005**, 152, J23-J26.
27. Jaramillo, T. F.; Jorgensen, K. P.; Bonde, J.; Nielsen, J. H.; Horch, S.; Chorkendorff, I., Identification of Active Edge Sites for Electrochemical H₂ Evolution from MoS₂ Nanocatalysts. *Science* **2007**, 317, 100-102.
28. Bonde, J.; Moses, P. G.; Jaramillo, T. F.; Nørskov, J. K.; Chorkendorff, I., Hydrogen Evolution on Nano-Particulate Transition Metal Sulfides. *Faraday Discussions* **2009**, 140, 219-231.

29. Grimaud, A.; May, K. J.; Carlton, C. E.; Lee, Y.-L.; Risch, M.; Hong, W. T.; Zhou, J.; Shao-Horn, Y., Double Perovskites as a Family of Highly Active Catalysts for Oxygen Evolution in Alkaline Solution. *Nature Communications* **2013**, *4*.
30. Calle-Vallejo, F.; Inoglu, N. G.; Su, H.-Y.; Martínez, J. I.; Man, I. C.; Koper, M. T. M.; Kitchin, J. R.; Rossmeisl, J., Number of Outer Electrons as Descriptor for Adsorption Processes on Transition Metals and Their Oxides. *Chemical Science* **2013**, *4*, 1245-1249.
31. Trotochaud, L.; Ranney, J. K.; Williams, K. N.; Boettcher, S. W., Solution-Cast Metal Oxide Thin Film Electrocatalysts for Oxygen Evolution. *Journal of the American Chemical Society* **2012**, *134*, 17253–17261.
32. Zhu, H.; Zhang, S.; Huang, Y.-X.; Wu, L.; Sun, S., Monodisperse $M_xFe_{3-x}O_4$ (M = Fe, Cu, Co, Mn) Nanoparticles and Their Electrocatalysis for Oxygen Reduction Reaction. *Nano Letters* **2013**, *13*, 2947-2951.
33. Schmidt, E., Electrochemical Properties of New Amorphous Molybdenum Oxysulfide Thin Films. *Solid State Ionics* **1995**, *76*, 243-247.
34. Ueda, K.; Hiramatsu, H.; Hirano, M.; Kamiya, T.; Hosono, H., Wide-gap Layered Oxychalcogenide Semiconductors: Materials, Electronic Structures and Optoelectronic Properties. *Thin Solid Films* **2006**, *496*, 8-15.
35. Asahi, R.; Morikawa, T.; Ohwaki, T.; Aoki, K.; Taga, Y., Visible-Light Photocatalysis in Nitrogen-Doped Titanium Oxides. *Science* **2001**, *293*, 269-271.
36. Zhou, W. J.; Leng, Y. H.; Hou, D. M.; Li, H. D.; Li, L. G.; Li, G. Q.; Liu, H.; Chen, S. W., Phase Transformation and Enhanced Photocatalytic Activity of S-Doped Ag_2O/TiO_2 Heterostructured Nanobelts. *Nanoscale* **2014**, *6*, 4698-4704.
37. Gong, Q.; Cheng, L.; Liu, C.; Zhang, M.; Feng, Q.; Ye, H.; Zeng, M.; Xie, L.; Liu, Z.; Li, Y., Ultrathin $MoS_{2(1-x)}Se_{2x}$ Alloy Nanoflakes For Electrocatalytic Hydrogen Evolution Reaction. *ACS Catalysis* **2015**, *5*, 2213–2219.

38. Xu, Z.; Wang, H.; Li, Z.; Kohandehghan, A.; Ding, J.; Chen, J.; Cui, K.; Mitlin, D., Sulfur Refines MoO₂ Distribution Enabling Improved Lithium Ion Battery Performance. *The Journal of Physical Chemistry C* **2014**, 118, 18387-18396.
39. Chen, Z.; Cummins, D.; Reinecke, B. N.; Clark, E.; Sunkara, M. K.; Jaramillo, T. F., Core-Shell MoO₃-MoS₂ Nanowires for Hydrogen Evolution: A Functional Design for Electrocatalytic Materials. *Nano Letters* **2011**, 11, 4168-4175.
40. Kibsgaard, J.; Jaramillo, T. F., Molybdenum Phosphosulfide: An Active, Acid-Stable, Earth-Abundant Catalyst for the Hydrogen Evolution Reaction. *Angewandte Chemie International Edition* **2014**, 53, 14433-14437.
41. Miguel Cabán-Acevedo, M. L. S., J. R. Schmidt, Joseph G. Thomas, Qi Ding, Hung-Chih Chang, Meng-Lin Tsai, Jr-Hau He, Song Jin, Efficient Hydrogen Evolution Catalysis Using Ternary Pyrite-Type Cobalt Phosphosulphide. *Nature Materials* **2015**.
42. Zhuo, J.; Miguel Caban-Acevedo; Liang, H.; Samad, L.; Ding, Q.; Fu, Y.; Li, M.; Jin, a. S., High-Performance Electrocatalysis for Hydrogen Evolution Reaction Using Se-Doped Pyrite-Phase Nickel Diphosphide Nanostructures. *ACS Catalysis* **2015**, 5, 6355-6361.
43. Sun, Y.; Liu, C.; Grauer, D. C.; Yano, J.; Long, J. R.; Yang, P.; Chang, C. J., Electrodeposited Cobalt-Sulfide Catalyst for Electrochemical and Photoelectrochemical Hydrogen Generation from Water. *Journal of the American Chemical Society* **2013**, 135, 17699-17702.
44. Sines, I. T.; Vaughn, D. D.; Biacchi, A. J.; Kingsley, C. E.; Popczun, E. J.; Schaak, R. E., Engineering Porosity into Single-Crystal Colloidal Nanosheets Using Epitaxial Nucleation and Chalcogenide Anion Exchange Reactions: The Conversion of SnSe to SnTe. *Chemistry of Materials* **2012**, 24, 3088-3093.

45. Xu, Y.; Wu, R.; Zhang, J.; Shia, Y.; Zhang, B., Anion-Exchange Synthesis of Nanoporous FeP Nanosheets as Electrocatalysts for Hydrogen Evolution Reaction. *Chemical Communications* **2013**, 49, 6656-6658.
46. Kong, D.; Cha, J. J.; Wang, H.; Lee, H. R.; Cui, Y., First-Row Transition Metal Dichalcogenide Catalysts for Hydrogen Evolution Reaction *Energy and Environmental Science* **2013**, 6, 3553-3558.
47. Callejas, J. F.; Read, C. G.; Popczun, E. J.; McEnaney, J. M.; Schaak, R. E., Nanostructured Co₂P Electrocatalyst for the Hydrogen Evolution Reaction and Direct Comparison with Morphologically Equivalent CoP. *Chemistry of Materials* **2015**, 27, 3769-3774.
48. Faber, M. S.; Lukowski, M. A.; Ding, Q.; Kaiser, N. S.; Jin, S., Earth-Abundant Metal Pyrites (FeS₂, CoS₂, NiS₂, and Their Alloys) for Highly Efficient Hydrogen Evolution and Polysulfide Reduction Electrocatalysis. *The Journal of Physical Chemistry C* **2014**, 118, 21347-21356.
49. Zhang, H.; Li, Y.; Zhang, G.; Xu, T.; Wan, P.; Sun, X., A Metallic CoS₂ Nanopyramid Array Grown on 3D Carbon Fiber Paper as an Excellent Electrocatalyst for Hydrogen Evolution. *Journal of Materials Chemistry A* **2015**, 3, 6306-6310.
50. Feng, L.-L.; Li, G.-D.; Liu, Y.; Wu, Y.; Chen, H.; Wang, Y.; Zou, Y.-C.; Wang, D.; Zou, X., Carbon-Armored Co₉S₈ Nanoparticles as All-pH Efficient and Durable H₂-Evolving Electrocatalysts. *ACS Applied Materials & Interfaces* **2015**, 7, 980-988.
51. Kong, D.; Wang, H.; Lu, Z.; Cui, Y., CoSe₂ Nanoparticles Grown on Carbon Fiber Paper: An Efficient and Stable Electrocatalyst for Hydrogen Evolution Reaction. *Journal of the American Chemical Society* **2014**, 136, 4897-4900.
52. Yin, Y.; Alivisatos, A. P., Colloidal Nanocrystal Synthesis and the Organic-Inorganic Interface. *Nature* **2004**, 437, 664-670.

53. Puentes, V. F.; Krishnan, K. M.; Alivisatos, A. P., Colloidal Nanocrystal Shape and Size Control: The Case of Cobalt. *Science* **2001**, 291, 2115-2117.
54. Peng, Z.; Yang, H., Designer Platinum Nanoparticles: Control of Shape, Composition in Alloy, Nanostructure and Electrocatalytic Property. *Nano Today* **2009**, 4, 143-164.
55. Milliron, D. J.; Hughes, S. M.; Cui, Y.; Manna, L.; Li, J.; Wang, L.-W.; Alivisatos, A. P., Colloidal Nanocrystal Heterostructures with Linear and Branched Topology. *Nature* **2004**, 430, 190-195.
56. Zhang, S.; Zhang, X.; Jiang, G.; Zhu, H.; Guo, S.; Su, D.; Lu, G.; Sun, S., Tuning Nanoparticle Structure and Surface Strain for Catalysis Optimization. *Journal of the American Chemical Society* **2014**, 136, 7734-7739.
57. Cargnello, M.; Chen, C.; Diroll, B. T.; Doan-Nguyen, V. V. T.; Gorte, R. J.; Murray, C. B., Efficient Removal of Organic Ligands from Supported Nanocrystals by Fast Thermal Annealing Enables Catalytic Studies on Well-Defined Active Phases. *Journal of the American Chemical Society* **2015**, 137, 6906-6911.
58. Fayette, M.; Robinson, R. D., Chemical Transformations of Nanomaterials for Energy Applications. *Journal of Materials Chemistry A* **2014**, 2, 5965-5978.
59. Niu, Z.; Li, Y., Removal and Utilization of Capping Agents in Nanocatalysis. *Chemistry of Materials* **2014**, 26, 72-83.
60. Li, D.; Wang, C.; Tripkovic, D.; Sun, S.; Markovic, N. M.; Stamenkovic, V. R., Surfactant Removal for Colloidal Nanoparticles from Solution Synthesis: The Effect on Catalytic Performance. *ACS Catalysis* **2012**, 2, 1358-1362.
61. Rosen, E. L.; Buonsanti, R.; Llordes, A.; Sawvel, A. M.; Milliron, D. J.; Helms, B. A., Exceptionally Mild Reactive Stripping of Native Ligands from Nanocrystal Surfaces by Using Meerwein's Salt. *Angewandte Chemie International Edition* **2012**, 51, 684-689.

62. You, H.; Wang, W.; Yang, S., A Universal Rule for Organic Ligand Exchange. *ACS Applied Materials and Interfaces* **2014**, *6*, 19035–19040.
63. Wu, J.; Zhang, J.; Peng, Z.; Yang, S.; Wagner, F. T.; Yang, H., Truncated Octahedral Pt₃Ni Oxygen Reduction Reaction Electrocatalysts. *Journal of the American Chemical Society* **2010**, *132*, 4984-4985.
64. Zhang, H.; Hu, B.; Sun, L.; Hovden, R.; Wise, F. W.; Muller, D. A.; Robinson, R. D., Surfactant Ligand Removal and Rational Fabrication of Inorganically Connected Quantum Dots. *Nano Letters* **2011**, *11*, 5356-5361.
65. Weber, D.; Sharma, R.; Botnaras, S.; Pham, D. V.; Steiger, J.; Cola, L. D., Base-Etch Removal of a Ligand Shell in Thin Films of ZnO Nanoparticles for Electronic Applications. *Journal of Materials Chemistry C* **2013**, *1*, 7111-7116.
66. Zhang, H.; Solomon, L. V.; Ha, D.-H.; Honrao, S.; Hennig, R. G.; Robinson, R. D., (NH₄)₂S, a Highly Reactive Molecular Precursor for Low Temperature Anion Exchange Reactions in Nanoparticles. *Dalton Transactions* **2013**, *42*, 12596-12599.
67. Yin, Y.; Rioux, R. M.; Erdonmez, C. K.; Hughes, S.; Somorjai, G. A.; Alivisatos, A. P., Formation of Hollow Nanocrystals through the Nanoscale Kirkendall Effect. *Science* **2004**, *304*, 711-714.
68. Park, J.; Zheng, H.; Jun, Y.-w.; Alivisatos, A. P., Hetero-Epitaxial Anion Exchange Yields Single-Crystalline Hollow Nanoparticles. *Journal of the American Chemical Society* **2009**, *131*, 13943–13945.
69. Cabot, A.; Puentes, V. F.; Shevchenko, E.; Yin, Y.; Balcells, L.; Marcus, M. A.; Hughes, S. M.; Alivisatos, A. P., Vacancy Coalescence during Oxidation of Iron Nanoparticles. *2007* **2007**, *129*, 10358–10360.
70. Shannon, R. D., Revised Effective Ionic Radii and Systematic Studies of Interatomic Distances in Halides and Chalcogenides. *Acta Crystallographica* **1976**, *A32*, 751-767.

71. Suntivich, J.; Gasteiger, H. A.; Yabuuchi, N.; Shao-Horn, Y., Electrocatalytic Measurement Methodology of Oxide Catalysts Using a Thin-Film Rotating Disk Electrode. *Journal of the Electrochemical Society* **2010**, 157, 81263-81268.
72. Casella, I. G., Electrodeposition of Cobalt Oxide Films from Carbonate Solutions Containing Co(II)-Tartrate Complexes. *Journal of Electroanalytical Chemistry* **2002**, 520, 119-125.
73. Casella, I. G.; Guascito, M. R., Electrochemical Preparation of a Composite Gold-Cobalt Electrode and Its Electrocatalytic Activity in Alkaline Medium. *Electrochimica Acta* **1999**, 45, 1113-1120.
74. Wang, Q.; Jiao, L.; Du, H.; Si, Y.; Wang, Y.; Yuan, H., Co₃S₄ Hollow Nanospheres Grown on Graphene as Advanced Electrode Materials for Supercapacitors. *Journal of Materials Chemistry* **2012**, 22, 21387.
75. Tao, F.; Zhao, Y.-Q.; Zhang, G.-Q.; Li, H.-L., Electrochemical Characterization on Cobalt Sulfide for Electrochemical Supercapacitors. *Electrochemistry Communications* **2007**, 9, 1282-1287.
76. Bockris, J. O. M.; Ammar, I. A.; Hug, A. K. M. S., The Mechanism of the Hydrogen Evolution Reaction on Platinum, Silver and Tungsten surfaces in Acid Solutions *Journal of Physical Chemistry* **1957**, 61, 879-886.
77. Conway, B. E.; Titak, B. V., Interfacial Processes Involving Electrocatalytic Evolution and Oxidation of H₂, and the Role of Chemisorbed H *Electrochimica Acta* **2002**, 47, 3571-3594.
78. Parsons, R., The Rate of Electrolytic Hydrogen Evolution and the Heat of Adsorption of Hydrogen *Transactions of the Faraday Society* **1958**, 54, 1053-1063.
79. Gerischer, H., Über den Zusammenhang zwischen dem Mechanismus der elektrolytischen Wasserstoffabscheidung und der Adsorptionsenergie des atomaren

Wasserstoffs an verschiedenen Metallen. *Zeitschrift für Physikalische Chemie, Neue Folge* **1956**, 8, 137-153.

80. Greeley, J.; Nørskov, J.; Kibler, L. A.; El-Aziz, A. M.; Kolb, D. M., Hydrogen Evolution Over Bimetallic Systems: Understanding the Trends. *ChemPhysChem* **2006**, 7, 1032-1035.

81. Sheng, W.; Myint, M.; Chen, J. G.; Yan, Y., Correlating the Hydrogen Evolution Reaction Activity in Alkaline Electrolytes with the Hydrogen Binding Energy on Monometallic Surfaces. *Energy and Environmental Science* **2013**, 6, 1509-1512.

82. Greeley, J.; Jaramillo, T. F.; Bonde, J.; Chorkendorff, I.; Nørskov, J. K., Computational High-throughput Screening of Electrocatalytic Materials for Hydrogen Evolution. *Nature Materials* **2006**, 5, 909-913.

83. Mitchell, D. R. G., Circular Hough Transform Diffraction Analysis: A Software Tool for Automated Measurement of Selected Area Electron Diffraction Patterns within Digital Micrograph™. *Ultramicroscopy* **2008**, 108, 367-374.

84. Luo, Z.; Vasquez, Y.; Bondi, J. F.; Schaak, R. E., Pawley and Rietveld Refinements Using Electron Diffraction From L1₂-Type Intermetallic Au₃Fe_{1-x} Nanocrystals During Their in-situ Order–Disorder Transition. *Ultramicroscopy* **2011**, 111, 1295-1304.

85. Williams, D. B.; Carter, C. B., *Transmission Electron Microscopy: A Textbook for Materials Science*. Springer-Verlag: 2009.

86. Goodenough, J. B., Direct Cation-Cation Interactions in Several Oxides. *Physical Review* **1960**, 117, 1442-1451.

87. Dinega, D. P.; Bawendi, M. G., A Solution-Phase Chemical Approach to a New Crystal Structure of Cobalt. *Angewandte Chemie International Edition* **1999**, 38, 1788-1791.

88. Haynes, W. M.; Bruno, T. J.; Lide, D. R., *CRC Handbook of Chemistry and Physics, 96th edition*. CRC Press: Boca Raton, FL, 2015.
89. Kresse, G.; Furthmüller, J., Efficient Iterative Schemes for ab initio Total-Energy Calculations Using a Plane-Wave Basis Set. *Physical Review B* **1996**, *54*, 11169.
90. Kresse, G.; Furthmüller, J., Efficiency of ab-initio Total Energy Calculations for Metals and Semiconductors Using a Plane-Wave Basis Set. *Computational Materials Science* **1996**, *6*, 15-50.
91. Kresse, G.; Hafner, J., Ab initio Molecular-Dynamics Simulation of the Liquid-Metal–Amorphous-Semiconductor Transition in Germanium. *Physical Review B* **1994**, *49*, 14251.
92. Kresse, G.; Hafner, J., Ab initio Molecular Dynamics for Liquid Metals. *Physical Review B* **1993**, *47*, 558.
93. Perdew, J. P.; Burke, K.; Ernzerhof, M., Generalized Gradient Approximation Made Simple. *Physical Review Letters* **1996**, *77*, 3865.
94. Blöchl, P. E., Projector Augmented-Wave Method. *Physical Review B* **1994**, *50*, 17953.
95. Kresse, G.; Joubert, D., From Ultrasoft Pseudopotentials to the Projector Augmented-Wave Method. *Physical Review B* **1999**, *59*, 1758.
96. Monkhorst, H. J.; Pack, J. D., Special Points for Brillouin-Zone Integrations. *Physical Review B* **1976**, *13*, 5188.
97. Jain, A.; Ong, S. P.; Hautier, G.; Chen, W.; Richards, W. D.; Dacek, S.; Cholia, S.; Gunter, D.; Skinner, D.; Ceder, G.; Persson, K. A., Commentary: The Materials Project: A Materials Genome Approach to Accelerating Materials Innovation. *APL Materials* **2013**, *1*, 011002.

98. Jain, A.; Hautier, G.; Ong, S. P.; Moore, C. J.; Fischer, C. C.; Persson, K. A.; Ceder, G., Formation Enthalpies by Mixing GGA and GGA + U Calculations.

Physical Review B **2011**, 84, 045115.

99. Kumar, N.; Raman, N.; Sundaresan, A., Synthesis and Properties of Cobalt Sulfide Phases: CoS_2 and Co_9S_8 . *Zeitschrift für anorganische und allgemeine Chemie*

2014, 640, 1069-1074.

CHAPTER 3

3 SELECTIVE ETCHING OF COPPER SULFIDE NANOPARTICLES AND HETEROSTRUCTURES THROUGH SULFUR ABSTRACTION: PHASE TRANSFORMATIONS AND OPTICAL PROPERTIES *

3.1. ABSTRACT

Integrating top-down methods, such as chemical etching, for the precise removal of excess material in nanostructures with the bottom-up size and shape control of colloidal nanoparticle synthesis could greatly expand the range of accessible nanoparticle morphologies. We present mechanistic insights into an unusual reaction in which trialkylphosphines (“phosphines”), which are commonly used to protect nanoparticle surfaces as a surfactant ligand, chemically etch copper sulfide, Cu_{2-x}S , nanostructures in the presence of oxygen. Furthermore, Cu_{2-x}S is removed highly selectively from zinc sulfide– Cu_{2-x}S heterostructures. Structural and optical characterizations show that the addition of phosphine destabilizes the highly Cu-deficient roxbyite phase and injects Cu into the interiors of the nanoparticles, even at room temperature. Analysis of the etching products confirms that chalcogens are removed in the form of phosphine chalcogenides and shows that the removed copper is solubilized as Cu^{2+} . The morphology of etched Cu_{2-x}S particles changes dramatically as the concentration of phosphine is reduced, producing anisotropically etched particles indicative of facet-selective surface chemical reactions. Additionally, ceric ammonium nitrate, another oxidizing agent, can be used to control the etching

* Reprinted with permission from: Nelson, A.; Ha, D.-H.; Robinson, R. D., Selective Etching of Copper Sulfide Nanoparticles and Heterostructures through Sulfur Abstraction: Phase Transformations and Optical Properties. *Chemistry of Materials* **2016**, 28 (23), 8530–8541. Copyright 2016 American Chemical Society.

reaction; the use of this redox agent affords strictly isotropically etched particles. These results demonstrate the highly pliable structural and chemical properties of nanocrystalline Cu_{2-x}S and raise the possibility of using surface-active ligands formerly thought to be passivating to dramatically reshape as-synthesized colloidal nanostructures into more functional forms.

3.2. INTRODUCTION

Proper understanding of chemical processes occurring at the solid–solution interface is critical in describing the properties of colloidal nanostructures due to their intrinsically high ratio of surface area to volume. For colloidal nanoparticles (NPs) in organic liquids, the need for this understanding has driven extensive research into the interactions between capping ligands (surfactants) and the underlying NP surface.¹⁻⁸ Ligands are critical for stabilizing the particle in solution and play a decisive role in determining the modes of growth of NPs during synthesis by controlling the size and shape of NPs.¹ Other roles for ligands in determining the properties of colloidal NPs include passivation of surface defects,^{3,9} control of NP stoichiometry and phase,^{2, 10, 11} or sources for precursor atoms.^{12, 13} Postsynthetic modification of NPs by alteration or replacement of the ligand shell is of enormous importance for the future application of NPs in devices, as it is necessary for cation exchange and heterostructure formation,^{14, 15} transfer of NPs between phases,^{5, 16} control of transport properties,^{17, 18} and even total reshaping of the as-synthesized particles.^{19, 20}

Trialkylphosphines (hereafter simply “phosphines”) and their derivatives, such as phosphine oxides and phosphine chalcogenides, have proven to be a vital family of chemicals in colloidal NP synthesis and modification due to their versatility. Phosphines and phosphine oxides work as common surfactant ligands to passivate the

surface of NPs for stabilization and for size and shape control.^{8, 21} In combination with chalcogens, they are utilized as chalcogenide precursors.^{22, 23} In addition, phosphines may be utilized as a phosphorus source at high temperature to dope NPs with phosphorus or to synthesize metal phosphide NPs.^{12, 13} Phosphines have been identified as the crucial agents in directing many cation-exchange processes in semiconductor NPs,^{14, 24} owing to their ability to make such reactions thermodynamically favorable via their affinities for different cations.²⁵ Previous work has also shown that phosphines may react aggressively with NPs, abstracting components of the NP lattice to the point that the NP stoichiometry may be drastically changed; for instance, metal chalcogenide NPs having a chalcogen-rich phase can be converted to comparatively chalcogen-poor NPs via treatment with phosphine, utilizing the affinity of phosphines for chalcogens.¹⁰ A similar reaction occurs in the case of microcrystalline Cu_{2-x}S .²⁶ In both cases, chemical transformation modified the chalcogenide stoichiometry while largely preserving morphology.

Chemical etching is a critical step in conventional top-down device fabrications to design complicated device architectures. An archetypal example is the wet etching of silicon with an aqueous base, which shows pronounced anisotropy in etch rate depending on the orientation of silicon.²⁷ Chemically selective etching methods are also instrumental in semiconductor microfabrication techniques.²⁸ Selectivity of wet etching of different materials and specific crystal directions enables the tailoring of nanostructure shapes during microfabrication.²⁷⁻³¹ Etching methods may also be used to tune the surface chemistry of the etched materials, which is crucial in the case of NPs; for example, nearly perfect silicon surfaces may be produced by wet etching,^{27, 32} and the optical properties of semiconductor NPs may be greatly improved by etching.^{9, 33, 34} Syntheses of single-phase materials with promising properties in which etching plays a role are widely reported;^{19, 35-37} however, phase- or

component-selective etching in NPs is not yet a common technique. Understanding the chemical behaviors underlying this unusual etching behavior is particularly important considering the material in question. Cu_{2-x}S is an emerging p-type semiconducting material since it exhibits stoichiometry-dependent properties, is less toxic than traditional semiconducting NPs such as cadmium and lead chalcogenides, and can be used to create visible-wavelength optically active materials, such as copper indium sulfide³⁸ or various quaternary copper–metal sulfides.³⁹⁻⁴¹ It is also a promising plasmonic material.⁴²⁻⁴⁵ Cu_{2-x}S exhibits a rich solid-state chemistry at the nanoscale owing to its high cationic mobility, making it an attractive platform both as a model system for nanoscale chemistry and as a building block for highly complex nanostructures.^{14, 46-50} The ability to reshape Cu_{2-x}S is therefore a benefit to a wide range of future projects. The uncontrolled etching of Cu_{2-x}S NPs has been observed in passing by Regulacio et al.⁵¹ Given the ill-formed morphologies of the resulting particles, prior workers might have disregarded similar results as undeserving of further exploration; however, we found that when colloidal Cu_{2-x}S heterostructures with ZnS ¹⁴ were exposed to phosphine in air, Cu_{2-x}S appeared to have been selectively dissolved from the nanoparticles (**Figure 3.A.1**). We were intrigued in particular by the selectivity of the etching reaction, which is a highly advantageous feature of many chemical etching processes used today.

3.3. RESULTS AND DISCUSSION

In this work, we report a novel method to selectively etch copper sulfide NPs with phosphine creating unique morphologies. As shown in **Figure 3.1**, Cu_{2-x}S can be etched isotropically to form smaller spherical particles or it may be removed from complex heterostructures with nearly perfect selectivity. Following exposure to air for

a few hours in a reaction solvent mixture that includes tributylphosphine (TBP) or trioctylphosphine (TOP), the single crystal and heterostructured Cu_{2-x}S NPs are selectively etched (shown schematically in **Figure 3.1**). This drastic behavior is surprising since, although the ability of phosphines to change the chemistry of NPs is now well-known, it is generally accepted that phosphines still serve as surface-protecting ligands that prevent NP aggregation rather than as aggressive etchants. We confirm that a component of this etching process is the removal of sulfur from the particle, which may itself be used to tune the charge carrier density of the NPs, as verified by changes in the localized surface plasmon resonance monitored via UV-vis-NIR spectroscopy. This abstraction process can induce phase changes at room temperature and cooperates with the oxidation of the particle surface in air both to regenerate oxidized S species and to remove Cu ions. Reducing the concentration of phosphine etchant, rather than just slowing down the reaction, instead produces anisotropically etched NPs having an unusual concave morphology. Finally, we show that the etching reaction can also be initiated with a redox agent, $(\text{NH}_4)_2\text{Ce}(\text{NO}_3)_6$, which demonstrates that dissolution of the particle may only require oxidation of the anion sublattice.

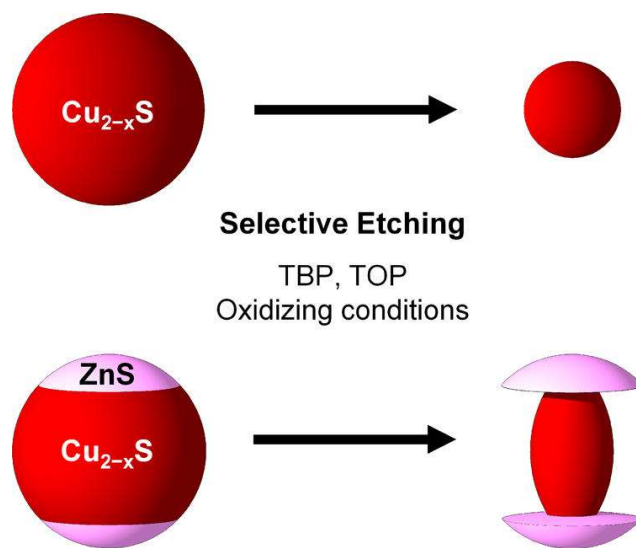


Figure 3.1. Schematic of the etching process. Cu_{2-x}S nanoparticles (top) and Cu_{2-x}S – ZnS heterostructures (bottom) are etched in the presence of trialkylphosphines following exposure to air.

3.3.1. Morphological and structural characterization

Upon the introduction of excess (P/S ratio > 250:1) tributylphosphine (TBP) to solutions of spherical Cu_{2-x}S NPs in toluene in the presence of air, the NPs are isotropically etched (gradually dissolved) over the course of several hours (if the reaction vessel is left open continuously to air) to days (if the vessel is closed between aliquots) (**Figure 3.2a–c**). The spherical Cu_{2-x}S NPs begin as single-crystal NPs (hereafter SC-NPs), as verified by HRTEM (**Figure 3.A.2**), with average diameter $d = 22$ nm, and have the roxbyite phase $\text{Cu}_{1.81}\text{S}$ (to be discussed). After 17 h, d decreases to 17.4 nm (a reduction in volume of $\sim 50\%$); after 48 h, d is 12.3 nm (overall volume loss of $\sim 83\%$). Formation of anisotropic structures such as disks or rods is not observed. After an initial rapid decrease in d immediately after adding TBP (see below), the etching rate is found to vary substantially, from 5 to 140 nm^3/h , and we find no obvious correlation between the etching rate and d . This variability likely results from uncontrolled changes in parameters such as atmospheric humidity, the

rate of uptake of oxygen by the solution, and the workup time needed to isolate NPs. When treating SC-NPs with TBP in the absence of air, the diameter is only slightly reduced, decreasing from 22 to ~20 nm (by TEM), which is apparent after only 5 min. The reaction then stops, and no significant change in SC-NP size occurs over the course of a 3-day reaction.

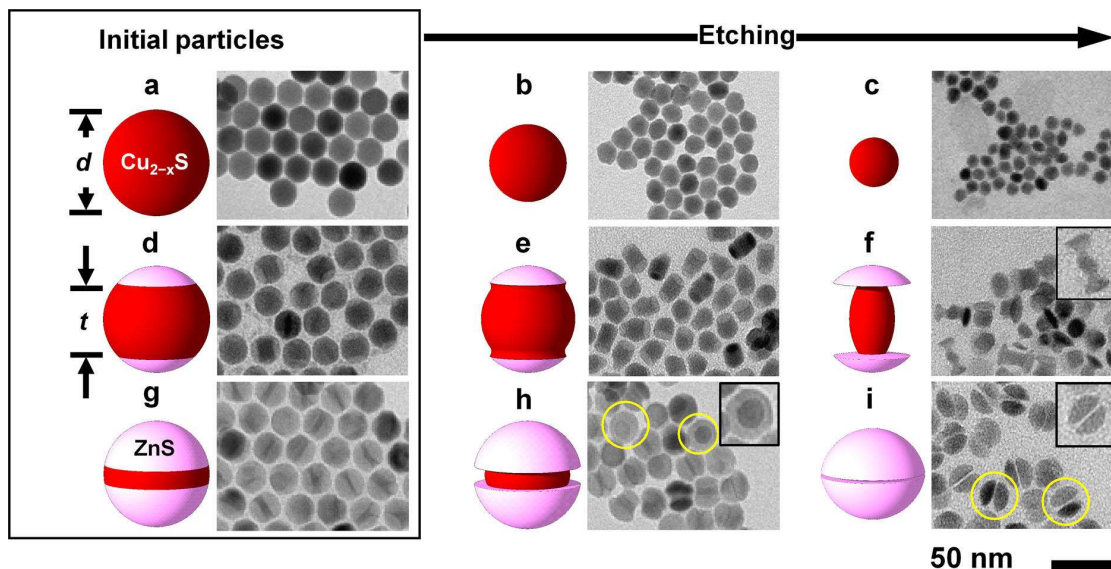


Figure 3.2. Schematic and TEM images of the etching of Cu_{2-x}S pure nanocrystals (SC-NPs; a–c) and Cu_{2-x}S –ZnS heterostructures (H-NPs; d–i) by trialkylphosphines. SC-NPs are slowly reduced in diameter, d , from $d \sim 22$ nm (a) to $d \sim 17$ nm over 17 h (b) and to $d \sim 12$ nm over 48 h (c). For H-NPs, Cu_{2-x}S is removed with nearly perfect selectivity: with an initial Cu_{2-x}S thickness $t = 15$ nm (d), the heterostructure takes on the appearance of a thick nanorod with ZnS tips after 15 min (e); eventually, the Cu_{2-x}S layer is reduced to a thin rod (f); a fraction of the particles have slightly enlarged centers (inset). For an initial $t = 4$ nm (g), etching of the Cu_{2-x}S layer is apparent after 2 min (h). A fraction of the particles (circled in yellow) have a c-axis parallel to the electron beam, showing that the etching is radially isotropic (h, inset). After 1 h, Cu_{2-x}S is completely removed (i), leaving apparently connected ZnS caps (i, inset); a few pairs of particles (circled) show different levels of contrast, indicating that they display different angles to the electron beam due to postsynthetic rotation of the initially epitaxial grains.

Etching of ZnS– Cu_{2-x}S heterostructure NPs (H-NPs) results in selective removal of the copper sulfide material (**Figure 3.2d–i**). As detailed in our previous

work,¹⁴ these ZnS–Cu_{2-x}S H-NPs synthesized through cation exchange consist of a central Cu_{2-x}S layer that is capped on both sides by ZnS. The ZnS grows epitaxially parallel to the a-axis⁵² of Cu_{2-x}S (c-axis of ZnS) to form caps on both sides of the particle (see **Figure 3.1**), reducing the thickness, *t*, of the Cu_{2-x}S layer.¹⁴ Etching reactions of H-NPs are shown in **Figure 3.2d–i**. The difference in the morphology of these initial H-NPs is the *t* of the Cu_{2-x}S: in one H-NP, the majority material is of Cu_{2-x}S (*t* = 15 nm) with small ZnS caps (**Figure 3.2d**), and the other H-NP consists mostly of ZnS caps with a thin Cu_{2-x}S layer (*t* = 4 nm) (**Figure 3.2g**). Etching the majority Cu_{2-x}S H-NPs (initial *t* = 15 nm, **Figure 3.2e,f**) leads to gradual etching of the surface of the Cu_{2-x}S layer; after 15 min, the H-NP takes on the appearance of a thick nanorod having ZnS tips (**Figure 3.2e**). The diameter of the Cu_{2-x}S region at this point is about 14 nm; this represents an estimated volume loss of Cu_{2-x}S of 60%. After 1 h, the Cu_{2-x}S grain is etched into a thin pillar linking the two ZnS grain caps (**Figure 3.2f**). Several of the copper sulfide pillars have a thicker midsection which, from TEM measurements, is approximately twice the thickness of the Cu_{2-x}S regions near the ZnS caps (inset). The apparent preferential etching of Cu_{2-x}S close to the epitaxial boundary suggests that strain, as we showed in our previous work, or Cu_{2-x}S stoichiometric changes induced by strain¹⁴ could play a role in the rate at which Cu_{2-x}S is dissolved. However, a different particle geometry may be needed to definitively establish this, as the initial H-NPs have a truncated-sphere midsection, which is, by definition, thinner near the ZnS caps.

Etching the majority ZnS H-NPs (initial *t* = 4 nm, with ~9 nm thick ZnS caps, **Figure 3.2g**) also results in selective etching of the Cu_{2-x}S layers (**Figure 3.2h,i**). Two minutes after adding TBP to the NP solution, the Cu_{2-x}S layer is etched at the NP surface, creating a Cu_{2-x}S layer with a smaller diameter than that of the starting Cu_{2-x}S disk (**Figure 3.2h**). After 2 min, the diameter of the etched Cu_{2-x}S layer is ~15 nm,

which is only $\sim 70\%$ of the diameter of the initial Cu_{2-x}S disk, meaning that the volume of Cu_{2-x}S has been reduced by $\sim 55\%$. The faster reaction (by a factor of about 6–7, comparing the relative volume fractions removed over time) of the Cu_{2-x}S with TBP for these $t = 4$ H-NPs as compared to the $t = 15$ H-NPs is further evidence that the ZnS caps affect the reaction via their interactions with the Cu_{2-x}S layer, either by strain or by stoichiometric modification.¹⁴ A few H-NPs in **Figure 3.2h** (circled and inset) appear to have dark cores; here, the orientation of the etched Cu_{2-x}S disk is perpendicular to the electron-beam of TEM (the axis of t is parallel to the beam). This indicates that the etching is isotropic, removing material equally from all Cu_{2-x}S surfaces exposed to the solution. The final H-NP sample, which is reacted with TBP for 1 h, shows a complete etching of the Cu_{2-x}S layer (**Figure 3.2i**), as no discernible material connection between the ZnS grains of the H-NP is observed from TEM. Moreover, the gap between the two ZnS grains, which were initially separated by a 4 nm thick Cu_{2-x}S layer, is significantly reduced to < 2 nm. The two ZnS grains from each initial H-NP are still paired, suggesting that there is a strong interaction or an atomically thin connection between them, and their size is unchanged. Interestingly, many paired ZnS grains now show a distinct contrast from each other (circled in **Figure 3.2i**) in TEM images, with one darker and the other lighter, indicating that the relative lattice orientations of the ZnS grains have changed; due to alignment of the ZnS caps via the epitaxial connections to the Cu_{2-x}S layer,¹⁴ this is never observed in the earlier stages of the reaction.

Upon close examination of TEM images, we also find that, in addition to etched SC-NPs or H-NPs, small clusters less than 2 nm in diameter are clearly visible; a closer view is shown in **Figure 3.A.3**. Previous work by Liu et al. described the digestion of Cu_{2-x}S NPs in the presence of excess oleylamine (OLA), which they attributed to a phase transformation of $\text{Cu}_{1.8}\text{S}$ to CuS controlled by the high affinity of

OLA for Cu^{2+} , resulting in small CuS clusters.⁵³ The formation of these clusters was believed to be controlled by a process similar to digestive ripening, where fragments of larger colloids are dissolved in an excess of surface-active ligand and coalesce into smaller NPs.^{20, 54} However, from their work, it is unclear how a process similar to digestive ripening might take place, as their results are consistent primarily with the oxidation of S^{2-} into SO_3^{2-} and their assignment of the oxidation states of Cu in Cu_{2-x}S is at odds with several reports that confirm that the sole oxidation state present from CuS through Cu_2S is Cu^+ .^{55, 56} Additionally, it is interesting to note that the etching process can be initiated in our case by a ligand (phosphine) with a much higher affinity for Cu^+ rather than for Cu^{2+} .^{57, 58} The use of phosphine allows access to more reduced, copper-rich phases (e.g., Cu_2S) in the system, despite the oxidizing conditions of the etching reaction.

X-ray powder diffraction (XRD) is used as the primary tool to assess structural changes in these highly nonstoichiometric Cu_{2-x}S phases. The as-synthesized Cu_{2-x}S SC-NPs have the roxbyite crystal structure (JCPDS 023-0958), with $x \approx 0.19$. We identify the phase of Cu_{2-x}S following etching by examining several characteristic reflections in the range of $2\theta = 30\text{--}35^\circ$. These are indicative of the particular superstructure of Cu vacancies distinct to the roxbyite structure.⁵² The vacancy ordering superlattice is apparent in the XRD pattern of the unetched, SC-NPs (**Figure 3.3**, curve 1; arrows point to peaks influenced by vacancy ordering). XRD of the SC-NPs and H-NPs show that the atomic lattice of Cu_{2-x}S is affected by the etching in air (**Figures 3.3, 3.4**, and **3.A.4**). To investigate the possible impact of atmospheric oxygen on the phase of Cu_{2-x}S , as has been observed by previous researchers,^{42, 59} we also examine the NPs under rigorously air-free conditions after they had been treated with TBP. Each of the three cases (SC-NPs, H-NPs with $t = 13$ nm, and H-NPs with t

= 6 nm) is found to behave slightly differently during the etching reaction, as discussed individually below.

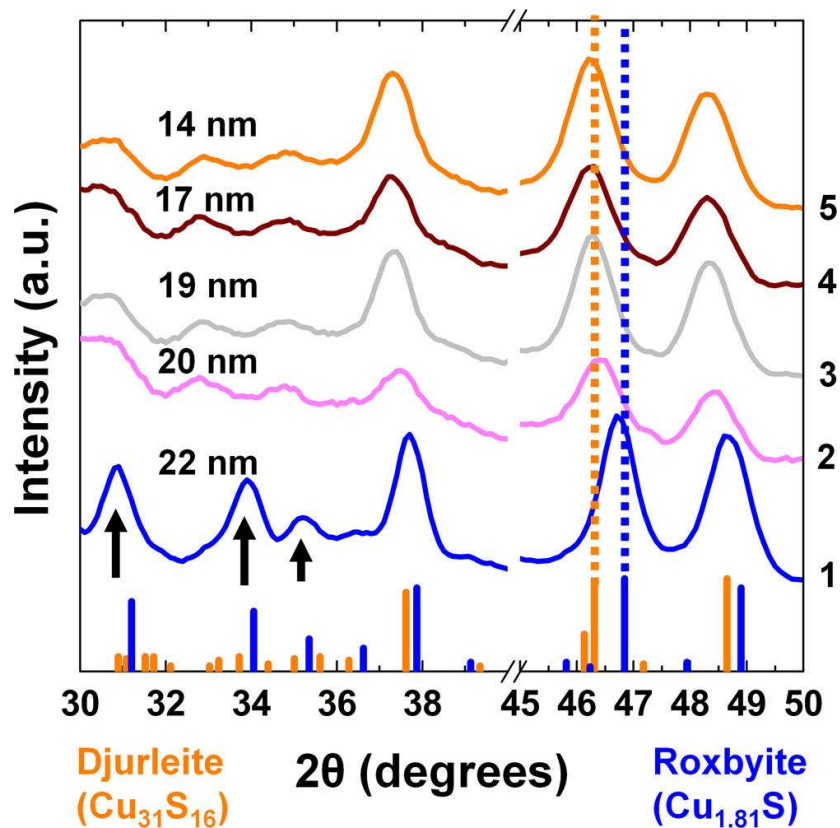


Figure 3.3. X-ray diffraction analysis of structural changes in pure Cu_{2-x}S nanocrystals (SC-NPs) during etching. Loss of Cu vacancy ordering characteristic of the roxbyite phase (curve 1; JCPDS 023-0958) is observed immediately as indicated by the disappearance of the three strong peaks indicated by the arrows (curve 2). This transformation is followed by a more gradual shift (curves 3, 4, 5) of the strong reflections near 38° , 46° , and 49° to smaller 2θ values, consistent with the larger lattice constant of djurleite (JCPDS 023-0959).

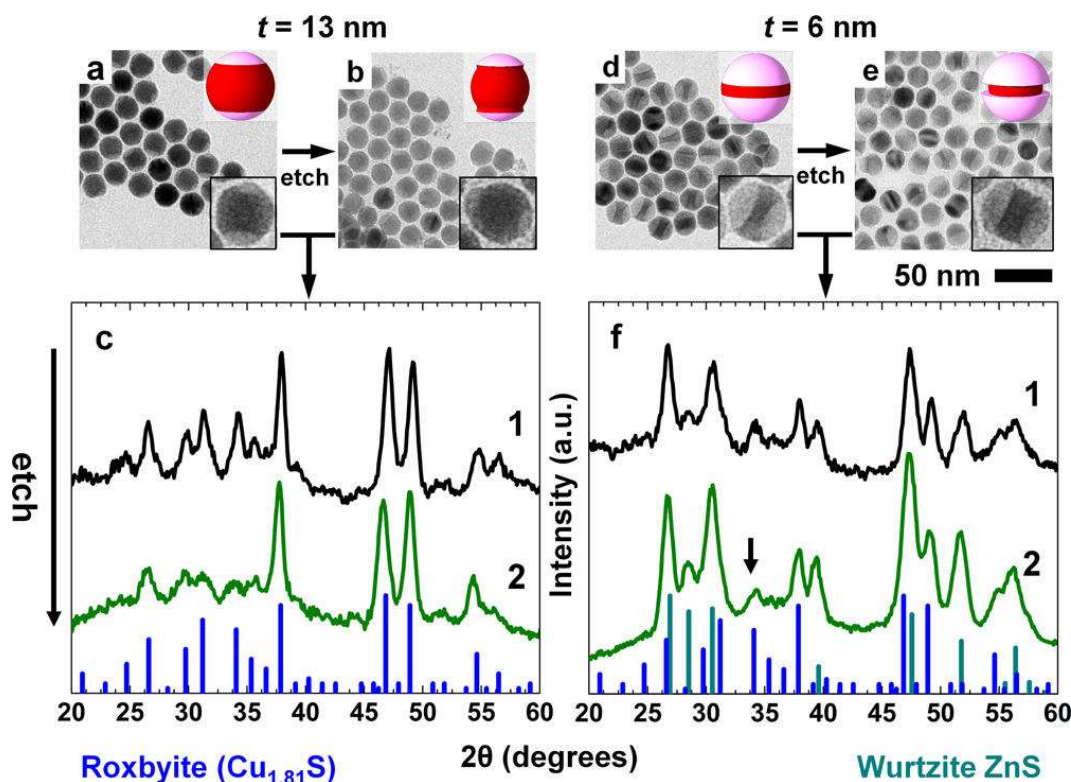


Figure 3.4. TEM images of heterostructured ZnS–Cu_{2-x}S nanoparticles (H-NPs) before (a, d) and after etching (b, e). The Cu_{2-x}S layer thickness t is ~ 13 nm in (a) and 6 nm in (d). t does not change substantially after etching the particles in (a) for 30 min (b) or in (d) for 15 min (e). The diameter of the approximately disk-shaped layer was reduced from 20.4 to 18.3 nm in (a, b) (volume loss of about 20%; aspect ratio d/t change from 1.6 to 1.4) and from 19.7 to 16.7 nm in (d, e) (volume loss of 28%; aspect ratio change from 3.2 to 2.6). Also shown is X-ray diffraction analysis ((c) $t = 13$ nm; (f) $t = 6$ nm) of structural changes in H-NPs before (curve 1) and after (curve 2) etching. In (f), the Cu_{2-x}S layer is highly strained by the ZnS caps (JCPDS 036-1450), so the etching process has little effect on the structure (no peak shifts or attenuation of the peak near 35°); however, in (c), the layer reverts to the djurleite phase. In H-NPs, the vacancy ordering seen in roxbyite (verified by the reflection below 35° indicated by the arrow) is stabilized by the presence of ZnS caps that are more closely lattice-matched to roxbyite.

The results of the etching reaction on a set of spherical, $d = 22$ nm SC-NPs are shown in **Figure 3.3**. After 5 min of etching, TEM images indicate that the SC-NPs are reduced in size from 22 to ~ 20 nm, a volume loss of $\sim 25\%$, and XRD patterns show the NPs do not exhibit the characteristic vacancy ordering of roxbyite, as shown by the disappearance of these strong reflections (**Figure 3.3**, curve 2). Additionally, a careful comparison of the positions of the diffraction peaks reveals that all reflections in the sample etched for 5 min ($d = \sim 20$ nm) have also shifted to smaller 2θ angles, indicating that the size of the unit cell has increased; the shift is the largest at 0.35° for the (0 16 0) (roxbyite) or (0 4 6) (djurleite) reflection near $46\text{--}47^\circ$, corresponding to an increase in interplanar spacing of $\sim 1\%$. As such, the diffraction pattern of this sample more closely resembles that of the $\text{Cu}_{1.94}\text{S}$ phase, djurleite (JCPDS 023-0959). Continued etching of the particles results in a reduction in particle diameter with corresponding powder diffraction patterns that confirm the structural change: as the size of the particles is reduced from 20 to 19 nm, the XRD peaks further shift (0.2° in 2θ) to smaller angles, bringing the diffraction pattern in excellent correspondence to that of djurleite phase (**Figure 3.3**; curves 3, 4, and 5 are 19, 17, and 14 nm diameter particles, respectively). XRD of samples protected from air indicates that treatment with phosphines can, in fact, transform the NPs to the compositional end-member, Cu_2S , in the low chalcocite phase (JCPDS 001-3280, **Figure 3.A.4a**). This phase disappears rapidly (less than 24 h) after exposure to air, with the SC-NPs reverting to the djurleite phase. We do not observe another transformation to more oxidized phases such as roxbyite. Other reports also find that the transformation of Cu_{2-x}S with oxidation stops at djurleite^{42, 60} and suggest that the change in stoichiometry found by XRD is accommodated by formation of an amorphous oxidized surface layer. However, it is not known whether the slow kinetics of further surface oxide growth or

the thermodynamic instability of roxbyite (lack of driving force) is responsible for the stability of the djurleite phase in this case.

The H-NPs with $t = 13$ nm, after 30 min of etching in air, also show structural changes upon TBP exposure, exhibiting an estimated 20% volume loss with the average diameter of the Cu_{2-x}S region decreasing from 20.4 to 18.3 nm (**Figure 3.4a,b**). As seen from XRD, the cation ordering in roxbyite before etching (**Figure 3.4c**, curve 1) largely disappears following etching of these H-NPs (**Figure 3.4c**, curve 2), and a shift of the entire pattern to smaller angles is seen, similar to the etched SC-NPs. If the $t = 13$ nm H-NPs are treated with TBP in an inert atmosphere, a phase transformation to low chalcocite (Cu_2S) is observed (**Figure 3.A.4b**). Immediately following exposure to air, the Cu_{2-x}S phase transforms back to djurleite. Interestingly, Cu_{2-x}S in $t = 13$ nm H-NPs reverts to roxbyite (unlike SC-NPs) after exposure to air for long periods (days). This shows, as discussed below, that the strain imposed by lattice mismatch between the ZnS caps and Cu_{2-x}S layer can stabilize otherwise unfavorable phases.

Finally, with larger ZnS caps ($t = 6$ nm), the Cu_{2-x}S layer is etched about 3 times more rapidly, as its diameter decreases from 19.7 to 16.7 nm, representing a volume loss of $\sim 28\%$, after 15 min of exposure to air (**Figure 3.4d,e**). The results of XRD characterization indicate that there are no significant changes in the characteristic roxbyite reflections following an etch of the Cu_{2-x}S layer (**Figure 3.4f**), as the intensity of the vacancy-ordering peak at 34° does not decrease and the diffraction angles of all observable roxbyite peaks do not shift. When treated with TBP under strictly air-free conditions, H-NPs with large ZnS caps were not transformed to low chalcocite. Instead, transformation only proceeded as far as the djurleite phase (**Figure 3.A.4c**), suggesting that the strain can limit the extent of stoichiometric modification as well. This observation is in accordance with our

previous studies showing that, due to the strong epitaxial match between ZnS and roxbyite and to the mismatch between ZnS and the sulfide sublattices of nonroxbyite phases, the presence of ZnS stabilizes bordering Cu_{2-x}S regions in the roxbyite phase.¹⁴

The disappearance of the roxbyite vacancy ordering and swelling of the Cu_{2-x}S unit cell indicate that sulfur has been preferentially removed from the crystalline Cu_{2-x}S regions of the NPs, decreasing the value of x in Cu_{2-x}S . Djurleite, in this case, is more thermodynamically favorable than roxbyite, and the high mobility of Cu atoms within the Cu_{2-x}S lattice allows for facile phase transformations.¹⁴ Whether the shift of the XRD peaks in the case of the H-NPs (both $t = 13$ and 6 nm) indicates a smooth transition to a less well-ordered roxbyite phase or a conversion of a fraction of the Cu_{2-x}S layer to djurleite is not certain. We note that in our previous work we observed the accommodation of multiple Cu_{2-x}S phases simultaneously via the formation of stacking faults,¹⁴ suggesting that the phase transformation was not continuous in a single Cu_{2-x}S layer. We also observed through both XRD and X-ray absorption spectroscopic measurements that, upon treatment with phosphine and Zn^{2+} ions in the formation of ZnS– Cu_{2-x}S H-NPs, the roxbyite phase was almost completely eliminated in the early stages of the reaction, when the strain influence at the interface with the epitaxial ZnS caps was minimal.¹⁴ However, as t decreases further and the strain energy imposed by the ZnS caps becomes larger, a more copper-deficient phase, roxbyite, is favored. From our XRD and TEM observations, we conclude that a phosphine treatment by itself is sufficient to induce a phase transformation by “injecting” Cu atoms into the lattice of the copper sulfide particle as well as by removing S. The preferential removal of S and overall size reduction of the particle is informative when considering potential etching mechanisms; we conclude that both

processes operate simultaneously, as confirmed by further spectroscopic evidence (see section 3.3.2 below).

3.3.2. Optical characterization

The Cu_{2-x}S NPs are characterized by UV–vis–NIR spectroscopy to understand how etching affects carrier concentration. Cu_{2-x}S in nanocrystalline form exhibits strong optical absorption in the near-infrared arising from a localized surface plasmon resonance (LSPR).^{14, 42–45, 47, 61, 62} For $x > 0$, holes are generated in Cu_{2-x}S to charge-compensate copper vacancies in the material, providing Cu_{2-x}S a high density of free carriers.⁴⁵ Thus, the character of the LSPR band reflects the stoichiometry of Cu_{2-x}S . The optical absorption of the starting Cu_{2-x}S SC-NPs is shown in **Figure 3.5a** along with the evolution of the LSPR band position over the course of the etching reaction. Immediately following the treatment of Cu_{2-x}S SC-NPs with TBP, a large (~ 200 nm) red shift in the LSPR position is observed. This is consistent with a reduction in the concentration of Cu vacancies following the transformation of the particle to the djurleite phase ($\text{Cu}_{1.94}\text{S}$), which can be induced by the extraction of S from the NP and injection of the excess Cu ions into vacancies, as we previously posited. After reduction of the particle size to 19 and 17 nm, the wavelength of the LSPR maximum increases by ~ 100 nm but, thereafter, remains nearly constant. This wavelength shift qualitatively corresponds to the phase transformation observed in the XRD results (see **Figure 3.3**), which shows a continuous but rapid and irreversible transformation to the more copper-rich djurleite phase.

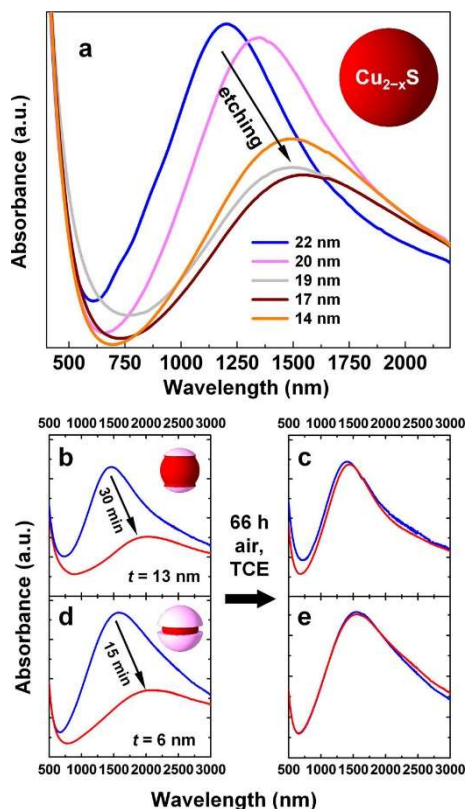


Figure 3.5. Optical properties of Cu_{2-x}S nanostructures after etching using tributylphosphine. LSPR changes for pure Cu_{2-x}S nanocrystals (SC-NPs) are shown in (a). A shift to longer wavelengths (near 1500–1550 nm) from the initial LSPR at ~ 1200 nm is seen over most of the series, but the final sample exhibits a slight blue shift. Optical properties of the $\text{ZnS-Cu}_{2-x}\text{S}$ heterostructures (H-NP) are shown in (b–d). H-NPs with $t = 13$ nm (b) and 6 nm (d) initially show LSPR resonances at 1445 and 1570 nm, respectively (blue curves). After etching the H-NPs with TBP for the time shown by the arrows, spectra were acquired after 3 h of standing in air; a red shift to 2015 nm is seen for $t = 13$ nm and to 2090 nm for $t = 6$ nm (b and d, respectively, red curves). Following long-term air exposure (66 h), the spectra were reacquired (c, e). The plasmon positions are now almost identical: 1400 (blue) to 1425 nm (red) for $t = 13$ nm (c) and 1570 (blue) to 1590 nm (red) for $t = 6$ (e). Spectra are normalized to the absorbance at 400 nm.

Optical absorption was also measured on H-NPs with characteristic Cu_{2-x}S dimensions of $t = 13$ and 6 nm (**Figure 3.4a,b,d,e**, the same particles discussed in section 3.3.1) before and after etching. Our optical measurements indicate that, before etching, the LSPRs of the H-NPs occur at $1400\text{--}1500$ nm (**Figure 3.5b,d**), with the two populations of H-NPs having remarkably similar optical characteristics despite their substantial differences in aspect ratio (1.6 for $t = 13$ nm and 3.2 for $t = 6$ nm). When measured a few hours following etching, the LSPR red-shifts to $2000\text{--}2100$ nm (**Figure 3.5b,d**); however, this effect proves to be temporary, and the LSPR blue-shifts back to its original energy after prolonged exposure to air over 3 days (**Figure 3.5c,e**). Such optical shifts following exposure to oxygen are well-known in Cu chalcogenides; previous work has proposed that the change in Cu vacancy concentration is effected by the ejection of Cu to the surface, rather than by its complete extraction from the particle, as discussed above.⁴² These results highlight the sensitivity of these chemically “soft” materials to the oxidizing or reducing nature of their environment,⁴² which may prove to be useful in future applications, such as oxygen sensing, but indicates that particular care must be taken to examine the effect of processing history and measurement conditions on optical properties. The contrast of these optical measurements with our previous work, where we found that the LSPR strongly and monotonically red-shifted as t decreased,¹⁴ may explain in part why the experimental data lacked agreement with theoretical models⁶¹ due to previously uncontrolled variations in the carrier concentration in Cu_{2-x}S . Overall, we find here that the location of the LSPR does not appear to depend strongly on the geometry of the absorber as characterized by its estimated Cu_{2-x}S volume (see **Figure 3.A.5**), both for SC-NPs and for H-NPs. However, now that the extent of the sensitivity of these materials to oxidation has been characterized, it can be more tightly controlled in future studies.

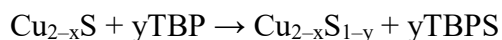
2.3. Mechanism of etching

The etching of copper sulfide is surprising since TBP is a common surfactant ligand that passivates the NP surface for stabilization in a solvent and prevents NP aggregation.^{2, 3, 10} To examine whether this etching reaction only occurs with TBP, the SC-NPs and H-NPs were exposed to an excess of different surfactant ligands (oleic acid, OLA, and dodecanethiol). None of the surfactants etched the copper sulfide layer of the H-NPs after an hour of reaction time (**Figure 3.A.6**). For comparison, on this time scale, TBP completely dissolved the copper sulfide layer of the H-NPs (see **Figure 3.2i**). When trioctylphosphine (TOP) was used in place of TBP, the TOP did act as an etchant, revealing that the phosphine group is the key moiety involved in the rapid etching of copper sulfide. The etching reaction with TOP, however, is much slower than that with TBP. A 1 h etching reaction with TOP only partially etches the copper sulfide layer, removing about as much Cu_{2-x}S as TBP removed in 2 min (**Figure 3.A.7**). The different reaction kinetics between TOP and TBP indicates that longer hydrocarbon chains yield slower rates in the etching reactions. We note that, without added ligands, the particle morphology and phase was stable during storage in toluene for at least six months. However, in accord with the results of Liu et al.,⁵³ the presence of a small amount (a few mg/mL, as might be introduced when adding a few drops to stabilize the NPs in solution for storage) of added OLA was found to result in etching of the particles over a period of several days (**Figure 3.A.8**).

This process could be explained by the dissolution of Cu from the surface as Cu^{2+} -amine complexes, followed by the reaction of the free amines with surface-bound sulfur or polysulfides⁶³ to form soluble reaction products such as thioamides, in analogy with the reaction mechanism discussed in more detail below. Additionally, in the presence of an excess of both TBP and OLA, etching of the particles proceeded much more rapidly than with only TBP, with the dissolution of SC-NPs being

complete in as little as 2 h. We suspect that in this each ligand may perform a complementary role, as OLA strongly stabilizes amine complexes and TBP, as discussed below, efficiently removes sulfide.

Phosphines are well-known to nanoparticle chemists as L-type neutral two-electron donor ligands.² Phosphines also easily form very stable oxidized species in which phosphorus assumes a higher oxidation state, as in the well-known phosphine oxides. Given our observation of the reduced phases of Cu_{2-x}S following etching, we hypothesize that phosphines remove S from the NPs by the following mechanism, in line with previous reports on the alteration of NP crystal structures using phosphines:¹⁰



In this case, S^{n-} , where $n < 2$, is reduced by TBP. As reported by previous studies on nanoparticulate copper sulfides, the nonstoichiometry of Cu_{2-x}S is established by changing the oxidation state of S rather than Cu, even when the composition is near CuS .⁴⁷ The presence of S^- in Cu_{2-x}S also explains why phosphines will not etch ZnS , since the only oxidation states occurring in this more ionic material are Zn^{2+} and S^{2-} , and nonstoichiometry is not expected to arise in the form of oxidized sulfur species.⁶⁴ Compositional analysis by energy dispersive X-ray spectroscopy (EDX) and inductively coupled plasma mass spectrometry (ICP-OES) were not useful for assessing stoichiometry changes; both methods found a ratio of Cu/S exceeding 2 with very high uncertainty, regardless of whether the sample had been etched or not. Difficulty in measuring stoichiometry due to difficult-to-remove residues has been noted by previous groups.^{24, 42} Due to the long-term stability of the isolated particles after synthesis (see section 3.3.1), we believe that these residues do not contribute to etching.

We also examine the residual liquid following complete dissolution of a highly concentrated solution of Cu_{2-x}S NPs in air using FTIR spectroscopy; a set of

absorption bands at 590–610 cm^{-1} , which can be unambiguously assigned to the P=S stretching vibration⁶⁵ (**Figure 3.6a**, blue curve), confirms, along with the previous XRD and optical measurements, that the abstraction of S by phosphines in the form of phosphine sulfides is at least partially responsible for dissolving Cu_{2-x}S . Following reduction, the NPs can easily be reoxidized at the surface by O_2 , forming more oxidized sulfide species.⁶⁶ These bands are not found in a sample of TBP exposed to air without NPs (**Figure 3.6a**, red curve), indicating that they do not arise from a phosphine oxidation product, nor are they found in a sample of Cu_{2-x}S NPs “etched” with TBP under an N_2 atmosphere, showing that the small amount of S removed from the particles during the initial transformation of the SC-NPs to the low chalcocite phase is not sufficient to give rise to detectable signatures of etching products (**Figure 3.6a**, gray curve).

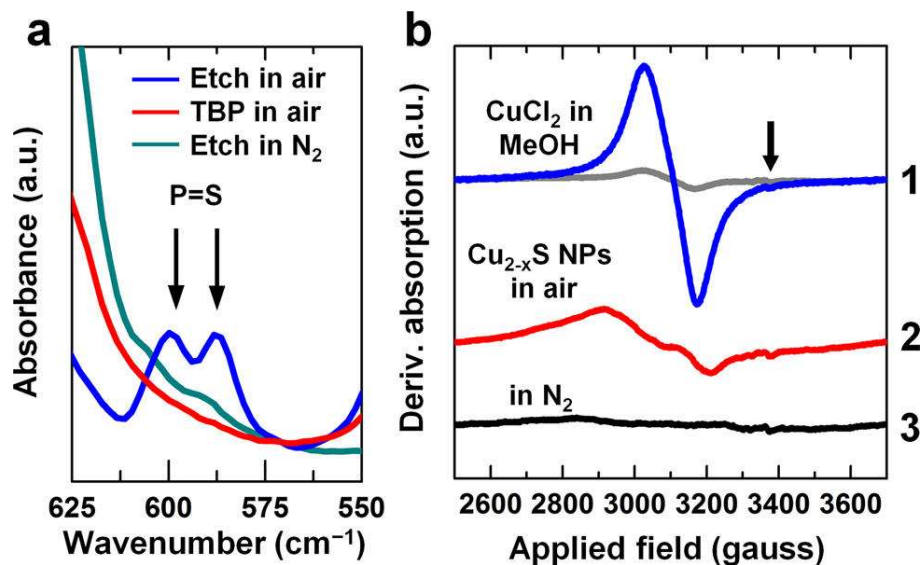


Figure 3.6. Cu_{2-x}S oxidative etching into Cu- and S-containing species. (a) The abstraction of sulfide from the particle in the form of phosphine sulfides is shown by FTIR spectra of the residual oxidized TBP liquids following evaporation of toluene.

Bands at approximately $580\text{--}600\text{ cm}^{-1}$ confirm the presence of the P=S bond attributed to TBPS and its isomers. Nominal path length: $200\text{ }\mu\text{m}$. (b) In air, oxidation of Cu into a solvated form of paramagnetic Cu^{2+} after etching is shown by EPR spectroscopy. Standards of CuCl_2 in methanol with concentrations of 10 or 1 mM (curve 1, blue and gray, respectively) are shown for comparison and have simple Lorentzian lineshapes. A signal from a solution of 5 mg/mL of Cu_{2-x}S NPs in toluene/TBP exposed to air for 2 weeks is observed (curve 2); however, an identical solution was kept in the glovebox for the same amount of time and showed no EPR signal (curve 3). The feature indicated by the arrow is believed to be a paramagnetic impurity in the glass capillary used.

Although the removal of S by phosphines and subsequent reoxidation of surface S by O_2 is accounted for by this mechanism, the form in which Cu is extracted from the NPs is unclear. A possibility, given the presence of oxygen, is that Cu^+ is

oxidized to Cu^{2+} and thereafter dissolved by phosphine oxides, sulfides, and other polar phosphine oxidation products. A summary of the possible etching mechanism by phosphines is depicted in **Figure 3.7** (top path). Previous studies of the oxidation of bulk Cu_{2-x}S in water have shown that the process involves the oxidation of surface Cu^+ to Cu^{2+} .⁶⁶ Cu^{2+} , which is paramagnetic, can be distinguished from Cu^+ in solution using electron paramagnetic resonance (EPR) spectroscopy. A typical example of the EPR signal from a Cu^{2+} solution (CuCl_2 in methanol), a simple Lorentzian peak, is shown in **Figure 3.6b**, curve 1. An EPR analysis of the residual solution following complete dissolution in air of Cu_{2-x}S (**Figure 3.6b**, curve 2) shows a similar EPR signal to the CuCl_2 standard. The presence of this EPR signal definitively establishes the presence of Cu^{2+} indicating that dissolved Cu was oxidized to Cu^{2+} in solution. A similar sample, which was instead kept in an N_2 atmosphere (**Figure 3.6b**, curve 3), shows no EPR signal (is EPR silent). This is consistent with earlier reports that pure Cu_{2-x}S is EPR silent regardless of its stoichiometry, since the only oxidation state present is Cu^+ .^{47, 55, 56} The line shape of the Cu^{2+} in solution following etching is distorted from the Lorentzian line shape obtained from a CuCl_2 -methanol reference, suggesting slow motion of the spins in solution, which could be caused by the complexation of Cu^{2+} in larger molecules which tumble more slowly.⁶⁷ Polymeric complexes of the form $[(\text{TBPO})_4\text{Cu}]^{2+}$ have been reported previously.⁶⁸ These results therefore suggest that Cu_{2-x}S NPs may be dissolved and oxidized to Cu^{2+} , followed by stabilization in solution as an ill-defined polymeric complex with phosphine oxides formed by autoxidation of the phosphine in air. We note that the oxidized phosphines, TBPO and TOPO, were totally ineffective in effecting any etching of the particle by themselves. However, upon auto-oxidation in air, phosphines also form a complex mixture of products, including phosphonic acids and dialkylphosphines, via a radical mechanism.⁶⁹ Owing to the reactive nature of these products and intermediates, we

also observed the etching reaction in the presence of a large excess of antioxidant (diphenylamine) to suppress free-radical concentrations or non-nucleophilic base (triethylamine) to scavenge acidic protons. Neither was effective in preventing the etching process, strongly suggesting intermediates formed in solution were not responsible.

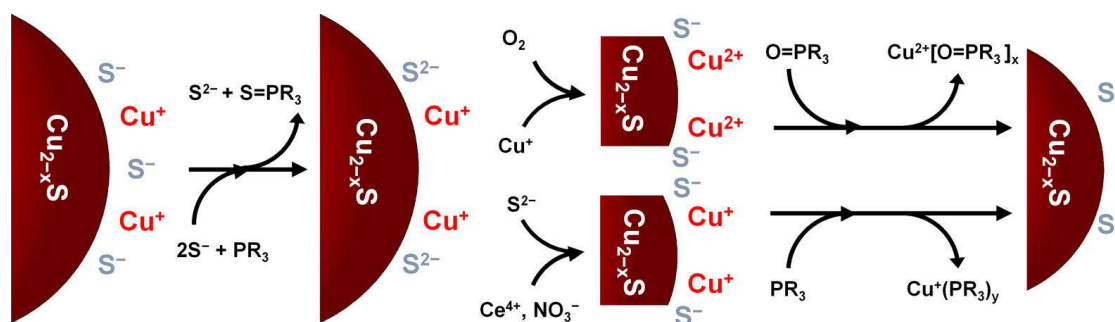


Figure 3.7. Summary of proposed mechanism for etching of Cu_{2-x}S . In air, initially oxidized surface S species are abstracted by phosphines in the form of phosphine sulfides (left). Cu and S^{2-} may then be oxidized by O_2 (top center), regenerating the oxidized S species. Finally, Cu is dissolved as a Cu^{2+} complex with oxidized phosphine species (top right). Etching can also be performed under inert atmosphere using Ce^{4+} (and/or NO_3^-). Oxidized S species are generated by electron transfer to the oxidant (bottom center); thereafter, surface-bound Cu^+ is directly removed by phosphines (bottom right). The reactions then repeat, eventually dissolving the particles.

To confirm that an oxidizing environment is necessary for the etching process, we study the etching reaction with an electron acceptor, Ce^{4+} , in the form of ceric ammonium nitrate, $(\text{NH}_4)_2\text{Ce}(\text{NO}_3)_6$ (CAN), as the oxidizing agent in the place of molecular oxygen. CAN has been observed to be highly effective for generating free

charge carriers in copper chalcogenide NPs.⁷⁰ CAN is not found to etch such particles by itself despite being a very powerful oxidant, but in the presence of TBP, the addition of small amounts of 0.1 M CAN in methanol to solutions of SC-NPs in toluene under an N₂ atmosphere results in rapid etching of the particles. This reaction is observed to go to completion in at most 1 h. Interestingly, the morphology of the etched particles remains consistently spherical at all phosphorus to sulfur (P/S) ratios. This differs from the TBP/air etching results where the lower P/S ratios resulted in anisotropic etching (to be discussed) (**Figure 3.A.9**). This indicates that etching of the particle by CAN and TBP does not entail strong facet-selective adsorption of the oxidant or TBP to the SC-NP surface; thus, it must be the facet-selective adsorption of oxygen that is the deciding factor in anisotropic structure formation. With sufficient CAN, the particles are fully dissolved in less than 1 h, but very little CAN is needed relative to the amount of Cu_{2-x}S present; if it is assumed that S is oxidized to S⁰ to completely dissolve the particle, as in the reaction $\text{Cu} + 2\text{S}^{2-} \rightarrow 2\text{Cu}^+ + \text{S}^0 + 2\text{e}^-$, then the titration requires that CAN removes 3–9 e⁻ per formula unit, far in excess of its nominal capacity as a one-electron oxidizer (**Figure 3.A.10**), indicating that NO₃⁻ may also serve as an oxidizing agent. We confirm that in a control experiment the nitrate anion by itself also appears to work as a (relatively slow) oxidizer for etching Cu_{2-x}S: NaNO₃ added to the NPs dissolves them over the course of several hours when added in sufficient amounts (approximately 1–3:1 NO₃⁻/S). However, EPR spectroscopic analysis of the reaction solutions for these experiments with CAN or with NaNO₃ showed that they exhibited no signal from Cu²⁺. This finding is consistent with the hypothesis that oxidation of the anion sublattice is sufficient for etching, although it does not rule out the possibility that the Cu⁺/Cu²⁺ redox couple may be transiently involved in electron transfer. This reaction is summarized in **Figure 3.7** (bottom path); we conclude that etching of Cu_{2-x}S by this simultaneous oxidation–reduction

mechanism requires the disproportionation of S^- to S^0 and S^{2-} , thereby allowing surface-bound S^0 to be reduced by phosphine. S^- is thereafter regenerated by the oxidizing agent (Ce^{4+} , NO_3^- , or O_2).

We gain further insight into the mechanism of the etching reaction by deliberately restricting the amount of phosphine available during etching by adding smaller amounts of TBP or TOP to SC-NP solutions in toluene or hexane to prevent the eventual complete digestion of the NPs. The amount of added phosphine was chosen based on the estimated P/S ratio and varied from $\sim 1:2$ P/S to $\sim 100:1$ P/S, and the reaction is run for 6–8 h. We were able to recover solid products for TEM analysis with added TBP/S ratios lower than 5:1. At higher concentrations than this, no NP precipitate was obtained, indicating the complete dissolution of $Cu_{2-x}S$. To our surprise, we find that the morphologies of the particles in these etching experiments with smaller concentrations of TBP/TOP differed considerably from those etched with a large excess of TBP ($P/S > 250:1$, as was shown in **Figure 3.2a–c**). Instead of isotropically etched spherical particles, we observe pronounced anisotropy in the dissolution of $Cu_{2-x}S$, showing that at lower nominal ligand coverages the nature of the etching reaction changes considerably (see below). At a TBP/S ratio of 1:2 (**Figure 3.A.11a**), the recovered particles exhibit a distinct, rounded notch at one end of the particle. At higher concentrations of TBP (TBP/S ratio 1:1), the notch develops into a dramatic concave hollow; furthermore, a second hollow area is observed at the opposite end of many particles, giving the NP the appearance of a biconcave disk (red blood cell shape; see **Figures 3.8a** and **3.A.11b**). During the etching process, the NPs remain single-crystalline, as confirmed by HRTEM (**Figure 3.8a,b**). Interestingly, the preferential etching occurs along the (400) direction in the crystal (either roxbyite⁵²) or djurleite,⁷¹ **Figure 3.8b,c**, the same direction along which ZnS or CdS caps grow during heterostructure formation¹⁴ and corresponds to the basal planes of the

pseudohexagonal structure. The highly concave morphology of the particles is similar to that observed by Liu et al. in the case of the oxidative digestion of Cu_{2-x}S NPs by OLA.⁵³ At still higher concentrations of TBP, the particles precipitate as large, ill-formed aggregates (**Figure 3.A.11c**).

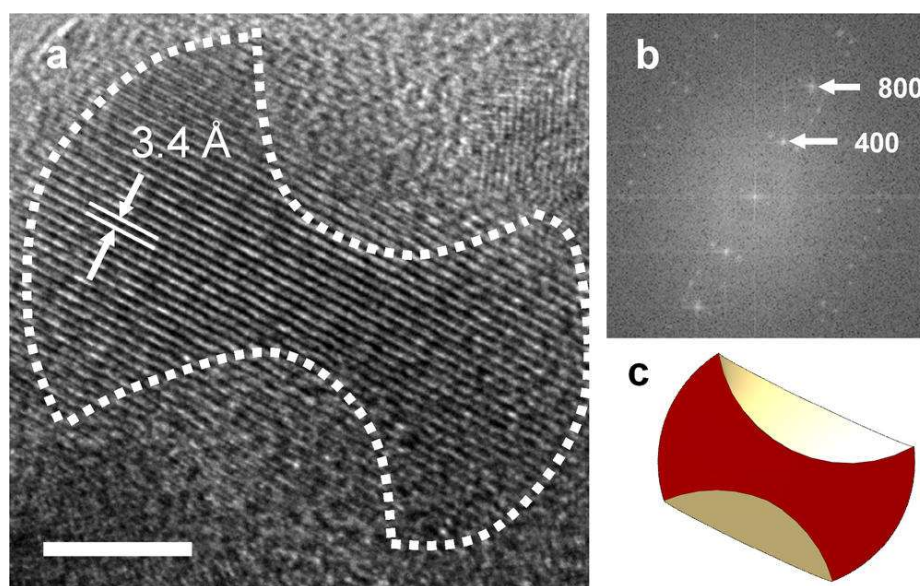


Figure 3.8. Anisotropic etching in the presence of low concentrations of phosphine. HRTEM image of an anisotropically etched, single-crystal Cu_{2-x}S nanoparticle (a), its Fourier transform (b), and a high-contrast schematic of the particle morphology (c). Scale bar is 5 nm; the dashed white outline is a guide for the eye. The lattice fringe with periodicity 3.4 \AA may be assigned to the (400) reflection either of djurleite (JCPDS 023-0959) or roxbyite (JCPDS 023-0958).

The crossover from anisotropic to isotropic etching may be explored more easily using TOP, which was shown to etch the NPs more slowly. During the controlled etching of SC-NPs with TOP, particles adopt notched and concave shapes at a TOP/S ratio 5:1 (**Figure 3.9a**) similar to that observed for etching using TBP.

Small rod-like particles are recovered at a TOP/S ratio 10:1; they have an irregular appearance, although some degree of anisotropy in etching behavior is still apparent through the appearance of distinct notches in these particles (**Figure 3.9b**). Increasing the TOP concentration again (TOP/S 50:1) generates a bimodal distribution of particle shapes, with one population being more rod-like and the second being nearly spherical (**Figure 3.9c**). At still higher concentrations of TOP (TOP/S 100:1, close to the concentrations used in the isotropic etching experiments), however, the etching reaction returns to its original isotropic etching behavior (**Figure 3.9d**). Thus, at low concentrations of, and presumably lower average surface coverage with, TOP, the dissolution proceeds anisotropically. TOP therefore plays decisive roles in the chemical reactivity of the NPs in solution both as an etchant and as a protective capping agent.

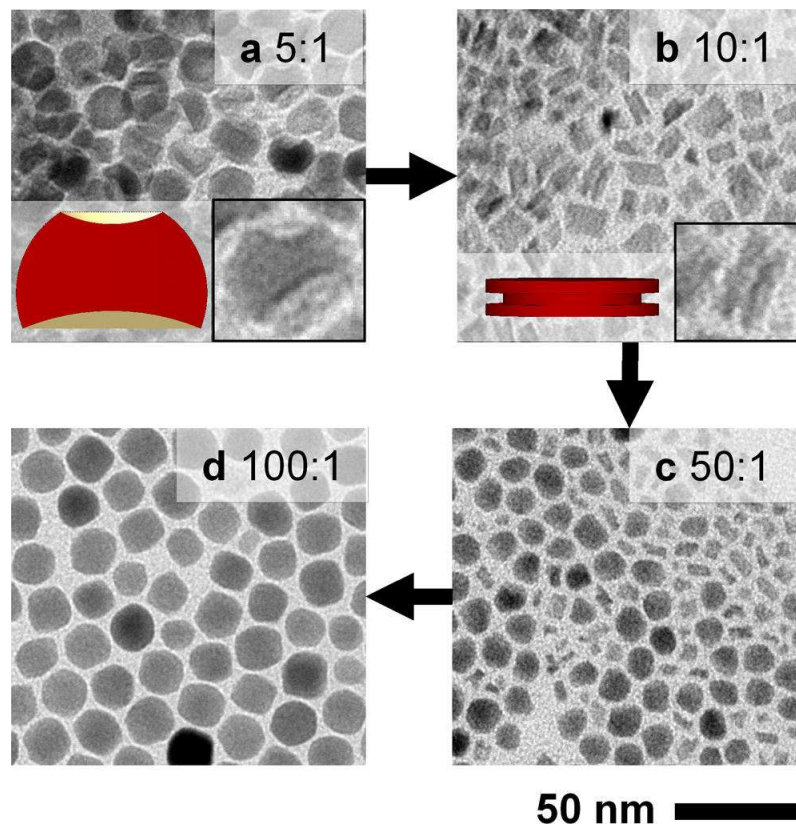


Figure 3.9. Crossover from anisotropic to isotropic etching behavior in the presence of TOP. TEM images, clockwise from top left: At low concentrations of TOP (low P/S ratio, (a)), particle etching occurs in the form of concave pits (inset) which may be at one or both ends of the particle. Larger P/S ratios (b) lead to pronounced faceting and additional erosion of the particle along the axis perpendicular to the facets (inset). At even higher phosphine concentrations, a bimodal population of (an)isotropically etched particles forms (c); at the largest P/S ratios, the etching reaction proceeds only isotropically (d).

Many previous studies on anisotropic etching of NPs attributed the observed anisotropy to selective stabilization of specific facets;^{33, 72-74} under appropriate conditions, crystalline materials are attacked more rapidly along certain crystal directions by the etchant so that etched surfaces assume a faceted, sharp

morphology.²⁷ However, the pitted particles observed in **Figures 3.8a, 3.9a, and 3.A.11** are highly concave and exhibit little faceting. Concave, even hollow, NPs have been reported previously during the oxidative etching of solid Pd nanocubes using water, O₂, and Cl⁻;³⁷ this was attributed to a pitting mechanism by which the exposure of unpassivated surface at localized corrosion sites leads to preferential, autocatalytic attack of O₂/Cl⁻ at this fresh surface. A similar mechanism may operate during the etching of Cu_{2-x}S by phosphines and oxygen. Incomplete passivation of the SC-NP surface at lower phosphine coverage would allow oxygen to preferentially attack the basal planes of the crystal structure. In the presence of excess phosphine, the surface of the particle becomes saturated with bulky hydrocarbon chains; in this case, phosphine does play a role as a passivating layer, which slows the etching and prevents the autocatalytic corrosion reaction responsible for anisotropic etching from occurring. However, the true nature of the oxygen–copper sulfide interactions remains highly uncertain since the complicated solid-solution interface is difficult to characterize in the presence of coexisting oxide and sulfide phases in addition to the organic capping agents.

3.4. CONCLUSION

This investigation clarifies the mechanistic details behind a complex, redox-driven, highly selective chemical etching reaction by which Cu_{2-x}S is removed from colloidal single-crystal (SC-NP) and heterostructured (H-NP) nanostructures in a multistep process entailing the removal of S from the NPs by phosphines and the subsequent diffusion of excess Cu ions into the remaining particle and reoxidation of the particle to regenerate oxidized S species and dissolve Cu. As confirmed by X-ray diffraction and optical measurements, this process requires the generation of more Cu-

rich phases, with consequent reduction in carrier concentration due to the quenching of Cu vacancies, in accordance with previous work on copper chalcogenides.^{46, 47, 70} At very high concentrations of phosphine, the etching reaction dissolves SC-NPs isotropically, but when they are insufficiently passivated with this surfactant, molecular oxygen selectively attacks the basal planes of the pseudo-hexagonal Cu_{2-x}S structures. Ultimately, when the reaction is allowed to run to completion in air, Cu_{2-x}S is dissolved to a mixture of oxidized phosphines, phosphine sulfides, and coordinated Cu^{2+} species, as confirmed by FTIR and EPR spectroscopy. We show that a redox reagent previously used for tuning the density of charge carriers in Cu chalcogenides, ceric ammonium nitrate, can be efficiently substituted for molecular oxygen in this reaction. We corroborate our previous observations¹⁴ that the presence of epitaxial ZnS, which is lattice-mismatched to the Cu-rich phases, in H-NPs strongly stabilizes the ordered-vacancy roxbyite phase even in the presence of aggressive etching by phosphines. In SC-NPs, the roxbyite structure is instead irreversibly transformed into djurleite during the etching. The ability to combine top-down and bottom-up processes in the fabrication of complex colloidal nanoparticles will be crucial in later synthetic strategies for the design of functional materials using these solution-processed nanostructures. Finally, we emphasize that these results are important not only for postsynthetic reshaping of nanoparticles but also for understanding stoichiometry, structure, and electronic properties in the initial particle “skeleton,” as the decidedly aggressive nature of the phosphine surfactant established by this and other works is crucial in understanding the growth of such chemically soft materials as transition metal chalcogenides.

3.A. APPENDIX

3.A.1. Funding

This work was supported in part by the National Science Foundation (NSF) under award numbers CMMI-1344562 and CHE-1507753. This work made use of the Cornell Center for Materials Research Shared Facilities, which are supported through the NSF MRSEC program (DMR-1120296). We thank Dr. Boris Dzikovski, who is supported by the National Institute of General Medical Sciences of the National Institutes of Health under award number P41GM103521, for obtaining the EPR data and Yizhi Zhu for assistance with a number of syntheses. We also thank Prof. Rüdiger Dieckmann and Dr. Ivan Keresztes for helpful discussions.

3.A.2. Materials and methods

Oleylamine (OLA, 70% [technical grade] or 98%), 1-octadecene (ODE, 90%), di(tert-butyl) disulfide (97%), tributylphosphine (TBP, 97%), tributylphosphine oxide (TBPO, 95%), trioctylphosphine (TOP, 97%), trioctylphosphine oxide (TOPO, 99%), copper (II) chloride (CuCl_2 , 99.999%) and copper (II) chloride dihydrate ($\text{CuCl}_2 \cdot 2\text{H}_2\text{O}$, 99.99%), zinc chloride (ZnCl_2 , 99.999%), dodecanethiol (99%), oleic acid (90%), tetrachloroethylene (TCE, 99%), ammonium cerium(IV) nitrate (CAN, >98.5%), sodium nitrate (>99.999%), molecular sieves UOP type 3A, triethylamine (>99%), diphenylamine (>99%), and methanol (99.8%) were all from Sigma-Aldrich and used as received except where noted. Acetone, hexane, and toluene (ACS grade) were from EMD Millipore or BDH. Ethanol (200 proof, KOPTEC) was from Decon Labs Inc. $\text{CuCl}_2 \cdot 2\text{H}_2\text{O}$, ZnCl_2 , TBP, and TOP were all stored under nitrogen in a glove box; where necessary, other chemicals were deaerated by bubbling with nitrogen before bringing them into to the glove box.

Nanomaterials synthesis

Copper sulfide (Cu_{2-x}S) NPs were synthesized as described in our previous work.¹⁴ We originally used technical grade, 70% OLA in this synthesis; however, we noted reproducibility problems using this solvent and substituted a mixed solvent, hereafter called OLA solution, consisting of 80% OLA (98% purity) and 20% ODE. Using only 98% OLA does not afford spherical particles. Standard Schlenk line techniques were used under an atmosphere of dry nitrogen or under a vacuum of 100-200 mTorr. In a 100 or 250 mL three-necked round-bottom flask with a condenser, a septum, a thermocouple well adapter, and a magnetic stirring bar, 341 mg $\text{CuCl}_2 \cdot 2\text{H}_2\text{O}$ was suspended in 59 mL OLA solution and degassed at room temperature and at 100°C for 30 minutes each under vacuum. Following heating to 200°C for 1 hour, the Cu precursor dissolved to form a bright yellow-green solution, which was cooled to 180°C. Di(*tert*-butyl) disulfide (8 mL) was quickly injected by syringe and the NPs were allowed to grow for 40 minutes. After quenching the reaction vessel in a water bath, the NPs were cleaned by precipitation with ethanol (1:1 v/v) followed by centrifugation at 4400 rpm for 10 minutes. After re-dissolving the precipitate in hexane, this washing procedure was repeated twice using acetone instead of ethanol. Cu_{2-x}S NPs were stored as hexane suspensions in air; when using the NPs for further procedures, a few drops of OLA were added to the suspension to re-solubilize the NPs followed by precipitation with acetone and centrifugation. The precipitate was dried under vacuum in a glove box airlock immediately before transfer to other solutions for further experiments.

Cu_{2-x}S -ZnS heterostructures were synthesized according to our previous procedure.¹⁴ In a 50 mL three-necked round-bottom flask with a condenser, a thermocouple well, a septum, and a magnetic stirring bar, a stock solution of 500 mg

ZnCl₂ and 20 mL OLA solution (originally made entirely from technical grade OLA; we later substituted the mixed solvent above) was prepared by degassing at room temperature and at 100°C for 30 minutes each under vacuum, followed by heating to 180°C for 30 minutes. The stock solution was kept at 100°C under flowing nitrogen for further use. For cation exchange, a 100 mL three-necked round-bottom flask with the same attachments as above was evacuated and refilled with nitrogen. 30 mL of toluene was added which is degassed for a few seconds under vacuum. 9.3 mL of the ZnCl₂-OLA solution was added by syringe, and the mixture was heated to 50°C. 35 mg of dry Cu_{2-x}S NPs were dissolved in 7 mL TOP with sonication, followed by stirring for 3 hours in a glove box. This solution was withdrawn from the glove box in a syringe and injected into the warm toluene/OLA/ZnCl₂ solution. The ZnS caps were allowed to grow over the course of 30 minutes to 3 hours; when the appropriate thickness of ZnS was achieved, the solution was quenched with cold acetone. If the particles are to be purified in air, the separation must be done as quickly as possible to avoid undue etching of the Cu_{2-x}S layer. After centrifugation of this mixture, the precipitate was washed by dissolution in hexane followed by the addition of an equal amount of methanol. After centrifugation, the particles were dissolved again in hexane, stabilized with a drop of OLA, and precipitated with acetone and centrifuged a third time. The finished heterostructures were stored in toluene or hexane and should not be allowed to dry completely.

NP etching

In calculating the amounts of phosphine or CAN to add to solutions of Cu_{2-x}S NPs, the composition of the nanoparticles was initially approximated as Cu₇S₄ (the composition assigned to roxbyite in JCPDS 023-0958). The molar concentration of S in the dry particles is then calculated to be approximately 6.98 μmol/mg.

In a general etching procedure using air, dry particles were suspended at a concentration of 1 mg/mL in toluene, which was mixed with an equal volume of TBP in a glove box (or, in phosphine-limited controlled etching experiments, with a lesser amount in accordance with a certain estimated molar ratio of P to S). With other etching reactions, identical volumes of TOP, dodecanethiol, oleylamine (70%), or oleic acid are used. The vial was withdrawn from the glove box and exposed to air for several minutes, after which it was resealed and the mixture was stirred (in phosphine-limited experiments, the vial is left loosely capped to allow the reaction to run to completion over 6-12 hours). The vial was thereafter opened each time aliquots were withdrawn over the following days or hours. As noted in the main text, the rate at which the particles are etched can vary substantially. The NPs were recovered by centrifuging the mixture directly; when the volume of TBP or TOP was reduced, it was necessary to add excess methanol as an antisolvent. Precipitation was followed by sonicating the precipitate in hexane, centrifuging again, and then re-dissolving the precipitate in hexane with a few drops of OLA and precipitating the NPs with acetone. The recovered product was stored in hexane under air.

In etching with CAN in the glove box, a 0.1 M solution of CAN in methanol previously dehydrated with molecular sieves was prepared immediately before use (it is unstable). Appropriate amounts of this reagent were added to NP-TBP-toluene or NP-TOP-toluene solutions prepared as above. In **Figure 3.A.10**, the Ce:S ratio was calculated on the basis of the composition $\text{Cu}_{1.81}\text{S}$ reported by the most reliable experimental data,⁵² giving an S concentration in the particles of 6.80 $\mu\text{mol}/\text{mg}$. An addition of 17.45 μL CAN solution (1:1 molar ratio of $\text{CAN}/\text{Cu}_7\text{S}_4$) to 2 mL NP-TBP-toluene solution (1 mg NPs) was therefore estimated to have a Ce/S ratio of 0.257, using the composition $\text{Cu}_{1.81}\text{S}$. The mixture was allowed to stir for 1 hour to complete the etching reaction. The particles were recovered by directly centrifuging the

solution, followed by washing with hexane, centrifuging, re-suspending the particles in hexane with a drop of OLA, and precipitating them with acetone. Following centrifugation, the precipitate is stored in hexane under air.

During etching with the addition of other reagents one of the following were also added to the NP-TBP-toluene solution prepared as above: diphenylamine (N:P 1:75 to 1:350), triethylamine (N:P 1:10 to 1:100), or oleylamine (N:S roughly 125:1). Sodium nitrate was added under inert atmosphere as a methanol solution (0.2 M); roughly 3:1 NO_3^- : S dissolved the particles over several hours.

Materials characterization

Transmission electron microscopy (TEM) images were acquired on an FEI Tecnai T12 operating at 120 kV with samples supported on carbon-coated copper grids. High-resolution TEM (HRTEM) images were acquired on an FEI Tecnai F20 operating at 200 kV. X-ray diffraction patterns were acquired on a Bruker GADDS microbeam diffraction instrument using graphite-monochromated Cu K-alpha radiation (40 kV, 40 mA) and a HI-STAR area detector with samples supported on Kapton tape (in transmission mode) or on single-crystal silicon (in reflection mode). The detector position was calibrated using standard polycrystalline alumina or silicon reference materials. Datasqueeze 3.0 software⁷⁵ was used to carry out the calibrations and obtain integrated θ - 2θ plots. Additional XRD data (**Figure 3.A.4**) was acquired on a Bruker D8 DISCOVER instrument with Ni-filtered Cu K-alpha radiation (40 kV, 40 mA) using a polycapillary collimator and a VANTEC 500 area detector. Data analysis of these scans was performed in the attached DIFFRAC.EVA software; spots arising from Laue reflections from the silicon wafer were masked manually. Samples were analyzed under air-free conditions by covering them with Kapton tape before removing them from the glove box.

UV-visible-NIR spectra were acquired on a Shimadzu UV3600 from 300 nm to 3300 nm, using TCE as a solvent with samples in quartz cuvettes. FTIR spectra were obtained in transmission from 4000 to 400 cm^{-1} on a Bruker Tensor II spectrometer which was part of a Hyperion FTIR microscope. A 5 mg/mL solution of Cu_{2-x}S NPs in toluene was mixed with TBP (volume ratio 4:1 solution:TBP), and the etching process was allowed to run to completion over 1 week in air and under the N_2 atmosphere of the glove box; for comparison, a mixture of toluene and TBP in equal volumes was allowed to oxidize in air for 1 week. Residual solids in the case of the NPs “etched” under N_2 were removed by centrifugation. The residual toluene was removed by evaporation under vacuum on the Schlenk line. Samples were then enclosed in a demountable infrared liquid cell using KBr windows (International Crystal Laboratories) and Teflon gaskets and spacers (from 15 to 200 microns) in a glove box.

Electron paramagnetic resonance (EPR) spectra were acquired at room temperature on samples contained in flame-sealed 100 μL soda-lime glass micropipets (Kimble) using a Bruker EMX continuous-wave spectrometer at the X-band. Standard solutions were prepared by dissolving the appropriate amounts of CuCl_2 in methanol (as in **Figure 3.6c**), and samples were prepared by adding to a 10 mg/mL solution of Cu_{2-x}S NPs in toluene an equal amount of TBP and allowing the etching process to run to completion over a week in air and under the N_2 atmosphere of the glove box. If using CAN or NaNO_3 instead, the appropriate amount was added as a 0.1 M (CAN) or 0.2 M (NaNO_3) methanol solution; EPR for these samples was acquired the next day.

3.A.3. Supporting figures

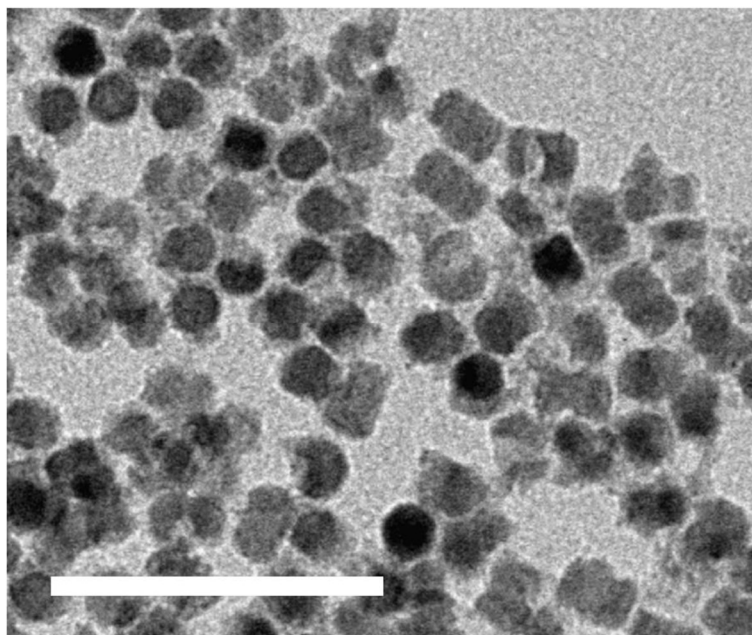


Figure 3.A.1. Exemplary TEM image of etched Cu_{2-x}S-ZnS heterostructures isolated from the cation-exchange reaction. Rather than being immediately precipitated by centrifugation, the mixture of the crude reaction solution with acetone was exposed to air for ~1 h. The heterostructures show distinctly eroded Cu_{2-x}S layers. Scale bar is 100 nm.

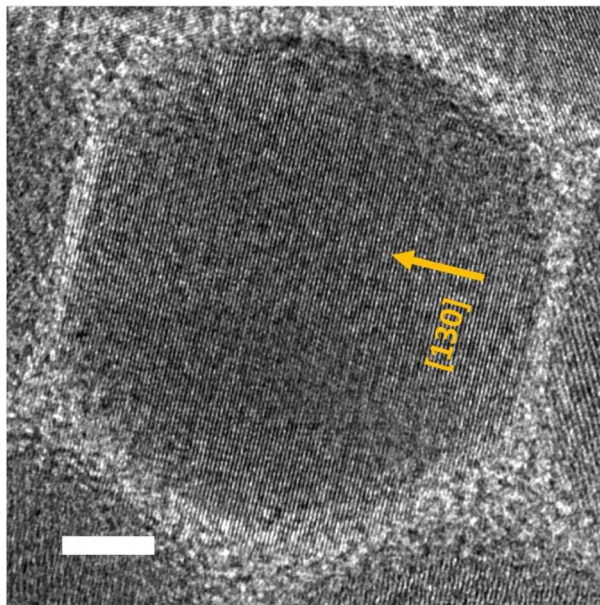


Figure 3.A.2. High-resolution TEM image of initial Cu_{2-x}S nanocrystal. The unbroken lattice fringes clearly indicate the single-crystalline nature of the particles. The lattice spacing corresponds to the (130) reflection of roxbyite. Scale bar is 5 nm.

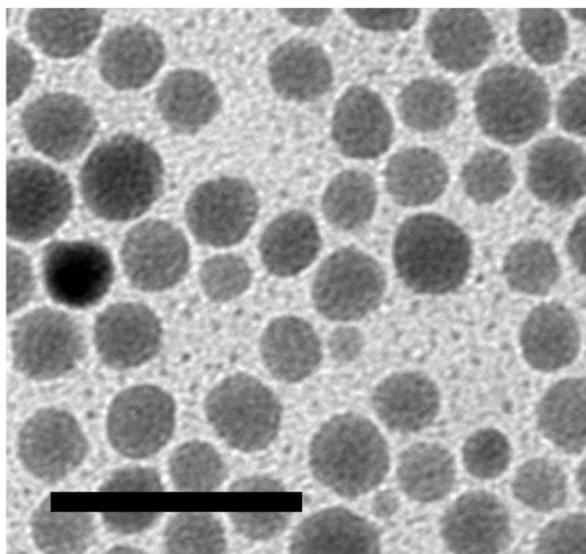


Figure 3.A.3. Closer view of isotropically etched Cu_{2-x}S nanocrystals showing small clusters that are believed to form by aggregation of Cu and S removed from the larger nanocrystals during etching. Scale bar is 50 nm.

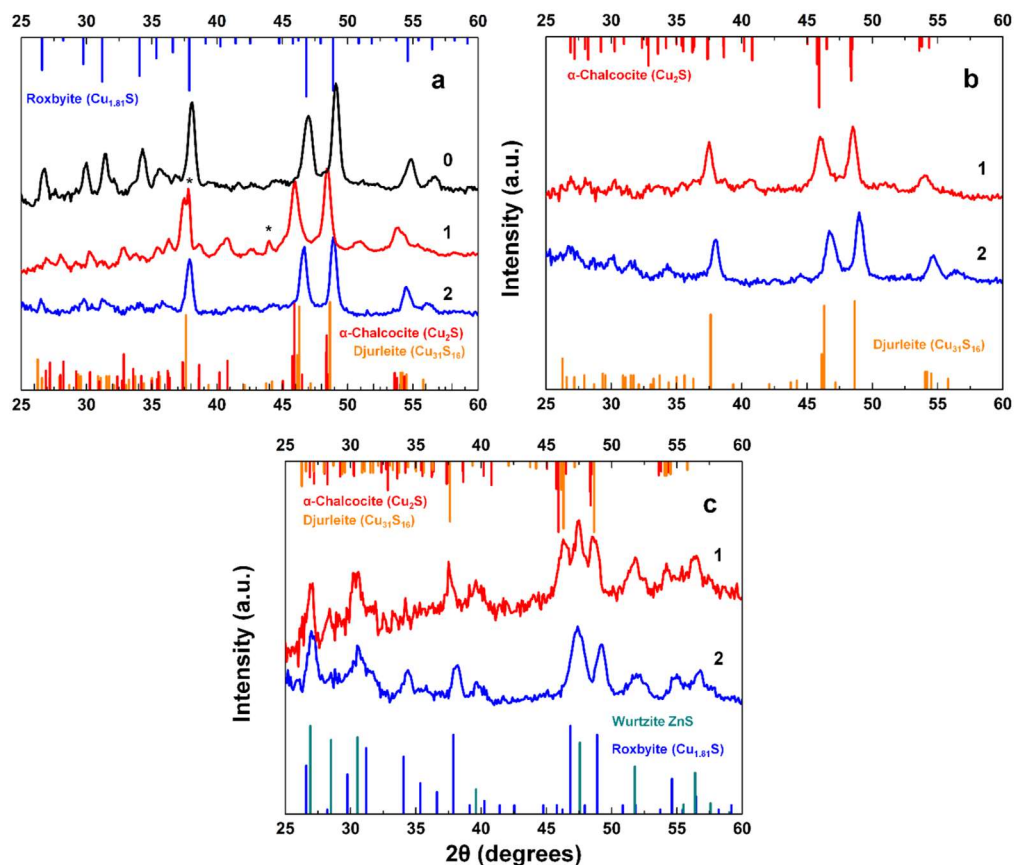


Figure 3.A.4. Effect of atmospheric exposure on the observed phase of Cu_{2-x}S in SC-NPs (a) and H-NPs (b,c). Samples of NPs were reduced using TBP for 30 min under inert atmosphere, and their patterns were acquired after covering sample spots on Si wafers with Kapton tape (curves 1). Afterwards the tape was removed and the samples exposed to air for 1 day before re-acquiring the pattern (curves 2). A pattern from the as-synthesized SC-NPs is also shown (a, curve 0). SC-NPs (a) and H-NPs with small ZnS caps (b) immediately convert to the low chalcocite structure, indicating complete reduction; in H-NPs with large caps (c), this transformation is not complete. The asterisks in (a, curve 1) indicate an impurity introduced during sample preparation that gave rise to sharp diffraction rings but was not observable when the tape was removed.

Roxbyite: JCPDS 023-0958; djurleite: 023-0959; low (α -)chalcocite: 001-3280;
wurtzite ZnS: 036-1450.

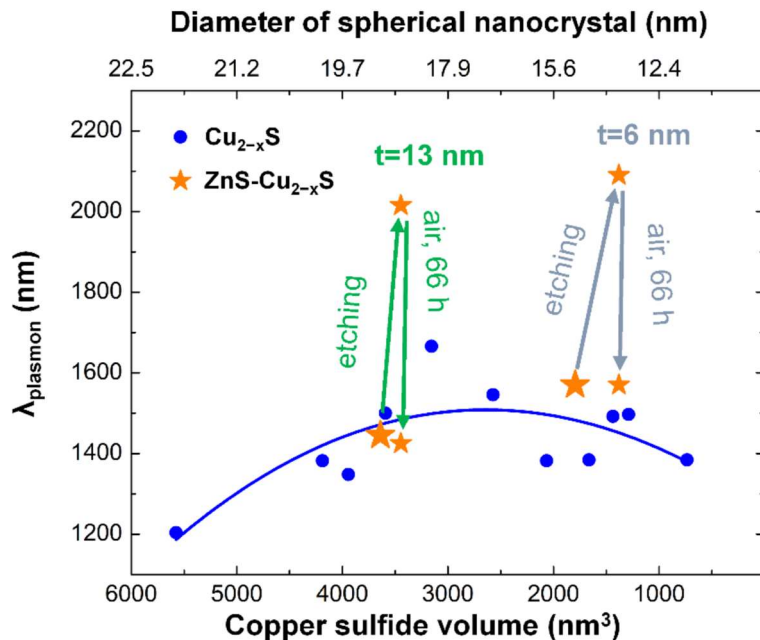


Figure 3.A.5. Summary of the observed LSPR peak positions for nanoparticles in which the volume of the Cu_{2-x}S region was changed by etching (for single crystal Cu_{2-x}S NPs, blue), or by formation of heterostructures with Cu_{2-x}S thickness t (large stars) followed by etching and exposure to air (smaller orange stars). In the case of the latter, the spectra after etching were measured ~ 3 h after etching and ~ 66 h after the first measurement, respectively. Solid line is a guide for the eye.

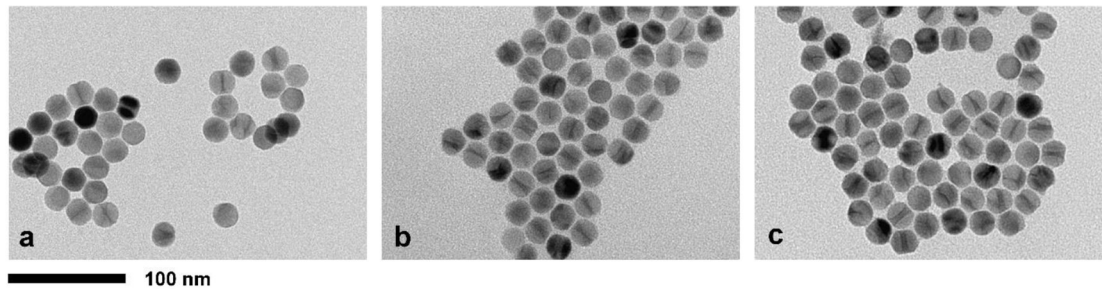


Figure 3.A.6. Preservation of heterostructure morphology in the presence of excess ligands of different types under conditions similar to those used in etching with a reaction time of 60 min: (a) oleic acid, (b) oleylamine, and (c) dodecanethiol. Scale bars are 100 nm.

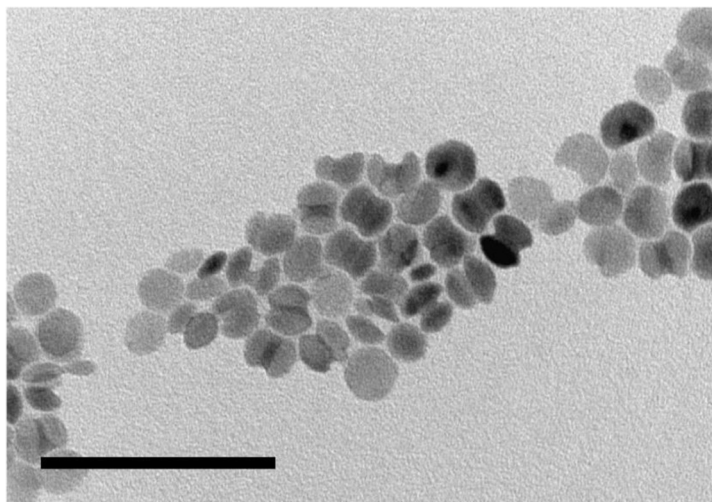


Figure 3.A.7. TEM image of the heterostructured NPs after 1 hour of the etching reaction with TOP. TOP etches copper sulfide much more slowly than TBP. Scale bar is 100 nm.

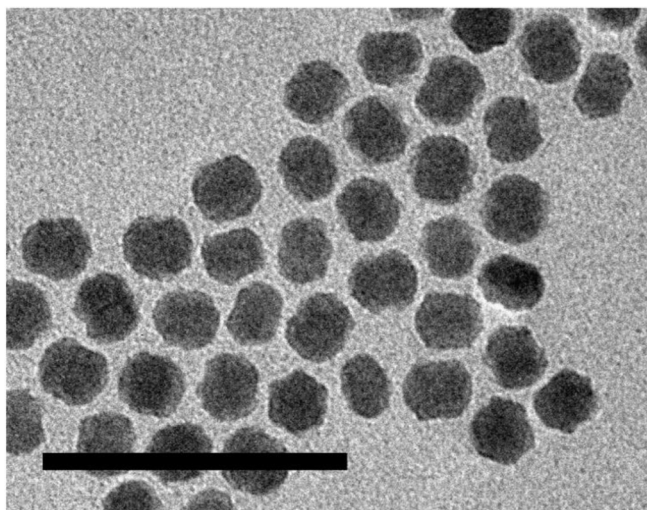


Figure 3.A.8. TEM image of Cu_{2-x}S SC-NPs with faceting/hollowing and slightly reduced diameter due to etching by oleylamine (few mg/mL) in toluene. The NPs had been stored under air for several days after the addition of oleylamine. Scale bar is 100 nm.

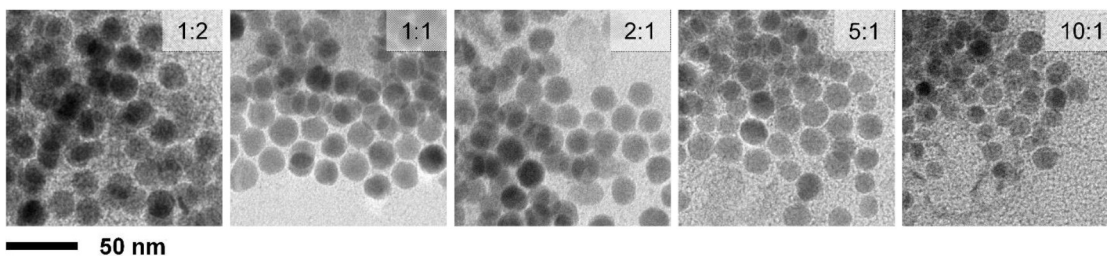


Figure 3.A.9. Purely isotropic etching behavior observed in “cross-over” experiment using ceric ammonium nitrate (CAN); adding smaller amounts of TBP (estimated P:S ratio shown in upper right corners) to solutions of Cu_{2-x}S SC-NPs in toluene followed by addition of CAN (0.1 M in methanol) with an approximate Ce:S ratio of 0.514 produces only spherical, smaller particles.

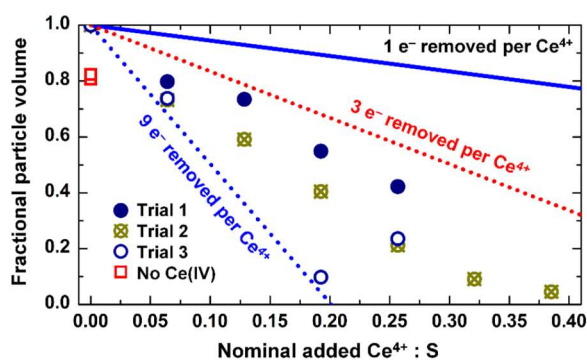


Figure 3.A.10. Titration of particle volume with $(\text{NH}_4)_2\text{Ce}(\text{NO}_3)_6$ (CAN), which may also be used as the oxidizing agent in the etching reaction. The equivalents are calculated on the basis of estimated S concentration in the Cu_{2-x}S powder with an assumed composition of $\text{Cu}_{1.81}\text{S}$. Results are given for three separate trials. The solid line gives the titration curve that would be obtained if one formula unit of CAN removed one electron, as in the reaction $(\text{Cu}^+)_{1.81}\text{S}^{-1.81} + 1.81\text{Ce}^{4+} \rightarrow 1.81\text{Cu}^+ + 1.81\text{S}^0 + 1.81\text{Ce}^{3+}$. Dashed lines indicate the hypothetical titration curves for 3 electrons removed per Ce atom (red) and 9 electrons removed per Ce atom (blue). The experimentally measured points lie between the two dashed curves, indicating that CAN does not operate as a “one-electron” oxidant in this case.

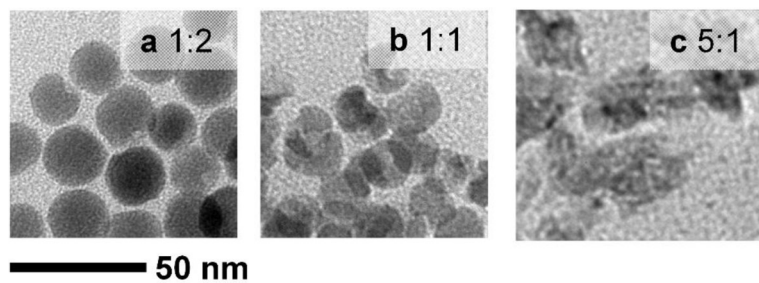


Figure 3.A.11. Anisotropic etching behavior observed by adding smaller amounts of TBP followed by allowing oxidation of the phosphine to run to completion over 8 hours in hexane. At P/S ratio > 5 , no solid product can be recovered when the sample is continuously exposed to air. Pronounced anisotropy of etching is visible for small concentrations of phosphines (a, b); eventually, particle disintegration occurs (c).

Scale bars are 50 nm.

3.B. REFERENCES

1. Yin, Y.; Alivisatos, A. P., Colloidal Nanocrystal Synthesis and the Organic–Inorganic Interface. *Nature* **2004**, 437, 664-670.
2. Anderson, N. C.; Hendricks, M. P.; Choi, J. J.; Owen, J. S., Ligand Exchange and the Stoichiometry of Metal Chalcogenide Nanocrystals: Spectroscopic Observation of Facile Metal-Carboxylate Displacement and Binding. *Journal of the American Chemical Society* **2013**, 135, 18536-18548.
3. Anderson, N. C.; Owen, J. S., Soluble, Chloride-Terminated CdSe Nanocrystals: Ligand Exchange Monitored by ^1H and ^{31}P NMR Spectroscopy. *Chemistry of Materials* **2013**, 25, 69-75.
4. Zhang, H.; Hu, B.; Sun, L.; Hovden, R.; Wise, F. W.; Muller, D. A.; Robinson, R. D., Surfactant Ligand Removal and Rational Fabrication of Inorganically Connected Quantum Dots. *Nano Letters* **2011**, 11, 5356-5361.
5. Nag, A.; Kovalenko, M. V.; Lee, J.-S.; Liu, W.; Spokoyny, B.; Talapin, D. V., Metal-free Inorganic Ligands for Colloidal Nanocrystals: S^{2-} , HS^- , Se^{2-} , HSe^- , Te^{2-} , HTe^- , TeS_3^{2-} , OH^- , and NH_2^- as Surface Ligands. *Journal of the American Chemical Society* **2011**, 133, 10612–10620.
6. Dong, A.; Ye, X.; Chen, J.; Kang, Y.; Gordon, T.; Kikkawa, J. M.; Murray, C. B., A Generalized Ligand-Exchange Strategy Enabling Sequential Surface Functionalization of Colloidal Nanocrystals. *Journal of the American Chemical Society* **2010**, 133, 998–1006.
7. Smith, J. G.; Jain, P. K., The Ligand Shell as an Energy Barrier in Surface Reactions on Transition Metal Nanoparticles. *Journal of the American Chemical Society* **2016**, 138, 6765–6773.

8. Wang, F.; Tang, R.; Buhro, W. E., The Trouble with TOPO; Identification of Adventitious Impurities Beneficial to the Growth of Cadmium Selenide Quantum Dots, Rods, and Wires. *Nano Letters* **2008**, 8, 3521-3524.
9. Talapin, D. V.; Gaponik, N.; Borchert, H.; Rogach, A. L.; Haase, M.; Weller, H., Etching of Colloidal InP Nanocrystals with Fluorides: Photochemical Nature of the Process Resulting in High Photoluminescence Efficiency. *Journal of Physical Chemistry B* **2002**, 106, 12659-12663.
10. Sines, I. T.; Schaak, R. E., Phase-Selective Chemical Extraction of Selenium and Sulfur from Nanoscale Metal Chalcogenides: A General Strategy for Synthesis, Purification, and Phase Targeting. *Journal of the American Chemical Society* **2011**, 133, 1294-1297.
11. Murray, C. B.; Sun, S.; Doyle, H.; Betley, T., Monodisperse 3d Transition-Metal (Co, Ni, Fe) Nanoparticles and Their Assembly into Nanoparticle Superlattices. *MRS Bulletin* **2001**, 26, 985-991.
12. Moreau, L. M.; Ha, D.-H.; Bealing, C. R.; Zhang, H.; Hennig, R. G.; Robinson, R. D., Unintended Phosphorus Doping of Nickel Nanoparticles during Synthesis with TOP: A Discovery through Structural Analysis. *Nano Letters* **2012**, 12, 4530-4539.
13. Zhang, H.; Ha, D.-H.; Hovden, R.; Kourkoutis, L. F.; Robinson, R. D., Controlled Synthesis of Uniform Cobalt Phosphide Hyperbranched Nanocrystals Using Tri-n-octylphosphine Oxide as a Phosphorus Source. *Nano Letters* **2011**, 11, 188-197.
14. Ha, D.-H.; Caldwell, A. H.; Ward, M. J.; Honrao, S.; Mathew, K.; Hovden, R.; Koker, M. K. A.; Muller, D. A.; Hennig, R. G.; Robinson, R. D., Solid-Solid Phase Transformations Induced through Cation Exchange and Strain in 2D Heterostructured Copper Sulfide Nanocrystals. *Nano Letters* **2014**, 14, 7090-7099.

15. Fan, Z.; Lin, L.-C.; Buijs, W.; Vlugt, T. J. H.; Huis, M. A. v., Atomistic Understanding of Cation Exchange in PbS Nanocrystals using Simulations with Pseudoligands. *Nature Communications* **2016**, 7, 11503.
16. Gaponik, N.; Talapin, D. V.; Rogach, A. L.; Eychmüller, A.; Weller, H., Efficient Phase Transfer of Luminescent Thiol-Capped Nanocrystals: From Water to Nonpolar Organic Solvents. *Nano Letters* **2002**, 2, 803-806.
17. Otelaja, O. O.; Ha, D.-H.; Ly, T.; Zhang, H.; Robinson, R. D., Highly Conductive Cu_{2-x}S Nanoparticle Films through Room-Temperature Processing and an Order of Magnitude Enhancement of Conductivity via Electrophoretic Deposition. *ACS Applied Materials and Interfaces* **2014**, 6, 18911–18920.
18. Ocier, C. R.; Whitham, K.; Hanrath, T.; Robinson, R. D., Chalcogenidometallate Clusters as Surface Ligands for PbSe Nanocrystal Field-Effect Transistors. *Journal of Physical Chemistry C* **2014**, 118, 3377-3385.
19. Long, R.; Zhou, S.; Wiley, B. J.; Xiong, Y., Oxidative Etching for Controlled Synthesis of Metal Nanocrystals: Atomic Addition and Subtraction. *Chemical Society Reviews* **2014**, 43, 6288-6310.
20. Stoeva, S.; Klabunde, K. J.; Sorensen, C. M.; Dragieva, I., Gram-Scale Synthesis of Monodisperse Gold Colloids by the Solvated Metal Atom Dispersion Method and Digestive Ripening and Their Organization into Two- and Three-Dimensional Structures. *Journal of the American Chemical Society* **2002**, 124, 2305–2311.
21. Kim, S.; Bawendi, M. G., Oligomeric Ligands for Luminescent and Stable Nanocrystal Quantum Dots. *Journal of the American Chemical Society* **2003**, 125, 14652–14653.

22. Murray, C. B.; Norris, D. J.; Bawendi, M. G., Synthesis and Characterization of Nearly Monodisperse CdE (E = S, Se, Te) Semiconductor Nanocrystallites *Journal of the American Chemical Society* **1993**, 115, 8706-8715.
23. Peng, Z. A.; Peng, X., Formation of High-Quality CdTe, CdSe, and CdS Nanocrystals Using CdO as Precursor. *Journal of the American Chemical Society* **2001**, 123, 183–184.
24. Li, H.; Zanella, M.; Genovese, A.; Povia, M.; Falqui, A.; Giannini, C.; Manna, L., Sequential Cation Exchange in Nanocrystals: Preservation of Crystal Phase and Formation of Metastable Phases. *Nano Letters* **2011**, 11, 4964–4970.
25. Gui, J.; Ji, M.; Liu, J.; Xu, M.; Zhang, J.; Zhu, H., Phosphine-Initiated Cation Exchange for Precisely Tailoring Composition and Properties of Semiconductor Nanostructures: Old Concept, New Applications. *Angewandte Chemie International Edition* **2015**, 127, 3754–3758.
26. Liu, Y.; Zhu, G.; Yang, J.; Bao, C.; Wanga, J.; Yuan, A., Phase Purification of Cu–S System Towards Cu_{1.8}S and Its Catalytic Properties for a Clock Reaction. *RSC Advances* **2015**, 5, 103458-103464.
27. Hines, M. A., IN SEARCH OF PERFECTION: Understanding the Highly Defect-Selective Chemistry of Anisotropic Etching. *Annual Review of Physical Chemistry* **2003**, 54, 29-56.
28. Otelaja, O. O.; Hertzberg, J. B.; Aksit, M.; Robinson, R. D., Design and Operation of a Microfabricated Phonon Spectrometer Utilizing Superconducting Tunnel Junctions as Phonon Transducers. *New Journal of Physics* **2013**, 15, 1-30.
29. Hertzberg, J. B.; Otelaja, O. O.; Yoshida, N. J.; Robinson, R. D., Non-Equilibrium Phonon Generation and Detection in Microstructure Devices *Review of Scientific Instruments* **2011**, 82, 104905.

30. Hertzberg, J. B.; Aksit, M.; Otelaja, O. O.; Stewart, D. A.; Robinson, R. D., Direct Measurements of Surface Scattering in Si Nanosheets Using a Microscale Phonon Spectrometer: Implications for Casimir-Limit Predicted by Ziman Theory. *Nano Letters* **2014**, 14, 403-415.
31. Otelaja, O. O.; Robinson, R. D., Enhancement of Phonon Backscattering due to Confinement of Ballistic Phonon Pathways in Silicon as Studied with a Microfabricated Phonon Spectrometer. *Applied Physics Letters* **2015**, 107, 173102.
32. Higashi, G. S.; Chabal, Y. J.; Trucks, G. W.; Raghavachari, K., Ideal Hydrogen Termination of the Si (111) Surface. *Applied Physics Letters* **1990**, 56, 656.
33. Lim, S. J.; Kim, W.; Jung, S.; Seo, J.; Shin, S. K., Anisotropic Etching of Semiconductor Nanocrystals. *Chemistry of Materials* **2011**, 23, 5029-5036.
34. Zeng, H.; Cai, W.; Liu, P.; Xu, X.; Zhou, H.; Klingshirn, C.; Kalt, H., ZnO-Based Hollow Nanoparticles by Selective Etching: Elimination and Reconstruction of Metal Semiconductor Interface, Improvement of Blue Emission and Photocatalysis. *ACS Nano* **2008**, 2, 1661-1670.
35. Chen, C.; Kang, Y.; Huo, Z.; Zhu, Z.; Huang, W.; Xin, H. L.; Snyder, J. D.; Li, D.; Herron, J. A.; Mavrikakis, M.; Chi, M.; More, K. L.; Li, Y.; Markovic, N. M.; Somorjai, G. A.; Yang, P.; Stamenkovic, V. R., Highly Crystalline Multimetallic Nanoframes with Three-Dimensional Electrocatalytic Surfaces. *Science* **2014**, 343, 1339-1343.
36. Sui, Y.; Fu, W.; Zeng, Y.; Yang, H.; Zhang, Y.; Chen, H.; Li, Y.; Li, M.; Zou, G., Synthesis of Cu₂O Nanoframes and Nanocages by Selective Oxidative Etching at Room Temperature. *Angewandte Chemie International Edition* **2010**, 49, 4282-4285.
37. Xiong, Y.; Wiley, B.; Chen, J.; Li, Z.-Y.; Yin, Y.; Xia, Y., Corrosion-Based Synthesis of Single-Crystal Pd Nanoboxes and Nanocages and Their Surface Plasmon Properties. *Angewandte Chemie International Edition* **2005**, 44, 7913-7917.

38. Han, W.; Yi, L.; Zhao, N.; Tang, A.; Gao, M.; Tang, Z., Synthesis and Shape-Tailoring of Copper Sulfide/Indium Sulfide-Based Nanocrystals. *Journal of the American Chemical Society* **2008**, 130, 13152–13161.
39. Song, W.-S.; Yang, H., Efficient White-Light-Emitting Diodes Fabricated from Highly Fluorescent Copper Indium Sulfide Core/Shell Quantum Dots. *Chemistry of Materials* **2012**, 24, 1961–1967.
40. Trizio, L. D.; Prato, M.; Genovese, A.; Casu, A.; Povia, M.; Simonutti, R.; Alcocer, M. J. P.; D'Andrea, C.; Tassone, F.; Manna, L., Strongly Fluorescent Quaternary Cu–In–Zn–S Nanocrystals Prepared from $\text{Cu}_{1-x}\text{InS}_2$ Nanocrystals by Partial Cation Exchange. *Chemistry of Materials* **2012**, 24, 2400–2406.
41. Perera, S. D.; Zhang, H.; Ding, X.; Nelson, A.; Robinson, R. D., Nanocluster Seed-Mediated Synthesis of CuInS_2 Quantum Dots, Nanodisks, Nanorods, and Doped Zn-CuInGaS₂ Quantum Dots. *Journal of Materials Chemistry C* **2015**, 3, 1044-1055.
42. Kriegel, I.; Jiang, C.; Rodríguez-Fernández, J.; Schaller, R. D.; Talapin, D. V.; Como, E. d.; Feldmann, J., Tuning the Excitonic and Plasmonic Properties of Copper Chalcogenide Nanocrystals. *Journal of the American Chemical Society* **2012**, 134, 1583-1590.
43. Kriegel, I.; Rodríguez-Fernandez, J.; Wisnet, A.; Zhang, H.; Waurisch, C.; Eychmuller, A.; Dubavik, A.; Govorov, A. O.; Feldmann, J., Shedding Light on Vacancy-Doped Copper Chalcogenides: Shape-Controlled Synthesis, Optical Properties, and Modeling of Copper Telluride Nanocrystals with Near-Infrared Plasmon Resonances. *ACS Nano* **2013**, 7, 4367-4377.
44. Hsu, S.-W.; On, K.; Tao, A. R., Localized Surface Plasmon Resonances of Anisotropic Semiconductor Nanocrystals. *Journal of the American Chemical Society* **2011**, 133, 19072–19075.

45. Luther, J. M.; Jain, P. K.; Ewers, T.; Alivisatos, A. P., Localized Surface Plasmon Resonances Arising from Free Carriers in Doped Quantum Dots. *Nature Materials* **2011**, 10, 361-366.
46. Lesnyak, V.; Brescia, R.; Messina, G. C.; Manna, L., Cu Vacancies Boost Cation Exchange Reactions in Copper Selenide Nanocrystals. *Journal of the American Chemical Society* **2015**, 137, 9315–9323.
47. Xie, Y.; Riedinger, A.; Prato, M.; Casu, A.; Genovese, A.; Guardia, P.; Sottini, S.; Sangregorio, C.; Miszta, K.; Ghosh, S.; Pellegrino, T.; Manna, L., Copper Sulfide Nanocrystals with Tunable Composition by Reduction of Covellite Nanocrystals with Cu^+ Ions. *Journal of the American Chemical Society* **2013**, 135, 17630-17637.
48. Rivest, J. B.; Fong, L.-K.; Jain, P. K.; Toney, M. F.; Alivisatos, A. P., Size Dependence of a Temperature-Induced Solid–Solid Phase Transition in Copper(I) Sulfide. *Journal of Physical Chemistry Letters* **2011**, 2, 2402–2406.
49. Zheng, H.; Rivest, J. B.; Miller, T. A.; Sadtler, B.; Lindenberg, A.; Toney, M. F.; Wang, L.-W.; Kisielowski, C.; Alivisatos, A. P., Observation of Transient Structural-Transformation Dynamics in a Cu_2S Nanorod *Science* **2011**, 333, 206-209.
50. Lesnyak, V.; George, C.; Genovese, A.; Prato, M.; Casu, A.; Ayyappan, S.; Scarpellini, A.; Manna, L., Alloyed Copper Chalcogenide Nanoplatelets via Partial Cation Exchange Reactions. *ACS Nano* **2014**, 8, 8407–8418.
51. Regulacio, M. D.; Ye, C.; Lim, S. H.; Bosman, M.; Polavarapu, L.; Koh, W. L.; Zhang, J.; Xu, Q.-H.; Han, M.-Y., One-Pot Synthesis of $\text{Cu}_{1.94}\text{S}$ –CdS and $\text{Cu}_{1.94}\text{S}$ – $\text{Zn}_x\text{Cd}_{1-x}\text{S}$ Nanodisk Heterostructures. *Journal of the American Chemical Society* **2011**, 133, 2052–2055.
52. Mumme, W. G.; Gable, R. W.; Petříček, V., The Crystal Structure of Roxbyite, $\text{Cu}_{58}\text{S}_{32}$. *The Canadian Mineralogist* **2012**, 50, 423-430.

53. Liu, L.; Zhong, H.; Bai, Z.; Zhang, T.; Fu, W.; Shi, L.; Xie, H.; Deng, L.; Zou, B., Controllable Transformation from Rhombohedral $\text{Cu}_{1.8}\text{S}$ Nanocrystals to Hexagonal CuS Clusters: Phase- and Composition-Dependent Plasmonic Properties. *Chemistry of Materials* **2013**, 25, 4828-4834.
54. Prasad, B. L. V.; Stoeva, S. I.; Sorensen, C. M.; Klabunde, K. J., Digestive Ripening of Thiolated Gold Nanoparticles: The Effect of Alkyl Chain Length. *Langmuir* **2002**, 18, 7515–7520.
55. Patrick, R. A. D.; Mosselmanns, J. F. W.; Charnock, J. M.; England, K. E. R.; Helz, G. R.; Garner, C. D.; Vaughan, D. J., The Structure of Amorphous Copper Sulfide Precipitates: An X-Ray Absorption Study. *Geochimica et Cosmochimica Acta* **1997**, 61, 2023-2036.
56. Luther, G. W.; Theberge, S. M.; Rozan, T. F.; Rickard, D.; Rowlands, C. C.; Oldroyd, A., Aqueous Copper Sulfide Clusters as Intermediates during Copper Sulfide Formation. *Environmental Science and Technology* **2002**, 36, 394-402.
57. Pearson, R. G., Hard and Soft Acids and Bases. *Journal of the American Chemical Society* **1963**, 85, 3533-3539.
58. Pearson, R. G.; Songstad, J., Application of the Principle of Hard and Soft Acids and Bases to Organic Chemistry. *Journal of the American Chemical Society* **1967**, 89, 1827–1836.
59. Riha, S. C.; Johnson, D. C.; Prieto, A. L., Cu_2Se Nanoparticles with Tunable Electronic Properties Due to a Controlled Solid-State Phase Transition Driven by Copper Oxidation and Cationic Conduction. *Journal of the American Chemical Society* **2011**, 133, 1383–1390.
60. Machani, T.; Rossi, D. P.; Golden, B. J.; Jones, E. C.; Lotfipour, M.; Plass, K. E., Synthesis of Monoclinic and Tetragonal Chalcocite Nanoparticles by Iron-Induced Stabilization. *Chemistry of Materials* **2011**, 23, 5491–5495.

61. Caldwell, A. H.; Ha, D.-H.; Ding, X.; Robinson, R. D., Analytical Modeling of Localized Surface Plasmon Resonance in Heterostructure Copper Sulfide Nanocrystals. *Journal of Chemical Physics* **2014**, 141, 164125.
62. Zhao, Y.; Pan, H.; Lou, Y.; Qiu, X.; Zhu, J.; Burda, C., Plasmonic Cu_{2-x}S Nanocrystals: Optical and Structural Properties of Copper-Deficient Copper(I) Sulfides. *Journal of the American Chemical Society* **2009**, 131, 4253-4261.
63. Thomson, J. W.; Nagashima, K.; Macdonald, P. M.; Ozin, G. A., From Sulfur–Amine Solutions to Metal Sulfide Nanocrystals: Peering into the Oleylamine–Sulfur Black Box. *Journal of the American Chemical Society* **2011**, 133, 5036-5041.
64. Kurbatov, D.; Kosyak, V.; Opanasyuk, A.; Melnik, V., Native Point Defects in ZnS Films. *Physica B* **2009**, 404, 5002-5005.
65. Socrates, G., *Infrared and Raman Characteristic Group Frequencies*. John Wiley & Sons: New York, 2001.
66. Fullston, D.; Fornasiero, D.; Ralston, J., Zeta Potential Study of the Oxidation of Copper Sulfide Minerals. *Colloids and Surfaces A: Physicochemical and Engineering Aspects* **1999**, 146, 113-121.
67. Freed, J. H.; Bruno, G. V.; Polnaszek, C. F., Electron Spin Resonance Line Shapes and Saturation in the Slow Motional Region. *Journal of Physical Chemistry* **1971**, 75, 3385-3399.
68. Karayannis, N. M.; Mikulski, C. M.; Pytlewski, L. L.; Labes, M., Complexes of Tri-n-Butylphosphine Oxide with Metal Perchlorates. *Inorganic Chemistry* **1970**, 9, 582-587.
69. Buckler, S. A., Autoxidation of Trialkylphosphines. *Journal of the American Chemical Society* **1962**, 84, 3093-3097.

70. Dorfs, D.; Härtling, T.; Miszta, K.; Bigall, N. C.; Kim, M. R.; Genovese, A.; Falqui, A.; Povia, M.; Manna, L., Reversible Tunability of the Near-Infrared Valence Band Plasmon Resonance in Cu_{2-x}Se Nanocrystals. *Journal of the American Chemical Society* **2011**, 133, 11175-11180.
71. Evans, H. T., Djurleite ($\text{Cu}_{1.94}\text{S}$) and Low Chalcocite (Cu_2S): New Crystal Structure Studies. *Science* **1979**, 203, 356-358.
72. Mulvihill, M. J.; Ling, X. Y.; Henzie, J.; Yang, P., Anisotropic Etching of Silver Nanoparticles for Plasmonic Structures Capable of Single-Particle SERS. *Journal of the American Chemical Society* **2010**, 132, 268-274.
73. Zhang, H.; Jin, M.; Xia, Y., Noble-Metal Nanocrystals with Concave Surfaces: Synthesis and Applications. *Angewandte Chemie International Edition* **2012**, 51, 7656-7673.
74. Hua, Q.; Shang, D.; Zhang, W.; Chen, K.; Chang, S.; Ma, Y.; Jiang, Z.; Yang, J.; Huang, W., Morphological Evolution of Cu_2O Nanocrystals in an Acid Solution: Stability of Different Crystal Planes. *Langmuir* **2011**, 27, 665-671.
75. Heiney, P. A., *IUCr Commission on Powder Diffraction Newsletter* **2005**, 32, 9-11.

CHAPTER 4

4 NANOCRYSTAL SYMMETRY BREAKING AND ACCELERATED SOLID-STATE DIFFUSION IN THE LEAD–CADMIUM SULFIDE CATION EXCHANGE SYSTEM *

4.1. ABSTRACT

The phenomenology of solid-state transformations in nanoparticles is important for applications utilizing their reactivity and for investigations into how nearby interfaces interact with the defects responsible for mass transport. We directly interrogate the structure and reaction kinetics of lead sulfide (PbS) nanocrystals undergoing cation exchange in organic solution to cadmium sulfide (CdS) via X-ray diffraction. The epitaxial relationship of zincblende CdS to rocksalt PbS breaks the overall symmetry of the core–shell nanocrystal without requiring the loss of unit cell symmetry, leading to anomalous peak shifts in the diffraction pattern. Conversion occurs in three stages: (1) surface exchange to form a metastable rocksalt CdS shell, (2) crystallization of this shell to zincblende, and (3) diffusive transport of ions through the completed shell. The interdiffusion coefficient, \tilde{D} , for ions diffusing through the shell follows the Arrhenius relationship with an activation energy of 160–180 kJ mol⁻¹, which exceeds that observed in many other experiments in diffusion in nanoparticles and is similar to values measured in bulk solids, suggesting the barrier to exchange is dominated by the energies of point defect formation rather than by surface-bound reactions. However, the magnitude of \tilde{D} is greater by a factor of 10⁴ or

* Reprinted with permission from: Nelson, A.; Honrao, S.; Hennig, R. G., Robinson, R. D., Nanocrystal Symmetry Breaking and Accelerated Solid-State Diffusion in the Lead–Cadmium Sulfide Cation Exchange System. *Chemistry of Materials* **2019**, *31* (3), 991-1005. Copyright 2018 American Chemical Society.

more relative to the self-diffusion coefficients of the slowest component in our system (Cd in CdS). This surprising result suggests that interdiffusion is much faster in nanocrystals. Cation exchange illustrates that the distinction between chemical diffusion in a potential gradient and diffusion at thermodynamic equilibrium has not been fully appreciated. Acceleration of interdiffusion in core–shell nanoparticles due to large chemical potential gradients will be important for understanding nanoscale heterostructure formation and stability.

4.2. INTRODUCTION

The kinetics of solid-state reactions and ionic transport via diffusion at the nanoscale are difficult to quantify, owing to the paucity of suitable high-resolution techniques for precisely measuring factors such as phase fraction, interface depth, and composition gradients in nanostructures, especially in situ. Such measurements are of great relevance for controlling and predicting the form, function, and stability of nanomaterials. Of concern is whether experiments to determine the dominant defects and their mobilities made in bulk solids may be extrapolated down to length scales (<1–10 nm) relevant for nanostructure growth and modification.¹ A direct demonstration of the solid-state reactivity of nanocrystals (NCs) is seen in the well-researched process of cation exchange, whereby the introduction of a new cation from the solution or vapor phase displaces the existing cations in a compound semiconductor NC.^{2,3} Much research has been conducted on an empirical basis using phase transformations by way of ion diffusion to produce novel nanostructures^{2–6} with desirable features such as enhanced luminescence,⁷ metastable phases,⁵ controlled dopant concentrations,⁸ and well-ordered epitaxial interfaces.^{4,9}

The diffusion processes that contribute to the formation of these new structures in cation exchange have so far not been systematized. Unresolved factors include the following: which phase in a heterostructure serves as the primary transport layer for incoming ions, what form of defect the ions take, and from which surfaces the defects originate. Some predictions have been made as to how atomic transport behavior in NCs might change.¹⁰ For example, free surfaces have been predicted to substantially affect the energetics of defect formation and motion in NCs.^{11, 12} High-quality kinetic data are necessary to verify these conjectures.

Probes of phase transformation kinetics in cation exchange begin with a NC precursor having a simple structure and a well-established synthetic chemistry in addition to a cation exchange reaction with kinetics slow enough to allow direct interrogation of the structure by powerful, established methods such as X-ray diffraction (XRD). Both of these requirements are met by the exchange of colloidal lead sulfide (PbS) NCs to cadmium sulfide (CdS) via treatment of the NCs with Cd²⁺ salts in organic solution at moderate to high temperatures (100–200 °C). This reaction and its variants have been investigated by numerous groups as a route to improving the luminescence and stability of promising lead chalcogenide materials.¹³⁻¹⁶ Outstanding questions include the possible existence of metastable phases during cation exchange,¹⁷ the contributions of different crystal surfaces,^{18, 19} and the reason for rapid increase in sample polydispersity that accompanies the reaction.²⁰

4.3. RESULTS AND DISCUSSION

In this work, we use in situ XRD to measure the kinetics of phase transformation in the cation exchange reaction $\text{PbS (NC)} + \text{Cd(oleate)}_2 \rightarrow \text{PbS@CdS (core-shell NC)} + \text{Pb(oleate)}_2$. We find that the exchange reaction is resolvable into

three distinct thermally activated transformation stages, which are described in **Figure 4.1**. We attribute these stages to the following processes: (A) an initial adsorption of ions onto the NC surface to form a conformal CdS phase in the rocksalt structure (hereafter rs-CdS), (B) the recrystallization of this phase into the zincblende structure (hereafter zb-CdS), and (C) diffusion-controlled growth of the zb-CdS shell. From the kinetics of the diffusion-controlled stage, we can calculate a value for the activation energy of chemical (inter)diffusion for the rate-limiting species in the zb-CdS shell of around 160–180 kJ mol⁻¹ (1.7–1.8 eV atom⁻¹). This value substantially exceeds previously reported activation energies for cation exchange in nanoparticles^{1, 21, 22} and approaches reported activation energies for point-defect migration in the bulk from high-temperature experiments.²³ However, the interdiffusion coefficients measured here still exceed those of self-diffusion coefficients of Cd in CdS from high-temperature data by 4 or more orders of magnitude.

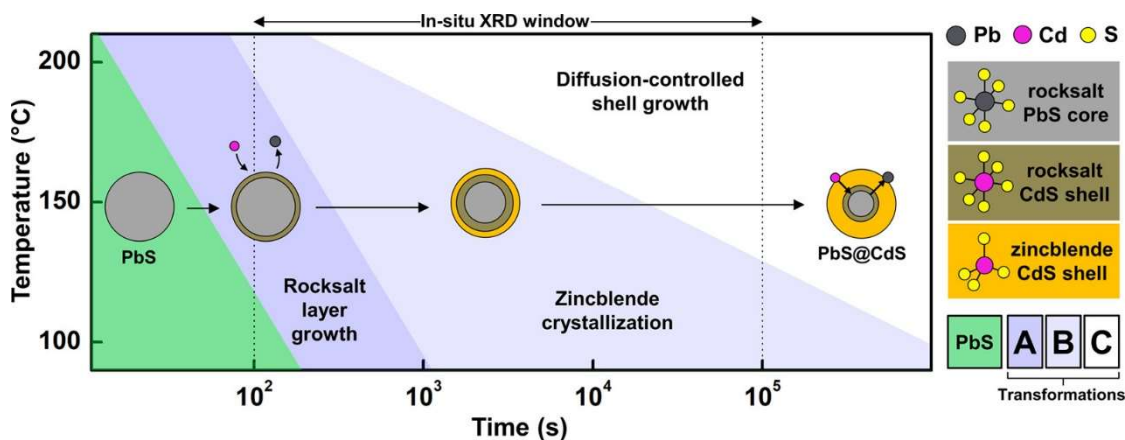


Figure 4.1. Schematic of isothermal transformation regimes observed with in situ XRD during the cation exchange of PbS NCs with Cd²⁺ at 100–200 °C. First, Cd²⁺ rapidly adsorbs to the NCs at all temperatures. A thin shell of rocksalt phase CdS (rs-CdS) then develops, which gradually crystallizes to the zincblende phase (zb-CdS). At

high temperatures, the growth of thicker zb-CdS shells is kinetically accessible. The stages of the reaction (A, B, C) are detailed in the text.

We also find line shifts in the diffraction patterns of epitaxial PbS@CdS core-shell NCs that indicate the breaking of the cubic symmetry of the NC structure. This appearance is deceptive, however, and we explain using kinematical diffraction theory that the commensurate, offset relationship between the Pb (rs) and Cd (zb) sublattices gives rise to a phase factor in the diffracted intensity that results in an apparent peak shift depending on the particular reciprocal lattice vector.²⁴ The interpretation in reciprocal space of complex NC structures that appear to have undergone, for example, tetragonal²⁵ or rhombohedral²⁶ distortions must therefore be done with the knowledge going forward that peak shifts do not necessarily indicate a change in the unit cell symmetry for the constituent phases.

4.3.1. Phase relations by XRD intensity quantification

We characterize the structure of PbS@CdS core-shell NCs via in situ XRD during cation exchange over a range of temperatures (100–200 °C, in increments of 20 or 50°). Monodisperse PbS NCs 7.1 ± 0.4 nm in diameter (**Figure 4.A.1**) were prepared by a previously described procedure²⁷ and treated with a slight excess of Cd²⁺ ions in the form of Cd oleate (molar ratio, Pb/Cd, of about 1:1.2) in hydrocarbon solution. Experimental details are given in section 4.A.2 (**Table 4.A.1**). XRD shows that pure PbS NCs transform into PbS@CdS core-shell NCs with zb-CdS as their majority component as the reaction proceeds. We did not observe any wurtzite CdS peaks. The data are characterized by complex and nonmonotonic changes in the positions, relative intensities, and widths of the three strongest reflections from the initial PbS rock salt phase, namely, the (111), (200), and (220) peaks. An example of

the XRD patterns from a typical measurement (at 200 °C) is shown in **Figure 4.2** at left. Patterns are plotted as a function of the momentum transfer, Q , which incorporates the Bragg scattering angle, θ_B , and the X-ray wavelength, λ

$$Q = \frac{4\pi \sin \theta_B}{\lambda} \quad (4.1)$$

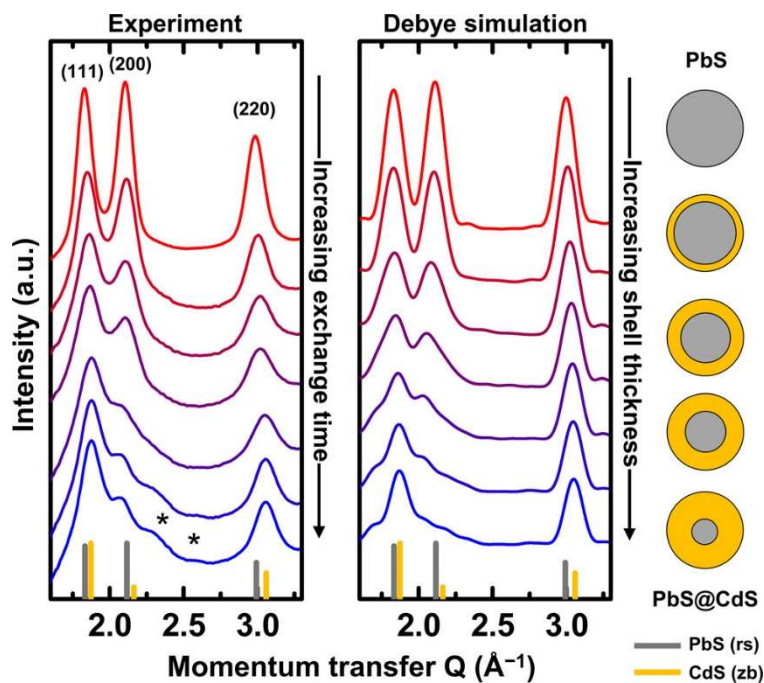


Figure 4.2. X-ray data (left) from the cation exchange of Cd^{2+} with PbS NCs at 200 °C. The intensity of the (200) peak decreases relative to that of (111) during shell growth, consistent with a transformation from PbS (gray vertical lines, JCPDS 01-072-4873) to zb-CdS. The reflection corresponding to the (200) plane shifts to smaller angles and splits, while the (111) and (220) reflections shift to larger angles in accordance with the smaller lattice constant of zb-CdS (yellow vertical lines, JCPDS 01-075-0581). Debye scattering simulations (right) of PbS@CdS core-shell NCs with varying zb-CdS shell thicknesses show that the anomalous peak shifts and splittings arise from diffraction effects dictated by the commensurate relationship between the

two phases. Asterisks mark a possible CdO degradation product. Diagram colors (far right) are as in **Figure 4.1**.

The relative intensities of the strongest diffraction peaks can be used as a proxy for the total extent of the phase conversion.^{28, 29} Here, the amplitudes of (111) and (200), I_{111} and I_{200} , respectively, can be used to track the contributions from the PbS and CdS. In as-synthesized PbS NCs, I_{111} and I_{200} are nearly equal, with I_{111}/I_{200} being about 0.96–0.98, within the margin of error of the bulk value of 0.96 (JCPDS 01-072-4873) (**Figures 4.3** and **4.A.2**). Changes in I_{111}/I_{200} following addition of Cd^{2+} are strongly temperature-dependent. At low temperatures, I_{111}/I_{200} initially decreases to approximately 0.92–0.93, and afterward, the ratio slowly and monotonically increases, remaining below 1.1 at 120° and 1.5 at 150 °C, even after 12 or more hours of exchange. At high temperatures (180–200 °C), however, cation exchange is much faster, and the initial decrease in I_{111}/I_{200} is not seen. The minimum observed in I_{111}/I_{200} for reactions at low temperature occurs at the first data point, less than 60 s after the start of the reaction, so that if a minimum in I_{111}/I_{200} occurs at higher temperatures, the temporal resolution of the experiment is too low to observe it. **Figure 4.A.2** shows that at the lowest temperatures (100 °C), I_{111}/I_{200} remains at a low value (0.9) without beginning to increase again, indicating that the thermal energy is insufficient to effect further growth of the shell. At high temperatures, I_{111}/I_{200} increases rapidly and monotonically, reaching a limiting value of 3.5–4 after ~4 h at 180 °C and less than 1 h at 200 °C. The nominal end product of the cation exchange reaction, zb-CdS, has an I_{111}/I_{200} of about 4.6 (JCPDS 01-075-0581, horizontal line at top of **Figure 4.3**). Our experimentally found smaller value (3.5–4) may be due to a decrease in the reaction driving force as the free Cd concentration becomes small. A continuous transformation from PbS to zb-CdS would cause I_{111}/I_{200} to increase

slightly nonlinearly but monotonically (i.e., without an initial decrease).^{28, 29} Thus, at low temperatures, our observed trends for I_{111}/I_{200} are not in accordance with a simple linear combination of PbS and zb-CdS. However, these trends become explicable after considering previously hypothesized metastable phases during cation exchange. The high-pressure rs phase of CdS (rs-CdS), with a lower I_{111}/I_{200} of about 0.6 (JCPDS 01-071-4151, horizontal line at bottom of **Figure 4.3**), has been proposed as an intermediate phase.^{17, 30} Our experimental results suggest that at low temperatures and/or small degrees of cation exchange, Cd is indeed introduced to the NCs as rs-CdS and causes an initial decrease in I_{111}/I_{200} . Because I_{111}/I_{200} increases at longer times, however, the final CdS phase formed must be zb.

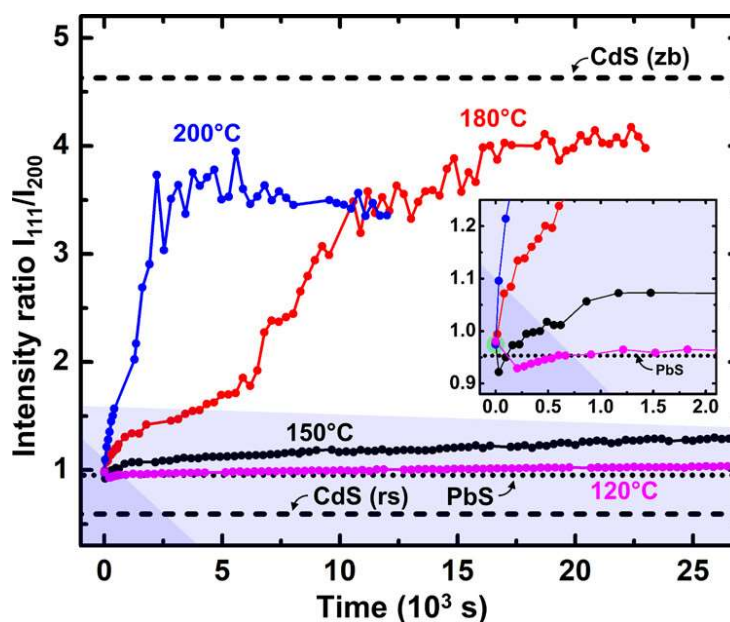


Figure 4.3. Intensity ratio I_{111}/I_{200} of the first two diffraction peaks (111) and (200) during cation exchange of PbS to CdS. The bulk values for PbS (0.96, rs phase) and CdS (4.6, zb phase, top, and 0.6, rs phase, bottom) are indicated by the dashed lines. At low temperatures and short exchange times, a drop in the intensity ratio occurs (inset), consistent with a PbS-to-rs-CdS transformation, but the direction of I_{111}/I_{200}

soon reverses, indicating the remainder of the CdS forms in the zb phase. The stages of the reaction (as in **Figure 4.1**) are indicated.

4.3.2. XRD peak shifts and symmetry breaking

The changes in relative intensities are initially accompanied by shifts of all three reflections to significantly larger momentum transfers Q (**Figures 4.4** and **4.A.3**), showing a decrease in the average lattice parameter, a_0 , of the NCs in accordance with the smaller (by a factor, $\Delta d/d$, of -2.2%) lattice constant of zb-CdS (5.81 \AA) compared to that of PbS (5.94 \AA). This immediate shift of $\Delta Q = 0.015$ to 0.02 \AA^{-1} , or $\Delta d/d = -0.3$ to -0.5% , occurs in the first several minutes of the reaction at all temperatures. Thereafter, the (111) and (220) peaks move more gradually to larger angles, remaining intermediate in the position between the bulk values for the two endmembers (PbS and zb-CdS). Surprisingly, after an initial increase in the diffraction angle, the (200) instead begins to move to smaller angles. This shift to smaller angles is very gradual ($< -0.005 \text{ \AA}^{-1}$, $\Delta d/d = 0.1$ to 0.2% , over 12 h) at low temperature, but at higher temperatures ($180\text{--}200 \text{ }^\circ\text{C}$) the (200) can shift by up to 0.02 \AA^{-1} ($\Delta d/d = -0.9$ to -1.0%) relative to the starting PbS. For phases of cubic symmetry, such as the NC component PbS/zb-CdS phases, the d -spacings assume a relationship to the lattice constant a_0 for the plane with Miller indices (hkl) : $d_{hkl} = a_0 / \sqrt{h^2 + k^2 + l^2}$. Because it is presumed that the deposition of CdS on PbS (and thus the development of any resulting strains) is nearly isotropic during cation exchange, it follows that $\Delta d/d$ should be the same for all peaks and that changes in the lattice parameter in a cubic structure should shift all peaks in the same direction in reciprocal space. This conflicts with our experimental results, so we necessarily conclude that cubic symmetry is lost in the core-shell NCs later in cation exchange. Reports of symmetry breaking in NCs in recent years have straightforwardly attributed this mismatch between peak positions

to a distortion of the unit cell^{25, 26, 31} (e.g., to tetragonal or rhombohedral phases). We will investigate this possibility shortly.

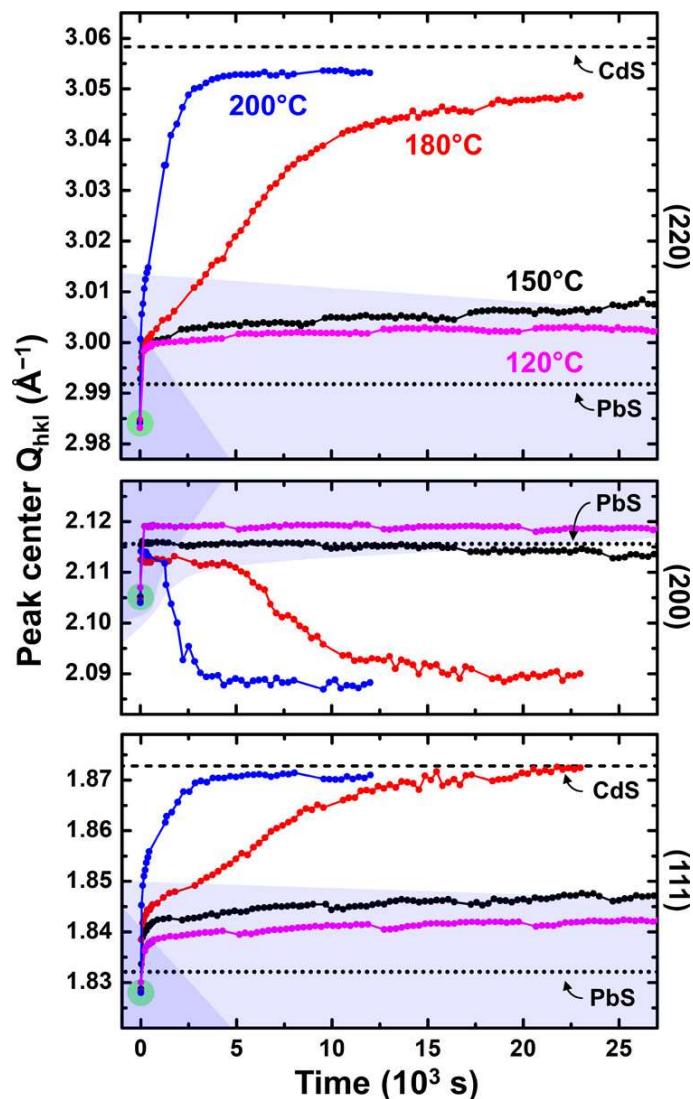


Figure 4.4. Fitted (111), (200), and (220) peak positions from in situ XRD data for the cation exchange of 7 nm PbS NCs to CdS. A continuous shift to larger angles for (111) and (220) indicates a change to interplanar spacings more like those of zb-CdS. The (200) peak briefly follows the same behavior as (111) and (220), but then reverses direction. The broken horizontal lines indicate the estimated line positions for bulk PbS and zb-CdS. Stages in the reaction (as in **Figure 4.1**) are indicated.

Along with the anomalous shift of (200), at long exchange times (hours) for temperatures of 150–200 °C, we observe the appearance of an additional reflection ($Q \approx 2.26$ to 2.38 \AA^{-1}) at angles larger than the (200) peak ($Q \approx 2.08$ to 2.12 \AA^{-1}). This reflection's position is not consistent with a peak from either a wurtzite CdS (JCPDS 01-070-2553) phase or from an isolated, unstrained zb-CdS (200) peak. It is consistent with the (111) reflection at 2.32 \AA^{-1} from a small amount of rs CdO (lattice parameter 4.70 \AA , JCPDS 00-005-0640), but the corresponding CdO (200) reflection, which should occur at 2.67 \AA^{-1} , appears to be very weak or absent in spite of its comparable theoretical intensity to CdO(111) ($I_{111}/I_{200} = 1.14$ for CdO). The appearance of CdO might be caused by thermal degradation of the Cd oleate at higher temperatures³² or by oxidation due to the imperfect sealing of the reactor. To fit these patterns with the additional peak (for temperatures 150–200 °C), we added an additional peak for the contaminant, which greatly improved the quality of the fits for the peak shapes while preserving the trends of the peak shifts and intensities (**Figure 4.A.4**). We confirm below that formation of rs-CdS from cation exchange should result in a monotonic increase of reflection angle for (111), (200), and (220) and that, in the case of zb-CdS, (200) is expected to move to smaller angles. Our experimental data for the peak positions follow the same trends as observed for the relative intensities, indicating the formation of a rs-like CdS phase followed by the gradual growth of the more thermodynamically stable zb phase.

4.3.3. Theoretical predictions: Debye scattering simulations

To quantitate the overall evolution of peak intensities and shifts for the core–shell NCs, we simulate the system by building an atomic model consisting of spherical particles of PbS and hollow spherical shells of zb-CdS having a completely commensurate anionic sublattice. Each phase is assigned its bulk lattice parameter and

is not relaxed for lattice matching at the interface. For 7 nm core–shell particles, the models comprise about 7000 atoms. We then calculate the diffraction patterns at varying degrees of cation exchange by means of the Debye scattering equation from a series of core–shell particles with progressively thicker zb-CdS shells (**Figures 4.2, 4.5a,b, and 4.A.5**). Results from these simulations show that I_{111}/I_{200} should increase monotonically with shell thickness (**Figure 4.A.5**), in agreement with the experimental data at longer times. The experimental limiting value of I_{111}/I_{200} at high temperature is about 3.5, corresponding to a conversion fraction of about 90%. We cross-checked this value of the conversion fraction against the value determined from the calculated dependence of (220) peak position on conversion (**Figure 4.5e**) and found them to be reasonably consistent. Importantly, the patterns also replicate the anomalous movement of the (200) peak to smaller angles (**Figure 4.5d**, filled circles). However, for simulated zb-CdS shells at low conversion fractions, peak parameter trends disagree somewhat with the experiment. Simulated peaks do not move uniformly to larger scattering angles: (111) does not change position and (200) only moves to smaller angles, while (220) moves to larger angles, its position being nearly linearly proportional to the phase fraction. Finally, the theoretical I_{111}/I_{200} does not decrease (**Figure 4.A.5a**). Thus, the simulated diffraction patterns indicate that the zb-CdS phase may not account for the trends in the peak parameters early in the experiments but is consistent with the results at larger conversion fractions.

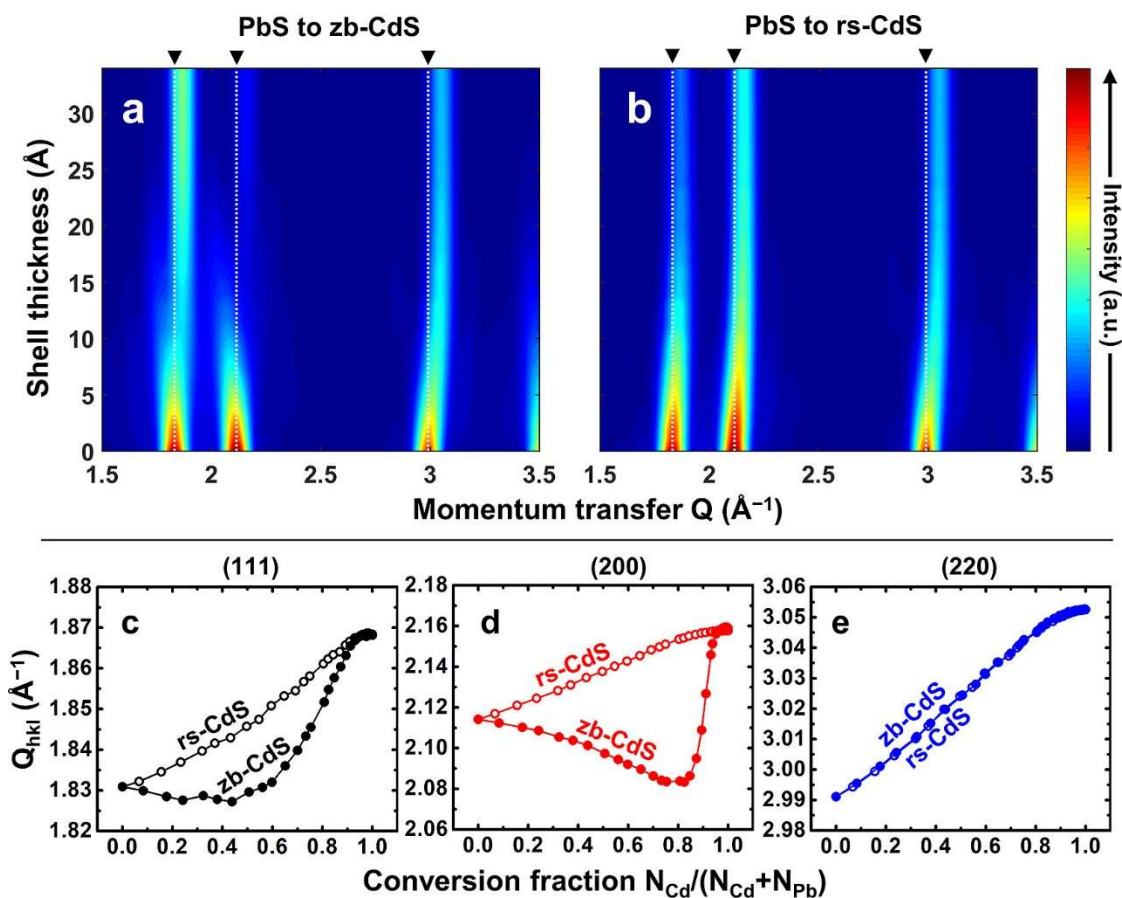


Figure 4.5. (a,b) Debye scattering equation simulations of the diffraction patterns for PbS@CdS core-shell NCs with increasing thickness of the CdS shell. With a zb-CdS shell (a), the peak centers of the (111) and (200) reflections have a complex and nonmonotonic relationship to the total conversion fraction (c,d, filled circles) and are split/broadened. However, when the CdS shell has the rs phase (b), all peaks move smoothly and monotonically to larger angles (c,d, open circles). Black arrows and dashed lines indicate the reference positions for PbS. Regardless of the phase chosen for CdS, (220) follows the same nearly linear relationship between position and phase fraction (e) and remains unsplit (a,b).

To confirm alternative hypotheses^{17, 30} about the phase of the CdS and investigate the deviation in experimentally determined parameters at short exchange

times from those from the Debye simulations, we also calculated the patterns with an rs-CdS shell. We adopted for this structure the same lattice parameter used for zb-CdS. Results from our model find that all peaks should shift smoothly to larger angles (**Figure 4.5c–e**, open circles) and that I_{111}/I_{200} should decrease (**Figure 4.A.5b**). That is, for an rs-CdS shell, the trends in intensities and peak positions are the opposite of those for the zb-CdS case. We found that our experimental data are consistent with a metastable rs-CdS shell during the initial growth of the CdS layer. The experimental magnitude of the initial isotropic shift of the NC lattice parameters to larger angles, compared to that from the simulations, suggests a total conversion fraction of ~10–20% total conversion of the NCs at maximum. This conversion fraction is in reasonable agreement with that derived by comparing our measured change in I_{111}/I_{200} from 0.97 to 0.92 to that from the simulations for an rs-CdS shell. A conversion fraction of 20% of the NC represents a shell thickness of about 0.25 nm, less than one unit cell, for NCs 3.5 nm in radius. It is possible that this thin rs layer persists as an interlayer between PbS and zb CdS as the cation exchange progresses, but the uncertainty in the data makes an interlayer's presence difficult to confirm.

4.3.4. NC disorder and peak width

Details of the NC structure are also reflected in changes in the width of diffraction peaks (**Figures 4.6 and 4.A.6**). In as-synthesized PbS, peak broadening is somewhat greater than expected for a 7 nm NC (effective domain size is ~5 nm). This intrinsic broadening does not change with time or temperature and may arise from an instrumental contribution (**Figure 4.A.7**). Additional broadening occurs immediately following the introduction of CdS (**Figures 4.6 and 4.A.6**), which is not predicted by the Debye simulations for PbS@rs-CdS rs NCs for small degrees of exchange (**Figure 4.A.8**). We therefore suggest that the formation of the initial shell adds high levels of

inhomogeneous strain, especially at the surface. Such strains might be introduced by nonuniform decoration of the surface with CdS domains large enough (>1 monolayer) to require defects to accommodate them. To explain the presence of large enough domains, we note that previous work found that the presence of excess ligand (Pb oleate) remodeled the surface of PbSe NCs, even at room temperature, by altering the relative proportions of each facet.³³ This effect requires the redistribution of a significant fraction of the cations around the NC if the anion number is to be conserved. As a result, it is possible that incoming Cd could take the place of Pb during faceting, which could redistribute the particle mass rapidly enough to form the required CdS domains. Alloying of PbS and CdS³⁰ may also be possible through this mechanism, thereby introducing strain via a $\text{Pb}_{1-x}\text{Cd}_x\text{S}$ shell with a lattice constant smaller than that of PbS. For the high degree of exchange (10–20%) in the first step of the reaction to occur, Cd must have considerable solubility in PbS NC surfaces, in contrast to the nearly negligible measured low-temperature solubility in bulk (Pb,Cd)S.³⁴ Increased miscibility of bulk-insoluble components has been previously observed in nanomaterials.³⁵⁻³⁷ However, for PbS@CdS observed here, the small experimentally determined decrease in I_{111}/I_{200} at very short exchange times at low temperature is more consistent with a very thin (<0.25 nm) surface alloy layer, so an increase in “bulk” miscibility is not clearly demonstrated.

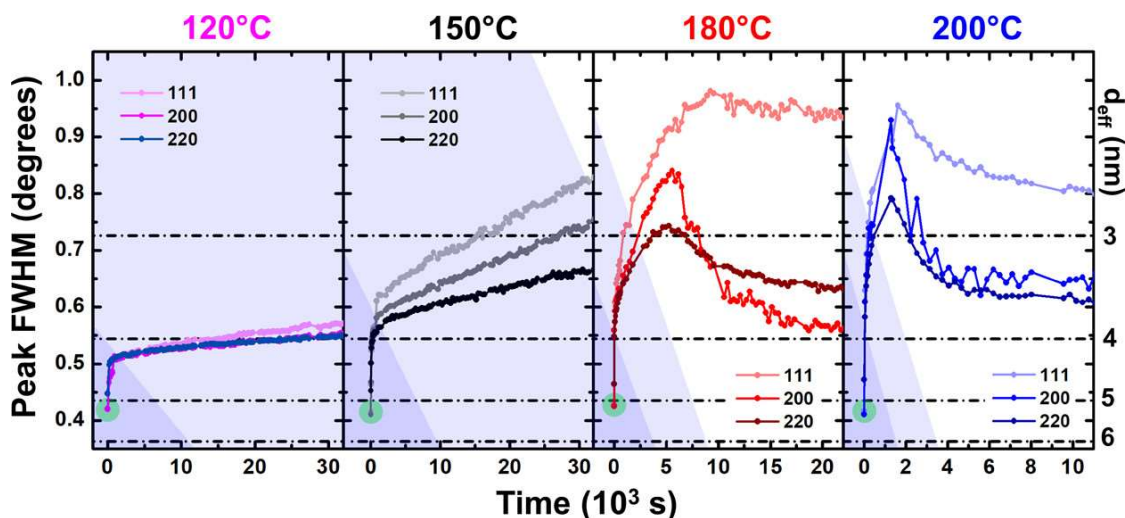


Figure 4.6. Extracted peak widths for the cation exchange runs from **Figure 4.3** for (111) (light-), (200) (medium-), and (220) (dark-colored) reflections. Broken horizontal lines give the peak widths estimated from the Scherrer equation ($K = 1$, $\cos \theta_B \approx 1$) for crystalline domains of various diameters d_{eff} (at right). Because of broadening from the thickness of the sample and mismatch between PbS and CdS, the peak widths are larger than expected for particles of 7 nm diameter. Stages in the reaction (as in **Figure 4.1**) are indicated.

Not only do the Debye scattering simulations for PbS@zb-CdS (**Figure 4.5**) replicate the shift of the (200) reflection to smaller angles in opposition to the movement of (111) and (220), they also show new weak peaks appearing at the tails of (111) and (200), causing them to appear substantially broader (**Figure 4.A.8**). These features do not appear in simulated patterns for rs-CdS shells. We find in the experiment that the widths of (111) and (200) are indeed greater than the width for (220) throughout cation exchange (**Figure 4.6**). A possible exception is seen for the case of 180 °C at longer exchange times, but as overlap between (111) and (200) is substantial, errors are expected in estimating individual peak widths and their average width is still substantially greater than that of (220).

4.3.5. Density functional theory calculations of phase stability

To investigate the stability of the rs-CdS layer, we performed density functional theory (DFT) calculations to determine the relative formation energies of PbS–zb-CdS, PbS–rs-CdS, and PbS–rs-CdS–zb-CdS interfaces. Details on these calculations are provided in section 4.A.3 (Tables 4.A.2–4). PbS(100) slabs were layered with 0 to 4 monolayers of rs-CdS followed by 0 to 2 monolayers of zb-CdS (Figure 4.A.9a). The relaxed surface energies for these interfaces showed that for the first monolayer of CdS on PbS, the rs phase was indeed favored, having an interface energy of $69 \text{ meV } \text{\AA}^{-2}$ versus $86 \text{ meV } \text{\AA}^{-2}$ for the zb phase. This trend continued for bilayers of CdS (89 vs $134 \text{ meV } \text{\AA}^{-2}$ for rs vs zb, respectively). Although the energy difference was less pronounced, a configuration with one rs and two zb CdS monolayers had a higher energy than one with two of rs and one of zb (161 vs $154 \text{ meV } \text{\AA}^{-2}$). In terms of energy per monolayer, a surface with only rs layers had the lowest energy at least up to thickness of 1 nm (Figure 4.A.9b). Our experimental results constrain the rs-CdS layer to be much thinner, but other work has conjectured that rs-CdS could be destabilized by the surface curvature.¹⁷ This would explain the greater stability of thicker rs-CdS epilayers in simulation, where, for reasons of computational expense, we used flat surfaces in one orientation. In general, however, the DFT calculations support the hypothesis that an rs-CdS layer could persist on the PbS surface in the absence of the high pressure normally required to stabilize bulk rs-CdS. Interestingly, in a similar system (PbTe–CdTe), an rs-CdTe interface has not been observed despite a much lower mismatch between PbTe and zb CdTe.³⁸ The stabilization of rs-CdS in the PbS–CdS system, despite (or owing to) pronounced lattice mismatch, could provide insight into band engineering^{39, 40} for devices using core–shell NCs because Cd chalcogenides are indirect narrow-gap semiconductors in the rs phase but have a much larger, direct gap in the zb phase.^{41, 42}

4.3.6. Origins of apparent symmetry breaking: kinematical diffraction theory

The anomalous shifts and peak broadening indicate that a linear combination of the patterns of the two isolated components cannot model the diffraction pattern because of a nonrandom relationship between the PbS and CdS lattices. Contributions to the diffracted intensity from core and shell cation pairs (i.e., Pb–Cd pairs) do not reflect either the r_s or z_b symmetries and result in changes in the position and intensities of certain peaks. If there were a random relationship of PbS and CdS domains (no epitaxy), the scattered intensities from PbS and CdS would again be linearly independent, and Bragg reflections would shift monotonically regardless of whether CdS adopted the r_s or z_b phase. These modeling results illustrate dramatically that cross-interactions between separate components of commensurate heterostructures can have a significant impact on the structure inferred from a less sophisticated structural analysis.

Fundamentally, the “unusual” diffraction behaviors can be understood to arise from a net translation of one sublattice (Cd) relative to another (Pb). Specifically, in the z_b phase, the cations, adopting tetrahedral coordination, are translated relative to the octahedrally coordinated r_s positions in the unit cell along the $\langle 111 \rangle$ direction. Previous work in electron microscopy has shown that such displacements between otherwise isostructural diffracting domains, as observed in stacking faults and antiphase boundaries, can lead to splitting of diffraction peaks when the overall size of the diffracting region is small (i.e., most atoms are near the interface).²⁴ The requirement for splitting of peaks is determined by the criterion $\mathbf{r}_{hkl} \cdot \mathbf{R}$, where \mathbf{r}_{hkl} is the reciprocal lattice vector and \mathbf{R} is the translation vector for a sublattice (**Figure 4.A.10**). If $\mathbf{r}_{hkl} \cdot \mathbf{R}$ is not an integer (i.e., the lattice is translated by a noninteger multiple of the plane spacing in that direction), peak splitting results. For adjacent z_b and r_s cation sublattices sharing a commensurate anion sublattice, $\mathbf{r}_{hkl} \cdot \mathbf{R}$ is $3/4$ for

(111), 1/2 for (200), and 1 for (220), so that splitting is expected for the first two. We clearly observe splitting of both (111) and (200) in the Debye simulations (**Figure 4.2**). However, in the experimental diffraction patterns, the peak splitting is not distinguishable in (111), possibly because of inhomogeneities in the thickness of the CdS layer within (if the core were off-center) or between (if different NCs are converted at different rates) particles, to the presence of significant inhomogeneous strains, or to nonisotropic thermal displacements. The peak at 2.26–2.28 which we previously suggested to be due to CdO may, in fact, result from the splitting of (200), but a definitive assignment remains uncertain.

The contributions to the scattered intensity from commensurate phases in small crystal domains, in which nearly all atoms are close to an interface, are difficult to describe by conventional profile-fitting methods such as Rietveld refinement. These methods assume that the crystal may be described by a single unit cell having translational symmetry in all directions, which is not the case here. As a result, diffraction effects such as peak splitting and anomalous shifts may have been overlooked in previous calculations of nanoparticle scattering patterns. Some studies have attributed anomalous peak shifts in diffraction patterns of cubic materials to a distortion (tetragonal, rhombohedral, etc.) of the unit cell,^{25, 31} while other workers have noted the influence of core–shell formation and the translation of sublattices.^{26, 43} Moreover, the shifts need not be restricted to the cationic sublattice: Bals et al.⁴⁴ show that the cation exchange of PbSe to CdSe leads to the formation of a displaced Se lattice in CdSe relative to the parent PbSe sublattice, as well as stacking faults. Our results show that it may not be necessary to change the space group of a single crystal domain to account for these shifts. Instead, an epitaxial domain where one component has a net displacement relative to a perfect extension of the substrate (as in a stacking fault) creates a particle with overall symmetry lower than either of its constituents’

space groups without a change in the unit cell symmetry of its constituents. Such displacement disorder effects⁴⁵ outside of the bulk crystal diffraction formalism and its corrections (such as the Scherrer equation) have significant implications for studies of epitaxially structured nanoparticles.

4.3.7. Transmission electron microscopy and Raman spectroscopy

The structure of the nanoparticles may be most directly interrogated using electron microscopy. As-synthesized PbS NCs are single-crystalline and lack extended defects in the core such as stacking faults or twin boundaries (**Figure 4.7a**); the high crystallinity leads to sharp and undivided peaks in the Fourier spectrum from images of individual nanoparticles. Following exchange at 150 °C for 11 h, the size and shape of the NCs are unaltered, but their degree of crystallinity changes markedly (**Figure 4.7b**). This manifests as inhomogeneity of the signal intensity across the particle, indicating variations in the alignment of the zone axis to the beam, and the distortion and bending of lattice fringes. In contrast to previous studies on the PbTe–CdTe exchange system,²⁰ where lattice mismatch is less than 0.3%, well-resolved core–shell structures with distinct rs and zb lattices are not observed so far for thin shells in the PbS–CdS system, which has a much larger mismatch of 2.2%. Anisotropic streaking of the peaks in the Fourier spectrum for the exchanged particles shows that the disorder introduced by the shell is nonuniform, lending credence to our conclusions from the Debye simulations that the CdS layer is epitaxially related to the PbS by a translation vector in the Cd sublattice (**Figure 4.A.10**). The vector necessarily points along one axis of the particle, thereby breaking cubic symmetry,²⁶ even if a new crystalline phase is not apparent due to the thinness of the shell.

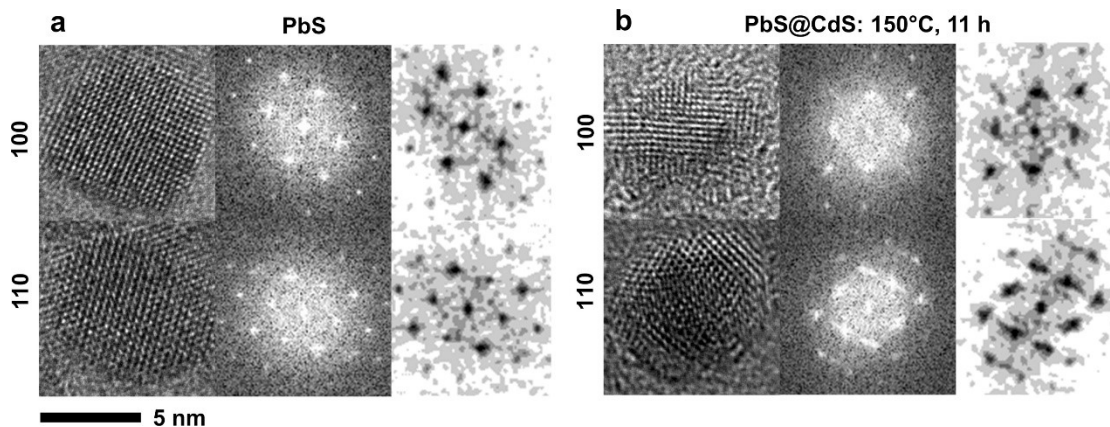


Figure 4.7. High-resolution TEM imaging of PbS and PbS@CdS NCs. Before transformation, PbS NCs (a) are single-crystalline with no strain gradients, grain boundaries, or stacking faults (left), resulting in sharp peaks in their Fourier transform (center). Following exchange, NCs show structural distortion as evidenced by Moiré fringes (b), which are reflected in the FT as streaking and splitting of the peaks due to core–shell lattice mismatch. At right in (a,b), the contrast of the FTs has been exaggerated for clarity; the zone axes are indicated at the left of (a,b).

Raman spectroscopy of PbS and PbS@CdS NCs allows us to definitively identify the CdS phase in thin shells because Raman spectra of materials are highly specific to crystal phase and symmetry. No first-order vibrational modes are expected to be Raman active in bulk PbS (or rs-CdS) owing to symmetry,⁴⁶ but signals from PbS nanoparticles arising from surface modes⁴⁷ or from photodegradation products^{48, 49} have been reported. However, zb-CdS exhibits a clear Raman spectrum with a sharp longitudinal optical (LO) phonon line at about 300 cm^{-1} and its overtones.⁵⁰ Shell thickness in Raman characterization experiments was controlled by the reaction temperature during 1 h of cation exchange.

We observed no Raman spectrum from the initial PbS NCs except for weak signals which could be attributed to Pb–O and SO_4^{2-} vibrations at 140 and 960 cm^{-1} ,

respectively (**Figure 4.A.11**).⁴⁸ Raman spectra of PbS@CdS NCs, however, are more complex (**Figures 4.8** and **4.A.12**) and depend on growth temperature, time of exchange, and laser power. We first consider samples in which the CdS shell was grown at 120 °C. For samples extracted immediately (60 s after start of exchange), for which no chemical change has occurred other than the initial adsorption of Cd oleate, we observe no Raman lines from CdS regardless of laser power (**Figure 4.A.12a**). After 300–3600 s exchange times, following which the NCs become completely coated with Cd and the slow growth of a CdS shell has begun, no lines are detected at low laser powers (**Figure 4.A.12b,c**). However, after increasing the incident power on the same spot tenfold, the zinc blende LO phonon signature abruptly appears (**Figure 4.8**) and persists in the spectrum even if the laser power is reduced again. Evidently, laser heating triggers the irreversible formation of the zb-CdS phase. Laser heating of the core–shell NCs can also be observed from a small shift of 3–5 cm^{-1} in the CdS LO phonon positions to smaller wavenumbers at the highest laser power. Raman spectra thus also point to the existence of a metastable rs-CdS layer crystallizing as zb-CdS at higher temperatures.

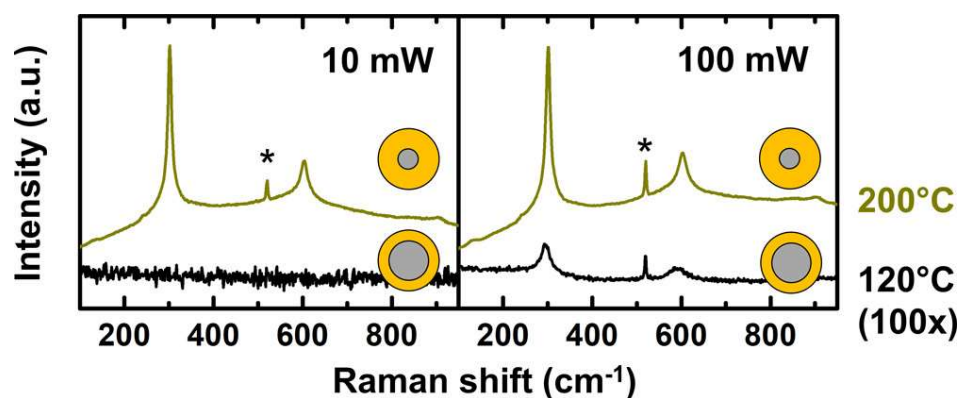


Figure 4.8. Raman spectra of PbS@CdS NCs, where the CdS shell was grown at the indicated temperature for 1 h. zb-CdS is distinguished by the 1LO line at 300 cm^{-1} and its overtones. NCs prepared at 120 °C initially have no Raman signal, but higher laser

powers induce crystallization of the rs shell to zb. After growth at 200 °C, the LO lines are visible even beginning at low laser powers, indicating the crystallization of the shell is thermally activated. The line marked with the asterisk is from the silicon substrate. Argon-ion laser $\lambda_{\text{exc}} = 488$ nm; diagram colors are as in **Figure 4.1**.

The Raman spectra for NCs exchanged at 200 °C reflect the much faster cation exchange. After 60 s of growth, the spectra are similar to those for samples exchanged at 120 °C for long time periods: the LO phonon is absent at first but appears after laser power is increased (**Figure 4.A.12d**). Samples exchanged for longer times (300–3600 s), however, always show a clear LO phonon peak, even when observation begins at laser powers as low as 0.1 mW (**Figure 4.A.12e,f**). On the basis of these observations and the preceding X-ray data, we conclude the initial CdS shell exists in the rs phase, possibly as an alloy phase $\text{Pb}_{1-x}\text{Cd}_x\text{S}$, and that its crystallization to zb-CdS is thermally activated. Shells grown for only 60 s at 200 °C precede any of the XRD data points in **Figure 4.3**, but laser-induced formation of zb-CdS still occurs. Therefore, this rs phase appears to be an intermediate at all growth temperatures, but the time resolution of in situ XRD was insufficient to detect it.

Previous work showed that photoluminescence quantum yield for PbS@CdS core–shell NCs was maximized at a particular shell thickness¹⁴ and proposed that this maximum arose from an rs-CdS to zb-CdS phase transformation, which we observe here.¹⁷ A maximum quantum yield at a specific shell thickness has been seen in other core–shell systems^{51, 52} and been attributed to the formation of defects due to accumulation of strain energy.^{53, 54} Owing to the difficulties of incorporating optical observation during the XRD experiment, parallel optical data cannot be given at present, but our XRD results confirm that metastable surface (and possibly interfacial) phases can be observed directly.

4.3.8. Kinetics: stages of cation exchange

By tracking the XRD peak intensities, positions, and widths for the rs- and zb-like (111), (200), and (220) reflections for reactions at several temperatures, we find three stages for the exchange (**Figures 4.1, 4.3, 4.4, and 4.6**, with 7.1 nm PbS NCs used as the model system), to which we assign the names A, B, and C. At all temperatures, there is an initial decrease in unit cell size and increase of peak width which is close to the time resolution of the experiment (much of the change occurs between the zero timepoint and the first data point). This large and isotropic change in lattice parameters, stage A, is completed in <300 s and is consistent with an effectively instantaneous introduction of an rs-CdS layer or group of domains making up about 20% of the NC, which decreases I_{111}/I_{200} . The increase in peak broadening in stage A (**Figure 4.6**) also suggests the introduction of significant inhomogeneous strain.

In the subsequent stage B ($t > 300$ s), at low temperatures (120 and 150 °C), peak positions and widths change much more slowly than in stage A, giving the kinetic curves an overall L-shape. I_{111}/I_{200} begins to increase again, while the positions of the peaks are nearly constant ((200) moves very slightly to smaller angles), indicating that stage B is primarily a recrystallization of the rs-CdS surface to zb-CdS because of the accumulation of strain energy.⁵³ As all peaks are still seen to shift (**Figure 4.5e** would lead us to believe that the (220) position is essentially independent of CdS phase), during stage B shell growth still continues, although more slowly.

At higher temperatures, stage C becomes thermally activated and comes to dominate the exchange, making the contribution of stage B difficult to discern. The onset of stage C is marked by an inflection in the shape of the curve (e.g., 180 °C curve in **Figure 4.4**). Such inflections were observed during kinetic experiments on ion exchange in NCs by other workers and were also attributed to changes in transport processes.⁵⁵ During stage C ($t > 300$ s at high temperatures), the zb-CdS phase grows

more rapidly and the conversion is able to run nearly to completion, so that at 200 °C, the (111) and (220) positions approach those of the pure zb-CdS phase after less than 1 h. The value of I_{111}/I_{200} and the position of (220) at the endpoint of the 200 °C reaction are, from the Debye simulations (**Figure 4.5**), consistent with a conversion fraction of 90%. The onset of stage C also changes the behavior of the peak width, which begins to decrease again (**Figures 4.6 and 4.A.6**). The widths of all peaks reach a maximum at about 1400 s at 200 °C and at 5000 s at 180 °C, which is consistent with overlapping, displaced peaks' having a maximum apparent width when their intensities are comparable. After undercoordinated surface cations are replaced during A and B, new cations must travel through the shell by way of energetically unfavorable defects, so slow ionic transport becomes the rate-limiting step in cation exchange during stage C.⁵⁶

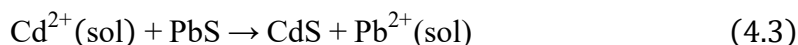
4.3.9. Quantitation of cation exchange kinetics: stages A and B

We now examine in more detail the changes of peak positions in the experimental diffraction patterns. Debye simulations showed that the (220) peak does not split and that its peak center, Q_{220} , has a nearly linear relationship to the conversion fraction (**Figure 4.5e**). Accordingly, we tracked Q_{220} to extract kinetic parameters. Previous studies of cation exchange kinetics with high time resolution by Moser et al.²² used a sum of exponential functions to obtain activation energies based on changes in the band gap E_g of NCs

$$E_g = C + \sum_{i=1}^{1,2,3,\dots} A_i \exp(-k_i t) \quad (4.2)$$

Here, C is some constant and A_i and k_i are the amplitude and rate constant of the i th process, respectively. **Equation 4.2** is intuitively useful because it describes a

sequence of pseudo-first-order reactions, such as the simple metathesis reaction where the concentrations of Cd and Pb in solution are very large and nearly zero, respectively



However, in fitting Q_{220} , we did not find our data to be well-described by a sum of two exponentials. Specifically, the large scatter of the derived rate constants k (especially at high temperatures) makes any derived activation energies meaningless (**Table 4.A.5, Figure 4.A.13a**). Furthermore, for the pseudo-first-order approximation (single exponential fit) to apply to our experiments across a given time scale, a large excess of Cd in solution would be required. This condition could not be met here because a high concentration of PbS NCs was needed for a strong XRD signal (see section 4.A.2). To account for the changing concentration of Cd, we tried fitting Q_{220} to a second-order rate law (**Table 4.A.6**) but also found this to be inadequate, even at low temperatures where stage C would not be operating (**Figure 4.A.13b**).

However, **Figures 4.4 and 4.A.3** suggest a rapid approach to a “limiting” value of Q_{220} at very short exchange times, namely, during stage A. We therefore avoided contributions from successive processes by fitting Q_{220} at very short times (up to about 1000 s, **Figure 4.9a**) to a single exponential function. Because stage A represents a maximum exchange fraction of about 20%, the concentration of Cd in solution does not change much over this interval. We obtained a reasonably straight Arrhenius plot (**Figure 4.9b, Tables 4.A.7-8**) corresponding to an activation energy, E_a , of 41 kJ mol⁻¹. This E_a is similar to those reported for surface exchange or adsorption of ions on NCs (42²² to 74⁵⁷ kJ mol⁻¹). Previous calculations of some ionic^{58, 59} and molecular⁶⁰ binding energies on ionic surfaces have also returned a similar E_a . Some experimental measurements of ion adsorption E_a on solids from solution have found lower values,⁶¹⁻⁶³ although they are inconsistent in the underlying process to which they attribute E_a (diffusion in solution, physisorption, or chemisorption). Bothe et al.

examined cation diffusion during exchange in the PbSe–CdSe system and found an E_a of 30–50 kJ mol⁻¹.¹ On the basis of this E_a , they concluded that the transformation proceeded through the diffusion of interstitial cations coupled with a kick-out mechanism, as other processes would require enthalpically unfavorable ($E_a > 100$ kJ mol⁻¹) vacancy generation within the nanoparticle. However, our results show that exchange up to degrees of 20% conversion for particles of this size can initially occur very rapidly because of replacement of the first few monolayers (0.25 nm) of undercoordinated atoms at the surface, which constitute a significant fraction of the atoms in the NC. Attributing this first step of exchange to a true diffusion process could lead to a misleadingly low activation energy. Additionally, Bothe et al. relied on elemental analysis rather than direct structural measures to gauge the progress of exchange, and weakly adsorbed ions or retained Cd precursor could thus contribute to the apparent degree of exchange. On the basis of our E_a , then, we conclude the kinetics of stage A describes surface-limited exchange at undercoordinated sites.

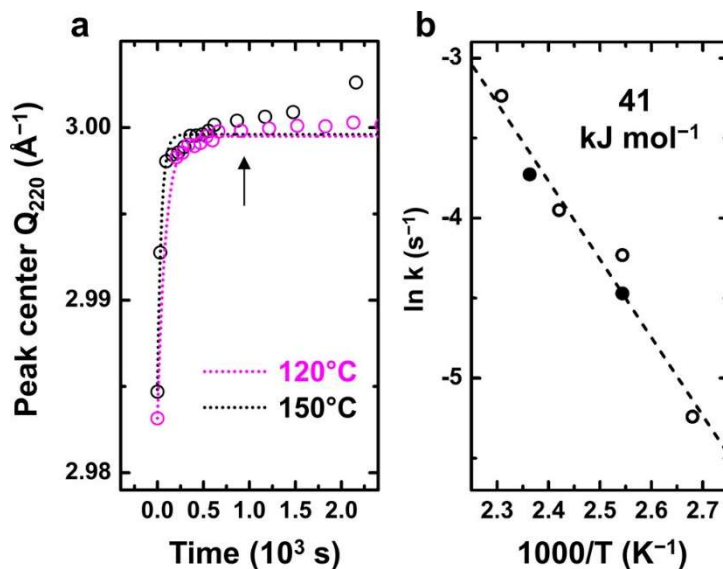


Figure 4.9. (a) Typical single-exponential fits of the evolution of the (220) peak position for cation exchange at 120 and 150 °C (from **Figure 4.4**) at very short times (~ 1000 s, cut-off range indicated by the arrow). An initial rapid shift of Q_{220} occurs (stage A) during the initial formation of the rs-CdS shell. Q_{220} continues to shift much more slowly (stages B and C) as zb-CdS is formed. (b) Arrhenius plot of rate constants extracted from (220) data at temperatures 100–160 °C. The activation energy is indicated. Data are from two separate experiments: **Figure 4.4** (closed points) and **Figure 4.A.3** (open points).

4.3.10. Quantitation of cation exchange kinetics: stage C

To quantify diffusive transport in our system (stage C), we make the key assumption in stage C that the shell is conformal to the core and relatively uniform,^{15, 16} implying that the relevant transport (diffusion) coefficients, D , for the growth of the shell reflect the diffusivities of the incoming and outgoing components (Cd or Pb, respectively) in the CdS shell. Because the value of D in this experiment should account for the diffusion of both Cd and Pb, we note that our experiment properly

measures the interdiffusion coefficient, \tilde{D} . Fick's second law describes the concentration change throughout the NC

$$\frac{\partial c}{\partial t} = \tilde{D} \frac{\partial^2 c}{\partial \xi^2} \quad (4.4)$$

where c is the concentration of solute, ξ is the spatial coordinate, and t is time. For one-dimensional diffusion, the characteristic time scale for the chemical transformation of a region with length scale l in one dimension follows a parabolic growth law with time

$$l = \sqrt{4\tilde{D}t} \quad (4.5)$$

Figure 4.4 shows that the experimental conversion curves do not, in general, have a parabolic dependence on time owing to the spherical geometry and finite size of the NCs and, more significantly, to convolution with processes A and B. Nevertheless, we can use Fick's law to place our data in the context of previous work on diffusion in nanoparticles. We observe that the driving force for cation exchange under our experimental conditions is large enough that, at high temperatures, exchange does not appear significantly slowed by the depletion of Cd in the solution until conversion is nearly complete. Because this high driving force must immediately replace outgoing Pb with Cd, we simplify the problem by assuming that Pb from an initially pure PbS particle is lost by diffusion to a solution having an effective Pb concentration of zero. The time scale of the fraction of exchange completed, X , can be estimated from the analytical solution (an infinite series in n) for diffusion in a spherical particle of radius R ⁶⁴

$$X = 1 - \frac{6}{n} \sum_{n=1}^{\infty} \frac{1}{n^2} \exp\left(-\frac{\tilde{D}n^2\pi^2t}{R^2}\right) \quad (4.6)$$

Here, t is the experimental time at the point of interest, and X can be estimated by interpolating the (220) peak center (Q_{220}) between the bulk values for PbS ($Q_{\text{PbS},220}^0$) and zb-CdS ($Q_{\text{CdS},220}^0$)

$$X = \frac{Q_{\text{CdS},220}^0 - Q_{220}}{Q_{\text{CdS},220}^0 - Q_{\text{PbS},220}^0} \quad (4.7)$$

Evaluation of **Equation 4.6** to $n = 40$ was more than sufficient to reach the limits of numerical precision. The resulting interdiffusion coefficients (**Figure 4.10** and **Table 4.A.9**) range from 10^{-21} to 10^{-17} $\text{cm}^2 \text{s}^{-1}$ at the lowest and highest temperatures used, respectively. For comparison, on the basis of **Equation 4.5**, the interdiffusion coefficient needed for cations to diffuse during exchange to a distance of 3.5 nm in about 5000 s (e.g., **Figure 4.4**, 200 °C) is on the order of 10^{-17} $\text{cm}^2 \text{s}^{-1}$. We also applied a shrinking-core model^{65, 66} to determine the diffusion coefficient of Cd through a spherical shell and found values for \tilde{D} in good agreement with those given by application of Fick's second law (**Figure 4.10a**, **Figure 4.A.14**, and **Table 4.A.10**). Therefore, the derived \tilde{D} is relatively insensitive to the chosen model. More details of the calculations are given in section **4.A.4**.

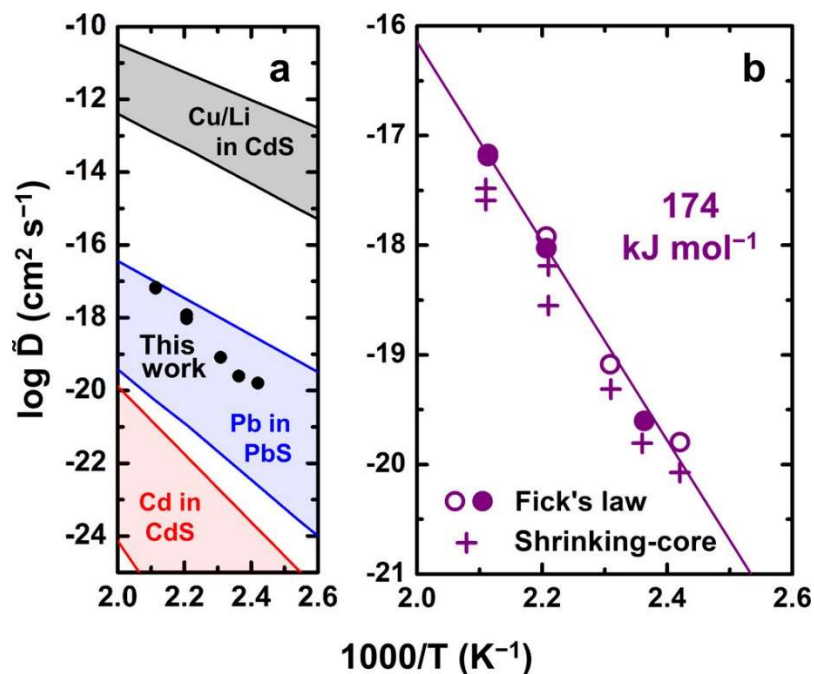


Figure 4.10. Arrhenius plots of interdiffusion coefficients, \tilde{D} , for ionic transport (Pb and Cd diffusion through shell) extracted from (220) data at temperatures above 140 °C and at long exchange times. In (a), points are given on an expanded scale to place the data in context with other measurements of self-diffusion coefficients (see main text). In (b), the points are given on a compact scale; the activation energy is indicated.

Points in (b) indicate \tilde{D} as determined using Fick's second law (open and closed circles) or the shrinking-core model (crosses). Closed circles in (b): from data of **Figure 4.4**; open circles: from data of **Figure 4.A.3**. Reference data are extrapolated from high temperature data described in **Table 4.A.11**.

4.3.11. Mechanism of chemical diffusion: magnitude of \tilde{D}

Interestingly, our estimated interdiffusion coefficients using Fick's law and the shrinking-core model exceed the range of self-diffusion coefficients for Cd in CdS (wurtzite phase) extrapolated from high-temperature data (red area at bottom in **Figure 4.10a**) by four or more orders of magnitude.^{23, 67} Additionally, our interdiffusion coefficients are lower by 4 orders of magnitude than those for fast-

diffusing impurities such as Cu or Li in CdS⁶⁷ (gray area at top in **Figure 4.10a**). Reference data are given in **Table 4.A.11**. Our measurements indicate that the particles are converted much faster than expected for an ideal solution model using bulk values for the component diffusivity of Cd in CdS would suggest. We were not able to find measurements for the diffusivity of Pb in CdS; however, because of the larger size of the Pb²⁺ cation relative to Cd²⁺, we expected that its diffusivity in CdS (rs or zb) would be reduced. DFT calculations to check the activation barriers to diffusion, ΔH_{diff} , for neutral vacancies and interstitials (**Table 4.A.4**) returned values in agreement with our expectations. Values of ΔH_{diff} in PbS and in both rs-CdS and zb-CdS are very similar for Cd and Pb (vacancy-mediated diffusion) or substantially larger for Pb relative to Cd (interstitial-mediated). Our measurements of the diffusion coefficient do fall within a range of values reported for self-diffusion of Pb in PbS⁶⁸ (blue area in **Figure 4.10a**). This surprising observation suggests, counterintuitively, that diffusion through the PbS template might be a rate-limiting process. Experimental evidence presented previously does not appear to rule this out. In Pb chalcogenides, cation exchange is associated with an increase in core polydispersity and displacement of the core from the center of the particle, sometimes to the extent that the “core” continues to form part of the surface.^{19, 20} However, because the PbS@CdS system has not been observed (by us or by others) to form Janus-type structures following addition of Cd²⁺ to PbS,^{17, 19} bulk-like diffusion in PbS appears unlikely to be the main rate-controlling process. If the CdS shell is conformal and uniform, then our results find accelerated diffusion by up to 4 orders of magnitude in \tilde{D} in the CdS shell at short length scales (up to 3.5 nm) relative to expectations from bulk measurements.

The nature of the interdiffusion coefficient \tilde{D} should be clarified. The self-diffusion coefficients in **Figure 4.10a** were obtained under conditions close to thermodynamic equilibrium where no chemical potential gradient exists (i.e., in a

tracer experiment). Cation exchange in NCs clearly does not reflect such a situation. The fluxes of Pb and Cd atoms in this case are coupled such that Cd displaces Pb in a one-to-one ratio, in spite of the fact that their component diffusion coefficients, D_{Cd} and D_{Pb} , are not, in general, expected to be equal. For an ideal solution of the two components in each other where the internal electric fields in the NC do not play a role, \tilde{D} would change with the phase fraction of Cd, X_{Cd} , in the following way⁶⁹

$$\tilde{D} = D_{Pb}X_{Cd} + D_{Cd}X_{Pb} \quad (4.8)$$

Here, $X_{Pb} = 1 - X_{Cd}$. Excess defect generation in the NC might also need to be considered to understand \tilde{D} . A notable example of the consequences of unequal component diffusivities is the nanoscale Kirkendall effect, where unequal diffusivities of anions and cations require the generation of vacancies in the cores of NCs to balance the outgoing cation flux.^{70, 71} Cation exchange in the PbS-to-CdS system does not exhibit such behavior, but other routes exist for coupling of cation fluxes. For example, if Cd diffuses more rapidly than Pb, interdiffusion at a PbS–CdS interface will lead to Cd penetrating further into PbS than Pb in CdS, leading to a net separation of charge at the interface. This gives rise to an electric field that opposes the further separation of charge. To preserve local electroneutrality, \tilde{D} takes a different form⁶⁹

$$\tilde{D} = \frac{D_{Pb}D_{Cd}}{D_{Pb}X_{Pb} + D_{Cd}X_{Cd}} \quad (4.9)$$

Given the small size of the system and the small value of the band gap E_g for PbS, we expect that the number of thermally generated charge carriers would be sufficient to satisfy the electroneutrality condition for any diffusion into PbS. The situation for zb-CdS, which has a larger band gap, is not clear. For both **Equations 4.8** and **4.9**, suppose that D_{Pb} and D_{Cd} in a hypothetical $Pb_{1-x}Cd_xS$ ideal solution take their values for the self-diffusion coefficients given in **Figure 4.10a**, which is reasonable in the limit of dilute impurities in a solid. Then, for $X_{Cd} = 1$ (the assumed case for a zb-

CdS shell containing a negligible amount of Pb), \tilde{D} has the value of D_{Pb} , which is, coincidentally, in agreement with our experimental magnitude of \tilde{D} . Thus, the transport of the minority (slowest) component controls the overall rate of the exchange.

4.3.12. Chemical diffusion in NCs: possible enhancement factors

The different structures for pure PbS and CdS in our NCs and the immiscibility of CdS and PbS in the bulk³⁴ indicate that the PbS–CdS system does not follow ideal solution behavior. Moreover, in nanoscale systems, impurities generally are not isolated (or dilute). The ideal solution interdiffusion coefficient, \tilde{D}_{ideal} , must be modified by a thermodynamic factor^{69, 72} (e.g., for Cd)

$$\tilde{D} = \tilde{D}_{\text{ideal}} \left(1 + \frac{d \ln \gamma_{\text{Cd}}}{d \ln X_{\text{Cd}}} \right) \quad (4.10)$$

γ_{Cd} is the activity coefficient of Cd, where the activity of Cd $a_{\text{Cd}} = \gamma_{\text{Cd}} X_{\text{Cd}}$. A crucial problem in describing diffusion in semiconductors is that component activity depends very strongly on the external conditions owing to deviations in stoichiometry and changes in dopant concentrations (in bulk solids). As a result, the thermodynamic factor can be very large with minuscule changes in composition and, in fact, can greatly exceed our reported factor of 10^4 difference between \tilde{D} and the self-diffusion coefficients D_{Cd} .⁷³ It therefore seems that the large chemical driving force, with the resulting bias in diffusive jumps, could account for the apparently enhanced diffusivity in cation exchange without invoking nanoscale effects such as quantum confinement. However, the distinction between chemical diffusion and self-diffusion is often not made in the nanoparticle literature. A careful description of defect and component activities in nanostructures will be crucial to elucidating true transport coefficients in future work.

We mention some other factors that could contribute to enhanced diffusion in NCs. Chan et al. argued that coupling of point defects to surface vibrations in NCs (breathing modes) could greatly reduce diffusion barriers in small (less than 2 nm in diameter) CdSe NCs.¹² Our PbS@CdS core-shell particles, however, are much larger, and the effect of such vibrations on diffusion barriers well below the surface of the NC is likely to be minimal. The contribution of strain at the PbS-CdS interface to observed mixing could also be significant because strain accommodation has been observed in many systems to take place through a degree of interface alloying.^{50, 74, 75} Such diffuse interfaces have been shown in some systems to extend over a few nm or more.⁷⁶ However, we note that arguments have been advanced showing that elastic strain energy should be much smaller than the activation energy for diffusion, and thus that \tilde{D} near interfaces should not be significantly affected.⁷⁷ Diffusion through extended defects, such as grain boundaries, is a third possibility. Such high-diffusivity paths⁷² are especially important in diffusion at low temperatures. The role of such paths in cation exchange has, in general, not been appreciated, which might be surprising given the loss in crystalline perfection that is observed in many cases of cation exchange, including the PbS-CdS system. If Pb leaves via the surface faster than arriving Cd can diffuse through the shell, transport through high-diffusivity paths, such as grain boundaries in the growing shell or along the PbS-CdS interface, could still provide Cd more quickly than can bulk-like ionic transport. Accordingly, the increased magnitude of the diffusion coefficient relative to bulk self-diffusion of Cd in CdS could reflect the introduction of a high concentration of extended defects, in accordance with the substantial (2.2%) lattice mismatch between PbS and zb CdS. We were unable to distinguish clearly any grain boundaries or stacking faults in our NCs (**Figure 4.7**), but Bals et al. have identified stacking faults unambiguously in PbSe@CdSe NCs, along with phase boundaries with displaced anionic sublattices.⁴⁴

To separate the chemical diffusion factor from contributions of high-conductivity paths, better high-resolution structural studies [i.e., through transmission electron microscopy (TEM)] on more particles are necessary to quantify the extent of such paths as grain boundaries or stacking faults in the shell. This will be particularly important in investigating the feasibility of a “layer-by-layer” exchange mechanism proposed to explain pronounced anisotropy of exchange even in cubic materials.^{19, 44}

Future experiments are necessary to examine the contribution of the large chemical potential gradient in cation exchange relative to the expected defect structure in the shell. We suggest that at length scales where the chemical potential gradient can be made small because of the low solubility of the two exchanging phases (the dilute solution limit) and where lattice strain can be completely accommodated (perhaps longer than 5 nm), the kinetics of diffusion should slow greatly. Further work in, for example, X-ray reflectivity measurements on PbS–CdS surfaces or diffusion experiments on larger particles would furnish quantitative results on the necessary length scale. Observation by these means of a drastic drop in the apparent rate of diffusion for thick layers would lend credence to previous suggestions that cation exchange in PbS@CdS^{15, 19, 56} or in very large nanoparticles³ is “self-limiting.” Similarly, in systems where no lattice strain or boundaries between immiscible phases is present to induce defect formation, transformation should reflect the kinetics of diffusion in the bulk solid. Diffusion experiments on slightly larger length scales could also offer insight into how the point defect structure of nanoparticles depends on their size.

4.3.13. Mechanism of diffusion: Arrhenius parameters

In spite of the expected contributions to the kinetics of diffusion from the factors above, we can still examine the activation barriers, E_a , to the diffusion reaction

to gain some insight into the reaction mechanism. An Arrhenius plot of the effective interdiffusion coefficients determined at temperatures greater than 140 °C is given in **Figure 4.10b**. Where identical temperatures were investigated in the two different experiments we carried out, the points are in excellent agreement with each other. Two different models (Fick's second law and the shrinking-core model) return nearly identical values for E_a (**Table 4.A.12**), with a fit of all measured interdiffusion coefficients in **Figure 4.10b** giving an E_a of 174 (Fick's law) or 164 kJ mol⁻¹ (shrinking-core). At high temperatures, the E_a of 174 kJ mol⁻¹ exceeds reported values of E_a for the diffusion of Cd in CdS determined from the sulfidation of large Cd nanoparticles (106 kJ mol⁻¹),⁷⁸ from the diffusion of Mn²⁺ in CdSe (also 106 kJ mol⁻¹),²¹ and the diffusion of Cd or Pb in CdSe (40–50 kJ mol⁻¹).¹ A more similar value of 154 kJ mol⁻¹ has been reported for the interdiffusion of CdSe–ZnSe.⁷⁹ Our activation energy is closer to some measured values of 179–258 kJ mol⁻¹ for the diffusion of Cd in wurtzite CdS^{23, 67} or of 98–146 kJ mol⁻¹ for Pb in PbS.⁶⁸ Theoretical predictions give a very wide range of values for point-defect formation energies, so that it may not be possible to make an assignment with certainty. Our measured E_a is also less than some predictions for the enthalpies of formation for point defects such as Schottky pairs,⁸⁰ which are generally >400 kJ mol⁻¹ (for a two-atom defect). It is important to note that previous experimental observations on diffusion in nanoparticles generally measured E_a as a combination of the energies for defect formation, ΔH_f , and migration, ΔH_m . More reliable data exist for Cd in wurtzite CdS²³ and indicate that ΔH_f tends to be large (>100 kJ mol⁻¹) regardless of the type of defect (interstitial or vacancy), while ΔH_m can be of the same order of magnitude but in the case of interstitial diffusion is often much smaller.⁶⁷ Because our E_a remains large, we conclude that the ΔH_f of a defect such as a Cd vacancy or Pb interstitial is a major contributor to the diffusion activation energy in our case. Theoretical simulations of

diffusion migration barriers in nanoparticles^{9, 71} also support this conjecture. Although our DFT simulations seem to explain the presence of an rs layer in the PbS–CdS heterosystem, we are less successful in determining activation energy barriers for diffusion. The estimated $\Delta H = \Delta H_f + \Delta H_m$ for diffusion was universally $>200 \text{ kJ mol}^{-1}$ (**Tables 4.A.3-4**) and exceeded considerably the measured values of E_a in our system for all paths considered (Cd or Pb interstitials or vacancies in PbS, zb CdS, or rs-CdS). We do note, however, that the lowest observed barrier is for Cd interstitial diffusion in rs-CdS at 209 kJ mol^{-1} . It is interesting to consider this in light of the possibility that a high-diffusivity path may be involved in atomic transport. The interfacial rs-CdS layer posited to exist following further growth of the shell might serve this role.

Finally, we consider the pre-exponential factor, \tilde{D}_0 , in the Arrhenius expression for the interdiffusion coefficient (**Table 4.A.12**). The corresponding \tilde{D}_0 for **Figure 4.10b** is 1.1×10^2 (Fick's law) or $3.3 \text{ cm}^2 \text{ s}^{-1}$ (shrinking-core). This value is rather large compared to numerous other measurements for ionic self-diffusion in semiconductor systems^{23, 68} and for chemical diffusion in nanoparticles,^{21, 78} which generally find values for a prefactor ranging from 10^{-7} to $10^{-3} \text{ cm}^2 \text{ s}^{-1}$. However, some measurements of self-diffusion in bulk solids give similar or even slightly larger values of D_0 (up to about $10^3 \text{ cm}^2 \text{ s}^{-1}$).⁶⁷ D_0 provides key information in self-diffusion measurements because the attempt frequency giving rise to D_0 in solids is related to a characteristic vibration frequency (Γ) on the order of $10^{11-13} \text{ s}^{-1}$.⁷² In pure stoichiometric substances, the diffusion coefficient is proportional to Γ times the square of the jump length a_0

$$D_0 \propto a_0^2 \Gamma \quad (4.11)$$

In solid-state diffusion mediated by point defect transport, a_0 is necessarily on the order of the unit cell length (a few Å), and the theoretical prefactor is therefore about 10^{-4} to $10^{-2} \text{ cm}^2 \text{ s}^{-1}$, or several orders of magnitude below our measured \tilde{D}_0 . An

enhanced value of \tilde{D}_0 could arise from an increase in the jump length due to the presence of extended defects, as we mentioned above. However, the magnitude of such an enhancement is ostensibly limited by the size of the system. As the size of the NCs here is only a factor of 10 larger than a jump length between lattice sites, the increase in the a_0^2 term in **Equation 4.11** is only 10^2 , which may be too small to explain the increase in \tilde{D}_0 observed here. An increase in the effective Γ , or a “biased” jump frequency, may originate from the thermodynamic factor mentioned above (**Equation 4.10**). Specifically, the concentration of defects may greatly exceed that expected from the enthalpy of defect formation, $\exp(-\Delta H_f/kT)$, owing to the presence of impurities or other changes in the external chemical boundary conditions that act to stabilize defects by charge compensation or other mechanisms.⁷² This further supports our conclusion that the small size of the region for diffusion leads to the significant enhancement of diffusive transport in NCs over length scales of a few nanometers due to the very large chemical potential gradients developed across the surface–shell–core region.

4.4. CONCLUSIONS

XRD characterization of lead sulfide (PbS) NCs undergoing transformation to cadmium sulfide (CdS) reveals that the cation exchange reaction proceeds in three stages with a complex series of intermediates. Upon the initial introduction of Cd (stage A), a thin shell of CdS rapidly develops on the surface of PbS. We confirm unambiguously that this shell adopts a metastable rs phase (rs-CdS) from the peak position and intensity shifts in agreement with those given by Debye scattering equation simulations, from Raman spectroscopy, and from DFT simulations. This phase may persist as an interlayer throughout the exchange, raising the possibility that

such interfaces can be made to serve useful roles in tuning the complex electronic structure of nanocrystalline heterostructures. As the shell grows and the overlying CdS recrystallizes (stage B) to the stable zb phase (zb-CdS), the peak intensities and positions become more like those of simulated PbS@zb-CdS particles, and we observe unusual diffraction effects manifesting as anomalous peak shifts. We identify such behaviors as emerging naturally from the commensurate relationship between rs PbS and zb CdS cation sublattices and show that such a relationship serves to break the symmetry of the core-shell quantum dot without requiring an actual change in the unit cell space group. During the third stage, C, the remainder of the particle is converted to zb-CdS via diffusive transport through the outer layers of the particle. The kinetics of the cation exchange reaction can be quantified using parameters from the XRD data that are insensitive to the particular phase of CdS. The kinetics of the cation exchange are complex and a number of processes contribute, so that the overall activation energies of the exchange at high and low temperatures appear to be different. However, using very general diffusion models, we estimate that interdiffusion coefficients in the PbS-CdS system, even at diffusion lengths larger than a few monolayers, are increased by a few orders of magnitude relative to those estimated from high-temperature data for self-diffusion of Cd in CdS. The interdiffusion coefficients have a large Arrhenius activation energy in comparison to several other reports of diffusion in nanoparticles, and we suggest that convolution of diffusion with surface reactions could produce anomalously low activation energies in prior experiments on nanocrystals. However, the magnitudes of our interdiffusion coefficients are still much larger than reported values for self-diffusion in CdS at high temperatures. The major cause of accelerated diffusion appears to be the very large chemical potential gradient involved in cation exchange, which by definition requires a change in the activities of component ions from zero to unity over a very short

distance. Such an enhancement can be expressed as a contributing thermodynamic factor in the interdiffusion coefficient, which can, for example, reflect a change in stoichiometry. Diffusion through high-conductivity paths, which could form due to mismatch between PbS and CdS and increase the distance that atoms move with every diffusive jump, is also a possible explanation. It is important to recognize the profound difference between experimental configurations with and without a chemical potential gradient and to provide much more detailed characterization of such factors as component activity and defect structure for quantifying transport coefficients of matter at the nanoscale.

4.A. APPENDIX

4.A.1. Funding and acknowledgments

This work was supported in part by the National Science Foundation (NSF) under award numbers CHE-1507753, CHE-1665305, CHE-1665310, DMR-1542776, and OAC 1440547. This work made use of the Cornell Center for Materials Research shared facilities, which are supported through the NSF MRSEC program (DMR-1719875), and the Cornell High Energy Synchrotron Source (CHESS) facilities, which are supported by the NSF (DMR-1332208). This work also made use of the computational resources provided by the University of Florida Research Computing Center. We thank S. Stoupin, D. Smilgies, and A. Itskovich (CHESS) for assistance with X-ray experiments, J. Kopsa and J. Houghton (CHESS) for preparation of apparatus, and R. Dieckmann (Cornell Materials Science and Engineering) for helpful discussions. We also thank S. Giri (Cornell Biological and Environmental Engineering) for an elemental analysis.

4.A.2. Materials and methods

All chemicals were used as received under air, except where specified. Where reactions were carried out under nitrogen, they were done in a glove box or on a Schlenk line. Trifluoroacetic anhydride (TFA₂O, >99%), acetonitrile (99.8%, anhydrous), oleic acid (OA, 99%), triethylamine (Et₃N, >99%), diphenyl ether (>=99%), hexadecane (99%), ethyl acetate (>=99.5%), hexyl isothiocyanate (95%), dodecylamine (98%), and octadecene (ODE, tech., 90%) were from Sigma-Aldrich. Lead(ii) oxide (99.999%) and methyl acetate (99%) were from Alfa Aesar. Cadmium oxide (99.999%) was from Strem. Trifluoroacetic acid (TFAOH, 99.5%), toluene (99.9%), and acetone (99.5%) were from Millipore. Isopropanol (>99.5%, semi

grade), hexane (>98.5% C6 isomers, ACS grade), and methanol (99.9%, semi grade) were from BDH. Cerium(iv) oxide powder (CeO_2 , 14 micron, 99.99%) was from Alfa Aesar.

Nanocrystal preparation

Procedures for the synthesis of PbS NC precursors are given in Hendricks et al.²⁷: Lead oleate ($\text{Pb}(\text{OA})_2$) was prepared on a 44.8 mmol scale from lead oxide dissolved in acetonitrile with TFAOH and TFA_2O , followed by precipitation from OA and triethylamine in isopropanol and recrystallization of the mixture. N-hexyl-N'-dodecylthiourea (14.5 mmol scale) were prepared by mixing the respective solutions of isothiocyanate and amine in 5 mL each of toluene followed by drying under vacuum. The precursors are stored under N_2 .

The PbS NC synthesis also followed from Hendricks et al.²⁷ PbS NCs of size 7.1 ± 0.4 nm ("7 nm") were prepared from reaction of N-hexyl-N'-dodecylthiourea with $\text{Pb}(\text{OA})_2$. 7.944 g $\text{Pb}(\text{OA})_2$ was added under N_2 to a 3-necked flask, which was then moved to a fume hood, loaded with 70 mL hexadecane filtered through 0.2 μm PTFE filters, fitted with a thermocouple, condenser, and stopper, and finally attached to a Schlenk line. 1.539 g N-hexyl-N'-dodecylthiourea was added to a vial under N_2 , which was sealed with a septum, moved to a fume hood, and loaded with 5 mL diphenyl ether. Both solutions were purged of air by gently bubbling N_2 through them for 10 min, while the flask was allowed to equilibrate at 150°C on an oil bath. With the flask now under flowing N_2 , the thiourea solution was rapidly injected into the $\text{Pb}(\text{OA})_2$ solution, and the NCs were allowed to grow for 20 minutes.

Following growth of the NCs, the flask was removed from the oil bath and allowed to cool to room temperature in air. The mixture was precipitated using excess methyl or ethyl acetate (1:1 by volume) and centrifuged at 7000 rpm for 10 min. The

precipitate was redissolved in toluene and centrifuged again at 4400 rpm for 10 min and insoluble material was removed. Thereafter the NC solution were cleaned three times more: the first time with ethyl acetate and 7000 rpm centrifugation, and the second and third time with acetone and 4400 rpm centrifugation. (A “cleaning” cycle for as-synthesized nanocrystals (NCs) indicates that a solution of the NCs was precipitated using a certain antisolvent (1:1 by volume) and centrifuged for 10 minutes at a certain speed, with the supernatant discarded and the precipitate re-dissolved in toluene.) After a final centrifugation at 4400 rpm to check for insoluble material, the NCs were precipitated from toluene with acetone and the solid product after centrifugation was dried under an N₂ flow followed by vacuum drying overnight. The NCs were stored as powders.

Cation exchange

Cadmium oleate (Cd(OA)₂) was prepared from cadmium oxide using a non-optimized adaptation of the method for Pb(OA)₂; excess TFAOH and TFA₂O were needed to completely dissolve the oxide. 1.15 g cadmium oxide (8.96 mmol) was stirred with 8 mL acetonitrile at room temperature with addition of 0.28 mL TFAOH (3.7 mmol) and 2.48 mL TFA₂O (17.8 mmol) for 48-72 h to give a slightly opalescent white solution. This solution was filtered and added to isopropanol (36 mL) containing 4.975 g OA (17.6 mmol) neutralized with 2.06 g triethylamine (20.4 mmol). More triethylamine (1.48 g, 14.6 mmol) was then added so that the precipitate did not re-dissolve. The mixture was then heated to boiling until all Cd(OA)₂ dissolved, then allowed to cool to room temperature over 2 hours. The solution was then cooled overnight in a refrigerator; the precipitate was vacuum filtered, washed and triturated with copious amounts of methanol, and vacuum dried overnight. The white, waxy powder was stored under nitrogen.

For in-situ x-ray observation, a stock solution of PbS NCs (5 wt% in ODE) was prepared by sonication. Another stock solution of 15 wt% Cd(OA)₂ in ODE was prepared by gently heating a vial sealed with the two components under N₂ on a hot plate until the Cd(OA)₂ fully dissolved. When cooled to room temperature, the mixture gels and eventually freezes. Immediately before measurement, an aliquot of the Cd(OA)₂ gel was warmed until it could be drawn into a syringe without any dead space or air bubbles (ca. 60-70°C). After cooling for a few seconds, this gel was rapidly mixed with an equal volume of PbS solution. While still free-flowing, the slightly warm mixture was dispensed by syringe into a Kapton capillary. The filled capillary was then placed in the preheated hot stage (see below). Equal volumes of the two solutions, mixed together, give an approximate ratio of Pb: Cd of 1:1, assuming a PbS stoichiometry of Pb_{1.25}S (but see below).

In-situ x-ray diffraction

Two experiments were run with slightly different configurations at beamline A1 at the Cornell High Energy Synchrotron Source (CHESS). The relevant experimental parameters are given in **Table 4.A.1**. Experiment 1 offered a much better signal-to-noise ratio and Q-space resolution, while experiment 2 afforded better time resolution. Photon energies were selected from the appropriate Bragg reflection of a diamond crystal monochromator, and the slit size was 0.1x0.1 mm².

Table 4.A.1. Experimental parameters for in-situ x-ray diffraction at CHESS A1.

Expt	Energy of photons, keV (wavelength, Å)	Detector	Approx. sample to detector dist., mm	Capillary dia., mm	Est. absorption, %	Est. mass of nanocrystals in beam, µg
1	32.5 (0.38)	ADSC Quantum 270	140	3.2	26	0.800
2	19.7 (0.629)	Dectris Eiger 1M	150	1.1	23	0.275

Additional notes on XRD

For experiment 1, the detector was protected from the hot stage by a 0.002" Kapton film and the capillary was capped at both ends by aluminum stoppers covered with PTFE pipe tape. One stopper had vent holes; the tape covering these was punctured during loading of the capillary to release heated air. In experiment 2 the capillary was sealed at both ends with fluorocarbon grease (Krytox, Dupont) and crimped into a sample carrier with set screws. Each experiment used a different aluminum hot stage custom-made by the machine shop at CHESS. The detector geometry was calibrated using CeO₂ powder in the capillary for experiment 1 and sandwiched between Kapton films for experiment 2.

To begin a measurement, the hot stage was pre-heated to the working temperature and the capillary was inserted. For experiment 1, acquisition of images began after 60-120 s; the first 10 were taken with exposure time of 30 s, while all later images had an exposure time of 60 s. For experiment 2, acquisition began after at most 60 s; the first 30 images were taken with an exposure time of 1s, the next 18 images with 5 s, then 28 images at 10 s, and all later images at 30 s. Measurements were also taken of ODE and the pure PbS NC solution in ODE at each temperature. Thermal expansion of lattice parameters was found to be small relative to the peak shifts during cation exchange. For all relevant figures, the zero-time point is given by

measurements from pure PbS NCs at the corresponding exchange temperature without added Cd.

We calculated the expected absorption of our samples using a web utility provided by R.B. Von Dreele, M.R. Suchomel, and B.H. Toby based on the Python package Absorb via <https://11bm.xray.aps.anl.gov/absorb/absorb.php>. On the basis of a sample composition of 2.5 wt% Pb_{1.25}S, 7.5 wt% Cd(C₁₈H₃₃O₂)₂, and 90 wt% C₁₈H₃₆, a rough estimate of the “molecular formula” of the sample is Pb_{1.25}Cd_{1.29}S_{1.00}O_{5.17}C_{793.5}H_{1579.2}. (Note: the absorption due to O, S, and H is nearly negligible.) Using this formula with an estimated density of 1 g cm⁻³ returns the estimated absorptivity of the sample in **Table 4.A.1**. The mass of nanocrystals in the beam is calculated from this density and the parameters above as:

$$\frac{0.025 \text{ g nanocrystals}}{\text{g solution}} \cdot \frac{1 \text{ g solution}}{1 \text{ cm}^3 \text{ solution}} \cdot (0.01 \text{ cm})^2 \cdot (0.11 \text{ or } 0.32 \text{ cm})$$

$$= 0.275 \text{ or } 0.8 \text{ } \mu\text{g}$$

Analysis of the solid constituents by inductively-coupled plasma optical emission spectrometry found that, on a mass basis, the Cd oleate synthesized here was 17.5% Cd (calculated for Cd(C₁₈H₃₃O₂)₂: 16.6%) and the PbS NCs were 83.5% Pb (calculated for PbS and Pb_{1.25}S: 86.6% and 88.9%, respectively). With these measured concentrations of Pb and Cd, the elemental ratio Cd:Pb used in the experiments is actually about 1.16. Sulfur could not be quantified in our analysis due to a high and variable blank value, the contaminant source of which we could not identify; thus, the agreement of our elemental analysis with calculated values is not ideal. However, a qualitative check of the absorption of the sample using a silicon PIN diode found the measured absorption to be in reasonable agreement with the values in the table. No absorption correction is necessary for this degree of sample transparency.

Notes on data quality

Substantial instrumental broadening in experiment 1 occurred due to the non-negligible thickness of the sample capillary (3.2 mm) compared to the sample-to-detector distance (140 mm). Because diffracted beams originate from each point along the intersection of the direct beam with the sample, the Debye-Scherrer cones comprising the diffraction pattern are smeared radially (relative to the beam axis) and the width of the rings on the detector face increases with diffraction angle. This broadening is shown for the CeO₂ powder sample in **Figure 4.A.7**.

Additionally, two types of scatter are observed in the experimental measurements. First, we attribute the noise level in intensity ratios at high temperature and long reaction times (**Figure 4.3** and **4.A.2**) and the (200) peak position (**Figure 4** and **4.A.3**) to limitations in the solvent background subtraction and peak-fitting procedure (see below). The quality of the fit at high values of I_{111}/I_{200} is relatively insensitive to the intensity of (200) (which also overlaps with the impurity peak and with the tail of (111)), and changes in (200) intensity are correlated to a certain extent with changes in peak width and position and background level. As a result, the apparent parameter value at the minimum in the goodness-of-fit measure can vary significantly. The second source of noise is the apparent serrations in the data, especially at low temperatures, in **Figure 4.4**. We attribute these to the non-linear response of the ADSC Quantum 270 detector, which in qualitative tests had a reduced response at high photon flux (its dynamic range saturating at 2^{16} or five orders of magnitude). As a result, as the beam intensity changes due to run-down and top-up of the synchrotron electron beam, the detector reading changes in a non-linear manner. This is confirmed in the lack of such serrations in the data from the second experiment with the Eiger 1M detector, which we found to have a linear response at any exposure time used here.

Data reduction

Cation exchange systems pose significant difficulties for in-situ XRD experiments. Even at the relatively high x-ray energies and concentrations of NCs, the strongest scattering arises from the carrier solvent, in this case ODE, and the oleate ligands used to dissolve Cd^{2+} , leading to a high background signal. While liquid hydrocarbons have a relatively simple solution structure,⁸¹ we find that the solvent background in the x-ray cell could not be described by a linear combination of signals from “pure” reference components, i.e., pure ODE and pure ODE/Cd oleate solutions. This is unsurprising in light of the high concentrations of PbS NCs and Cd oleate used in the experiment (about 10 wt% total); nanoparticles induce significant changes in their local solvent structure,⁸² and the solution structure of Cd oleate, which forms a mesophase at high concentrations, is poorly defined.^{83, 84} Fluorescence from cadmium (K edge energy 26.7 keV) also contributes to the observed intensity for experiment 1. No correction for absorption or multiple scattering was applied (see above).

In both experiments, flat-field corrections were applied by the detector software. Dark current correction was not applied. The frames from each experiment were azimuthally integrated using pyFAI 0.15.0⁸⁵ and the resulting 1D patterns were curve-fitted using GSAS-II⁸⁶ after subtraction of the empty stage background and the pure ODE background (the latter weighted by 0.9). In the absence of more sophisticated treatments, we have limited fitting of the data to ranges enclosing the three strongest reflections from PbS/CdS. The fitting ranges consisted of two windows to avoid over-fitting the background, with the first enclosing the (111) and (200) peaks and the second enclosing the (220) peak. Within each window, the peaks could be reasonably well-fit with Lorentz line shapes overlaid on a linear background.

For experiment 2, the data at first appeared to exhibit some unphysical behaviors. At late times in the experiment the measured peak centers would eventually

move to diffraction angles larger than the estimated positions corresponding to bulk zincblende CdS. We examined the possible sources of error in this system, and we believe that this effect arises from a small difference between the sample-to-detector distances, d , for the samples (enclosed in capillaries) relative to the standard (a thin layer enclosed in flexible Kapton foil, used because CeO₂ loaded into the sample capillary was opaque to 19.7 keV x-rays in this experiment). Adjusting the wavelength λ during conversion of the scattering angle to Q shows that using a wavelength of 0.632 Å (0.48% larger than the normal value of 0.629 Å) returns the measured Q_{220} at long times for the experiment at 200° to a physical value of less than the reference position for CdS (zincblende). Within the small angle approximation for the Bragg angles, θ , $\lambda_1/\lambda_2 \approx \theta_1/\theta_2 \approx d_1/d_2$, so the deviation in wavelength is identical to the deviation in effective sample-to-detector distances. The nominal distance is about 150 mm, so that the possible error in the detector distance is about 0.7 mm, which is comparable to the diameter of the sample capillary. We suggest that flexing of the CeO₂-loaded Kapton foil could lead to a distortion of this order of magnitude. Therefore, for experiment 2 we converted the peak positions to Q using a wavelength of 0.632 Å, which is reflected in the results for all applicable figures. However, this correction has little to no effect on the derived chemical diffusion coefficients.

4.A.3. Computational and other results and procedures

Debye simulations

XYZ files for the atomic positions of Pb, Cd, and S in PbS or PbS@CdS NCs were created by generating slabs of PbS or CdS with the appropriate lattice constant (5.94 Å or 5.81 Å). These were generated using the same set of basis vectors so that the S sublattices were otherwise fully commensurate: (0 0 0), ($\frac{1}{2}$ $\frac{1}{2}$ 0), ($\frac{1}{2}$ 0 $\frac{1}{2}$), and (0

$\frac{1}{2} \frac{1}{2}$). The basis for PbS was (0 0 0) (S) and (0 0 $\frac{1}{2}$) (Pb); the bases for CdS was (0 0 0) (S) and (0 0 $\frac{1}{2}$) (Cd, rocksalt) or ($\frac{1}{4}$ $\frac{1}{4}$ $\frac{1}{4}$) (Cd, zincblende). A PbS core with radius r_{core} was obtained by removing atoms in the PbS slab further than r_{core} from the origin. For the CdS shell, atoms closer to the origin than r_{core} and further from the origin than $r_{\text{core}}+t_{\text{shell}}$ were removed. For particles of consistent diameter, $r_{\text{core}}+t_{\text{shell}}$ was fixed at 35 Å. The models thus comprise about 7000 atoms. Patterns were obtained for t_{shell} from 0 to 34 Å. The simulations were carried out using the program Debyer (available through <https://debyer.readthedocs.io/en/latest/> as of December 2018). The step size was 0.001 degrees, the simulated wavelength was 0.3875 Å, and the bin size (quantum) for the interatomic distance histograms was 0.001 Å. Lorentzian functions were fitted to the data to obtain peak positions, widths, and intensities using GSAS-II.⁸⁶

Other characterization

To prepare small samples of exchanged NCs for TEM and Raman analysis, an exchange experiment identical to the XRD experiments above was run off-line in the laboratory outside of CHESS, with the sample capillary (experiment 1 configuration) being inserted into the preheated (120 or 200 °C) sample stage for the appropriate amount of time (60, 300, or 3600 s). After quick removal from the stage, the solution was diluted with a small amount of hexane, and the NCs were cleaned twice using acetone as counter-solvent and hexane as solvent.

High-resolution TEM was carried out on an FEI F20 at 200 keV. Samples were drop-cast from hexane solutions onto carbon-coated copper grids and cleaned with an O₂ plasma (Fischione Model 1020) for 5 s before insertion into the microscope. The Fourier transforms in **Figure 4.7** were obtained using Gatan DigitalMicrograph 3 and have been enhanced using a Wiener filter via the HRTEM filter script provided by

D.R.G. Mitchell (as of December 2018, available through http://www.dmscripting.com/hrtem_filter.html). This image was further processed using a Gaussian filter and contrast enhancement to give the cartoons shown as guides for the eye.

Raman spectra were acquired using a Renishaw InVia confocal Raman microscope with an excitation wavelength of 488 nm (Ar-ion laser). Hexane solutions of NCs at varying stages of exchange were drop-cast on single-crystal silicon substrates.

Density functional theory calculations

Density-functional calculations were performed with the Vienna Ab-initio Software Package (VASP)⁸⁷⁻⁹⁰ using the PBE exchange-correlation functional⁹¹ and the projector augmented wave method.^{92, 93} The Brillouin zone integration was performed using a Monkhorst and Pack k-point mesh.⁹⁴ 3x3x3 k-points meshes were employed for all structural relaxations and nudged-elastic band (NEB) calculations.⁹⁵ The kinetic energy cutoff for the plane wave basis was set to 400 eV and the corresponding cutoff energies for the augmentation functions were set to 650 eV for all our calculations. POSCAR files used in our calculations were obtained from the Materials Project Website.⁹⁶ On relaxation with DFT, we find the lattice constants for the bulk phases to be: PbS, 6.00 Å; CdS(rs), 5.51 Å; and CdS(zb), 5.94 Å. We also calculated the formation energies for CdS(rs) (-0.84 eV) and CdS(zb) (-0.97 eV), using Cd and S as references, to confirm that CdS(zb) is the more stable phase at zero applied pressure. We use Kröger-Vink notation⁷² to describe the point defects in the tables below (**Tables 4.A.3-4**).

A cell having the (100) orientation was made with 5 monolayers of PbS. To calculate interface energies, additional monolayers of CdS(rs) and/or CdS(zb) were

added to form cells with the composition $\text{PbS}_5\text{-CdS(rs)}_m\text{-CdS(zb)}_n$, where $m = 0\text{-}4$ and $n = 0\text{-}2$. The bottom three PbS layers were fixed to the bulk lattice parameter calculated above, and only the CdS layers and the top two layers of PbS were allowed to relax during optimization. We calculate interface energies as follows:

$$\frac{E_{\text{struct}} - n_{\text{PbS}} \cdot E_{\text{PbS}}^{\text{ref}} - n_{\text{CdS}} \cdot E_{\text{CdS}}^{\text{ref}}}{2A} \quad (4.12)$$

n_{PbS} or n_{CdS} are the number of PbS or CdS layers in the slab, respectively; $E_{\text{PbS}}^{\text{ref}}$ or $E_{\text{CdS}}^{\text{ref}}$ are the reference energies of the stable bulk phases; A is the surface area of the interface, in \AA^2 ; and E_{struct} is the energy of the mixed-phase slab being considered. An example of a slab geometry is shown in **Figure 4.A.9a**.

Table 4.A.2. Results of density functional theory calculations for surface energies, in meV \AA^{-2} , of PbS slabs capped with varying numbers of CdS(rs) and CdS(zb) monolayers. Also shown are the equivalent energy added per monolayer of CdS regardless of phase in meV \AA^{-2} .

PbS	Layers CdS(rs)	CdS(zb)	(100) Surface energy	per CdS monolayer	
5	0	0	24.06		
		1	86.26	86.26	
		2	133.60	66.80	
	1	0	0	68.55	68.55
			1	126.19	63.10
			2	161.49	53.83
	2	0	0	88.51	44.26
			1	154.28	51.43
			2	190.65	47.66
	3	0	0	112.09	37.36
			1	175.96	43.99
			2	209.02	41.80
4	0	0	137.93	34.48	
		1	201.96	40.39	
		2	234.39	39.07	

Table 4.A.3. Enthalpies of formation ΔH_f , in eV atom⁻¹, for neutral point defects in PbS, CdS(rs), and CdS(zb) calculated using DFT.

Defect type	Formula*	ΔH_f , PbS	ΔH_f , CdS(rs)	ΔH_f , CdS(zb)
Vacancy	V_{Pb}^x	2.06	2.36	4.13
	V_{Cd}^x			
Substitutional	Cd_{Pb}^x	0.38	0.19	0.80
	Pb_{Cd}^x			
Substitutional-vacancy pair	$Cd_{Pb}^x + V_{Pb}^x$	2.49	2.17	3.73
	$Pb_{Cd}^x + V_{Cd}^x$			
Interstitial	Pb_i^x, T_d	2.52	3.59	3.50
	Pb_i^x, O_h			
	Cd_i^x, T_d	1.60	1.53	2.40
	Cd_i^x, O_h			
Schottky	$V_{Pb}^x + V_S^x$	2.12	1.09	3.14
	$V_{Cd}^x + V_S^x$			
Frenkel	$V_{Pb}^x + Pb_i^x, T_d$	2.97	2.29	3.62
	$V_{Cd}^x + Cd_i^x, T_d$			
	$V_{Cd}^x + Cd_i^x, O_h$			

* T_d = tetrahedral interstitial; O_h = octahedral interstitial.

Table 4.A.4. Results of density functional theory calculations for diffusion barriers (ΔH_f , enthalpy of formation; ΔH_m , enthalpy of migration; ΔH_{diff} , total activation enthalpy of diffusion), in eV, of neutral point defects in PbS, CdS(rs), and CdS(zb).

Defect	PbS(rocksalt)			CdS(rocksalt)			CdS(zincblende)		
	ΔH_f	ΔH_m	ΔH_{diff}	ΔH_f	ΔH_m	ΔH_{diff}	ΔH_f	ΔH_m	ΔH_{diff}
V_{Cd}^x	2.49	0.29	2.78	2.36	0.71	3.07	4.13	0.95	5.08
V_{Pb}^x	2.06	1.64	3.70	2.17	1.20	3.37	3.73	1.68	5.41
Cd_i^x	1.60	0.83	2.43	1.53	0.64	2.17	2.37	0.31	2.68
Pb_i^x	2.52	1.11	3.63	3.59	0.07	3.66	3.50	0.75	4.25

4.A.4. Kinetic parameter determination

Simultaneous kinetic parameters for stages A and C. We attempted to describe the (220) peak position, Q_{220} , over the entire experimental time by nonlinear least squares fitting to the following function of time (t), or a sequence of pseudo-first-order reactions (**Table 4.A.5**):

$$Q_{220} = C + \sum_{i=1}^2 A_i \exp\left(-\frac{t}{\tau_i}\right) \quad (4.13)$$

Where C is a constant and A_i and τ_i are the amplitude and relaxation times of the two processes (A and C). Although the curves may be individually well-fit by the function and both A and C appear to have the expected positive activation energies, the extracted rate constants show far too much scatter in the Arrhenius plot (**Figure 4.A.13a**) for an extracted E_a to be meaningful. The scatter is especially pronounced for the slower of the two processes because the noise in the data, combined with their extremely small slope, introduces large uncertainties in the estimated k .

Table 4.A.5. Parameters for the double-exponential fit to the value of Q_{220} in **Figures 4.4** and **4.A.3**.

Experiment	Temp., °C	C, Å ⁻¹	A ₁ , Å ⁻¹	τ ₁ , s	A ₂ , Å ⁻¹	τ ₂ , s
1	120	3.004	-0.0166	101.5	-0.0041	14786.5
	150	3.023	-0.0153	82.0	-0.0221	81206.6
	180	3.052	-0.0065	7160.6	-0.0505	7160.6
	200	3.053	-0.0163	11.2	-0.0530	1166.0
2	100	3.001	-0.0057	227.5	-0.0133	24181.8
	120	3.004	-0.0101	57.5	-0.0138	5072.0
	140	3.006	-0.0126	69.2	-0.0100	13535.1
	160	3.019	-0.0133	26.1	-0.0246	11877.5
	180	3.054	-0.0163	90.7	-0.0478	7019.5
	200	3.056	-0.0248	60.7	-0.0465	1643.1

We also attempted a second-order-like rate law fit (**Table 4.A.6**):

$$Q_{220} = C + \frac{A_0}{1 + A_0 k t} \quad (4.14)$$

With A_0 being another constant (assuming Q_{220} is proportional to the total fractional conversion plus an offset) and k being the rate constant. Again, whether or not a given curve may appear to be well-described by this function, the Arrhenius plot (**Figure 4.A.13b**) makes clear the function is not suited to modeling the kinetics of the exchange reaction, even over restricted temperature ranges for A or C .

Table 4.A.6. Parameters for the second-order rate law fit to the value of Q_{220} in **Figures 4.4** and **4.A.3**.

Experiment	Temp., °C	$C, \text{Å}^{-1}$	$A_0, \text{Å}^{-1}$	$k, \text{Å}^{-1} \text{s}^{-1}$
1	120	3.003	0.0193	0.45391
	150	3.017	0.0176	0.00229
	180	3.071	0.0761	0.00167
	200	3.058	0.0672	0.02605
2	100	3.002	0.0163	0.00578
	120	3.005	0.0176	0.02489
	140	3.005	0.0136	0.02775
	160	3.024	0.0311	0.00336
	180	3.061	0.0616	0.00362
	200	3.059	0.0626	0.02631

Kinetic parameters for stage A

We described the temperature dependence of the (220) peak position, Q_{220} , at early times by nonlinear least squares fitting to the following function of time (t):

$$Q_{220} = C + A \cdot \exp\left(-\frac{t}{\tau}\right) \quad (4.15)$$

Here C and A are constants and τ is the relaxation time or the inverse of the rate constant k . We chose to fit only times up to about the first 1000 seconds. We see that at $T > 160^\circ\text{C}$, where the diffusion process begins very early, τ increases sharply, indicating that layers of the particle below the surface are also undergoing exchange and that the rate constant no longer reflects the surface-only reaction.

Table 4.A.7. Exponential-fit parameters for the value of Q_{220} at short times in **Figures 4.4 and 4.A.3.**

Experiment	Temp., $^\circ\text{C}$	Time, s	C, \AA^{-1}	A, \AA^{-1}	τ , s
1	120	1214	2.9995	-0.0163	87.4
	150	1170	2.9996	-0.0148	41.6
	180	1173	3.0006	-0.0159	15.6
	200	423	3.0122	-0.0265	54.4
2	100	1022	2.9880	-0.0059	188.8
	120	1036	2.9910	-0.0106	68.8
	140	982	2.9949	-0.0130	52.0
	160	981	2.9945	-0.0135	25.4
	180	974	3.0101	-0.0189	139.0
	200	980	3.0244	-0.0345	155.0

Table 4.A.8. Arrhenius parameters for the rate constants of **Table 4.A.7.**

Temperature region, $^\circ\text{C}$	Q, kJ mol^{-1} (eV)	k_0 , s^{-1}
100-160	41 (0.42)	$2.83 \cdot 10^3$

Interdiffusion coefficient extraction

Diffusion models make use of the conversion fraction X (fraction of the particle converted to CdS), which is approximated here as:

$$X = \frac{Q_{CdS,220}^0 - Q_{220}}{Q_{CdS,220}^0 - Q_{PbS,220}^0} \quad (4.16)$$

Q_{220} is the present (220) peak center and $Q_{i,220}^0$ is the reference (220) peak position for species i , which is CdS (zincblende phase) or PbS.

Fick's law model

The experimental data, in general, deviate significantly from model curves calculated using Fick's second law. However, the time scale of a "diffusion-equivalent" process can be determined by calculating the effective chemical diffusion coefficient needed to produce a degree of exchange X at time t . We pose the problem of cation exchange as the diffusion-limited loss of Pb from a spherical particle, for which the analytical solutions of Fick's second law are given by Crank (§6.3).⁶⁴ The fractional completion of the reaction has already been given as **Equation 4.6**.

From the experimental curves (**Figures 4.4** and **4.A.3**) we chose X and t which correspond to the maximum observed extent of exchange (the end of the observation period) for $T = 100\text{-}160^\circ\text{C}$ and an X of about 0.8, where the reaction rate begins to decrease due to loss of Cd, for $T = 180\text{-}200^\circ\text{C}$. We calculated terms up to $n = 40$. X can be calculated at time t given a diffusion coefficient D_{th} and a particle radius (3.55 nm). We then estimated \tilde{D} to one decimal place by adjusting D_{th} to match the X calculated by the above equation to the experimental value of X .

Table 4.A.9. Parameters from extraction of effective diffusion coefficients using Fick's second law.

Experiment	Temp., °C	Time, s	Value of X	Est. \tilde{D} , cm ² s ⁻¹
1	120	42395	0.178	$9.1 \cdot 10^{-21}$
	150	50280	0.308	$2.5 \cdot 10^{-20}$
	180	7713	0.639	$9.4 \cdot 10^{-19}$
	200	1611	0.738	$6.8 \cdot 10^{-18}$
2	100	48151	0.112	$3.1 \cdot 10^{-21}$
	120	58432	0.185	$7.2 \cdot 10^{-21}$
	140	52032	0.255	$1.6 \cdot 10^{-20}$
	160	25159	0.383	$8.2 \cdot 10^{-20}$
	180	9231	0.739	$1.2 \cdot 10^{-18}$
	200	2082	0.787	$6.5 \cdot 10^{-18}$

Shrinking-core model

The shrinking-core model⁶⁶ was also used to estimate the interdiffusion coefficient \tilde{D} . For diffusion-controlled conversion of a spherical particle the following relationship holds as a function of time t , the right-hand side of which is calculated to linearize the conversion data:

$$\frac{t}{\tau} = 1 - 3(1 - X)^{\frac{2}{3}} + 2(1 - X) \quad (4.17)$$

The value τ , the total time to conversion, is related to the diffusion coefficient:

$$\tau = \frac{\rho_{cds}R^2}{6\tilde{D}C_{cd}} \quad (4.18)$$

ρ_{CdS} is the atomic density of Cd for CdS, R is the overall nanocrystal radius (3.55 nm), and C_{Cd} is the concentration of Cd in solution. \tilde{D} is in nm^2s^{-1} . Some ad-hoc assumptions must be applied to calculate \tilde{D} by this approach. The value for ρ_{CdS} , assuming that the lattice parameter is the same as zincblende CdS (0.581 nm) and that $Z = 4$, was estimated to be:

$$\rho_{\text{CdS}} = \frac{4 \text{ atoms}}{(0.581 \text{ nm})^3} \approx 20.395 \text{ atoms} \cdot \text{nm}^{-3}$$

The Cd(oleate)₂ has a molar mass of about 675.318 g mol⁻¹ and makes up approximately 7.5 wt% of the solution during cation exchange, PbS NPs make up 2.5 wt%, and ODE makes up the balance. The Cd oleate density was estimated to be the weighted average of the densities of cadmium (8.6 g cm⁻³) and oleic acid (0.89 g cm⁻³) giving 2.18 g cm⁻³. The density of the PbS NPs was taken to be the same as the bulk solid, or:

$$\frac{4 \text{ atoms} \cdot 239.3 \text{ g} \cdot \text{mol}^{-1}}{(0.594 \text{ nm})^3 \cdot 6.022 \cdot 10^{23} \text{ atoms} \cdot \text{mol}^{-1}} = 7.58 \text{ g} \cdot \text{cm}^{-3}$$

The density of ODE is 0.789 g cm⁻³. Therefore, the average density of the solution is 1.06 g cm⁻³. The initial concentration of Cd, C_{Cd}^0 , in the solution is then:

$$C_{\text{Cd}}^0 = \frac{0.075 \cdot 1.06 \text{ g} \cdot \text{cm}^{-3}}{675.318 \text{ g} \cdot \text{mol}^{-1}} \cdot \frac{6.022 \cdot 10^{23} \text{ atoms} \cdot \text{mol}^{-1}}{10^{21} \text{ nm}^3 \cdot \text{cm}^{-3}} \approx 0.0711 \text{ atoms} \cdot \text{nm}^{-3}$$

However, given the large driving force for the cation exchange reaction, the effective concentration of Cd could plausibly be much higher. If we assume that the concentration of Cd is actually equal to the atomic density of Cd in CdS (as in a thin surface layer), then C_{Cd}^0 takes the value of $\rho_{\text{CdS}} = 20.395 \text{ atoms nm}^{-3}$ above. This approximation also avoids the difficulty with accounting for the changing concentration of Cd in solution.

$1/\tau$ is given by the slope m of the linearized conversion data, which in the absence of any other process follows a straight line from 0 to 1 over the time interval 0 to τ . Therefore, \tilde{D} is calculated from the linearized data as follows:

$$\tilde{D} = m \frac{\rho_{CdS} R^2}{6C_{Cd}^0} \quad (4.19)$$

To obtain the slope by extrapolation of the kinetics at short times (and thus nearly constant C_{Cd}), points up to a given time (the “limit”) were fitted to a straight line having an intercept at $(t, X) = (0, 0)$. The time window over which the linearized data were fitted, the values for the estimated slope, and the corresponding D are given in **Table 4.A.10**. The windows over which \tilde{D} was determined are also shown graphically in **Figure 4.A.14**. If C_{Cd}^0 is equal to ρ_{CdS} as mentioned above, we find that the values for \tilde{D} obtained in this way are in good agreement with those calculated using Fick’s second law. This is consistent with our observation that the driving force for cation exchange is large and therefore that any incoming Cd should immediately replenish the layer at the surface.

Table 4.A.10. Shrinking core model parameters for determining the chemical diffusion coefficient.

Expt.	Temp., °C	Limit, s	Linearized slope, s ⁻¹	\tilde{D} , cm ² s ⁻¹
1	120	42395	$3.709 \cdot 10^{-7}$	$7.79 \cdot 10^{-21}$
	150	50280	$7.439 \cdot 10^{-7}$	$1.56 \cdot 10^{-20}$
	180	1784	$1.341 \cdot 10^{-5}$	$2.82 \cdot 10^{-19}$
	200	423	$1.218 \cdot 10^{-4}$	$2.56 \cdot 10^{-18}$
2	100	48151	$9.184 \cdot 10^{-8}$	$1.93 \cdot 10^{-21}$
	120	58432	$2.989 \cdot 10^{-7}$	$6.28 \cdot 10^{-21}$
	140	52032	$4.026 \cdot 10^{-7}$	$8.46 \cdot 10^{-21}$
	160	25159	$2.314 \cdot 10^{-6}$	$4.86 \cdot 10^{-20}$
	180	17065	$3.079 \cdot 10^{-5}$	$6.47 \cdot 10^{-19}$
	200	4893	$1.572 \cdot 10^{-4}$	$3.30 \cdot 10^{-18}$

Table 4.A.11. Reference data points for self-diffusion coefficients in materials given in **Figure 4.10**.

Region label	Upper bound				Lower bound			
	T range, °C	Ref.	E _a , eV	D ₀ , cm ² s ⁻¹	T range, °C	Ref.	E _a , eV	D ₀ , cm ² s ⁻¹
Li/Cu in CdS	620-960 ^a	⁶⁷	0.68	$3 \cdot 10^{-6}$	146-400 ^b	⁶⁷	0.96	$2 \cdot 10^{-3}$
Pb in PbS	500-800 ^c	⁶⁸	1.01	$5.5 \cdot 10^{-7}$	500-800 ^d	⁶⁸	1.52	$8.6 \cdot 10^{-5}$
Cd in CdS	700-850	⁶⁷	1.85	$5.8 \cdot 10^{-2}$	500-700	⁶⁷	2.67	$6.72 \cdot 10^2$

^a for Li impurity in CdS. ^b for Cu impurity in CdS. ^c for non-stoichiometric PbS_{1+x}. ^d for stoichiometric PbS.

Table 4.A.12. Arrhenius parameters for the chemical diffusion coefficients of **Tables 4.A.2,3.**

Temperature region, °C	E_a , kJ mol ⁻¹ (eV)		\tilde{D}_0 , cm ² s ⁻¹	
	Fick	Shrinking-core	Fick	Shrinking-core
140-200	174 (1.81)	164 (1.71)	$1.1 \cdot 10^2$	$3.3 \cdot 10^0$

4.A.5. Supporting figures

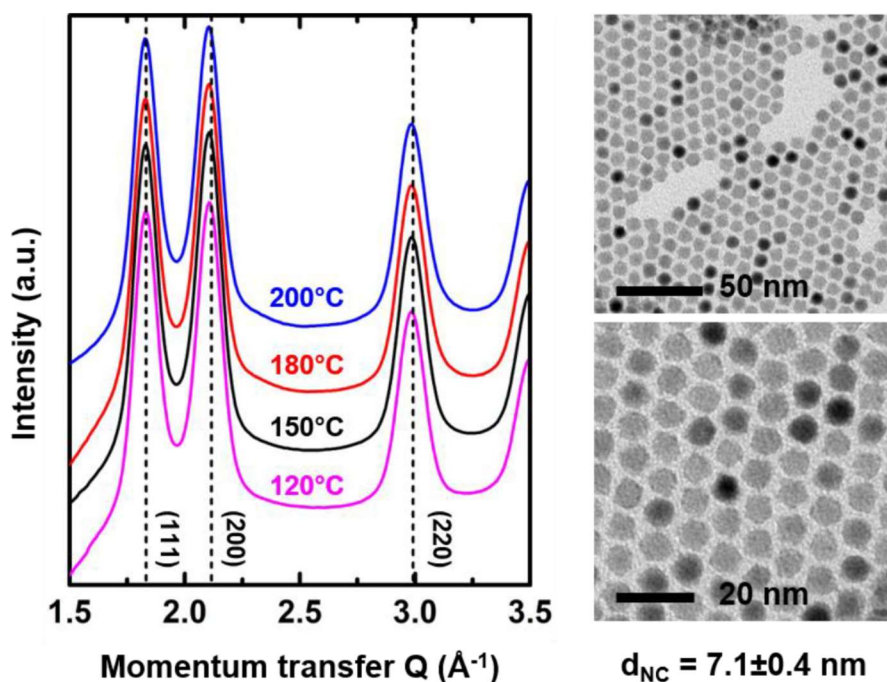


Figure 4.A.1. PbS nanocrystals before cation exchange. XRD (in the in-situ experimental cell) at left; TEM at right. NCs with 7.1 ± 0.4 nm diameter were used for the experiments from the main text figures. The NCs are nearly monodispersed and approximately spherical and stable under the experimental conditions.

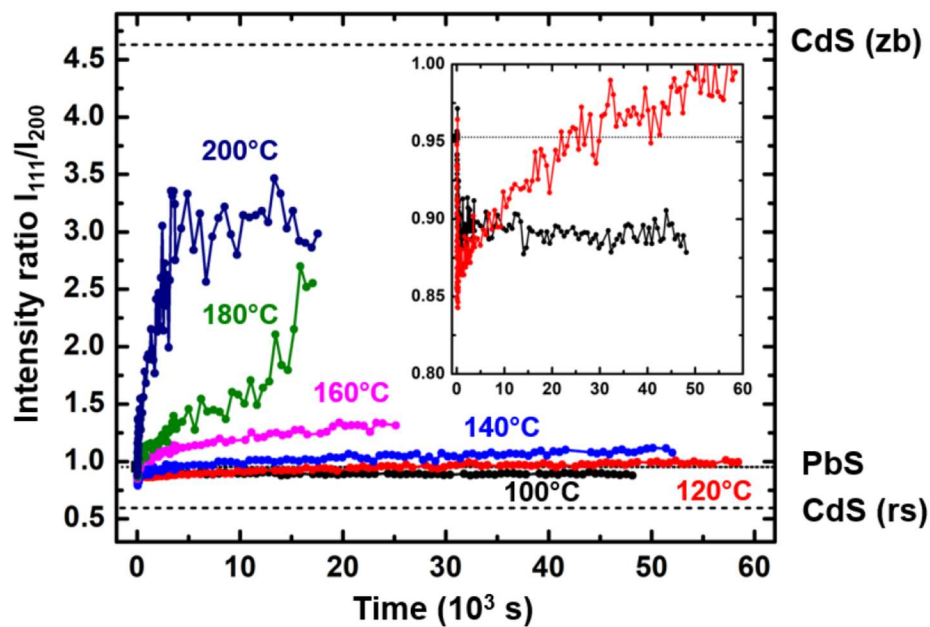


Figure 4.A.2. Intensity ratio I_{111}/I_{200} of the first two diffraction peaks (111) and (200) during cation exchange of PbS to CdS (second experiment). Notation is as in main **Figure 4.3**. Inset is an expanded scale of the two lowest-temperature runs showing that I_{111}/I_{200} clearly decreases steadily at 100°C, while at 120°C I_{111}/I_{200} reaches a minimum of about 0.85-0.87 at ca. 400-500 s.

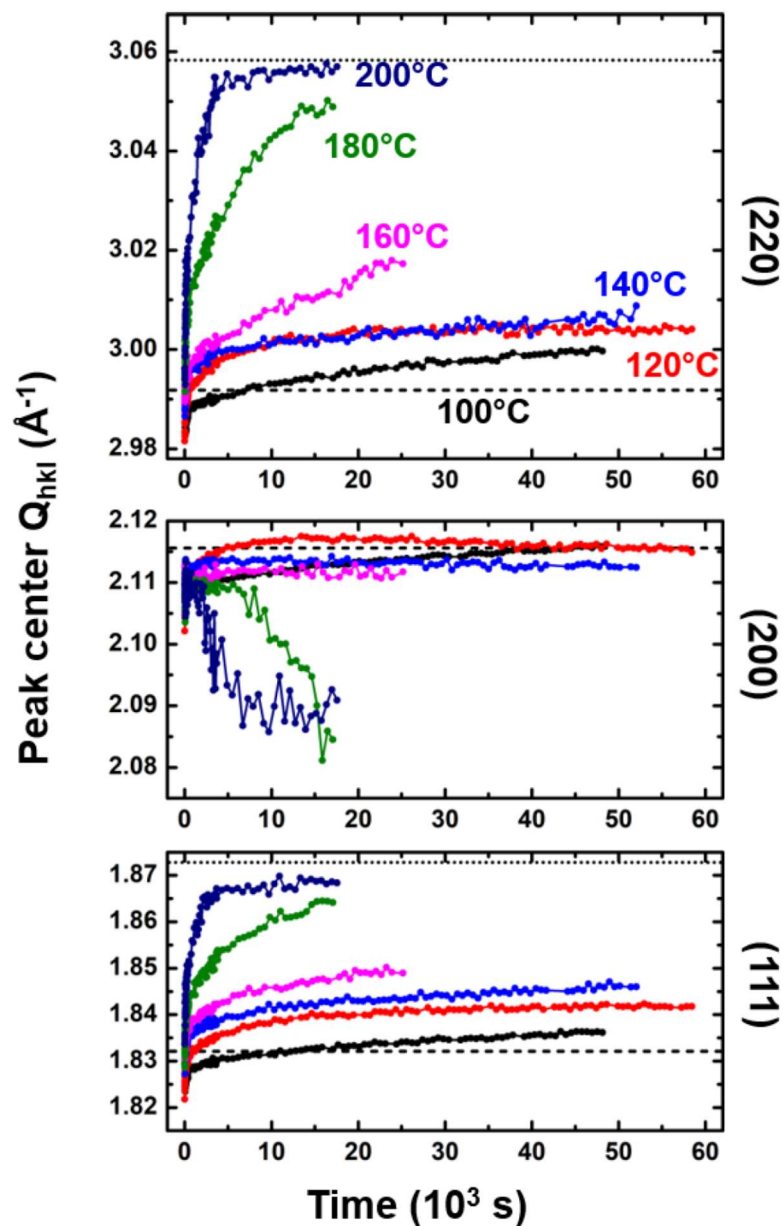


Figure 4.A.3. Fitted (111), (200), and (220) peak positions from in-situ XRD data for the cation exchange of 7 nm PbS NCs to CdS (second experiment). Notation is as in

Figure 4.4. At even lower temperatures (100°C) stage A becomes significantly slower, such that a clear maximum in the initial shift of (200) to larger angles can be seen.

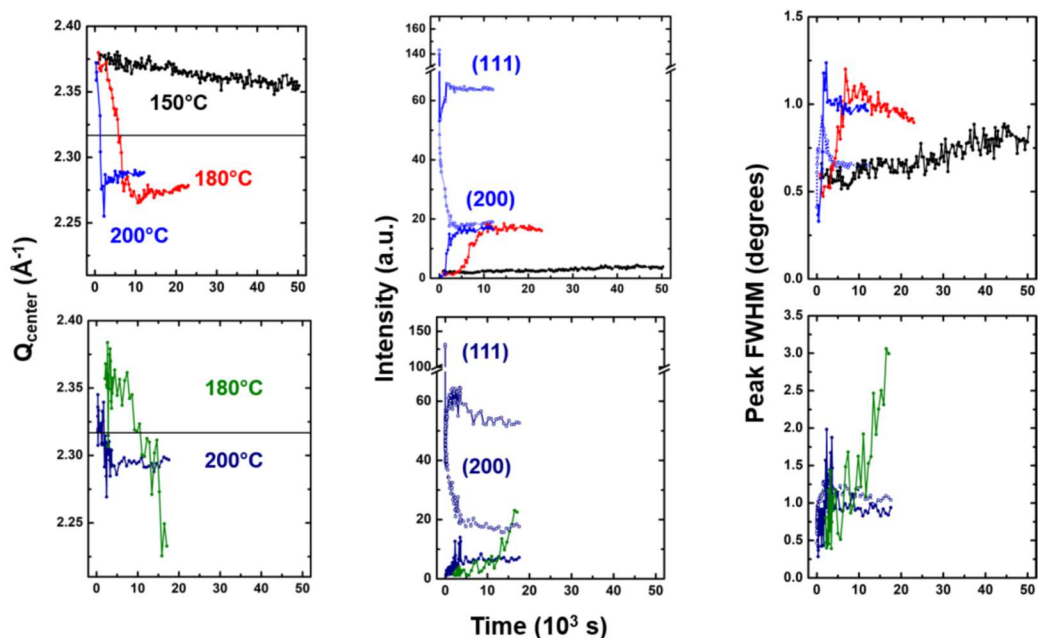


Figure 4.A.4. From right to left: Contaminant position, intensity, and width from experiment 1 (top) and experiment 2 (bottom). For position measurements, the line indicates the bulk position of CdO(111) (JCPDS 00-005-0640); for intensity measurements, the open symbols give the integrated intensities of (111) (solid line) and (200) (dotted line); and for width measurements the open symbols indicate the value for (200).

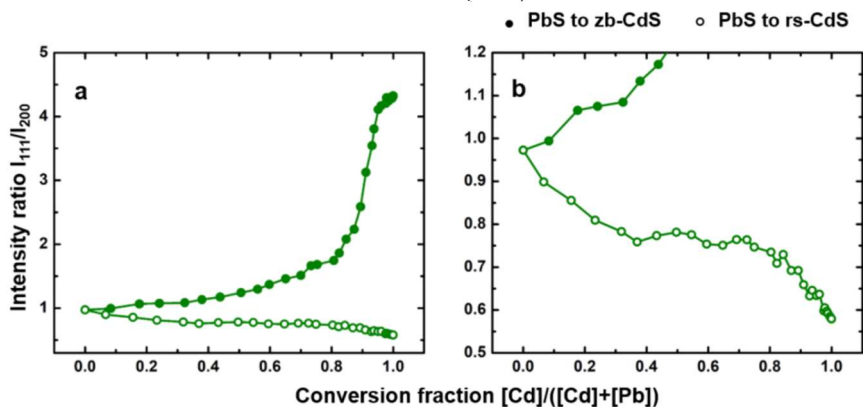


Figure 4.A.5. Results for the peak integrated intensity ratio, I_{111}/I_{200} , from fitting of Debye simulations of PbS@CdS core-shell NCs. For a zincblende CdS shell, I_{111}/I_{200} increases nearly monotonically. For a rocksalt shell, I_{111}/I_{200} decreases monotonically instead.

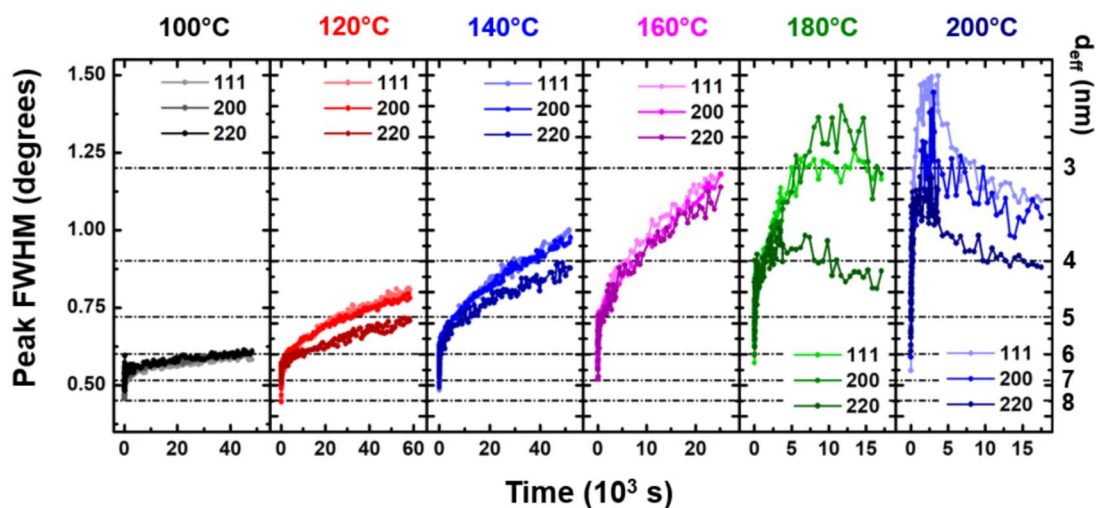


Figure 4.A.6. Extracted peak widths for the cation exchange runs from experiment 2 for (111) (light-), (200) (medium), and (220) (dark-colored) reflections. Notation is as in **Figure 4.5**. Because this experimental setup used a thinner sample, apparent peak width decreases.

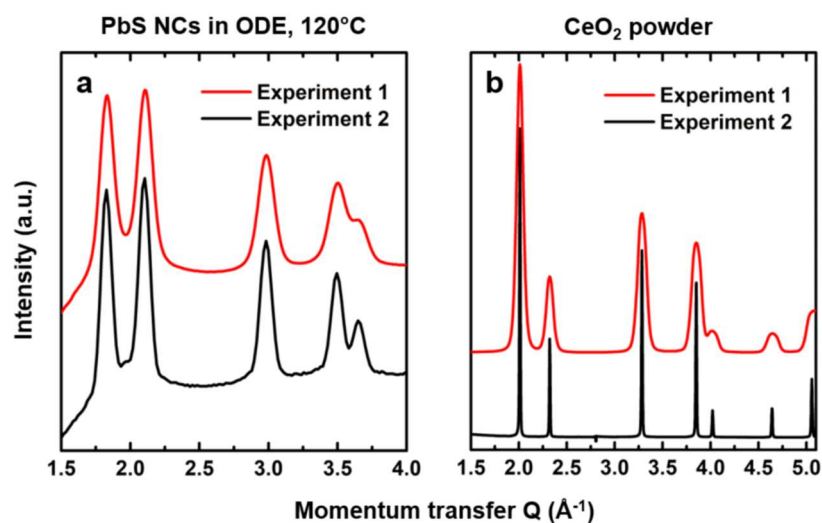


Figure 4.A.7. (a) Instrumental broadening increases the apparent width of PbS lines in experiment 1, which uses a 3.2 mm diameter capillary, versus experiment 2, which uses a 1.1 mm capillary. (b) Example of instrumental broadening of CeO₂ lines imposed by using a 3.2 mm capillary (experiment 1) versus a thin layer sandwiched between Kapton foil (experiment 2).

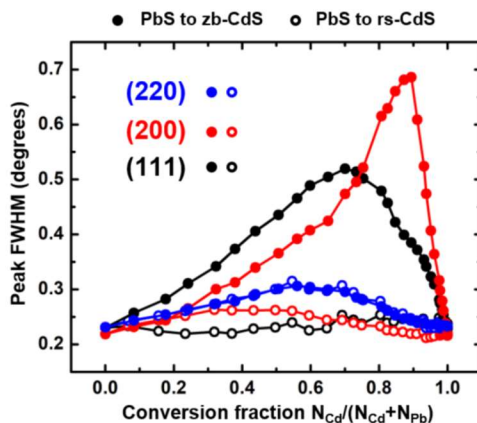


Figure 4.A.8. Results for peak width from fitting of Debye simulations of PbS@CdS core-shell NCs (simulated $\lambda = 0.3875$ Å). In accordance with experimental observations in **Figures 4.5** and **4.A.4**, the widths of (111) and (200) greatly exceed that of (220) when CdS adopts the zincblende phase. However, the width of (220) is practically unaffected by the crystal phase of CdS.

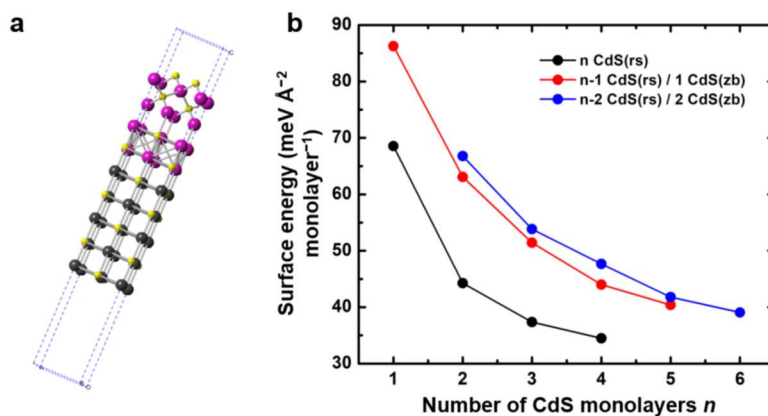


Figure 4.A.9. (a) Example of geometry used during DFT calculations for the (001) surface energy. The composition corresponds to 5 monolayers of PbS, 2 monolayers of CdS(rs), and 2 monolayers of CdS(zb) [$\text{PbS}_5\text{-CdS(rs)}_2\text{-CdS(zb)}_2$]. Yellow atoms: S; gray atoms: Pb; purple atoms: Cd. (b) The energies of configurations of n CdS monolayers corresponding from 1-4 rocksalt layers and 1-2 zincblende layers show that the energy per monolayer added increases monotonically with the number of zincblende surface layers for the configuration explored here.

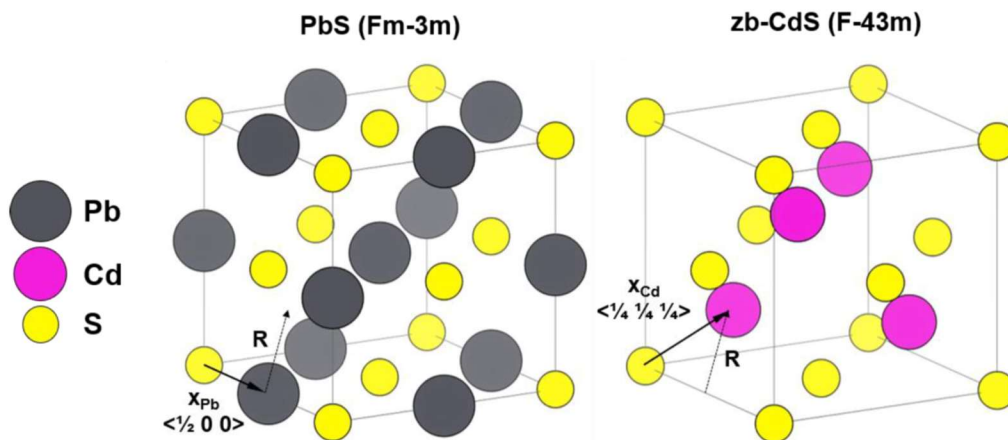


Figure 4.A.10. Unit cells of PbS and CdS showing their crystallographic relationship. The displacement vector \mathbf{R} gives the relationship between the Cd and Pb sublattices (assuming commensurate S sublattices). One possible \mathbf{R} is given by $\mathbf{X}_{\text{Cd}} - \mathbf{X}_{\text{Pb}} = \langle -\frac{1}{4} \frac{1}{4} \frac{1}{4} \rangle$, which is in the $[1\ 1\ 1]$ family of directions.

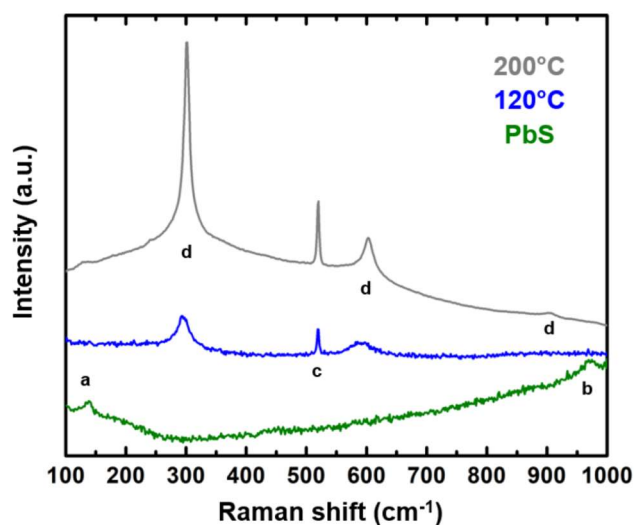


Figure 4.A.11. Raman spectrum of PbS NCs (bottom). Spectra are also shown for PbS@CdS nanocrystals in which the CdS shell was grown at 120° or 200°C for 3600 s (top), as in **Figure 4.8b** (laser power 100 mW). Assignments are as follows: (a) Pb-O stretching vibrations from photo-oxidized PbS, (b) S-O stretching vibrations from SO_4^{2-} in photo-oxidized PbS, (c) zone center optical phonon in the silicon substrate, and (d) longitudinal optical phonon in zincblende CdS (up to third order).

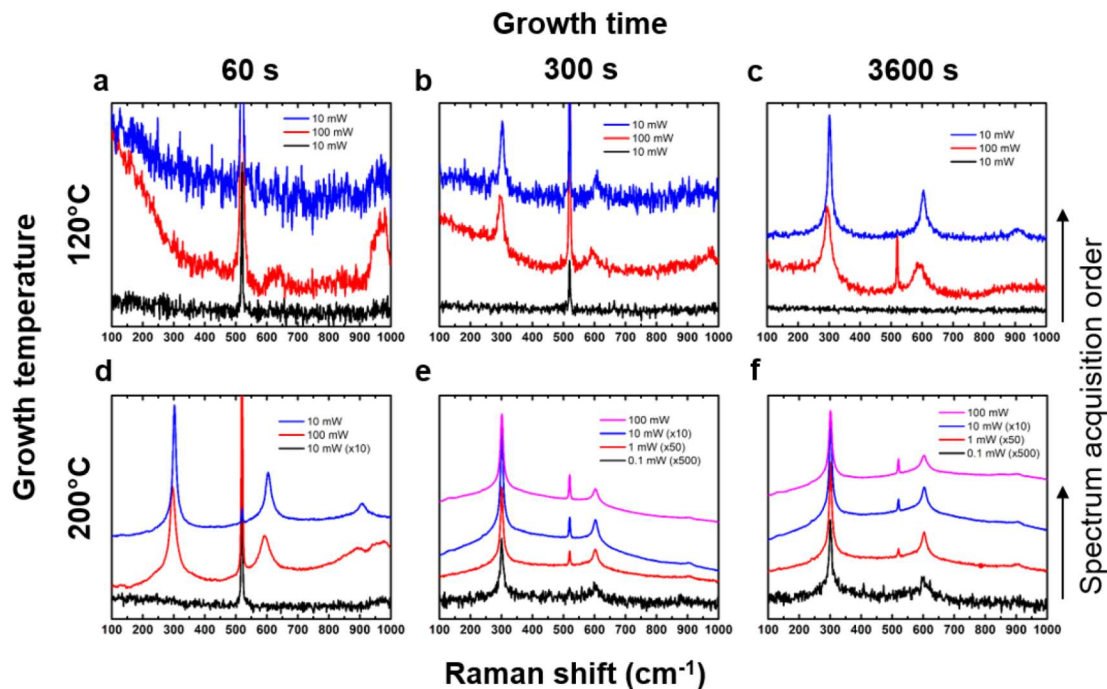


Figure 4.A.12. Raman spectra of PbS@CdS nanocrystals in which the CdS shell was grown at 120° or 200°C for various times. In (a-d), the spectrum was recorded at a power of 10 mW before increasing the laser power 10-fold to thermally transform the CdS shell to the zincblende phase (b-d) or demonstrate the absence of any zincblende phase (a). In (e-f), the laser power was increased gradually from 0.1 mW to demonstrate that the zincblende phase existed in the NCs before any additional heating was applied. The sharp line at 520 cm⁻¹ arises from the silicon substrate.

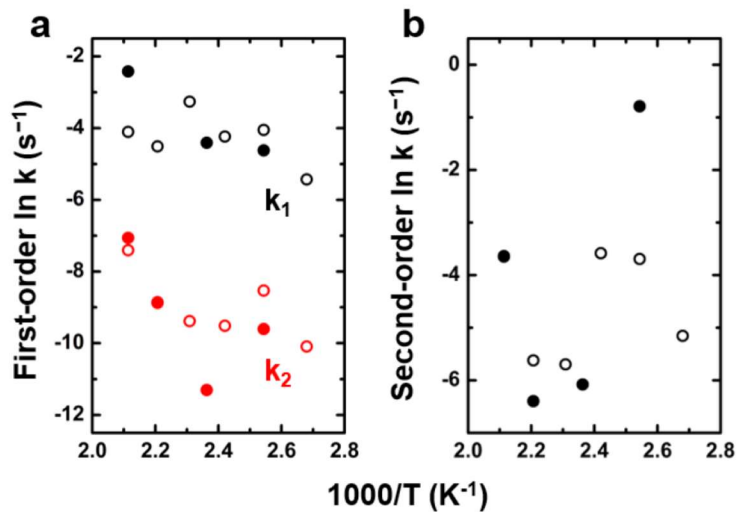


Figure 4.A.13. Arrhenius representation of extracted rate constants from whole-curve fitting of the (220) peak position showing poor linearity: (a) fit to sum of two exponentials with rate constants k_1 (black) and k_2 (red) representing a sequence of pseudo-first-order reactions; (b) fit to second-order rate law representing reaction of Cd ions in solution with random vacant sites in the NC without diffusion limitations.

Closed points: data of **Figure 4.4**; open points: data of **Figure 4.A.3**.

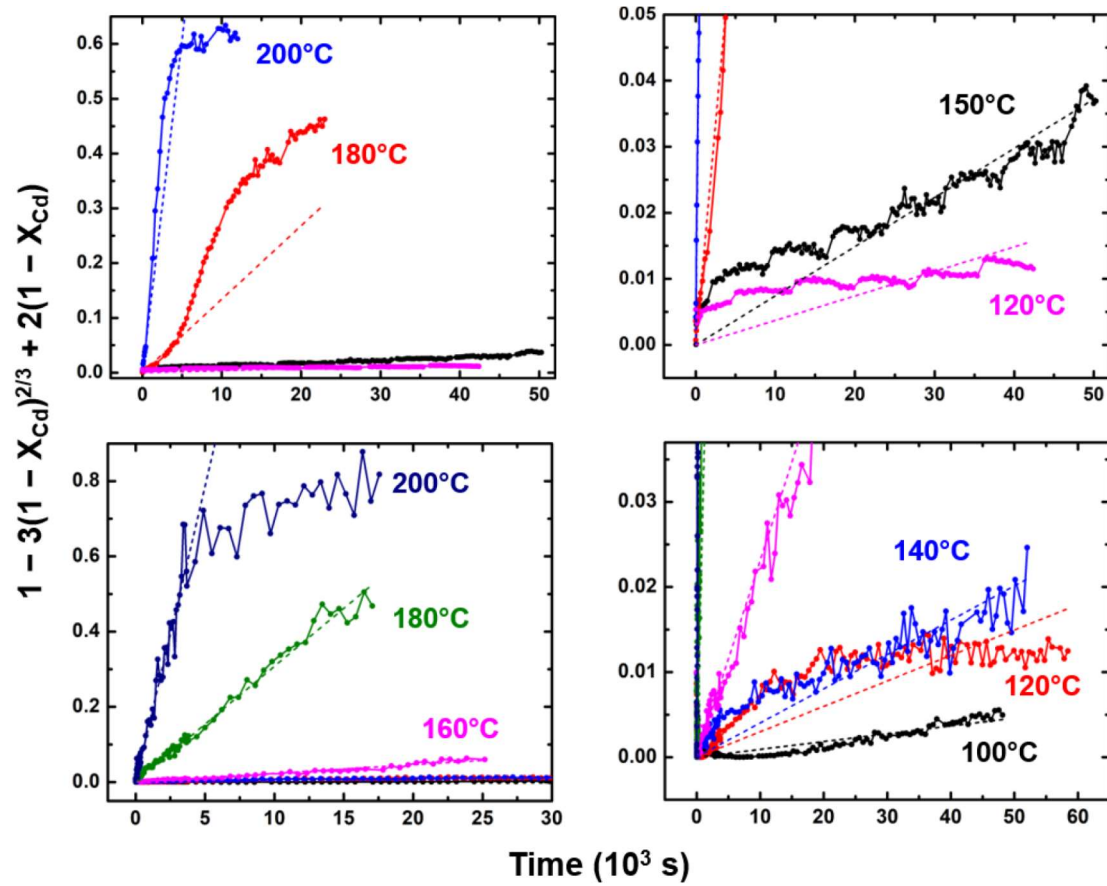


Figure 4.A.14. Shrinking core model values for experiment 1 (top) and experiment 2 (bottom). Left: full scale; right: expanded scale. The dashed lines indicate the slope obtained from the data (see **Table 4.A.3**) from which the diffusion coefficient was derived.

4.B. REFERENCES

1. Bothe, C.; Kornowski, A.; Tornatzky, H.; Schmidtke, C.; Lange, H.; Maultzsch, J.; Weller, H., Solid-State Chemistry on the Nanoscale: Ion Transport through Interstitial Sites or Vacancies? *Angewandte Chemie International Edition* **2015**, 54, 14183-14186.
2. Beberwyck, B. J.; Surendranath, Y.; Alivisatos, A. P., Cation Exchange: A Versatile Tool for Nanomaterials Synthesis. *Journal of Physical Chemistry C* **2013**, 117, 19759-19770.
3. Son, D. H.; Hughes, S. M.; Yin, Y.; Paul Alivisatos, A., Cation Exchange Reactions in Ionic Nanocrystals. *Science* **2004**, 306, 1009-1012.
4. Robinson, R. D.; Sadtler, B.; Demchenko, D. O.; Erdonmez, C. K.; Wang, L.-W.; Alivisatos, A. P., Spontaneous Superlattice Formation in Nanorods through Partial Cation Exchange. *Science* **2007**, 317, 355-358.
5. Li, H.; Zanella, M.; Genovese, A.; Povia, M.; Falqui, A.; Giannini, C.; Manna, L., Sequential Cation Exchange in Nanocrystals: Preservation of Crystal Phase and Formation of Metastable Phases. *Nano Letters* **2011**, 11, 4964–4970.
6. Fenton, J. L.; Steimle, B. C.; Schaak, R. E., Tunable Intraparticle Frameworks for Creating Complex Heterostructured Nanoparticle Libraries. *Science* **2018**, 360, 513-517.
7. Pietryga, J. M.; Werder, D. J.; Williams, D. J.; Casson, J. L.; Schaller, R. D.; Klimov, V. I.; Hollingsworth, J. A., Utilizing the Lability of Lead Selenide to Produce Heterostructured Nanocrystals with Bright, Stable Infrared Emission. *Journal of the American Chemical Society* **2008**, 130, 4879-4885.
8. Kroupa, D. M.; Hughes, B. K.; Miller, E. M.; Moore, D. T.; Anderson, N. C.; Chernomordik, B. D.; Nozik, A. J.; Beard, M. C., Synthesis and Spectroscopy of

- Silver-Doped PbSe Quantum Dots. *Journal of the American Chemical Society* **2017**, 139, 10382-10394.
9. Ha, D.-H.; Caldwell, A. H.; Ward, M. J.; Honrao, S.; Mathew, K.; Hovden, R.; Koker, M. K. A.; Muller, D. A.; Hennig, R. G.; Robinson, R. D., Solid-Solid Phase Transformations Induced through Cation Exchange and Strain in 2D Heterostructured Copper Sulfide Nanocrystals. *Nano Letters* **2014**, 14, 7090-7099.
10. Maier, J., Point-Defect Thermodynamics and Size Effects. *Solid State Ionics* **2000**, 131, 13-22.
11. Dalpian, G. M.; Chelikowsky, J. R., Self-Purification in Semiconductor Nanocrystals. *Physical Review Letters* **2006**, 96, 226802.
12. Chan, T. L.; Zayak, A. T.; Dalpian, G. M.; Chelikowsky, J. R., Role of Confinement on Diffusion Barriers in Semiconductor Nanocrystals. *Physical Review Letters* **2009**, 102, 025901.
13. Neo, D. C. J.; Cheng, C.; Stranks, S. D.; Fairclough, S. M.; Kim, J. S.; Kirkland, A. I.; Smith, J. M.; Snaith, H. J.; Assender, H. E.; Watt, A. A. R., Influence of Shell Thickness and Surface Passivation on PbS/CdS Core/Shell Colloidal Quantum Dot Solar Cells. *Chemistry of Materials* **2014**, 26, 4004-4013.
14. Zhao, H.; Chaker, M.; Ma, D., Effect of CdS Shell Thickness on the Optical Properties of Water-Soluble, Amphiphilic Polymer-Encapsulated PbS/CdS Core/Shell Quantum Dots. *Journal of Materials Chemistry* **2011**, 21, 17483-17491.
15. Justo, Y.; Sagar, L. K.; Flamee, S.; Zhao, Q.; Vantomme, A.; Hens, Z., Less is More. Cation Exchange and the Chemistry of the Nanocrystal Surface. *ACS Nano* **2014**, 8, 7948-7957.
16. Justo, Y.; Geiregat, P.; Hoecke, K. V.; Vanhaecke, F.; De Mello Donega, C.; Hens, Z., Optical Properties of PbS/CdS Core/Shell Quantum Dots. *Journal of Physical Chemistry C* **2013**, 117, 20171-20177.

17. Lechner, R. T.; Fritz-Popovski, G.; Yarema, M.; Heiss, W.; Hoell, A.; Schüllli, T. U.; Primetzhofer, D.; Eibelhuber, M.; Paris, O., Crystal Phase Transitions in the Shell of PbS/CdS Core/Shell Nanocrystals Influences Photoluminescence Intensity. *Chemistry of Materials* **2014**, 26, 5914-5922.
18. Hewavitharana, I. K.; Brock, S. L., When Ligand Exchange Leads to Ion Exchange: Nanocrystal Facets Dictate the Outcome. *ACS Nano* **2017**, 11, 11217–11224.
19. Casavola, M.; van Huis, M. A.; Bals, S.; Lambert, K.; Hens, Z.; Vanmaekelbergh, D., Anisotropic Cation Exchange in PbSe/CdSe Core/Shell Nanocrystals of Different Geometry. *Chemistry of Materials* **2012**, 24, 294-302.
20. Lambert, K.; De Geyter, B.; Moreels, I.; Hens, Z., PbTe|CdTe Core|Shell Particles by Cation Exchange, a HR-TEM Study. *Chemistry of Materials* **2009**, 21, 778-780.
21. Chakraborty, P.; Jin, Y.; Barrows, C. J.; Dunham, S. T.; Gamelin, D. R., Kinetics of Isovalent (Cd^{2+}) and Aliovalent (In^{3+}) Cation Exchange in $\text{Cd}_{1-x}\text{Mn}_x\text{Se}$ Nanocrystals. *Journal of the American Chemical Society* **2016**, 138, 12885-12893.
22. Moser, A.; Yarema, M.; Lin, W. M. M.; Yarema, O.; Yazdani, N.; Wood, V., In Situ Monitoring of Cation-Exchange Reaction Shell Growth on Nanocrystals. *The Journal of Physical Chemistry C* **2017**, 121, 24345-24351.
23. Kumar, V.; Kröger, F. A., Self-Diffusion and the Defect Structure of Cadmium Sulfide. *Journal of Solid State Chemistry* **1971**, 3, 387-400.
24. Van Dyck, D.; Van Tendeloo, G.; Amelinckx, A., Diffraction Effects due to a Single Translation Interface in a Small Crystal. *Ultramicroscopy* **1984**, 15, 357-370.
25. Qadri, S. B.; Yang, J. P.; Skelton, E. F.; Ratna, B. R., Evidence of Strain and Lattice Distortion in Lead Sulfide Nanocrystallites. *Applied Physics Letters* **1997**, 70, 1020-1021.

26. Bertolotti, F.; Dirin, D. N.; Ibáñez, M.; Krumeich, F.; Cervellino, A.; Frison, R.; Voznyy, O.; Sargent, E. H.; Kovalenko, M. V.; Guagliardi, A.; Masciocchi, N., Crystal Symmetry Breaking and Vacancies in Colloidal Lead Chalcogenide Quantum Dots. *Nature Materials* **2016**, 15, 987-994.
27. Hendricks, M. P.; Campos, M. P.; Cleveland, G. T.; Jen-La Plante, I.; Owen, J. S., A Tunable Library of Substituted Thiourea Precursors to Metal Sulfide Nanocrystals. *Science* **2015**, 348, 1226-1230.
28. Huang, F.; Banfield, J., Size-Dependent Phase Transformation Kinetics in Nanocrystalline ZnS. *Journal of the American Chemical Society* **2005**, 127, 4523-4529.
29. Spurr, R. A.; Myers, H., Quantitative Analysis of Anatase-Rutile Mixtures with an X-ray Diffractometer. *Analytical Chemistry* **1957**, 29, 760-762.
30. Abel, K. A.; FitzGerald, P. A.; Wang, T.-Y.; Regier, T. Z.; Raudsepp, M.; Ringer, S. P.; Warr, G. G.; van Veggel, F. C. J. M., Probing the Structure of Colloidal Core/Shell Quantum Dots Formed by Cation Exchange. *Journal of Physical Chemistry C* **2012**, 116, 3968–3978.
31. Gilbert, B.; Zhang, H.; Chen, B.; Kunz, M.; Huang, F.; Banfield, J. F., Compressibility of Zinc Sulfide Nanoparticles. *Physical Review B* **2006**, 74, 115405.
32. Hamachi, L. S.; Plante, I. J.-L.; Coryell, A. C.; Roo, J. D.; Owen, J. S., Kinetic Control over CdS Nanocrystal Nucleation Using a Library of Thiocarbonates, Thiocarbamates, and Thioureas. *Chemistry of Materials* **2017**, 29, 8711–8719.
33. Peters, J. L.; van den Bos, K. H. W.; Van Aert, S.; Goris, B.; Bals, S.; Vanmaekelbergh, D., Ligand-Induced Shape Transformation of PbSe Nanocrystals. *Chemistry of Materials* **2017**, 29, 4122-4128.
34. Bethke, P. M.; Barton, P. B., Sub-Solidus Relations in the System PbS-CdS. *American Mineralogist* **1971**, 1971, 2034-2039.

35. Shibata, T.; Bunker, B. A.; Zhang, Z.; Meisel, D.; Vardeman, C. F.; Gezelter, J. D., Size-Dependent Spontaneous Alloying of Au–Ag Nanoparticles. *Journal of the American Chemical Society* **2002**, 124, 11989–11996.
36. Jesser, W. A.; Schamp, C. T., Nanoparticle Semiconductor Compositions in the Miscibility Gap. *physica status solidi c* **2008**, 5, 539-544.
37. Burch, D.; Bazant, M. Z., Size-Dependent Spinodal and Miscibility Gaps for Intercalation in Nanoparticles. *Nano Letters* **2009**, 9, 3795–3800.
38. Groiss, H.; Hesser, G.; Heiss, W.; Schäffler, F.; Leitsmann, R.; Bechstedt, F.; Koike, K.; Yano, M., Coherent {001} Interfaces between Rocksalt and Zinc-Blende Crystal Structures. *Physical Review B* **2009**, 79, 235331.
39. Chuang, C.-H. M.; Brown, P. R.; Bulović, V.; Bawendi, M. G., Improved Performance and Stability in Quantum Dot Solar Cells through Band Alignment Engineering. *Nature Materials* **2014**, 13, 796-801.
40. Lai, L.-H.; Protesescu, L.; Kovalenko, M. V.; Loi, M. A., Sensitized Solar Cells with Colloidal PbS–CdS Core–Shell Quantum Dots. *Physical Chemistry Chemical Physics* **2014**, 16, 736-742.
41. Tolbert, S. H.; Herhold, A. B.; Johnson, C. S.; Alivisatos, A. P., Comparison of Quantum Confinement Effects on the Electronic Absorption Spectra of Direct and Indirect Gap Semiconductor Nanocrystals. *Physical Review B* **1994**, 73, 3266-3269.
42. Martín-Rodríguez, R.; González, J.; Valiente, R.; Aguado, F.; Santamaría-Pérez, D.; Rodríguez, F., Reversibility of the Zinc-Blende to Rock-Salt Phase Transition in Cadmium Sulfide Nanocrystals. *Journal of Applied Physics* **2012**, 111, 063516.
43. Alayoglu, S.; Zavalij, P.; Eichhorn, B.; Wang, Q.; Frenkel, A.; Chupas, P., Structural and Architectural Evaluation of Bimetallic Nanoparticles: A Case Study of Pt–Ru Core–Shell and Alloy Nanoparticles. *ACS Nano* **2009**, 3, 3127-3137.

44. Bals, S.; Casavola, M.; Huis, M. A. v.; Aert, S. V.; Batenburg, K. J.; Tendeloo, G. V.; Vanmaekelbergh, D., Three-Dimensional Atomic Imaging of Colloidal Core-Shell Nanocrystals. *Nano letters* **2011**, 11, 3420-3424.
45. Guinier, A., *X-Ray Diffraction in Crystals, Imperfect Crystals, and Amorphous Bodies*. Dover: Mineola, New York, 1994.
46. Ovsyannikov, S. V.; Ponosov, Y. S.; Shchennikov, V. V.; Mogilenskikh, V. E., Raman Spectra of Lead Chalcogenide Single Crystals. *physica status solidi c* **2004**, 1, 3110-3113.
47. Krauss, T. D.; Wise, F. W.; Tanner, D. B., Observation of Coupled Vibrational Modes of a Semiconductor Nanocrystal. *Physical Review Letters* **1996**, 76, 1376-1379.
48. Blackburn, J. L.; Chappell, H.; Luther, J. M.; Nozik, A. J.; Johnson, J. C., Correlation between Photooxidation and the Appearance of Raman Scattering Bands in Lead Chalcogenide Quantum Dots. *Journal of Physical Chemistry Letters* **2011**, 2, 599-603.
49. Batonneau, Y.; Bremard, C.; Laureyns, J.; Merlin, J. C., Microscopic and Imaging Raman Scattering Study of PbS and Its Photo-Oxidation Products. *Journal of Raman Spectroscopy* **2000**, 31, 1113-1119.
50. Dzhagan, V. M.; Valakh, M. Y.; Milekhin, A. G.; Yeryukov, N. A.; Zahn, D. R. T.; Cassette, E.; Pons, T.; Dubertret, B., Raman- and IR-Active Phonons in CdSe/CdS Core/Shell Nanocrystals in the Presence of Interface Alloying and Strain. *Journal of Physical Chemistry C* **2013**, 117, 18225–18233.
51. Chen, Y.; Vela, J.; Htoon, H.; Casson, J. L.; Werder, D. J.; Bussian, D. A.; Klimov, V. I.; Hollingsworth, J. A., “Giant” Multishell CdSe Nanocrystal Quantum Dots with Suppressed Blinking. *Journal of the American Chemical Society* **2008**, 130, 5026–5027.

52. Nan, W.; Niu, Y.; Qin, H.; Cui, F.; Yang, Y.; Lai, R.; Lin, W.; Peng, X., Crystal Structure Control of Zinc-Blende CdSe/CdS Core/Shell Nanocrystals: Synthesis and Structure-Dependent Optical Properties. *Journal of the American Chemical Society* **2012**, 134, 19685–19693.
53. Gong, K.; Kelley, D. F., Lattice Strain Limit for Uniform Shell Deposition in Zincblende CdSe/CdS Quantum Dots. *Journal of Physical Chemistry Letters* **2015**, 6, 1559-1562.
54. Cretí, A.; Zavelani-Rossi, M.; Lanzani, G.; Anni, M.; Manna, L.; Lomascolo, M., Role of the Shell Thickness in Stimulated Emission and Photoinduced Absorption in CdSe Core/Shell Nanorods. *Physical Review B* **2006**, 73, 165410.
55. Koscher, B. A.; Bronstein, N. D.; Olshansky, J. H.; Bekenstein, Y.; Alivisatos, A. P., Surface- vs Diffusion-Limited Mechanisms of Anion Exchange in CsPbBr₃ Nanocrystal Cubes Revealed through Kinetic Studies. *Journal of the American Chemical Society* **2016**, 138, 12065-12068.
56. Fan, Z.; Lin, L.-C.; Buijs, W.; Vlught, T. J. H.; Huis, M. A. v., Atomistic Understanding of Cation Exchange in PbS Nanocrystals using Simulations with Pseudoligands. *Nature Communications* **2016**, 7, 11503.
57. Roy, S.; Bhandari, S.; Chattopadhyay, A., Quantum Dot Surface Mediated Unprecedented Reaction of Zn²⁺ and Copper Quinolate Complex. *Journal of Physical Chemistry C* **2015**, 119, 21191–21197.
58. Erwin, S. C.; Zu, L.; Haftel, M. I.; Efros, A. L.; Kennedy, T. a.; Norris, D. J., Doping Semiconductor Sanocrystals. *Nature* **2005**, 436, 91-94.
59. Kerisit, S.; Parker, S. C., Free Energy of Adsorption of Water and Metal Ions on the {10-14} Calcite Surface. *Journal of the American Chemical Society* **2004**, 126, 10152-10161.

60. Murphy, R.; Strongin, D. R., Surface Reactivity of Pyrite and Related Sulfides. *Surface Science Reports* **2009**, 64, 1-45.
61. Boparai, H. K.; Joseph, M.; O'Carroll, D. M., Kinetics and Thermodynamics of Cadmium ion Removal by Adsorption onto Nano Zerovalent Iron Particles. *Journal of Hazardous Materials* **2011**, 186, 458-465.
62. Lakshmipathiraj, P.; Narasimhan, B. R. V.; Prabhakar, S.; Raju, G. B., Adsorption of Arsenate on Synthetic Goethite from Aqueous Solutions. *Journal of Hazardous Materials* **2006**, 136, 281-287.
63. Argun, M. E., Use of Clinoptilolite for the Removal of Nickel Ions from Water: Kinetics and Thermodynamics. *Journal of Hazardous Materials* **2008**, 150, 587-595.
64. Crank, J., *The Mathematics of Diffusion*. 2nd ed.; Clarendon Press: Oxford, 1975.
65. Ethayaraja, M.; Bandyopadhyaya, R., Model for Core–Shell Nanoparticle Formation by Ion-Exchange Mechanism. *Industrial & Engineering Chemistry Research* **2008**, 47, 5982-5985.
66. Levenspiel, O., *Chemical Reaction Engineering*. 3rd ed.; John Wiley and Sons: New York, 1999.
67. Fedorov, V. A.; Ganshin, V. A.; Korkishko, Y. N., Ion Exchange in II-VI Crystals: Thermodynamics, Kinetics, and Technology. *physica status solidi a* **1993**, 139, 9-65.
68. Simkovich, G.; Wagner, J. B., Self-Diffusion of Lead 210 in Single Crystals of Lead Sulfide as a Function of Stoichiometry and Doping Additions. *Journal of Chemical Physics* **1963**, 38, 1368-1375.
69. Mehrer, H., *Diffusion in Solids*. Springer: Heidelberg, 2007.

70. Yin, Y.; Rioux, R. M.; Erdonmez, C. K.; Hughes, S.; Somorjai, G. A.; Alivisatos, A. P., Formation of Hollow Nanocrystals through the Nanoscale Kirkendall Effect. *Science* **2004**, 304, 711-714.
71. Ha, D.-H.; Moreau, L. M.; Honrao, S.; Hennig, R. G.; Robinson, R. D., The Oxidation of Cobalt Nanoparticles into Kirkendall-Hollowed CoO and Co₃O₄: The Diffusion Mechanisms and Atomic Structural Transformations. *Journal of Physical Chemistry C* **2013**, 117, 14303-14312.
72. Shewmon, P. G., *Diffusion in Solids*. 2nd ed.; Minerals, Metals, & Materials Society: Warrendale, Pa., 1989.
73. Stevenson, D. A., Diffusion in the Chalcogenides of Zn, Cd, and Pb. In *Atomic Diffusion in Semiconductors*, Shaw, D., Ed. Plenum Publishing Company: New York, 1973.
74. Tschirner, N.; Lange, H.; Schliwa, A.; Biermann, A.; Thomsen, C.; Lambert, K.; Gomes, R.; Hens, Z., Interfacial Alloying in CdSe/CdS Heteronanocrystals: A Raman Spectroscopy Analysis. *Chemistry of Materials* **2012**, 24, 311-318.
75. Dandrea, R. G.; Duke, C. B., Strain-induced interdiffusion at semiconductor interfaces. *Physical Review B* **1992**, 45, 14065-14068.
76. Nakagawa, N.; Hwang, H. Y.; Muller, D. A., Why Some Interfaces Cannot be Sharp. *Nature Materials* **2006**, 5, 204-209.
77. Gillin, W. P.; Dunstan, D. J., Strain and interdiffusion in semiconductor heterostructures. *Physical Review B* **1994**, 50, 7495-7498.
78. Cabot, A.; Smith, R. K.; Yin, Y.; Zheng, H.; Reinhard, B. M.; Liu, H.; Alivisatos, A. P., Sulfidation of Cadmium at the Nanoscale. *ACS Nano* **2008**, 2, 1452-1458.

79. Sung, Y.-M.; Lee, Y.-J.; Park, K.-S., Kinetic Analysis for Formation of Cd_{1-x}Zn_xSe Solid-Solution Nanocrystals. *Journal of the American Chemical Society* **2006**, *128*, 9002-9003.
80. Wright, K.; Gale, J. D., Interatomic Potentials for the Simulation of the Zinc-Blende and Wurtzite Forms of ZnS and CdS: Bulk Structure, Properties, and Phase Stability. *Physical Review B* **2004**, *70*, 035211.
81. Habenschuss, A.; Narten, A. H., X-ray Diffraction Study of Some Liquid Alkanes. *Journal of Chemical Physics* **1990**, *92*, 5692-5699.
82. Zobel, M.; Neder, R. B.; Kimber, S. A. J., Universal Solvent Restructuring Induced by Colloidal Nanoparticles. *Science* **2015**, *347*, 201-204.
83. García-Rodríguez, R.; Liu, H., Solution Structure of Cadmium Carboxylate and Its Implications for the Synthesis of Cadmium Chalcogenide Nanocrystals. *Chemical Communications* **2013**, *49*, 7857-7859.
84. Nevers, D. R.; Williamson, C. B.; Savitzky, B. H.; Hadar, I.; Banin, U.; Kourkoutis, L. F.; Hanrath, T.; Robinson, R. D., Mesophase Formation Stabilizes High-purity Magic-sized Clusters. *Journal of the American Chemical Society* **2018**, *140*, 3652–3662.
85. Ashiotis, G.; Deschildre, A.; Nawaz, Z.; Wright, J. P.; Karkoulis, D.; Picca, F. E.; Kieffer, J., The Fast Azimuthal Integration Python Library: pyFAI. *Journal of Applied Crystallography* **2015**, *48*, 510-519.
86. Toby, B. H.; Von Dreele, R. B., GSAS-II: the Genesis of a Modern Open-Source All Purpose Crystallography Software Package. *Journal of Applied Crystallography* **2013**, *46*, 544-549.
87. Kresse, G.; Hafner, J., Ab initio Molecular Dynamics for Liquid Metals. *Physical Review B* **1993**, *47*, 558.

88. Kresse, G.; Hafner, J., Ab initio Molecular-Dynamics Simulation of the Liquid-Metal–Amorphous-Semiconductor Transition in Germanium. *Physical Review B* **1994**, 49, 14251.
89. Kresse, G.; Furthmüller, J., Efficiency of ab-initio Total Energy Calculations for Metals and Semiconductors Using a Plane-Wave Basis Set. *Computational Materials Science* **1996**, 6, 15-50.
90. Kresse, G.; Furthmüller, J., Efficient Iterative Schemes for ab initio Total-Energy Calculations Using a Plane-Wave Basis Set. *Physical Review B* **1996**, 54, 11169.
91. Perdew, J. P.; Burke, K.; Ernzerhof, M., Generalized Gradient Approximation Made Simple. *Physical Review Letters* **1996**, 77, 3865.
92. Blöchl, P. E., Projector Augmented-Wave Method. *Physical Review B* **1994**, 50, 17953.
93. Kresse, G.; Joubert, D., From Ultrasoft Pseudopotentials to the Projector Augmented-Wave Method. *Physical Review B* **1999**, 59, 1758.
94. Monkhorst, H. J.; Pack, J. D., Special Points for Brillouin-Zone Integrations. *Physical Review B* **1976**, 13, 5188.
95. Jónsson, H.; Mills, G.; Jacobsen, K. W., Nudged Elastic Band Method for Finding Minimum Energy Paths of Transition. In *Classical and quantum dynamics in condensed phase simulations*, World Scientific: 1998; pp 385-404.
96. Jain, A.; Ong, S. P.; Hautier, G.; Chen, W.; Richards, W. D.; Dacek, S.; Cholia, S.; Gunter, D.; Skinner, D.; Ceder, G.; Persson, K. A., Commentary: The Materials Project: A Materials Genome Approach to Accelerating Materials Innovation. *APL Materials* **2013**, 1, 011002.

CHAPTER 5

5 ASSESSMENT OF SOFT LIGAND REMOVAL STRATEGIES: ALKYLATION AS A PROMISING ALTERNATIVE TO HIGH-TEMPERATURE TREATMENTS FOR COLLOIDAL NANOPARTICLE SURFACES *

5.1. ABSTRACT

Advances in nanocrystal syntheses over the past decades now enable routine manipulation of particle shape, size, and chemistry with unprecedented precision. Building on decades of knowledge in colloidal chemistry, researchers have created notable high-performance, low-cost energy conversion catalysts. However, in almost all cases, controlling the surface chemistry—in particular, to remove the surfactants used during the syntheses—is a challenge. Aggressive physical treatments such as thermal pyrolysis and plasma etching have become the methods of choice, but these aggressive treatments test the material's phase and chemical stability. In this work, we analyze softer methods to post-synthetically remove surfactants using chemical treatments. We performed various surface treatments to deprotect colloidal nanocrystals of a well-known electrocatalyst, manganese oxide (Mn_3O_4), passivated with hydrophobic ligands. We employed a suite of characterization techniques (transmission electron microscopy, infrared spectroscopy, voltammetry, and thermogravimetric analysis) to evaluate their surface chemistry. Although the four studied treatments (bases, alkylating agents, Lewis acids, or heat) could remove nearly all organic ligands, the surface chemistries of the treated nanomaterials differed

* Adapted from the manuscript: Nelson, A.; Zong, Y.; Fritz, K.E.; Suntivich, J.; and Robinson, R.D., Assessment of Soft Ligand Removal Strategies: Alkylation as a Promising Alternative to High-Temperature Treatments for Colloidal Nanoparticle Surfaces. Under review at *ACS Materials Letters*.

significantly from treatment to treatment. These chemical differences arise from the reactions between the treatment agent and the surfactant or from side reactions of the agent with atmospheric water or carbon dioxide, leaving behind residues such as hydrolyzed ligand removal agent, metal hydroxide, and metal carbonate on the surface. From our study we find that treatment using alkylating agents is the most promising approach for soft room-temperature stripping of nanocrystal ligands, producing Mn_3O_4 with the highest electrochemical activity.

5.2. INTRODUCTION

The search for high-performance, inexpensive, and scalable catalysts for renewable energy storage and conversion is one of the biggest challenges facing the scientific community in the 21st century. Being a surface phenomenon, heterogeneous (electro)catalysis relies on a solid catalyst, whose surface chemistry still presents a formidable obstacle to optimization. In order to explain catalyst performance in terms of parameters such as particle size and surface orientation, well-defined model systems must be prepared: that is, nanoparticles with sharp size distributions and well-defined shape must be isolated. Thus far, the best strategies for preparing size-controlled nanoparticles have come from research on colloidal nanocrystals (NCs), where solution chemistry can tightly control morphology (size, shape, and surface orientation), stoichiometry, and electronic properties.^{1,2} In addition to allowing size effects to be assessed, the monodispersity afforded by the NC syntheses can allow the assignment of activities to the specific crystal planes.

Current NC syntheses require metal-binding surfactants, i.e., ligands, to control particle solubility, growth rates, and relative surface energies.³ For applications requiring pristine surfaces, the ligands (usually hydrocarbons functionalized with polar

head groups) must be removed, as otherwise they could interfere with the catalyst performance. For example, in electronic devices, the ligands are insulating and can prevent electron transfer to/from the particles.⁴⁻⁶ In catalysis, the ligands can block the catalysts from participating in the reaction.^{7, 8} While numerous protocols for physically and/or chemically removing ligands from NCs have been studied, such as thermal annealing,⁹ ligand displacement through chemical treatment,¹⁰⁻¹² ligand leaching into excess solvent,¹³ plasma cleaning,^{14, 15} and electrochemical activation,^{7, 16} their efficacies were often studied in isolation. As a result, it has been unclear how effective the removal methods are compared to each other.

5.3. RESULTS AND DISCUSSION

In this work, we compare four methods for ligand removal. We focus on post-synthetic chemical treatments with inorganic base, alkylating agent, or Lewis acid, and with heat (**Figure 5.1**). We term these procedures the “base,” “alkylation,” “Lewis acid,” and “thermal” methods, respectively. We focus on manganese(II,III) oxide (Mn_3O_4), a well-known electrocatalyst for several electrochemical reactions, as our model system. Mn_3O_4 and other Mn oxides have been investigated by many groups for their oxygen reduction reaction (ORR) and oxygen evolution reaction (OER) activity.¹⁷⁻²² Both ORR and OER are of critical importance to future renewable electrochemical energy technologies and have been exhaustively researched due to the lack of a suitable high-activity, low-cost replacement for Pt-based catalyst systems.²³⁻²⁶ Mn_3O_4 and related Mn oxides have recently stood out among some of the possible candidates for Pt replacement.¹⁷⁻²² In addition to being inexpensive and nontoxic metal oxides, Mn oxides also have been targeted by nanoparticle synthesis groups, and

several colloidal synthesis approaches have been found.²⁷⁻³¹ Mn-oxides are thus a relevant model system for our surface chemistry studies.

We show through transmission electron microscopy (TEM) that the model oxide NC morphology and crystal phase are stable when treated with the four studied strategies. However, their surface chemistries are clearly different, as shown by infrared spectroscopy, cyclic voltammetry, and thermal analyses, implying each treatment is associated with a particular set of side reactions or surface changes. Thermal treatment is effective at cleaning off surface ligands; however, heat-treating the NCs also results in agglomeration of nanoparticles and loss in electrochemically active surface area. Chemical treatments with base and Lewis acid leave residual contaminants and blocking layers that can reduce effective surface area. Alkylation offers a way to avoid both thermal and chemical degradation, making it an effective treatment protocol for future studies on nanocrystal catalysts. Our systematic examination of post-synthetic chemical strategies for cleaning the NC surface provides a guideline on how to enhance the NC surface reactivity and emphasizes a need for surface characterizations to understand the nature of the NC surface chemistry beyond bulk parameters.

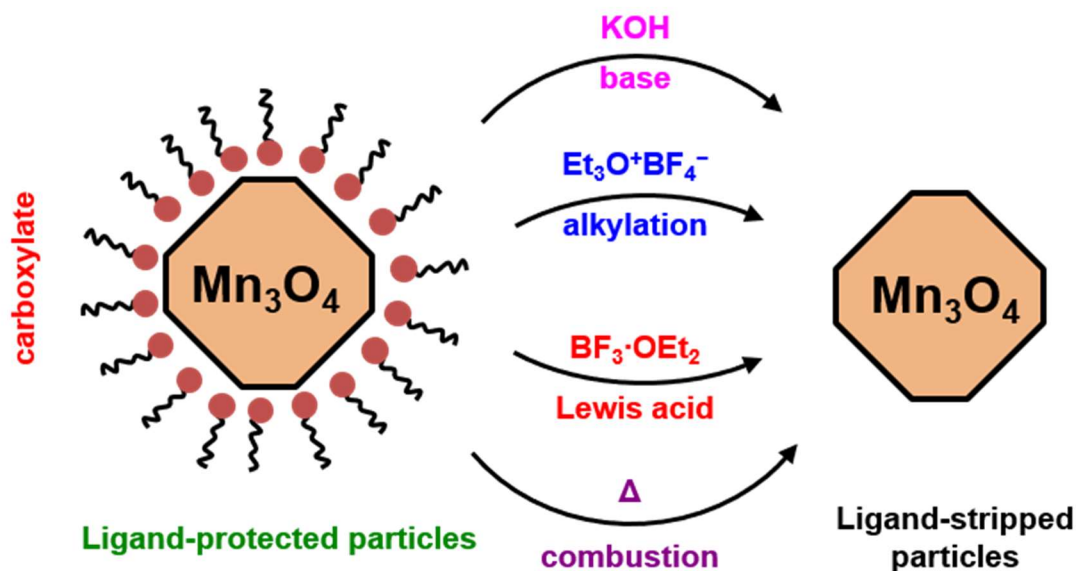
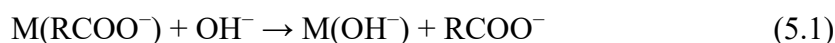


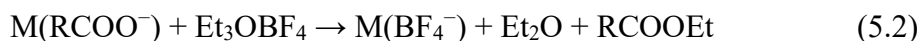
Figure 5.1. Schematic of surface treatments to remove ligands from metal oxide surfaces for electrocatalysis. Four popular ligand removal strategies were evaluated: bases (potassium hydroxide) displace ligands e.g., with hydroxyl groups; alkylating agents (triethyloxonium tetrafluoroborate) displace carboxylate ligands by esterification; Lewis acids (boron trifluoride as diethyl ether complex) form dative bonds with ligands; and heating in air (300°C) removes ligands by combustion.

The “base” method is the metathesis reaction between the carboxylate-passivated surface and an inorganic base such as potassium hydroxide (KOH) in alcohol solution.



Here, R is a hydrocarbon group ($\text{C}_{17}\text{H}_{33}$ for oleate ligands used here). Reaction with small-molecule bases has been used for phase transfer of nanocrystals from nonpolar to polar solvents,^{12, 32} removal of ligands from NCs for electronic applications,^{4, 33} and in our own work for ligand stripping.^{34, 35}

In the second method, an alkylating agent is used to strip the ligands by esterification of the COO^- moiety, for example by ethylation with triethyloxonium tetrafluoroborate (Et_3OBF_4):¹⁰



This method has been used for removing ligands from a variety of NC surface chemistries and for solubilizing hydrophobic NCs in polar solvents,¹⁰ but its impact on surface electrochemistry is unknown.

The third method, which has been used for the same purposes as the alkylation method, abstracts the ligands by reaction of the Lewis-basic carboxylate group with a Lewis acid, followed by displacement of the complex with solvent molecules. An example is the reaction of oleate-protected surfaces with boron trifluoride (as the etherate):¹¹



Finally, ligands may be removed from NCs by combustion in air at high temperatures ($>200^\circ\text{C}$, thermal method). This method has been frequently used for preparation of oxide electrocatalysts³⁶⁻³⁸ and for removing ligands from noble metal surfaces.⁷⁻⁹ While this method can be said to be a “gold standard,” the use of such extreme oxidizing conditions can strongly alter the surface chemistry of the NCs, as elevated temperature may induce unintended structural transitions and, in the case of multi-component NCs, alter compositional distributions. High temperatures may also affect particle morphology by sintering, thereby reducing the surface area,^{8,9} and decompose a metastable phase, thereby preventing an exploration of novel electrocatalysts that may not necessarily be at the room-temperature ground state.³⁴

To assess the impact of these methods on the surface chemistry and morphology of electrocatalytic materials, we synthesized colloidal Mn_3O_4 NCs by addition of water to manganese acetate in the presence of oleylamine and oleic acid in

xylene.²⁷ For electrochemical testing, Mn₃O₄ NCs were dispersed on carbon black (Vulcan XC-72) in a 1:1 mass ratio by mechanically mixing the two in hexane,³⁶ producing a Mn₃O₄/C composite.³⁹ All samples undergo one of the following ligand-removal protocols: for the base procedure, samples were suspended in a 0.1 M KOH isopropanol solution at a concentration of 1-5 mg mL⁻¹; for alkylation and Lewis acid treatments, samples were treated with a 1:1 mass ratio of NC or composite to ligand-removal agent in acetonitrile; and for thermal treatment, samples were heat-treated in air at 300°C for 1 hr. Experimental procedures and materials are given in more detail in section 5.A.2.

TEM was used to determine effects on particle size and shape following treatment of the Mn₃O₄/C composites. TEM images of the Mn₃O₄/C composites show distinguishable spherical NCs atop the amorphous carbon support. No sign of shape change was observed in the studied treatments (**Figure 5.2a**, top). The as-synthesized narrow particle size distributions (~10% relative standard deviation = the standard deviation divided by the mean, **Figure 5.2a**, bottom) were maintained with little change in size. Although a small degree of faceting cannot be ruled out at this resolution, the Mn₃O₄ NCs appear to be stable after the ligand-removal processes. BF₃ treatment is an exception: a small decrease in diameter from 7.5 to 7.0 nm (20% decrease in particle volume) was observed. The mechanism by which metal oxides such as Mn₃O₄ would be dissolved in this way can be explained by considering that the proton may be produced by hydrolysis of BF₃ if there were adventitious water in the atmosphere:⁴⁰



Having shown that the NC morphology is stable, we next examine the crystal structure after each chemical treatment. MnO_x can exist as a number of phases, including MnO, Mn₅O₈, Mn₃O₄, Mn₂O₃, etc.⁴¹⁻⁴³ To determine the crystalline phase

we examined the selected area electron diffraction (SAED) patterns from the NC ensembles following ligand removal. To avoid the contribution from carbon, we prepared films of unsupported Mn_3O_4 NCs directly on the TEM grids and performed the ligand removal procedures on these films. SAED patterns from the as-prepared NCs are in good agreement with the tetragonal Mn_3O_4 hausmannite structure (JCPDS 01-074-6605, **Figure 5.2b**). As we observed no change in the peak positions, we conclude that the phase of the NCs is stable in the presence of the ligand-removal agents used in this study. Interestingly, for alkylation and Lewis acid treatments, we observed a broad peak at an approximate momentum transfer $Q = 1.23 \text{ \AA}^{-1}$, corresponding to an interplanar distance of $d = 5.11 \text{ \AA}$. Because this peak appears only with the alkylation (containing BF_4^-) or Lewis acid (containing BF_3) treatments, we suggest that hydrolysis of the boron fluoride species (which is known to occur over time when the storage conditions are imperfect^{40, 44}) produces an amorphous residue contributing to scattering observed in SAED. However, we are not able to assign an exact structure to this feature at this time.

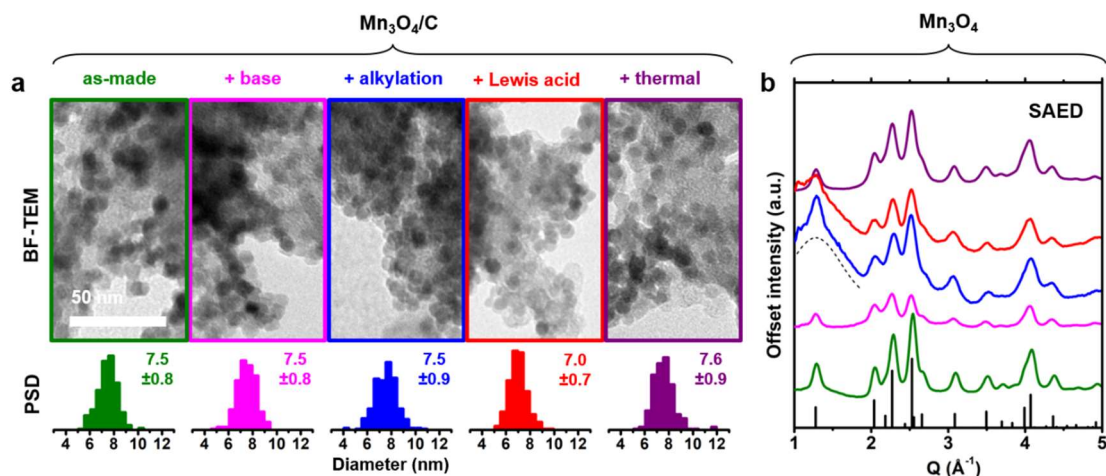


Figure 5.2. Transmission electron microscopy assessment of morphology and structure of Mn₃O₄ nanocrystals subjected to various treatments. (a) Nanocrystals supported on carbon in bright field TEM (BF-TEM, top) along with particle size distribution (PSD) histograms ($N > 300$) of measured particle diameters (bottom). Chemical or thermal treatment leaves morphology and size largely unaffected with one exception (Lewis acid). (b) Selected area electron diffraction (SAED) patterns from unsupported nanocrystals. Structure is likewise unchanged following treatment. The stick diagram gives the positions for bulk Mn₃O₄, hausmannite (JCPDS 01-074-6605), and the dashed line shows a broad line at $Q = 1.23 \text{ \AA}^{-1}$ ($d = 5.11 \text{ \AA}$). Curves have been offset for clarity.

We observe that alkylating agents or Lewis acids can etch unsupported Mn₃O₄ NCs. Specifically, the diameter of the Mn₃O₄ NCs decreased from 6.9 nm to 4.8 and 5.0 nm following the alkylation and Lewis acid exposure, respectively (**Figure 5.A.1**). The pronounced difference in the degree of etching between treatments of Mn₃O₄/C versus unsupported Mn₃O₄ is likely due to differences in the amount of Mn₃O₄ present. We confirmed this by examining the aggregates produced from NCs treated in solution (**Figure 5.A.2**). In contrast to the NCs deposited directly on a grid, no change

in diameter was seen when ligand removal conditions were more similar to those used for preparing Mn₃O₄/C composites. It is apparent that when a very small amount of NCs on a TEM grid are treated by immersion in several mL of ligand-stripping solution, the excess of alkylating agent or Lewis acid is much larger than in the case of treatment of Mn₃O₄/C, where the composite is dispersed at concentrations of 1-5 mg mL⁻¹. The etching by the alkylation agent was unexpected, and we suspect that the etching may occur indirectly via the generation of acid following hydrolysis by adventitious water in the atmosphere:⁴⁴



We did not observe any preferential etching along specific facets in Mn₃O₄ NCs. As shown in the TEM images, the samples retained their original spherical morphology after the treatment. For the purpose of this work, the most important observation from TEM is that the shape and phase of NCs appear to be unchanged after the chemical treatment. Based on assessment of the particle size distributions (PSDs), we only observed a statistically significant change in size for treatment with Lewis acid (*p*-value $\sim 10^{-15}$), while size differences were not significant for other treatments (see **Table 5.A.1** for particle size statistics). Nonetheless, to exclude the possibility of etching and size change, scrupulously dry conditions and pure reagents must be used. Otherwise, side reactions of the alkylating agent or Lewis acid with adventitious water will produce acids that can dissolve the oxide NCs.

To verify whether the treatments were able to remove the surfactant molecules tethered to the NCs, we utilize a common^{7, 10-12, 35} assay, Fourier transform infrared (FTIR) spectroscopy, to determine the presence or absence of absorption bands arising from these species. For Mn₃O₄/C composites, the strong absorption from the carbon support precluded an observation of the mid-IR region. As a result, the FTIR spectra from **Figure 5.3a** are given for unsupported NCs. The major peak assignments are

given in **Table 5.1**. The 3000-2800 cm^{-1} band (feature 1) is important, as it corresponds to the C-H stretching vibrations for alkyl and alkene moieties.⁴⁵ The absorbance in this region is an indicator of the overall surfactant content. In as-synthesized (ligand-protected) NCs, peaks from the C-H stretching vibrations were readily visible (**Figure 5.3a**, left). As expected from a ligand removal process, all treatments drastically reduce the strength of the C-H peaks, indicating the removal of oleate groups, and the signals completely disappear in the case of thermal treatment. Based on this observation, the thermal treatment is likely the most aggressive for removing the organic content from the NCs. However, the generation of inorganic carbon from the pyrolysis cannot be ruled out.⁴⁶ Since we did not observe the N-H stretching vibration band, we conclude that the oleylamine used in synthesis is removed during separation of the NCs from the solvent-surfactant mixture used during synthesis.

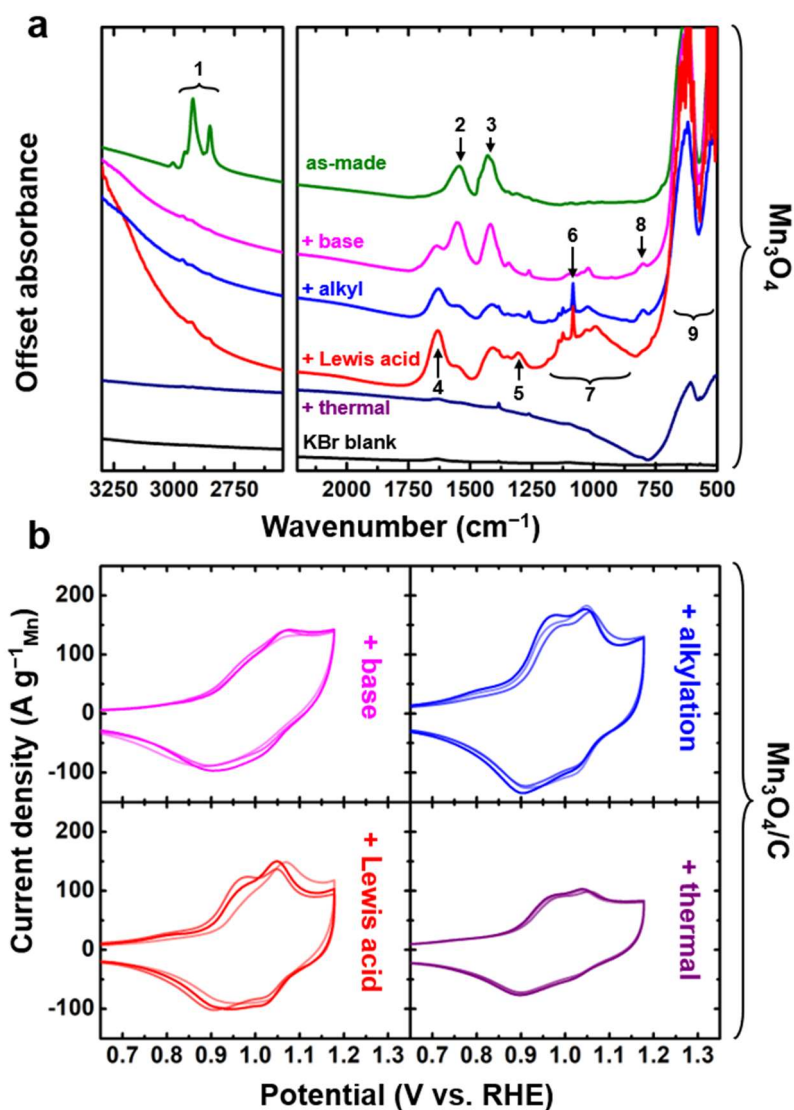
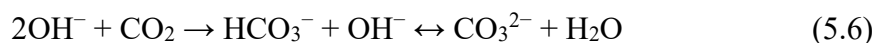


Figure 5.3. Surface chemistry of Mn_3O_4 nanocrystals subject to various treatments. (a) Fourier transform infrared spectroscopy of unsupported NCs, KBr matrix. Shown are the C-H stretching bands (left) and the lower-frequency skeletal and inorganic bands (right). Curves have been offset for clarity. For peak assignments, see main text. (b) Cyclic voltammetric characterization, with NCs supported on Vulcan XC-72. To show the reproducibility of the measurement, three electrodes are shown for each condition (lighter curves). 0.1 M KOH, Ar-saturated solution; 50 mV s^{-1} scan rate.

Table 5.1. Assignment of functional groups from infrared bands. U = untreated Mn₃O₄ nanocrystals; B = base-treated; A = alkylation-treated; L = Lewis acid-treated; T = thermally treated.

Feature No.	Range, cm ⁻¹	Width	Absent in	Strong in	Assignment
1	3000-2800	sharp	T	U	Aliphatic C-H stretch
2	1550-1540	broad	T	UB	Asymmetric COO ⁻ stretch, carbonate
3	1430-1410	broad	T	UB	Symm. COO- stretch, carbonate
4	1635-1625	broad	UT	U	H-O-H bending
5	1310-1300	broad	UBT	L	B-O stretch
6	1084	very sharp	UBT	AL	BF ₄ ⁻ asymm. B-F stretch
7	1200-800	very broad	UBT	L	O-H deformation
8	805-795	sharp	ULT	-	unknown
9	625-615	broad	-	UBALT	Mn-O lattice

The FTIR absorption bands at lower wavenumbers (**Figure 5.3a**, right) are consistent with residual inorganic species. Features 2 and 3 were observed in all samples with the exception of the thermally treated one. These features most closely correspond to the C-O vibrations from the carboxyl groups.⁴⁵ Interestingly, in all chemically treated samples the C-O peaks remain prominent, even though the C-H stretching region indicates that nearly all aliphatic hydrocarbons from the oleate ligands have been removed. Therefore, we hypothesize that such features could arise from carbonate, CO₃²⁻. The particularly strong absorbance of these peaks in the base-treated sample would appear to support this, as KOH is known to take up ambient CO₂:



We assign features 4 ($\sim 1630\text{ cm}^{-1}$) and 7 to bending and deformation vibrations from adsorbed water.⁴⁵ Both bands are most intense in the Lewis acid-treated sample, indicating the presence of hydroxyl groups either from hydrolyzed BF_3 or adsorbed to the bare oxide surfaces. Additionally, we note that in the base-, alkyl-, and acid-treated samples these two peaks are inversely related to the strength of features 2 and 3. Therefore, we propose that carbonate and water (from the atmosphere or the product of the hydrolysis) competitively adsorb onto the NC surfaces. These “contaminants” form the bulk of the passivation layer on the unsupported NCs.

Features 5 and 6 appear only in the alkyl- and Lewis acid-treated samples. Thus, we assign them to the B-F or B-O vibrations from unreacted and hydrolyzed borate species, respectively.⁴⁵ The assignment of Feature 5 agrees well with the reported locations for the B-O stretching bands, while the very sharp feature 6 originates from the stable tetrafluoroborate. A weak peak (feature 8) appears at low energies in both the base- and alkyl-treated samples; because the solution chemistries of these two treatments have no component in common, at present, we are unable to make an assignment to this peak, although it appears to be very minor.

The features (9) at 620 cm^{-1} and lower frequencies are observed in all samples. This series of peaks corresponds to the infrared-active vibrational modes of the Mn_3O_4 lattice, where the precise locations have been reported across a range of values in literature. Our peak positions of $625\text{-}610$ and $525\text{-}505\text{ cm}^{-1}$ are in good agreement with the Mn_3O_4 hausmannite phase, which is consistent with the SAED results.^{42, 47, 48} The asymmetric curvature of the baseline is suggestive of a Fano resonance as has been observed in microporous and other nanostructured oxides,^{49, 50} but identifying the origin of this resonance requires further measurements and is beyond the scope of the present paper.

In summary, our FTIR measurements show that all treatments examined are effective at removing surface alkyl groups; however, chemical treatments left behind various residues. First, carboxylate groups were apparent, suggesting that Mn_3O_4 NC surfaces react with CO_2 in the atmosphere or solutions during treatment to form carbonates on the surface.⁵¹ Chemically treated surfaces also react with atmospheric water, as indicated by the observation of adsorbed hydroxyl groups. In the case of alkylation and Lewis-acid-treated NCs, we observe boron-containing residues, which may be detrimental to the electrocatalytic activity.

To analyze the surface chemistry of treated NCs, we examined their surface electrochemical behaviors by testing the Mn_3O_4 redox couples^{52, 53} via cyclic voltammetry (CV) of the composite samples (**Figure 5.3b**). We prepared a NC ink for the composites from each treatment³⁹ (see section **5.A.2**). Three curves are shown for each treatment to show the reproducibility of the measurement. In general, two oxidation/reduction waves were observed ~ 0.95 and 1.05 V vs. the reversible hydrogen electrode (RHE) at pH ~ 13 (0.1 M KOH; see section **5.A.2** for the determination of this voltage⁵⁴). We compare these redox features to assess the efficacy of the chemical treatment, specifically by integrating the charge underneath the redox waves to approximate the oxide electrochemically active surface area (ECSA).

We normalize the integrated charge (ECSA) by the mass of Mn in the composite as measured by inductively coupled plasma optical emission spectrometry (ICP-OES). This metric controls for a possible catalyst-loading change that may occur during the surface cleaning. We observed that the chemically treated composites had a similar Mn content (approximately 35 wt%). However, the thermally treated $\text{Mn}_3\text{O}_4/\text{C}$ was 60 wt% Mn. Because the carbon black used here is, by itself, thermally stable in oxidizing atmospheres well above 300°C , the observed carbon loss likely arises from

catalysis of carbon oxidation by the Mn_3O_4 NCs. A similar observation has been found with metals such as Pt, which can greatly lower the temperatures at which carbon supports begin to oxidize.⁵⁵ The heat-treated Mn_3O_4 was found to still be well-dispersed on the support by TEM, and the weight fraction of carbon remained large; thus, we do not expect that the loss of carbon significantly affects the conductivity and hence the electrochemical accessibility of individual Mn_3O_4 NCs. The specific charge calculations are given in section **5.A.2**.

The results of these determinations for all treatments are shown in **Table 5.A.2**. Thermally-treated Mn_3O_4 , despite producing the least contaminated surfaces by FTIR, showed the smallest specific charge ($118 \pm 3 \text{ C g}^{-1}_{\text{Mn}}$) of all treatments. This finding corroborates the common knowledge that while heat treatment can efficiently remove surface ligands, it can have undesirable side effects such as agglomeration and sintering of nanoparticles. As expected from the clean FTIR, thermally treated Mn_3O_4 showed well-defined redox waves, indicating that the surface sites are clean. In comparison, the Mn_3O_4 NCs that underwent alkylation have the largest CV response (specific charge $222 \pm 4 \text{ C g}^{-1}_{\text{Mn}}$) with redox features nearly identical to the CV of the thermally treated Mn_3O_4 . This finding suggests that ligand detachment by esterification of the ligands produces a surface that is remarkably similar to that following the thermal treatment without causing agglomeration.

Treatment with Lewis acid, BF_3 , produces Mn_3O_4 with similar CVs to those with alkylation- or thermally-treated Mn_3O_4 , but the curves are less reproducible, as indicated by the varying shape of the CVs, and the specific charge ($161 \pm 4 \text{ C g}^{-1}_{\text{Mn}}$) is smaller than that for alkylating agent-treated NCs. We conjecture that the Lewis acid treatment based on highly reactive BF_3 produces more degradation products, which are difficult to remove following ligand stripping. The presence of these reactive species could alter the surface redox properties of Mn_3O_4 NCs. KOH treatment is not

as effective for exposing the oxide surfaces as the fluoroborate agents were; the specific charge was the least improved over thermal treatment. KOH-treated $\text{Mn}_3\text{O}_4/\text{C}$ also had a less well-defined wave structure, which indicates less-accessible redox sites. In sum, alkylating-agent-treated Mn_3O_4 had the highest specific charge and produced CV curves that were comparable to those of the thermal-treated Mn_3O_4 , which indicates that the oxide surfaces were (1) free of contaminating passivants as in the base-treated case and (2) relatively free of reactive or blocking contaminants that were present following treatment with base or Lewis acid. The high ECSA of the Mn_3O_4 NCs following alkylation is also consistent with the FTIR results that showed that alkylation minimized contamination from carbonates and boron-containing species.

We characterize the presence of the surface ligands (both organic and inorganic) by thermogravimetric analysis (TGA) of Mn_3O_4 NCs (**Figure 5.4**). NC powders were heated at $5\text{ }^\circ\text{C min}^{-1}$ under flowing air atmosphere up to 550°C . The differing surface chemistries of the NCs following various treatments are clearly indicated by the dramatic variation in the TGA curves. Untreated Mn_3O_4 NCs undergo a single, rapid mass loss at $\sim 180^\circ\text{C}$ (**Figure 5.4**, green curve), which we assign to the decomposition of the organic layer. On the other hand, base-, alkylation-, and acid-treated NCs lose mass more rapidly relative to untreated NCs at temperatures below about 150°C , probably owing to the slow desorption of the surface water/solvent molecules that remained as a result of the treatments. We note that we do not expect large amounts of surface water in untreated NCs; as shown by the absence of feature 4 in **Figure 5.3a** (green curve), the amount of water in the hydrophobic untreated NCs is small. It has been previously reported that Mn carbonate, MnCO_3 , decomposes around 200°C , but the reaction is relatively slow.^{48, 51} Decomposition of MnCO_3 could also

contribute to the mass loss, because significant amounts of carbonate remain on the surface of the chemically treated NCs.

The conventional thermal treatment appears to remove all volatile surface molecules, as the TGA measurements indicate that the NCs do not undergo any further mass loss once they are heated to 300°C, the temperature used for the thermal treatment. Among the treatments studied, the KOH treatment showed the least amount of mass loss in comparison to alkylation and Lewis-acid agent treatments. This observation does not necessarily mean that KOH was the most effective of the chemical treatments at surfactant removal; in fact, the CV and FTIR results indicated the opposite. We explain this observation of low mass loss by pointing out that it is also possible for residual products on the NC surface to react with oxygen and therefore show mass gains in TGA. Mn₃O₄ NCs treated with alkylation or Lewis-acid agents may have larger mass losses because the residues following treatment decompose to volatile products. Residues in samples treated by KOH may instead be oxidized to form involatile contaminants: KOH-treated Mn₃O₄ underwent a mass increase at 450-470°C, which can be assigned to an oxygen uptake.⁴³ The increase in mass at higher temperatures is likely due to the decomposition of a reduced MnO_x(OH)_y phase (a hydroxide or oxyhydroxide) to pure Mn oxide at a critical temperature.

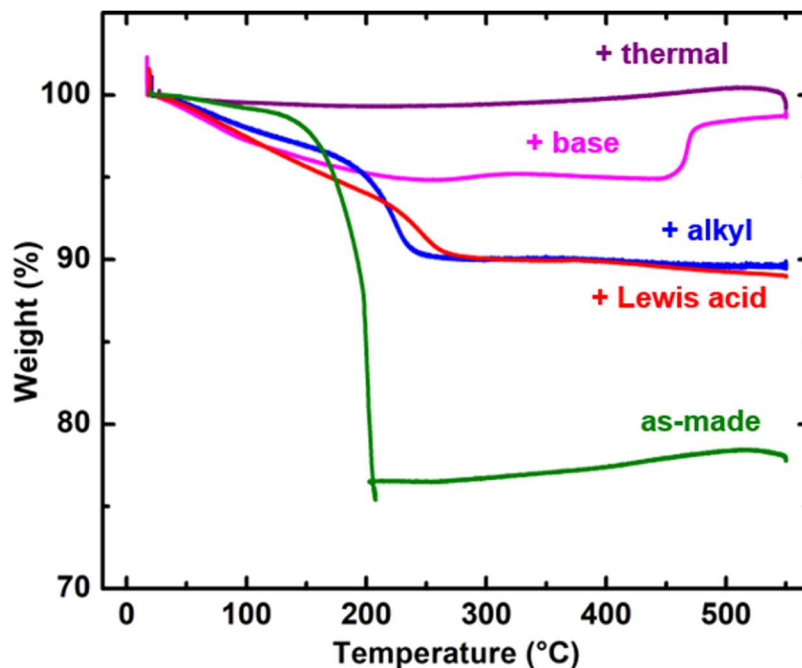


Figure 5.4. Thermogravimetric analysis in flowing air atmosphere of unsupported Mn_3O_4 nanocrystals subjected to various treatments. Samples were held at room temperature for 15 min, and then the temperature was ramped at $5\text{ }^\circ\text{C min}^{-1}$ before being held constant at 550°C for 15 min.

$\alpha\text{-Mn}_2\text{O}_3$ (bixbyite) is the stable phase of Mn oxide in air at room temperature up to about 900°C , whereas MnO or Mn_3O_4 are only thermodynamically stable under reducing conditions.⁴¹ In the case of our Mn_3O_4 NCs, it appears this phase transformation is kinetically slow in our TGA experiment, as mass uptake is minimal after 250°C for all but the base-treated samples. In the case of KOH-treated Mn_3O_4 , the base treatment likely resulted in a new oxide or oxyhydroxide layer that rapidly decomposed at around 450°C . Given that the KOH-treated NCs suffer an ECSA loss as measured by CV, this layer may be electrochemically inactive, which could be due to low electronic conductivity. The untreated NCs appear to already exist in their (kinetically) stable oxidation state up to at least 500°C before ligand stripping. This

kinetic stabilization seems to persist in the alkylation, Lewis acid, or thermal treatments, for which we did not observe any notable redox-state alteration.

5.4. CONCLUSION

In conclusion, we present a systematic evaluation of ligand-removal strategies for colloidal Mn_3O_4 NCs. We focus on treatments with bases, alkylation agents, Lewis acids, and heat. The effectiveness of each treatment is summarized in **Table 5.2**. TEM and SAED confirmed that the native oxide NC phases and morphology were stable following all treatments, although for Lewis acid and alkylation treatments a side reaction may occur to create acids that etch the NCs. All treatments were effective in removing the original ligands (oleate) as measured by the C-H stretching vibrations in FTIR. The reactions between the NC surfaces and the chemical reagents, however, leave residual water or metal hydroxides, carbonates, ligand-stripping reagent counter ions, and other degradation products. Alkylation-agent treatment produced the cleanest NC CVs, comparable to NCs processed by the “gold standard” thermal treatment. However, unlike heat-treated NCs, which had a reduced electrochemical surface area following NC sintering during heat treatment, the NCs undergoing alkylating-agent treatments did not agglomerate. Lewis-acid and KOH treated NCs showed a lower integrated charge density than for the case of alkylation. These two chemical treatments also showed lower reproducibility and poorly defined redox couples during voltammetry. TGA analysis showed that chemical treatments left some volatiles, likely bound water, carbonate, and side reaction products on the NC surface. For KOH treatment, TGA also indicated the likely presence of a partially crystallized oxide or oxyhydroxide layer. Consideration of the factors in **Table 5.2** leads us to conclude that ligand removal by treatment with alkylating agents such as Et_3OBF_4 is the most

promising surface-cleaning method, since it produces surfaces as clean as the heat treatment without suffering from possible surface area loss or structure alteration. By establishing a new low-temperature cleaning method, our work provides an opportunity to revisit electrochemistry on colloidal redox-active oxide NCs that were previously untested because their ligands could not be removed without resorting to structurally detrimental high-temperature treatments.

Table 5.2. Effectiveness of ligand removal procedures for various surface chemistry outcomes. Redox = specific charge; carboxyl removal = organic COO^- or carbonate CO_2^{3-} ; volatiles = total loss after thermogravimetric analysis.

Method	Redox	Carboxyl removal	Bound H ₂ O	Volatiles removed
<i>Base</i>	Light Red	Red	Light Blue	Light Blue
<i>Alkylation</i>	Blue	Light Blue	Light Red	Light Red
<i>Lewis acid</i>	Light Blue	Light Red	Red	Light Red
<i>Thermal</i>	Red	Blue	Blue	Blue

Most	Light Blue	Light Red	Least
------	------------	-----------	-------

5.A. APPENDIX

5.A.1. Funding and acknowledgments

This work was supported in part by the National Science Foundation (NSF) under award number CHE-1665305. This work made use of the Cornell Center for Materials Research shared facilities, which are supported through the NSF MRSEC program (DMR-1719875). We also thank D. Zheng (Cornell Materials Science and Engineering) for experimental assistance and S. K. Giri (Cornell Biological and Environmental Engineering) for an elemental analysis.

5.A.2. Materials and methods

Manganese(ii) acetate ($\text{Mn}(\text{Ac})_2$, 98%), oleic acid (90%), oleylamine (98% by primary amine), xylene (>98.5% xylenes and ethylbenzenes), and boron trifluoride diethyl etherate ($\text{BF}_3 \cdot \text{Et}_2\text{O}$, >46.5% BF_3), acetonitrile (anhydrous, >99.8%), and sulfuric acid (H_2SO_4 , 99.999%) were obtained from Sigma-Aldrich. Triethyloxonium tetrafluoroborate (Et_3OBF_4 , 1.0 M in dichloromethane) was from Alfa Aesar. Ethanol (99.5%, anhydrous) was from Decon Labs. Methanol (semiconductor grade, >99.9%) and nitric acid (HNO_3 , Aristar) were from BDH. Hexane (98.5%, ACS) was from EMD Millipore. Hydrogen peroxide (H_2O_2 , 30%) was from Macron. Water (18.2 $\text{M}\Omega\text{-cm}$) was obtained from a Direct-Q system (Millipore). Carbon black (Vulcan XC-72) was obtained from the Fuel Cell Store. Reactions were performed in air except where otherwise specified.

Synthesis of Mn_3O_4 nanoparticles

The synthesis of Mn_3O_4 nanocrystals as starting materials followed a previously outlined procedure.²⁷ An example is given here. To a round-bottomed

three-necked flask were added 60 mL xylene, 8 mmol oleic acid, 40 mmol oleylamine, and 4 mmol $\text{Mn}(\text{Ac})_2$. Two septa were added, and one was pierced with a thermocouple to control reaction temperature. An air-cooled condenser served to reduce evaporation losses; otherwise, the reaction was open to air. The mixture was heated to 90°C with magnetic stirring, whereupon 4 mL of water was added by syringe. After further reaction at 90°C for 3 h, the mixture was quenched by pouring into 400 mL ethanol, and the nanocrystals were obtained by centrifugation at 4400 rpm. Further purification was effected by dissolving the nanocrystals in hexane (ca. 25 mL total) followed by precipitation with ethanol (1:1 by volume) and re-centrifugation. The nanocrystal precipitate was stored in hexane; its concentration was measured by drying a specific volume in a glass vial and weighing by difference.

Catalyst loading and ligand removal

The nanocrystals self-attached to carbon black in hexane without further treatment. 80-100 mg of carbon black was added to a centrifuge tube followed by an equal mass of Mn_3O_4 nanocrystals (in the corresponding volume of hexane). The mass concentration of the ligand-protected Mn_3O_4 was measured beforehand by drying an aliquot of solution in a glass vial and weighing by difference. The mixture was diluted with hexane to 40-50 mL and sonicated in a water bath for 1 h, followed by centrifugation. The resulting $\text{Mn}_3\text{O}_4/\text{C}$ was dried under low vacuum (0.1 atm).

To remove the oleate ligands by heat treatment, the dry $\text{Mn}_3\text{O}_4/\text{C}$ powder was heated in air at 300°C in an oven for 1 h.

To remove the ligands by alkylation¹⁰ or Lewis acid treatment¹¹, the $\text{Mn}_3\text{O}_4/\text{C}$ was suspended ($1\text{-}5\text{ mg mL}^{-1}$) in acetonitrile in N_2 atmosphere. An amount of Et_3OBF_4 solution or $\text{Et}_2\text{O}\cdot\text{BF}_3$ was added containing an equal mass of reactive ligand, and the mixture was sonicated for 1-2 min before centrifugation. The mixture was then

brought into air to decant the supernatant, and the precipitate was washed once more with methanol by sonication followed by centrifugation.

Characterization methods

Bright field transmission electron microscopy (BF-TEM) images and selected area diffraction (SAED) patterns were acquired using an FEI Tecnai T12 microscope with an accelerating voltage of 120 keV. SAED calibration and integration was done using a script for circular Hough transform analysis in Gatan DigitalMicrograph 2.32. A double-exponential background was subtracted from the experimental patterns by fitting to baseline points estimated by eye in OriginPro 8.5. The camera length was calibrated for each SAED image separately using an evaporated Al standard (Electron Microscopy Sciences).

Fourier transform infrared (FTIR) spectroscopy was performed using unsupported nanoparticles. For ligand stripping, the same procedure above was carried out except that an equivalent mass of NCs in hexane solution was added to the reactive chemical mixture or weighed out for heating. After isolation by centrifugation and washing with methanol, the NCs were dried under low vacuum overnight. The resulting powders were well-mixed by grinding in an agate mortar and pestle with infrared-grade KBr powder (International Crystal Laboratories) with an approximate ratio of 1 mg powder to 300-500 mg KBr. The mixture was compacted with a hydraulic press into a 5 mm pellet, and FTIR spectra were acquired in transmission mode.

Inks were prepared by dispersing 3mg of $\text{Mn}_3\text{O}_4/\text{C}$ ($\text{Mn}_3\text{O}_4:\text{C}=1:1$ by mass) composites in 2948.52 μL isopropanol/water (1:4 by volume, carrier) with addition of 51.48 μL of 0.1M aqueous KOH neutralized Nafion® 117 solution as a binder to an ink concentration of 0.5 $\text{mg}_{\text{Mn}_3\text{O}_4} \text{mL}^{-1}$. The ink was then sonicated for 10 minutes using a probe sonicator. Subsequently, to improve the reproducibility of the cyclic

voltammograms, the concentrated ink was diluted by adding carrier to a final ink composition of $0.3 \text{ mg}_{\text{Mn}_3\text{O}_4/\text{C}} \text{ mL}^{-1}$ and $0.3 \text{ mg}_{\text{Nafion}} \text{ mL}^{-1}$. The diluted ink was dispersed using a probe sonicator for 10 minutes, and $10 \mu\text{L}$ was deposited on a glassy carbon electrode (disk area= 0.196 cm^2). The film was dried overnight in an ad-hoc drying chamber consisting of an upturned beaker containing an open vial of isopropanol to increase the alcohol vapor pressure in the chamber.

A Bio-Logic SP-300 potentiostat was used with a traditional three electrode cell (Pine Research Instrumentation) for all electrochemical characterization. The counter electrode was a platinum wire, while an Ag/AgCl reference electrode (Pine) was used with 0.1 M KOH as the supporting electrolyte. All reported potentials are referenced to the reversible hydrogen electrode (RHE) scale which was calibrated by measuring the onset voltage of hydrogen evolution/oxidation current on a polycrystalline platinum disk (Pine) in hydrogen (Airgas, ultra-high purity) saturated 0.1 M KOH.⁵⁴ Using this approach, we measured 0 V vs RHE to be -0.9807 V vs Ag/AgCl. All cyclic voltammetry measurements on the $\text{Mn}_3\text{O}_4/\text{C}$ composites were conducted in 0.1 M KOH saturated with argon (Airgas, ultra-high purity) at a scan rate of 50 mV/s. The electrochemically active surface area (ECSA) was calculated by subtracting the double-layer capacitance region from the cyclic voltammograms. Since the double-layer capacitance slightly increases with voltage, two sloped lines were used to fit the double-layer region boundaries, and the ECSA was finally integrated based on the sloped lines.

Thermogravimetric analysis (TGA) was performed using a TA Instruments Q50 thermogravimetric analyzer. Approximately 1 mg of unsupported nanoparticles were added to a clean platinum pan and exposed to a 90 mL/min flow of oxygen (Airgas, medical grade). Each sample was then held at room temperature for 15 minutes, ramped at $5^\circ\text{C}/\text{min}$ to 550°C , and held for 15 minutes.

The derived specific charge values were normalized to the mass of Mn in the Mn₃O₄/C composites, which was determined by inductively coupled plasma optical emission spectrometry (ICP-OES). 0.25-2.50 mg Mn₃O₄/C was weighed out in a glass vial, then 1.5 mL H₂SO₄ was added. At room temperature with fast stirring, 0.5 mL H₂O₂ was very slowly added to the vial. **Warning:** *The acid digestion mixture (piranha solution) is an extremely powerful oxidizer and should be used with great care; it becomes very hot after mixing at room temperature.* After heating the mixture on a 150°C hot plate for 1 h, the carbon dissolved to give a dark solution. 2 mL HNO₃ was slowly added and the solution was heated for 1 h, dissolving the carbon and any remaining solids to give a clear to very faint yellow solution. After cooling to room temperature, the digest was quantitatively transferred to a centrifuge tube with 1 mL additional HNO₃ and diluted to 50 mL with water. Finally, the mixtures were diluted with an appropriate amount of dilute nitric acid (proportions 1 mL HNO₃ to 49 mL H₂O) to a concentration of 0.4-0.6 mg L⁻¹ of solids. The ICP-OES analysis was carried out at the Soil & Water Lab, Cornell Biological and Environmental Engineering, Ithaca, NY.

Differences in particle size distributions were considered significant based on the results of a simple inference on the difference of mean diameters d_{method} and $d_{\text{as-made}}$ assuming normally distributed particle sizes with standard deviations σ_{method} and $\sigma_{\text{as-made}}$ calculated from N_{method} and $N_{\text{as-made}}$ measurements respectively.⁵⁶ Using these parameters a z -statistic is calculated, from which a p -value is derived. The p -value represents the likelihood that, if the true values of the mean diameters were identical and normally distributed, the sampled d and σ would arise by chance. For example, for the Lewis acid-treated NCs in **Figure 5.2a**, $d_{\text{method}} = 6.99$ nm, $\sigma_{\text{method}} = 0.72$ nm, and $N_{\text{method}} = 302$, versus $d_{\text{as-made}} = 7.47$ nm, $\sigma_{\text{as-made}} = 0.80$ nm, and $N_{\text{as-made}} = 300$.

$$z = \frac{d_{\text{as-made}} - d_{\text{method}}}{\sqrt{\frac{\sigma_{\text{as-made}}^2}{N_{\text{as-made}}} + \frac{\sigma_{\text{method}}^2}{N_{\text{method}}}}} = \frac{7.47 - 6.99}{\sqrt{\frac{0.80^2}{300} + \frac{0.72^2}{302}}} = 7.82 \quad (5.7)$$

The p -value can be determined using any program that gives the value of the standard normal cumulative distribution for the statistic z . For this work the p -value was determined using the Matlab function `normcdf(-|z|)`. The number of decimal places given for diameter measurements likely overestimates the precision with which diameter could be measured as well as the microscope calibration, so only extremely small p -values were considered significant.

5.A.3. Supporting figures and tables

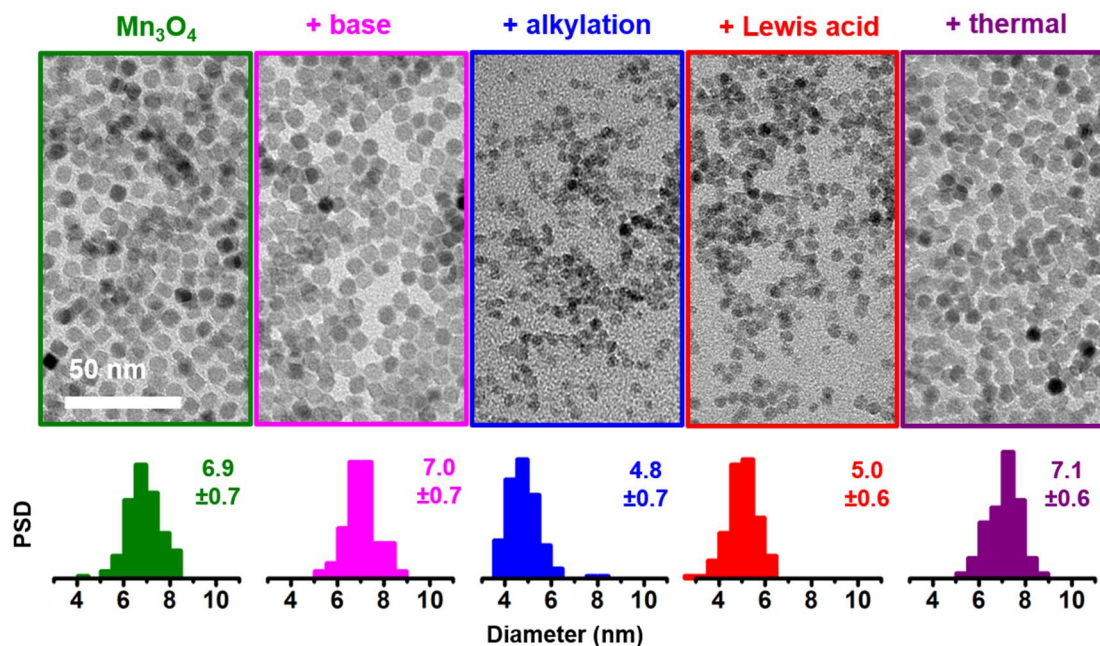


Figure 5.A.1. BF-TEM observations (top) of Mn_3O_4 etching in unsupported NCs subjected to ligand-removal treatment after deposition on a grid from colloidal solution. PSD histograms ($N > 150$) are shown below. NCs are from a different synthesis batch and thus have a slightly smaller untreated diameter than those of

Figure 5.2.

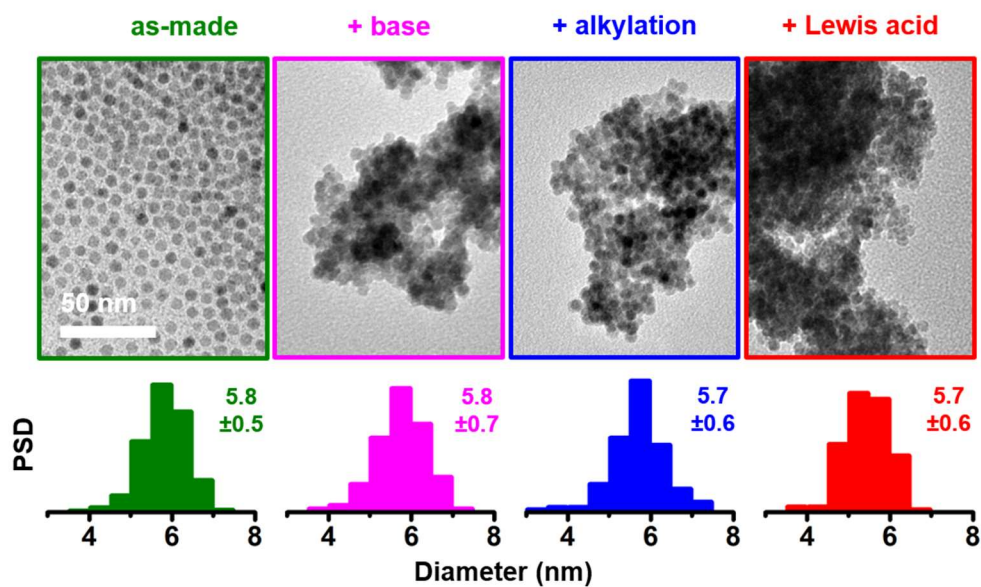


Figure 5.A.2. BF-TEM observations (top) of Mn₃O₄ etching in unsupported NCs subjected to ligand-removal treatment in solution. PSD histograms (N > 100) are shown below. NCs are from a different synthesis batch and thus have a smaller untreated diameter than those of **Figure 5.2**.

Table 5.A.1. Statistical comparison of nanoparticle size distributions.

Figure	Method	Number of measurements	Mean diameter (nm)	Standard deviation (nm)	z-statistic vs. as-made	p-value
5.2	as-made	300	7.47	0.80		
	+ base	301	7.49	0.78	0.30	0.38
	+ alkylation	303	7.52	0.93	0.72	0.23
	+ Lewis acid	302	6.99	0.72	7.81	$2.7 \cdot 10^{-15}$
	+ thermal	305	7.57	0.88	1.45	0.073
5.A.1	as-made	152	6.87	0.69		
	+ base	152	7.02	0.69	2.00	0.023
	+ alkylation	153	4.81	0.70	25.80	$4.6 \cdot 10^{-147}$
	+ Lewis acid	152	5.02	0.62	24.60	$6.5 \cdot 10^{-134}$
	+ thermal	151	7.07	0.65	2.66	0.0039
5.A.2	as-made	301	5.81	0.54		
	+ base	104	5.76	0.65	0.73	0.23
	+ alkylation	131	5.70	0.65	1.82	0.033
	+ Lewis acid	135	5.70	0.61	1.84	0.034

Table 5.A.2. Specific charge derived from three independent CV measurements on nanoparticle-carbon composites for each ligand-removal method. The charge was rounded to the nearest C.

Method	Specific charge ($C g^{-1}Mn$)			
	Base	Alkylation	Lewis acid	Thermal
Mn concentration (g_{Mn} per $g_{Mn3O4/C}$)	0.34	0.35	0.37	0.61
CV #1	148	218	157	115
CV #2	146	222	162	118
CV #3	149	225	165	120
Average	148	222	161	118
STD (%)	1.0	1.6	2.4	2.2
Change relative to thermal treatment (%)	+25	+88	+37	n/a

5.B. REFERENCES

1. Yin, Y.; Alivisatos, A. P., Colloidal nanocrystal synthesis and the organic–inorganic interface. *Nature* **2005**, 437, 664–670
2. Jia, C.-J.; Schüth, F., Colloidal Metal Nanoparticles as a Component of Designed Catalyst. *Physical Chemistry Chemical Physics* **2011**, 13, 2457-2487.
3. Boles, M. A.; Ling, D.; Hyeon, T.; Talapin, D. V., The Surface Science of Nanocrystals. *Nature Materials* **2016**, 15, 141-153.
4. Rosen, E. L.; Sawvel, A. M.; Milliron, D. J.; Helms, B. A., Influence of Surface Composition on Electronic Transport through Naked Nanocrystal Networks. *Chemistry of Materials* **2014**, 26, 2214-2217.
5. Lee, J.-S.; Kovalenko, M. V.; Huang, J.; Chung, D. S.; Talapin, D. V., Band-Like Transport, High Electron Mobility and High Photoconductivity in All-Inorganic Nanocrystal Arrays. *Nature Nanotechnology* **2011**, 6, 348–352.
6. Baumgardner, W. J.; Whitham, K.; Hanrath, T., Confined-but-Connected Quantum Solids via Controlled Ligand Displacement. *Nano Letters* **2013**, 13, 3225–3231.
7. Li, D.; Wang, C.; Tripkovic, D.; Sun, S.; Markovic, N. M.; Stamenkovic, V. R., Surfactant removal for colloidal nanoparticles from solution synthesis: the effect on catalytic performance. *ACS Catalysis* **2012**, 2, 1358-1362.
8. Niu, Z.; Li, Y., Removal and utilization of capping agents in nanocatalysis. *Chemistry of Materials* **2014**, 26, 72-83.
9. Cargnello, M.; Chen, C.; Diroll, B. T.; Doan-Nguyen, V. V. T.; Gorte, R. J.; Murray, C. B., Efficient removal of organic ligands from supported nanocrystals by fast thermal annealing enables catalytic studies on well-defined active phases. *Journal of the American Chemical Society* **2015**, 137, 6906–6911.

10. Rosen, E. L.; Buonsanti, R.; Llordes, A.; Sawvel, A. M.; Milliron, D. J.; Helms, B. A., Exceptionally mild reactive stripping of native ligands from nanocrystal surfaces by using Meerwein's salt. *Angewandte Chemie International Edition* **2012**, 51, 684-689.
11. Doris, S. E.; Lynch, J. J.; Li, C.; Wills, A. W.; Urban, J. J.; Helms, B. A., Mechanistic Insight into the Formation of Cationic Naked Nanocrystals Generated under Equilibrium Control. *Journal of the American Chemical Society* **2014**, 136, 15702-15710.
12. Nag, A.; Kovalenko, M.; Lee, J.; Liu, W.; Spokoyny, B.; Talapin, D. V., Metal-free inorganic ligands for colloidal nanocrystals: S^{2-} , HS^- , Se^{2-} , HSe^- , Te^{2-} , HTe^- , TeS_3^{2-} , OH^- , and NH_2^- as surface ligands. *Science* **2011**, 333, 10612-10620.
13. Lopez-Sanchez, J. A.; Dimitratos, N.; Hammond, C.; Brett, G. L.; Kesavan, L.; White, S.; Miedziak, P.; Tiruvalam, R.; Jenkins, R. L.; Carley, A. F.; Knight, D.; Kiely, C. J.; Hutchings, G. J., Facile Removal of Stabilizer-Ligands from Supported Gold Nanoparticles. *Nature Chemistry* **2011**, 3, 551-556.
14. Shaw, S.; Tian, X.; Silva, T. F.; Bobbitt, J. M.; Naab, F.; Rodrigues, C. L.; Smith, E. A.; Cademartiri, L., Selective Removal of Ligands from Colloidal Nanocrystal Assemblies with Non-Oxidizing He Plasmas. *Chemistry of Materials* **2018**, 30, 5961-5967.
15. Aliaga, C.; Park, J. Y.; Yamada, Y.; Lee, H. S.; Tsung, C.-K.; Yang, P.; Somorjai, G. A., Sum Frequency Generation and Catalytic Reaction Studies of the Removal of Organic Capping Agents from Pt Nanoparticles by UV-Ozone Treatment. *Journal of Physical Chemistry C* **2009**, 113, 6150-6155.
16. Solla-Gullón, J.; Montiel, V.; Aldaz, A.; Clavilier, J., Electrochemical Characterisation of Platinum Nanoparticles Prepared by Microemulsion: How to

- Clean Them without Loss of Crystalline Surface Structure. *Journal of Electroanalytical Chemistry* **2000**, 491, 69-77.
17. Gorlin, Y.; Chung, C.-J.; Nordlund, D.; Clemens, B. M.; Jaramillo, T. F., Mn₃O₄ Supported on Glassy Carbon: An Active Non-Precious Metal Catalyst for the Oxygen Reduction Reaction. *ACS Catalysis* **2012**, 2, 2687-2694.
18. Huynh, M.; Bediako, D. K.; Nocera, D. G., A Functionally Stable Manganese Oxide Oxygen Evolution Catalyst in Acid. *Journal of the American Chemical Society* **2014**, 136, 6002-6010.
19. Lima, F. H. B.; Calegario, M. L.; Ticianelli, E. A., Investigations of the Catalytic Properties of Manganese Oxides for the Oxygen Reduction Reaction in Alkaline Media. *Journal of Electroanalytical Chemistry* **2006**, 590, 152-160.
20. Ramírez, A.; Hillebrand, P.; Stellmach, D.; May, M. M.; Bogdanoff, P.; Fiechter, S., Evaluation of MnO_x, Mn₂O₃, and Mn₃O₄ Electrodeposited Films for the Oxygen Evolution Reaction of Water. *Journal of Physical Chemistry C* **2014**, 118, 14073-14081.
21. Gliech, M.; Klingenhof, M.; Görlin, M.; Strasser, P., Supported Metal Oxide Nanoparticle Electrocatalysts: How Immobilization Affects Catalytic Performance. *Applied Catalysis A: General* **2018**, 568, 11-15.
22. Gorlin, Y.; Jaramillo, T. F., A Bifunctional Nonprecious Metal Catalyst for Oxygen Reduction and Water Oxidation. *Journal of the American Chemical Society* **2010**, 132, 13612-13614.
23. Cook, T. R.; Dogutan, D. K.; Reece, S. Y.; Surendranath, Y.; Teets, T. S.; Nocera, D. G., Solar Energy Supply and Storage for the Legacy and Nonlegacy Worlds. *Chemical Reviews* **2010**, 110, 6474-6502.

24. Hong, W. T.; Risch, M.; Stoerzinger, K. A.; Grimaud, A.; Suntivich, J.; Shao-Horn, Y., Toward the Rational Design of Non-Precious Transition Metal Oxides for Oxygen Electrocatalysis *Energy and Environmental Science* **2015**, 8, 1404-1427.
25. Yan, D.; Li, Y.; Huo, J.; Chen, R.; Dai, L.; Wang, S., Defect Chemistry of Nonprecious-Metal Electrocatalysts for Oxygen Reactions. *Advanced Materials* **2017**, 29, 1606459.
26. Man, I. C.; Su, H. Y.; Calle-Vallejo, F.; Hansen, H. A.; Martínez, J. I.; Inoglu, N. G.; Kitchin, J.; Jaramillo, T. F.; Nørskov, J. K.; Rossmeisl, J., Universality in Oxygen Evolution Electrocatalysis on Oxide Surfaces. *ChemCatChem* **2011**, 3, 1159-1165.
27. Yu, T.; Moon, J.; Park, J.; Park, Y. I.; Na, H. B.; Kim, B. H.; Song, I. C.; Moon, W. K.; Hyeon, T., Various-Shaped Uniform Mn₃O₄ Nanocrystals Synthesized at Low Temperature in Air Atmosphere. *Chemistry of Materials* **2009**, 21, 2272-2279.
28. Wang, N.; Guo, L.; He, L.; Cao, X.; Chen, C.; Wang, R.; Yang, S., Facile Synthesis of Monodisperse Mn₃O₄ Tetragonal Nanoparticles and Their Large-Scale Assembly into Highly Regular Walls by a Simple Solution Route. *Small* **2007**, 3, 606-610.
29. Sun, X.; Zhang, Y. W.; Si, R.; Yan, C. H., Metal (Mn, Co, and Cu) Oxide Nanocrystals from Simple Formate Precursors. *Small* **2005**, 1, 1081-1086.
30. Seo, W. S.; Jo, H. H.; Lee, K.; Kim, B.; Oh, S. J.; Park, J. T., Size-Dependent Magnetic Properties of Colloidal Mn₃O₄ and MnO Nanoparticles. *Angewandte Chemie International Edition* **2004**, 43, 1115-1117.
31. Zhao, N.; Nie, W.; Liu, X.; Tian, S.; Zhang, Y.; Ji, X., Shape- and Size-Controlled Synthesis and Dependent Magnetic Properties of Nearly Monodisperse Mn₃O₄ Nanocrystals. *Small* **2008**, 4, 77-81.

32. Dong, A.; Ye, X.; Chen, J.; Kang, Y.; Gordon, T.; Kikkawa, J. M.; Murray, C. B., A generalized ligand-exchange strategy enabling sequential surface functionalization of colloidal nanocrystals. *Journal of the American Chemical Society* **2011**, 133, 998-1006.
33. Otelaja, O. O.; Ha, D.-H.; Ly, T.; Zhang, H.; Robinson, R. D., Highly Conductive Cu_{2-x}S Nanoparticle Films through Room-Temperature Processing and an Order of Magnitude Enhancement of Conductivity via Electrophoretic Deposition. *ACS Applied Materials and Interfaces* **2014**, 6, 18911–18920.
34. Nelson, A.; Fritz, K. E.; Honrao, S.; Hennig, R. G.; Robinson, R. D.; Suntivich, J., Increased Activity in Hydrogen Evolution Electrocatalysis for Partial Anionic Substitution in Cobalt Oxysulfide Nanoparticles. *Journal of Materials Chemistry A* **2016**, 4, 2842-2848.
35. Zhang, H.; Hu, B.; Sun, L.; Hovden, R.; Wise, F. W.; Muller, D. A.; Robinson, R. D., Surfactant ligand removal and rational fabrication of inorganically connected quantum dots. *Nano Letters* **2011**, 11, 5356-5361.
36. Guo, S.; Zhang, S.; Wu, L.; Sun, S., Co/CoO nanoparticles assembled on graphene for electrochemical reduction of oxygen. *Angewandte Chemie International Edition* **2012**, 124, 11940-11943.
37. Wu, L.; Li, Q.; Wu, C. H.; Zhu, H.; Mendoza-Garcia, A.; Shen, B.; Guo, J.; Sun, S., Stable Cobalt Nanoparticles and Their Monolayer Array as an Efficient Electrocatalyst for Oxygen Evolution Reaction. *Journal of the American Chemical Society* **2015**, 137, 7071-7074.
38. Zhu, H.; Zhang, S.; Huang, Y.-X.; Wu, L.; Sun, S., Monodisperse $\text{M}_x\text{Fe}_{3-x}\text{O}_4$ (M = Fe, Cu, Co, Mn) nanoparticles and their electrocatalysis for oxygen reduction reaction. *Nano Letters* **2013**, 13, 2947–2951.

39. Suntivich, J.; Gasteiger, H. A.; Yabuuchi, N.; Shao-Horn, Y., Electrocatalytic measurement methodology of oxide catalysts using a thin-film rotating Disk electrode. *Journal of The Electrochemical Society* **2010**, 157, B1263.
40. Wamser, C. A., Equilibria in the System Boron Trifluoride—Water at 25°. *Journal of the American Chemical Society* **1951**, 73, 409-416.
41. Grundy, A. N.; Hallstedt, B.; Gauckler, L. J., Assessment of the Mn-O System. *Journal of Phase Equilibria* **2003**, 24, 21-39.
42. Gillot, B.; El Guendouzi, M.; Laarj, M., Particle Size Effects on the Oxidation–Reduction Behavior of Mn₃O₄ Hausmannite. *Materials Chemistry and Physics* **2001**, 70, 54-60.
43. Al Sagheer, F. A.; Hasan, M. A.; Pasupulety, L.; Zaki, M. I., Low-Temperature Synthesis of Hausmannite Mn₃O₄. *Journal of Materials Science Letters* **1999**, 18, 209-211.
44. D’Ulivo, A.; Pagliano, E.; Onor, M.; Pitzalis, E.; Zamboni, R., Vapor Generation of Inorganic Anionic Species after Aqueous Phase Alkylation with Trialkyloxonium Tetrafluoroborates. *Analytical Chemistry* **2009**, 81, 6399-6406.
45. Socrates, G., *Infrared and Raman Characteristic Group Frequencies*. John Wiley & Sons: New York, 2001.
46. Mohapatra, P.; Shaw, S.; Mendivelso-Perez, D.; Bobbitt, J. M.; Silva, T. F.; Naab, F.; Yuan, B.; Tian, X.; Smith, E. A.; Cademartiri, L., Calcination does not Remove All Carbon from Colloidal Nanocrystal Assemblies. *Nature Communications* **2017**, 8, 2038.
47. Ishii, M.; Nakahira, M.; Yamanaka, T., Infrared Absorption Spectra and Cation Distributions in (Mn, Fe)₃O₄. *Solid State Communications* **1972**, 11, 209-212.

48. El-Shobaky, G. A.; Ghozza, A. M.; Hassan, H. A., Thermal Decomposition of Manganese Carbonate Supported on Active Alumina. *Journal of Thermal Analysis* **1998**, 51, 529-539.
49. Shang, G. L.; Fei, G. T.; Zhang, Y.; Yan, P.; Xu, S. H.; Ouyang, H. M.; Zhang, L. D., Fano Resonance in Anodic Aluminum Oxide Based Photonic Crystals. *Scientific Reports* **2014**, 4, 3601.
50. Banerjee, S.; Kim, D.-I.; Robinson, R. D.; Herman, I. P.; Mao, Y.; Wong, S. S., Observation of Fano Asymmetry in Raman Spectra of SrTiO₃ and Ca_xSr_{1-x}TiO₃ Perovskite Nanocubes. *Applied Physics Letters* **2006**, 89, 223130.
51. Reidies, A. H., Manganese Compounds. In *Ullmann's Encyclopedia of Industrial Chemistry*, Elvers, B., Ed. John Wiley and Sons: New York, 2000.
52. Gorlin, Y.; Jaramillo, T. F., Investigation of Surface Oxidation Processes on Manganese Oxide Electrocatalysts using Electrochemical Methods and ex situ X-ray Photoelectron Spectroscopy. *Journal of The Electrochemical Society* **2012**, 159, H782-H786
53. McBreen, J., The Electrochemistry of β -MnO₂ and γ -MnO₂ in Alkaline Electrolyte. *Electrochimica Acta* **1975**, 20, 221-225.
54. Sheng, W.; Gasteiger, H. A.; Shao-Horn, Y., Hydrogen Oxidation and Evolution Reaction Kinetics on Platinum: Acid vs. Alkaline Electrolytes. *Journal of the Electrochemical Society* **2010**, 157, B1529-B1536.
55. Baturina, O. A.; Aubuchon, S. R.; Wynne, K. J., Thermal Stability in Air of Pt/C Catalysts and PEM Fuel Cell Catalyst Layers. *Chemistry of Materials* **2006**, 18, 1498-1504.
56. Montgomery, D. C.; Runger, G. C., *Applied Statistics and Probability for Engineers*. 5th ed.; John Wiley and Sons: New York, 2011.

CHAPTER 6

6 CONCLUSIONS AND OUTLOOK

6.1. SUMMARY AND CONCLUDING REMARKS

The previous chapters have explored the impact of changes in nanoparticle surface chemical transformations on their properties. Anion exchange in oxide nanocrystals, which had been proven to be feasible in a previous work, provided a simple route toward more active electrocatalysts for hydrogen reduction. Enhancement in activity at an intermediate oxysulfide composition relative to both oxides and sulfides supported theoretical calculations showing that optimization of adsorbed hydrogen intermediate bonding energies could be achieved through substitution of anions as well as cations in ionic electrocatalytic materials. Structural and spectroscopic investigations uncovered the nature of an unusual etching reaction by which ligands formerly understood to be passivating or protecting reacted aggressively but selectively with certain chemically soft chalcogenide nanomaterials. Oxidation by the atmosphere or chemical reagents combined with the reducing properties of the non-innocent ligand to abstract both cations and anions in a synergistic process which has already found utility by other workers¹ in synthesizing new shapes and structures of nanomaterials. Cation exchange in a semiconductor nanocrystal model system allowed quantitation of diffusion coefficients over length scales of less than 2 nm, and demonstrated that chemical diffusion can be greatly accelerated at the nanoscale through rapid changes in the activity of each component as dictated by the large chemical potential gradients across phase boundaries. Detailed structural analysis also verified unequivocally the existence of metastable phases at interfaces between dissimilar cubic structures, even where the metastable phase might have a smaller

lattice constant than both of the parent phases. Finally, direct comparison of the efficacy of ligand removal techniques through electrochemical and spectroscopic methods identified a promising approach to ligand removal for future well-defined electrocatalysts prepared from colloidal nanoparticles.

As discussed in **Chapter 1**, these results emphasize the mobility of the underlying inorganic structure of nanoparticles in response to changes in the surface boundary conditions. They support in a dramatic fashion the hypothesis—laid out in the original article bringing cation exchange to wider scientific attention²—that near-surface layers of crystals, especially in colloidal nanoparticles, are much more dynamic and flexible than the rigidity of bulk materials would suggest. The acceleration of solid-state transformations at the nanoscale has already permitted a much richer variety of nanoparticle structures and compositions to be produced than can be achieved through one-step synthesis, even when such procedures have reached a very high level of sophistication. Integration of chemical transformations of colloidal nanoparticles into rationally designed, step-by-step procedures will be of prime importance in fully realizing the advantages of nanotechnology, just as procedural optimization has been critical in realizing the potential of bulk materials in engineering.

Future experiments which would most immediately extend the results of each chapter are summarized briefly below, and some are described in more detail in section **6.2** below.

Anion exchange in metal oxides for electrocatalysis

- A more comprehensive coverage of the parameter space in sulfide content, sulfurization temperature, and annealing temperature could be achieved, since the number of oxysulfide compositions in **Chapter 2** is quite small. As

discussed below, anion exchange reactions are extensible to other transition metal sulfides (Fe, Mn, Ni, etc.), and simulations have suggested that some may also be useful in improving hydrogen evolution and oxidation catalysis.

- HRTEM studies of the oxysulfides were tentatively explored, but remained incomplete due to difficulties in observation. Better sample preparation or choice of sulfurization or material parameters could result in a better model system for high-resolution structural analysis.

Cation exchange and selective etching of copper sulfide

- Previous work showed that cation exchange of Cu_{2-x}S with Cd produced CdS- Cu_{2-x}S heterostructures imposing tensile rather than compressive strains on the Cu_{2-x}S layer.³ A full structural characterization of the heterostructure system for Cd exchange was not performed due to experimental difficulties, but the reversal of the strain direction may prove to have interesting consequences. For example, stoichiometric Cu_2S , which is more desirable for some applications,^{4,6} might be stabilized in tension.
- The optical properties analysis demonstrated that tighter control of the oxidizing or reducing potential of the nanoparticle solutions were needed to obtain reproducible plasmonic peak positions, as suggested by prior observations in the literature.⁷⁻⁹ Optical measurements in situ with addition of redox agents can clarify the extent to which heterostructure formation affects the maximum achievable doping in the Cu_{2-x}S layer.

Solid state transport in the PbS-to-CdS cation exchange reaction

- Due to the presence of a relatively large degree of lattice mismatch, the PbS-CdS system may not be the simplest for measuring diffusion kinetics purely as

a function of domain size. The PbTe-CdTe system,¹⁰ as discussed in **Chapter 4**, has a much smaller lattice mismatch.

- Experiments on slightly larger or smaller crystal sizes should be carried out to see if, for example, the activation barrier for diffusion depends on particle size. Preliminary experiments on smaller (diameter 5 nm and below) PbS nanocrystals indicated that the kinetics of transformation were much faster than in 7 nm nanocrystals, presumably owing to the larger fraction of surface atoms undergoing fast exchange.
- More complete HR(S)TEM studies were underway at the time of this publication, but were stymied by contamination of the samples, likely due to residual metal oleates and ligands. More effective cleaning procedures or cryo-TEM would be required to perform these high-resolution experiments.

Standardization of ligand removal procedures for electrocatalytic materials

- In hindsight, the alkylation ligand removal procedure discussed in **Chapter 5** may provide cleaner surfaces for more accurate activity determination of the oxysulfide materials synthesized in **Chapter 2**.
- Other treatments, such as oxidizing and non-oxidizing plasma exposure,^{11, 12} have shown promising results for cleaning nanoparticle surfaces, and future comparisons of ligand-removal methods should naturally include them.

6.2 FUTURE WORK

Some preliminary results building on the work of **Chapters 2-5** are discussed in more detail below and placed in context with other experimental and theoretical techniques for providing deeper insight into nanoparticle surface chemistry and solid-

state transport. When considered in light of pre-existing scientific infrastructure, the results in this work immediately suggest a number of intriguing experiments and opportunities to revisit the data and systems analyzed previously.

6.2.1. High-resolution structural analysis by use of the pair distribution function

The XRD results of the foregoing chapters relied primarily on the Bragg formalism and its corrections to illustrate changes in the crystal structure, size, and disorder of nanocrystal domains using the intense Bragg peaks at small scattering angles. While this approach remains useful due to its simplicity, much more information can be obtained about local structure by analyzing the scattered intensity from the entire diffraction pattern at small and large angles, rather than just the intensity and shape of the Bragg reflections.¹³ As outlined in **Chapter 1**, the XRD pattern is a reciprocal-space projection of the real-space atomic structure, and the two are related by a Fourier transform. Specifically, the XRD intensities reflect constructive and destructive interference of diffracted beams, and this modulation of the scattered intensity as a function of scattering angle or momentum transfer Q is described by an interference function.¹⁴ In current practice, this function is usually referred to as a structure factor, $S(Q)$. For the purposes of this discussion, it suffices to say that $S(Q)$ is related to the experimentally measured diffracted intensity by normalizing the scattered intensity from separate atoms (in the Debye scattering equation, **Equation 1.4**, terms for which $i \neq j$) by the overall squared mean scattering power $\langle f \rangle^2$ of the entire collection of atoms.¹⁵ Note that the equation below is valid only for the case of powder diffraction where the scattering is averaged over all possible orientations of the crystal, as in the Debye equation:

$$S(Q) - 1 = \frac{1}{N\langle f \rangle^2} \sum_{i \neq j} f_i^* f_j \frac{\sin Qr_{ij}}{Qr_{ij}} \quad (6.1)$$

Here r_{ij} is the interatomic distance between atoms i and j , N is the total number of atoms in the structure being considered, and f_i is the atomic form factor (as a function of Q) for each atom. From this normalized intensity $S(Q) - 1$, which oscillates about zero, a weighted structure factor $F(Q)$ is derived: $F(Q) = Q (S(Q) - 1)$. It can be shown that $F(Q)$ is related to a pair distribution function (PDF) $G(r)$, which is ideally a histogram of interatomic distances in the sample:^{15, 16}

$$G(r) = \frac{2}{\pi} \int_{Q_{min}}^{Q_{max}} F(Q) \sin Qr \, dQ \quad (6.2)$$

Q_{min} and Q_{max} are limits imposed on the integration of $F(Q)$ by the experimental inability to collect data at very low angles (due to the proximity of the direct beam) and very high angles (due to low intensity or as the instrumental scattering angle 2θ approaches π radians or 180 degrees).

The PDF is of great value for structural analysis because it describes in real space (and thus more intuitively for many scientists) the distribution of interatomic bond lengths, and thus the local to mid-range order, in the sample. An illustrative example of $G(r)$ from the prior literature¹⁶ is given in **Figure 6.1**. Here, diffraction patterns were collected out to very large Q (45 \AA^{-1}) of a composition series of the important semiconductor $\text{In}_x\text{Ga}_{1-x}\text{As}$. The sets of $G(r)$ derived therefrom show well-resolved peaks, each corresponding to a high density of interatomic distances (Ga-Ga, Ga-In, Ga-As, etc.). Of great importance is the appearance of a pair of closely spaced, but still resolvable, peaks around about 2.5 \AA for ternary compositions.

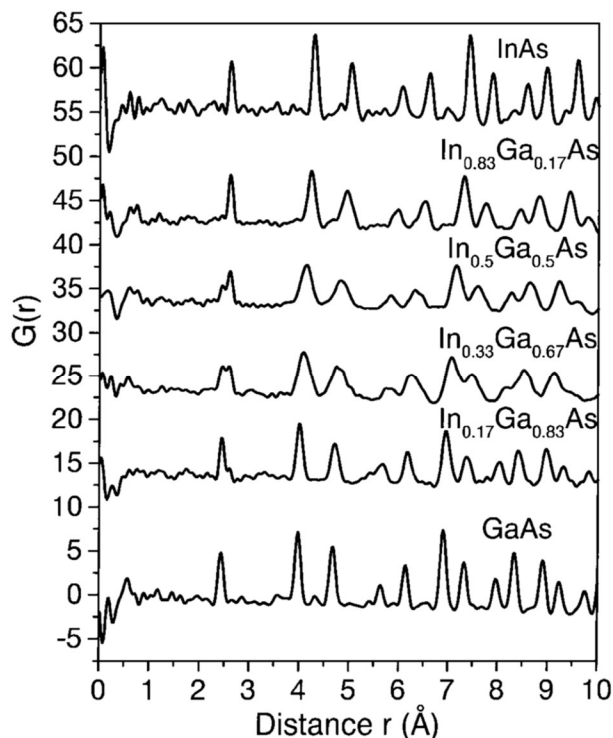


Figure 6.1. High-resolution location of atomic bond lengths in real space through analysis of the pair distribution function obtained by x-ray total scattering. At 2.4 and 2.6 Å, two peaks in intermediate compositions of $\text{In}_x\text{Ga}_{1-x}\text{As}$, corresponding to Ga-As and In-As bond lengths, respectively, are clearly distinguished. Reproduced from figure 2 of reference 16 by permission of the American Physical Society.

This interatomic distance corresponds to the metal-As bond length, and the separate peaks prove that two different bond lengths exist in ternary compositions—in fact, the peaks remain in nearly the same position as they assume in the bulk compounds. Thus, this ternary semiconductor retains intrinsic inhomogeneity of its bond lengths throughout its entire compositional range. This conclusion would be nearly impossible to draw from reciprocal-space diffraction data, where the position of the Bragg peaks represents an average interplanar distance rather than a bond length.¹³ The existence of different Ga-As and In-As bond lengths in ternary compounds is

immediately apparent in real space but would lead only to a slight broadening of Bragg peaks in reciprocal space, and this broadening could be attributed to many different factors.^{14, 17}

The power of pair-distribution methods will be of use in clarifying the local structure of heterostructured nanoparticles produced by cation exchange. As a prelude to a more complete experiment, preliminary x-ray total scattering data were collected[†] from a PbS nanocrystal sample (diameter 7.1 nm, as in **Chapter 4**) and from a sample nearly completely cation-exchanged with Cd (**Figure 6.2**). The data were obtained with an x-ray wavelength of 0.166 Å (photon energy 74.8 keV) at beamline 28-ID-1, National Synchrotron Light Source-II, Brookhaven National Laboratory. In the original NC sample, peaks in $G(r)$ remain sharp and distinguishable out to at least 35 Å, while in the PbS@CdS sample $G(r)$ falls off very rapidly to a nearly flat baseline, reflecting a much higher degree of close- to mid-range disorder in the sample. This accords with the sharp decrease in crystallinity seen during cation exchange in **Figure 4.7**.

[†] The author thanks Curtis Williamson and Anuj Bhargava for collection of the scattering data.

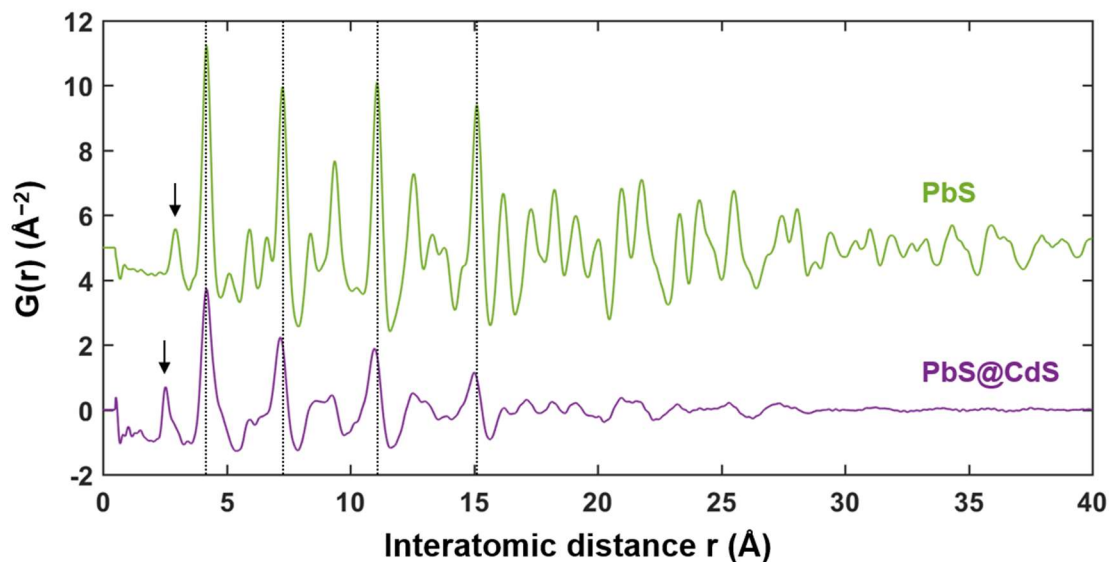


Figure 6.2. Example of pair distribution functions (PDFs) obtained from 7 nm PbS nanocrystals (top) and core-shell PbS@CdS nanoparticles (bottom). The NCs were subjected to cation exchange with Cd oleate at 180°C for 12 h (see **Chapter 4** for experimental details). Dashed lines clarify the contraction of the outer coordination spheres following cation exchange; arrows indicate the location of the metal-sulfur nearest neighbor bond.

Future work should complete a more definite assignment of the features in $G(r)$ seen here across a wider range of degrees of cation exchange. The nearest-neighbor (NN) peak, which corresponds to Pb-S or Cd-S bond lengths, shifts substantially following exchange, indicating to a change from octahedral to tetrahedral bonding, presumably for Cd atoms in the zincblende CdS phase. A shoulder remains just above the NN peak in PbS@CdS, which could arise either from residual PbS or from rocksalt CdS. Finally, the peak in $G(r)$ at ~ 4 Å arises from metal-metal and sulfur-sulfur NN distances, and its location is preserved (within the limits of the small change in lattice parameter going from PbS to CdS) following cation exchange. Peaks

further out at multiples of this bond distance shift to smaller distances, indicating that the outer coordination spheres in fact contract, perhaps as a result of strain from lattice mismatch. Finally, overall smearing of the peaks in the PDF is readily apparent, suggesting considerable mid-range disorder, and new experiments or analyses should be directed toward separating the contributions of bond length and bond angle heterogeneity. It should be noted that a simpler cation exchange system can still be adopted: for example, in the PbTe-CdTe system, the lattice mismatch is reduced by a factor of almost 10 (see **Chapter 4**), which could greatly simplify identification of metastable or separated phases in the system.

An ambitious future project would be to perform the experiments of **Chapter 4** with a Q -range appropriate to PDF analysis on a specialized synchrotron beamline, several of which are now in place for such in-situ experiments. However, the problems with solvent scattering mentioned in **Chapter 4.A.2** remain unresolved, and for this reason an alternative experimental configuration is suggested. An in-situ PDF (or smaller-angle XRD) characterization of cation exchange could utilize instead nanocrystals, supported on an inert, low-atomic-weight substrate such as boron nitride or aluminum oxide, within a flow of dilute solution of incoming cation. This allows the density of the nanoparticle sample in the beam path to be maximized, while the actual kinetics of the exchange are simplified by maintaining a constant concentration of incoming ion in the solution and removing outgoing host ions immediately. Some prior work has suggested the possibility of introducing the guest ions for ion exchange in the form of molecules in the vapor phase.^{18, 19} In this case, the guest ions could be introduced as organometallic gases, and scattering from liquids is removed. Similar flow-cell sample holders have already been designed and utilized.²⁰

6.2.2. Expansion of parameter space in metal oxysulfides and other anion-exchanged nanomaterials

The work of **Chapter 2** followed from a previous publication²¹ demonstrating the lability of CoO nanocrystals toward anion exchange with S^{2-} ions. The demonstration of activity enhancement for important electrocatalytic reactions in metastable colloidally synthesized oxysulfides naturally suggests an exploration of other metal oxysulfides as well as other mixed-anion materials, such as oxyselenides, oxynitrides, etc. Some results of preliminary experiments on extensions of the sulfurization procedure to manganese oxide (Mn_3O_4) are given here.

Mn_3O_4 is a promising oxygen evolution and reduction electrocatalyst,^{22, 23} and some preliminary calculations (data not shown) by the Hennig group indicated that favorable tuning of H adsorption, as in **Figure 2.5**, could be achieved by limited substitution of S^{2-} for O^{2-} on an $MnO(100)$ surface. Spherical Mn_3O_4 nanocrystals were synthesized by a previous procedure,²⁴ as in **Chapter 5.A.2**, and initially subjected to the same sulfurization procedure outlined in **Chapter 2.A.2**. However, sulfurization using $(NH_4)_2S$ appeared to be unworkable for Mn_3O_4 . S^{2-} did not react with Mn_3O_4 at low temperatures, and at high temperatures (200 °C) the highly basic $(NH_4)_2S$ -oleylamine mixture dissolved the nanocrystals followed by re-precipitation as separate particles of wurtzite MnS (**Figure 6.3**). The apparent reluctance of Mn oxide to undergo transformation to sulfides, a reaction which is facile for Co oxide,²¹ prompted an analysis of the thermodynamics of such reactions for a number of transition metal oxides. Results of some calculations of the free energies of various oxide-to-sulfide metathesis reactions are shown in **Table 6.1**.

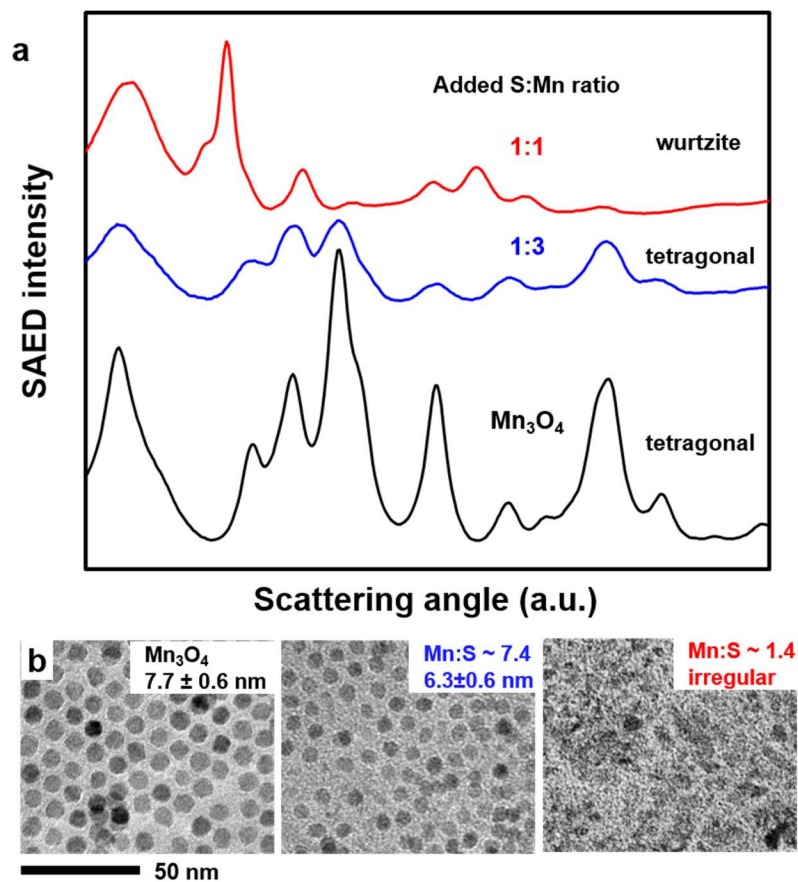


Figure 6.3. Results of attempted anion exchange at 200 °C of Mn_3O_4 to MnO_xS_y or MnS_z using ammonium sulfide, $(\text{NH}_4)_2\text{S}$. (a) SAED shows Mn_3O_4 (black curve) reacted with S^{2-} does not undergo a change of lattice parameters; instead, the particles are etched as indicated by an increased in peak broadening (blue). At high ratios of added sulfide, the particles dissolve and re-precipitate as irregular wurtzite MnS particles (red curve). TEM images of the particles corresponding to each SAED pattern are shown in (b). The ratio of Mn:S found by energy-dispersive x-ray spectroscopy in the TEM is shown in the label for each sample, as well as particle diameter where applicable.

Table 6.1. Thermodynamic analysis for some anion exchange reactions of oxides to sulfides. Standard free energies of the reactions, in kJ mol^{-1} at 298 K, were calculated using data from reference ²⁵.

Reaction	Metal oxide, <i>M</i>				
	Mn	Fe	Co	Ni	Cu
$2MO(s) + 2S(s) \rightarrow 2MS(s) + O_2(g)$	+127	+137	+112	+125	+57
$M_3O_4(s) + 3S(s) \rightarrow 3MS(s) + 2O_2(g)$	+549		+433		
$2MO(s) + 3S(s) \rightarrow 2MS(s) + SO_2(g)$	-24	-14	-40	-52	-94
$M_3O_4(s) + 5S(s) \rightarrow 3MS(s) + 2SO_2(g)$	-55	+40	-172		
$MO(s) + H_2S(g) \rightarrow MS(s) + H_2O(g)$	-51	-41	-66	-53	-120
$2M_3O_4(s) + 7H_2S(g) \rightarrow 6MS(s) + 6H_2O(g) + SO_2(g) + H_2(g)$	-74	-18	-230		
$2M_3O_4(s) + 3H_2S(g) + H_2(g) \rightarrow 3MS(s) + 4H_2O(g)$	-203	-107	-320		

Two conclusions can be drawn from the thermodynamic analysis. First, elemental sulfur, which has been used as an analogue to oxygen in producing metal sulfide nanoparticles from metal NCs,^{26,27} is usually unfavorable for producing sulfides from oxides, with a possible exception for reduced divalent oxides MO. This reflects the greater oxidizing power of O_2 relative to S. On the other hand, the metathesis reaction of metal oxides and hydrogen sulfide to metal sulfides and water is universally favorable, particularly under highly reducing conditions. In fact, preliminary experiments have found promising results for the reaction of colloidal Mn_3O_4 with H_2S generated from the reaction of metal sulfides with acid. Mn_3O_4 was treated in ligand-free hydrocarbon solution with a molar excess of H_2S gas in N_2 generated by the reaction of H_2SO_4 with Na_2S . At high temperatures (180-210°C) Mn_3O_4 transforms smoothly to irregular particles of Mn sulfide, which crystallize after

further annealing to rocksalt MnS (data not shown). The cubic phase of MnS indicates that, in contrast to the experiments of **Figure 6.3**, the new MnS particles are probably templated by the underlying cubic Mn₃O₄.

A condensed diagram of the preliminary apparatus developed is shown in **Figure 6.4**. Briefly, carrier nitrogen from a Schlenk line is passed via hose into gas dispersion tube **A** in a three-neck flask **B** containing Na₂S, NaSH, or FeS chips (**C**). A syringe pump **D** is used to dispense dilute H₂SO₄ or HCl from syringe **E** through cannula **F** to a pierced septum **G** in flask **B**. The H₂S formed by reaction of acid with metal sulfide is carried in N₂ through hose **H** to another gas dispersion tube, **I**, and into a second three-neck flask containing the hot Mn₃O₄ nanocrystal solution, **J**. Another septum, **K**, can be pierced with a needle for withdrawing aliquots. The Mn₃O₄ flask is heated with an electric mantle (**M**) controlled by feedback from thermocouple **N**. The gas flow containing residual H₂S, N₂, and vaporized solvent (if any) passes out to hose **L**, which connects to an inlet **O** in a Drechsel gas-washing bottle filled with concentrated KMnO₄ solution (**P**). This scrubbed solution decomposes virtually all H₂S to elemental S as long as the KMnO₄ is not exhausted. Finally, the exit hose **Q** on the bottle leads to a gas-dispersion tube **R** in a Schlenk flask **S** containing either additional base (KOH) or a metal ion solution (e.g. Cu²⁺) which precipitates metal sulfide to indicate exhaustion of the KMnO₄. The scrubbed N₂ gas flow is free of H₂S and passes via outlet **T** to the air in the fume hood.

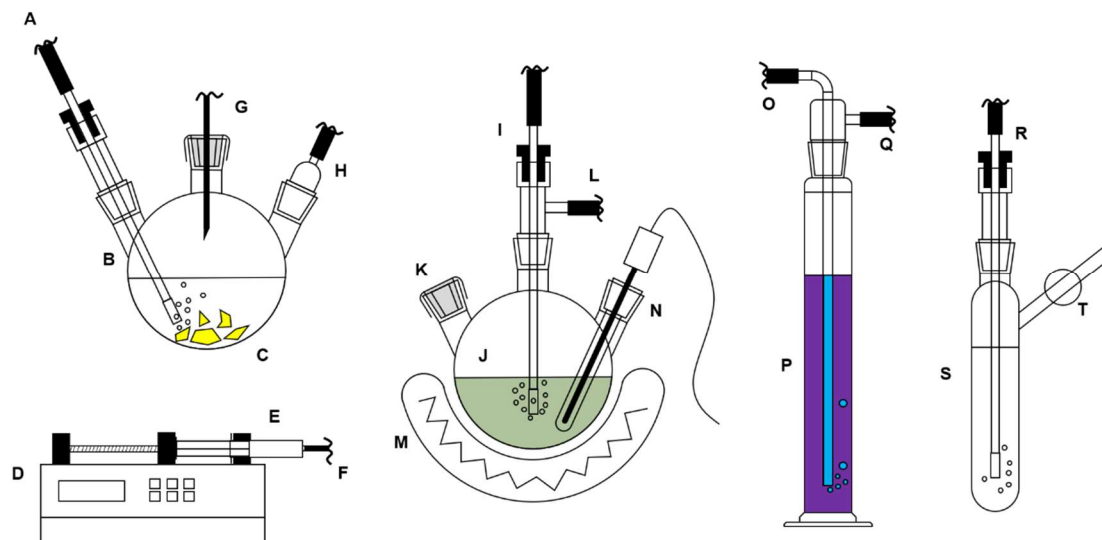


Figure 6.4. Diagram of the gas-liquid phase sulfurization apparatus.

Future developments contributing to the oxysulfide research program will seek to explore the generality of the hydrogen sulfide anion exchange process, clarifying the reactivities of different metal sulfide NCs with H_2S . These NCs can be assessed for their electrocatalytic performance by the methods already outlined, possibly with the inclusion of the promising ligand removal process by treatment with alkylating agents described in **Chapter 5**. Syntheses of a broader compositional space of transition metal (Mn, Fe, Co, Ni, Cu) oxysulfides will enable benchmarking of the existing DFT calculations and could lead to insights into the underlying electronic properties of such NCs, especially with the addition of chemically sensitive methods such as x-ray photoelectron spectroscopy (XPS) and x-ray absorption spectroscopy.^{3, 28, 29}

Additionally, an opening exists for establishing a highly general synthesis method for metal oxychalcogenides and possibly oxypnictides. Although hydrogen chalcogenides (H_2S , H_2Se , etc.) and pnictides (NH_3 , PH_3 , etc.) are hazardous gases, relatively simple apparatus can be constructed in which the gases may be generated by reaction of two much less dangerous precursors.^{30, 31} After reaction of the product with

a colloidal solution of NCs in inert solvent, any residual gas can be immediately destroyed by passage to an oxidizing or basic scrubber, which eliminates the possibility of release to the environment. This “gas-phase” anion exchange has obvious advantages in that the colloidal integrity of the NCs is preserved for further convenient solution processing while maintaining the high reactivity of the chalcogen/pnictogen hydrides.

6.2.3. Physical electrochemistry and surface science of nanocrystals

Chapters 2, 3, and 5 assessed the impact (or lack thereof) of the surface chemistry of nanocrystals on the underlying crystalline “substrate.” Although section **6.2.2** above has stressed the importance of finding active electrocatalysts from a broad compositional space, much of the surface chemistry of the nanoparticles in question remains uncharacterized. **Chapters 2 and 5** left the nature of the transition metal redox couples ambiguous, for example, and the extent of coupling of Cu_{2-x}S redox state to the actual crystal structure is not finalized as of yet, as **Chapter 3** illustrated.

Electrochemistry provides a promising tool for investigation of nanoparticle surface science even without considering electrocatalysis because (1) charge transfer across interfaces, and therefore measurable current or voltage, is intrinsic to surface reactivity and (2) the high surface-area-to-volume ratio of nanoparticles removes the difficulty of electrochemically characterizing the surfaces of insulators and semiconductors by embedding the particles in nanostructured conductive electrodes such as carbon black.³²

In the case of the metal oxides and oxysulfides discussed in **Chapters 2 and 5**, the assignment of redox potentials was based on a relatively simple cyclic voltammetric analysis. A more careful electrochemical characterization could be as simple as using a much slower voltage sweep rate during anodization/cathodization, as

the ability to resolve separate reduction potentials is inversely proportional to the scan rate.³³ For example, redox peak assignments for MnO_x ³⁴ as mentioned in **Chapter 5** were based on a scan rate more than 10^3 times slower than used in the characterization of ligand-stripped Mn_3O_4 . More advanced voltammetric techniques, such as differential pulse voltammetry, also aid in characterizing faradaic (oxidation-reduction) reactions by reducing the magnitude of the capacitive double-layer charging current measured during a potential scan. Other experiments to consider for assessing the chemical origin of different redox couples include changing the solution pH and ionic strength and using different electrolytes (for example, changing the cation).^{35,36} Preliminary measurements during the work described in **Chapter 5** in fact showed that Mn_3O_4 nanocrystals were redox-active even when not treated to remove surface ligands (data not shown), indicating that they may have been incompletely protected and raising interesting possibilities for examining oxide reactivity as a function of surface coverage.

As might be suggested by their high ionic mobility, copper sulfide and other copper chalcogenides are particularly suited to surface analysis using electrochemical methods. The carrier concentration, and thus the LSPR, can be tuned by electrochemically reducing or oxidizing Cu_{2-x}S nanocrystal films.³⁷ Future work could, therefore, begin by analyzing the Cu intercalation/redox behavior of Cu_{2-x}S as a function of particle size and initial structure. The author's group has related measurements of the size-dependent lithiation and delithiation of Cu_{2-x}S in non-aqueous solvent,³⁸ but examination of the Cu_{2-x}S phase diagram in nanoparticles may be as simple as titrating the sample in aqueous solution with Cu^{2+} ions.³⁹ These measurements can be combined with ex-situ XRD analyses and possibly optical measurements.

A particularly important question raised in **Chapter 3** and references therein was the nature by which Cu ions were reversibly inserted and removed from nanocrystals, especially where no mechanism for depositing or dissolving Cu ions was apparent (i.e., no excess ligands were present). A surface layer of Cu^{2+} ions was proposed as a sink for oxidized Cu in certain cases.⁹ Because such a layer is likely only stable in-situ, surface analysis using vacuum chamber techniques is excluded. In combination with the phase diagram information inferred from experiments above, another test can be suggested. Electron paramagnetic resonance examination would unambiguously confirm or rule out presence of these Cu^{2+} species. Oxidation or reduction could be carried out in nonaqueous solvent, either by electrochemical titration^{37, 40} or using an appropriate reagent.^{7, 8} Knowledge of the true surface species in this important class of nanocrystals under different chemical environments would be an invaluable contribution for virtually all aspects of copper chalcogenide nanoscience.⁴¹

6.2.4. Direct identification of the defects and chemical gradients in nanoparticles

In **Chapter 4**, a major scientific question was raised in that the identity of the point defects responsible for mass transport during cation exchange could not be identified from the experimental data on cation exchange in NCs so far, even from the detailed kinetic work on the PbS-to-CdS reaction. In fact, the prior literature suggests that the unambiguous determination of the rate-controlling defect transport process in solid-state diffusion can be very difficult for semiconductors.⁴²⁻⁴⁵ The chemical lability of such materials, reflected in the multiple valence states cations and anions can adopt depending on the external chemical potential, suggests that diffusion mechanisms could change based on the overall nanoparticle charge, the relative proportions of different crystal facets, and the presence or absence of dopants. Further kinetic

experiments demand a sound starting point for the main type of defect to consider in mass transport.

A major test of structural models will thus be the definitive detection of vacancies and/or interstitials in nanocrystals. In recent years, advances in atomic-level structural characterization have permitted direct imaging of defects, including point defects; such a determination is impossible to perform in an ensemble diffraction measurement using x-rays or neutrons. These improvements have made high-precision structural determination for arbitrary objects, including individual semiconductor nanocrystals, much more accessible. Two avenues of attack for characterization of chemically transformed nanomaterials are suggested here: modern methods of high-resolution (scanning) transmission microscopy (HR(S)TEM) and atom probe tomography (APT). A number of novel experiments are now available.

For instance, transmission electron microscopy techniques, specifically electron tomography and holography, can now be employed with sufficient resolution to locate every atom, including undercoordinated surface atoms, in a nanoparticle.⁴⁶ **Figure 6.5** shows a notable example of such a determination of the structure of an intermetallic FePt nanoparticle. In that experiment, the nanoparticle was tilted in steps through a wide range of angles, and at each step a single STEM image provided a two-dimensional projection of the atomic lattice. From there, newly developed algorithms for tomographic reconstruction incorporating physical and instrumental constraints allow the three-dimensional coordinates of each atom to be assigned. Although the report of Yang et al. does not identify vacancies or interstitials in the relatively refractory FePt, very fine structural details such as local deviations from perfect chemical ordering (in the form of swap and antisite defects), antiphase boundaries, and grain boundaries are visible. Chemically transformed nanomaterials, such as core-shell

semiconductor nanocrystals produced through cation exchange or layer-by-layer growth, would be ideal targets for such a tomographic analysis.

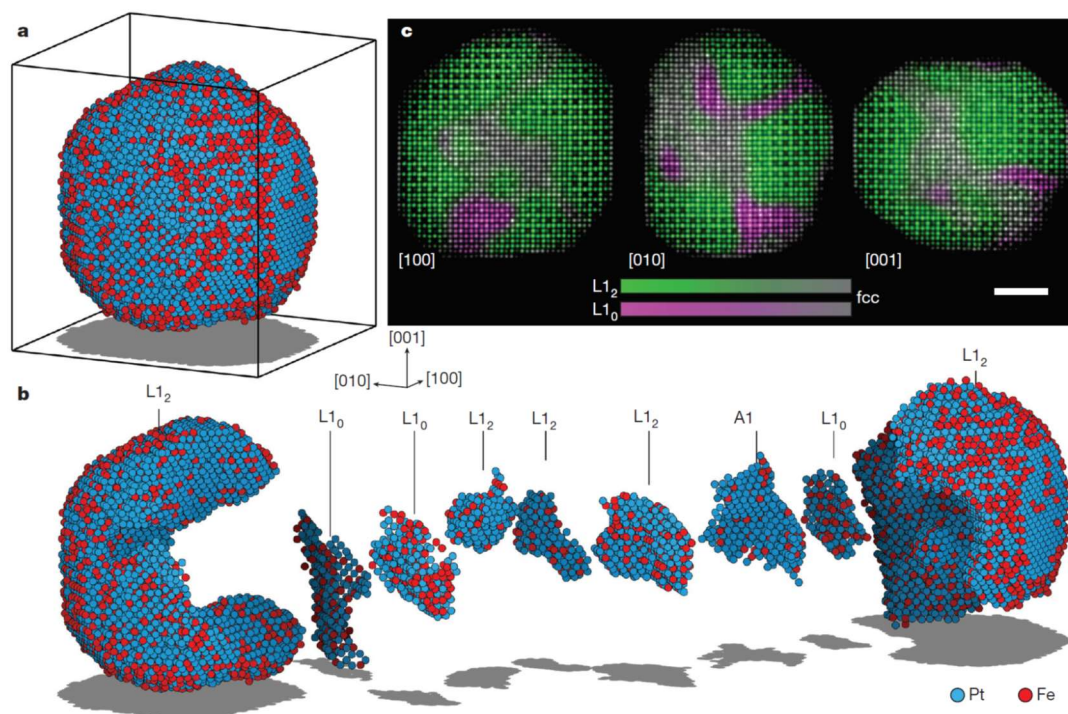


Figure 6.5. Example of quantitative 3D structural characterization of a FePt nanoparticle. The structure of the overall nanoparticle (a) was determined directly from a tilt series of images (c) in an aberration-corrected STEM. Knowledge of the location and chemical identity of each atom permits unambiguously assigning the order parameter of each subdomain (L₁₀: chemically ordered tetragonal; L₁₂: chemically ordered fcc; A1: chemically disordered fcc phases). Reproduced from figure 1 of reference 46 by permission of Springer Nature.

Even where tomographic analysis may not be practical, it is still possible to register fine structural details without locating every single atom. Methods have been laid out for quantitating the density in the atomic columns registered in a STEM image, based on careful consideration of the instrumental aberrations. Using image

simulation and statistical techniques, the actual shape of a nanocrystal can be retrieved from a single projection. STEM imaging has advanced to the point where individual vacancies and impurities within a nanostructure can be detected.⁴⁷⁻⁵⁰ Work has already been carried out demonstrating the imaging of shape transformations following changes in the ligand environment of Pb chalcogenides by quantitative STEM analysis from a single projection.⁵¹ Observations in **Chapter 4** suggested mass redistribution during cation exchange could take place by such surface rearrangements of atoms. Future experiments would thus be able to assess the lability of the anion sublattice, which in some cases has proven to be considerably more mobile than suggested by the term “cation” exchange.² Some in-situ TEM experiments in cation exchange have already been carried out by exploiting the evaporation of volatile Cd from CdSe-PbSe heterostructures to advance the heterostructure interface using excess adsorbed Pb.⁵²

A major concern in EM experiments is the possibility of transformation or sample damage due to the interaction of high-energy electrons with the sample, either by heating, by knock-on effects, or by chemical reduction.⁵³ Electron beam heating could possibly be used as a source of energy for in-situ observation of reactions in nanostructures, including cation exchange. For example, phase transformations in copper sulfide (Cu_2S) can be triggered in the TEM with the system at room temperature.⁵⁴ However, other forms of sample damage such as amorphization or deposition of carbon contaminants are universally undesirable. Sample damage is especially hard to avoid in the STEM configuration, which uses an intense scanned electron beam to form the image. These effects can be reduced or mitigated using appropriate instrumentation in the TEM, and for characterization of semiconductors sensitive to oxidation such as Pb chalcogenides,⁵⁵ these may prove to be required. An obvious tactic would be cooling of the sample cryogenic temperatures, but it bears noting that recently developed techniques now allow HRTEM images to be acquired

with very low electron doses, as demonstrated by high-resolution imaging studies of lead halide perovskites, which are known to be exquisitely sensitive to beam damage.^{56, 57}

The final technique, APT, forms images in a completely different manner from TEM and x-ray imaging, but offers comparable resolution.^{58, 59} In APT, a solid sample is formed into a sharply pointed tip with a radius of curvature comparable to the size of a nanocrystal. In a high vacuum chamber, a high voltage applied to the probe induces extreme electric fields around the probe tip, causing atoms to evaporate one-by-one by field emission. The field also ionizes these atoms and accelerates them to a position-sensitive detector in a deterministic manner. From the energy, location, and time of impact of the ions, experimenters can retrace the ion paths to find the starting positions and chemical identity of each atom. Originally restricted to metals due to the need for electrically conducting tips, modern APT instrumentation using laser evaporation allows reconstruction of the composition of virtually any material. Moreover, the technique can visualize relatively large volumes (millions of nm³), which would allow near-ensemble measurements with sub-nm resolution.⁵⁹ An APT experiment for chemically transformed nanoparticles would require the nanoparticles to be deposited on or in an appropriate matrix. It may be possible to form an appropriate nanoscale aggregate by sintering⁶⁰ or encapsulation in an inorganic matrix as a result of ligand removal, as has been done for “all-inorganic” nanocrystal solids for application in various optical and electronic devices in the past.⁶¹⁻⁶³ Alternatively, the particles could be embedded in a polymer.^{64, 65} A newer approach is to attach the particles to a prefabricated metal tip, either chemically or by electrodeposition, followed by encapsulation with additional electrodeposited metal.⁶⁶ Following the preparation of the embedded particles, a focused ion beam (FIB) is used to cut out or refine the shape of the probe for the tomography. An APT approach would allow for

high-resolution chemical profiling of nanoparticles which are not amenable to EM analysis, either due to electron beam damage or lack of statistical power inherent in sampling very small numbers of particles.

6.3. PRELIMINARY STUDY: X-RAY DIFFRACTION AND PAIR DISTRIBUTION FUNCTION ANALYSIS OF INTERNALLY CORRELATED NANOMATERIALS

Presented here are results of a preliminary investigation of a toy model of molecular aggregates to determine guidelines for interpreting unusual features of XRD patterns, specifically sharply asymmetric peak profiles, in real-space PDF and reciprocal-space analyses. Molecular aggregates are common in dyes, liquid crystals, and organic electronics, and determining the exact relationship of subunits in a chain to each other is essential in establishing the connection between crystal structure and electronic or optical properties. In particular, wide-angle diffraction methods for isolated (solvated) aggregates are not well established for examining inter-monomer correlations in aggregates. It is shown here that a peculiar x-ray diffraction line shape observed in work to which the author contributed⁶⁷ can be fairly well understood by Debye scattering simulations of XRD patterns from periodic linear chains of very small (<1-2 nm) lateral diameter. The peak shape arises as a mathematical consequence of the spherical averaging of strongly anisotropically distributed intensities around the reciprocal lattice points. Important types of disorder, specifically inter-monomer spacing disorder, chain flexibility, and monomer orientation, contribute in different ways to the wide-angle XRD pattern, showing that simple, easily distinguished features of the pattern may be used to better inform structural

analyses. Some experiments are suggested for direct determination of inter-monomer correlations from the pair distribution function from x-ray total scattering.

6.3.1. Motivation

It was established in prior work that monodisperse clusters of CdS less than 2 nm in diameter could be prepared through a high-concentration synthesis⁶⁸ where the ripening and agglomeration of the clusters was prevented through the formation of a columnar or hexagonal mesophase. These nanoparticles are part of a class of molecules with tens to hundreds of atoms, termed magic-size clusters (MSCs) owing to their atomic monodispersity.⁶⁹⁻⁷³ Their well-defined stoichiometry indicates that they have a particularly low-energy structure relative to clusters with slightly more or fewer atoms.^{74, 75} Such “closed-shell” structures have been extensively studied in the case of metal clusters and fullerenes.⁷⁶⁻⁷⁸ It has been suggested that MSCs act as a reservoir for supplying monomers in nanoparticle growth or as building blocks of nanoparticles, but their role in nanoparticle synthesis remains a topic of vigorous research.⁷⁹⁻⁸¹

During detailed structural characterization of the CdS MSCs,⁶⁷ it was observed that certain features of the XRD (total scattering) patterns depended strongly on the method of sample preparation. Under certain conditions, strongly asymmetric peak profiles were observed for the most intense line corresponding to the interplanar spacing of the basal plane of bulk CdS ((0001) for wurtzite and (111) for zincblende phases). Examples of these patterns are given in **Figure 6.6**. Thick pressed pellets of purified α -Cd₃₇S₂₀ MSCs analyzed in the Bragg-Brentano configuration in a laboratory diffractometer showed extremely broad lines whose symmetry could not be ascertained due to strong overlapping (**Figure 6.6**, top). When thinner pressed or cut (sheared) sheets of the MSC mesophase were prepared for XRD in transmission

(either at a synchrotron for PDF acquisition or in a laboratory diffractometer), the basal-plane peak at about 26° with respect to Cu $K\alpha$ equivalent x-ray wavelength showed a pronounced asymmetry in addition to greatly decreasing in width (**Figure 6.6**, middle and bottom). This asymmetric line is characterized by a sharp rising edge beginning at low angles which is followed by a more gradually declining heavy tail at larger angles. The sharpening of the patterns correlated with an increasing shear strain with subsequent alignment of the columnar mesophase. In the structure determination of α - $\text{Cd}_{37}\text{S}_{20}$ it was not necessary to invoke simulated diffraction patterns of long chains,⁶⁷ but Debye simulations from other structures showed that strongly asymmetric line shapes similar to those observed in **Figure 6.6** could be obtained; these are discussed in section **6.3.3**. Similar peak shapes have also been observed by earlier work by other groups in a variety of materials,^{71, 82-84} but the fine details of the diffracted intensity are still somewhat unclear, especially for this new class of mesophase-stabilized cluster assemblies.

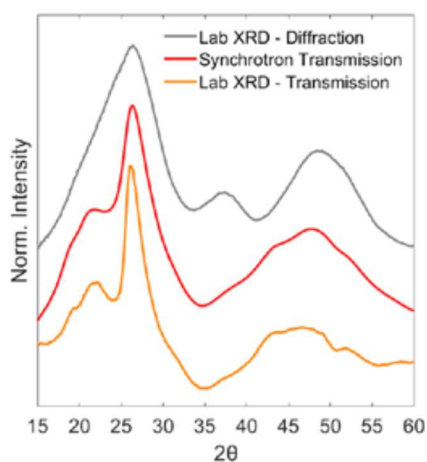


Figure 6.6. X-ray diffraction patterns of α - $\text{Cd}_{37}\text{S}_{20}$ assemblies in various experimental configurations. Top: the MSCs were pressed into a pellet 2-3 mm in thickness. Middle: MSCs were pressed and sheared into a sample holder for synchrotron XRD,

giving the sample a thickness of about 1 mm. Bottom: A film of MSCs was cut with a razor blade to a thickness of 100-200 μm . The geometry and source are noted (Diffraction: Bragg-Brentano). Reproduced from figure S2J of reference 67 by permission of the American Association for the Advancement of Science.

The asymmetric line shape in wide-angle XRD has long been noted for graphitic carbon materials.⁸⁵⁻⁸⁸ Perfect graphite crystals adopt a regular three-dimensional arrangement in which each single-layer sheet is displaced by a fixed lattice vector in the in-plane axes relative to the neighboring layers.^{89,90} In disordered carbons these displacement vectors instead adopt a distribution of lengths and angles, resulting in random translation and rotation of the layers relative to each other while remaining parallel. Such turbostratic disorder has been known to give rise to an asymmetric line shape for many years, and was first analyzed in detail by Warren,⁸⁴ who gave a limiting form for the powder diffraction pattern for the case of a purely two-dimensional lattice. However, in the case of MSCs the order within the columnar mesophase is presumed to be one- rather than two-dimensional. Analogous one-dimensional carbon nanostructures are known as carbon nanotubes (CNTs) and have also been studied extensively in powder x-ray diffraction.^{82,83}

Figure 6.7 shows some illustrative examples of peak shapes similar to those of **Figure 6.6** as observed by other workers. Simulated diffraction patterns from multiwalled carbon nanotubes⁸² (**Figure 6.7a**) demonstrates a sharp peak at $Q = 5.13 \text{ \AA}^{-1}$ ($d = 1.225 \text{ \AA}$) with a heavy large-angle tail. This interplanar distance is notable because it is nearly equal to one half of the distance between parallel edges of the hexagonal subcells of graphite (carbon-carbon bond length of about 1.42 \AA ^{89,90}). This is consistent with a description of a nanotube as a one-dimensional stack of rings of carbon atoms, and so the sharp reflection is termed “axial.” Additionally, a much

broader peak appears at about 5.2 \AA^{-1} . This peak can be attributed to “nonaxial” reflections from planes tilted relative to the tube axis, which have a smaller spacing. The additional broadening reflects the much smaller effective size of the “crystal” along directions that are not parallel to the tube axis. The multiple curves in **Figure 6.7a** were calculated with varying levels of ordering of the different nanotube walls relative to each other. The appearance of (112) reflections with increasingly good registry between tube shells is as expected for a formation of a larger effective crystallite with dimensions nearly perpendicular to the tube axis. An experimental demonstration of asymmetrical peaks in a different work (**Figure 6.7b**) arises from weakly crystalline aggregates of small CdSe clusters with the proposed monomer unit $(\text{CdSe})_{13}$.⁷¹ In this case, planes at a number of different angles (about 26° , 29° , 37° , and 48° with 15 keV synchrotron radiation) show pronounced asymmetry, indicating mesophase ordering in a number of directions. Small-angle scattering (SAXS) and other observations corroborated this hypothesis by demonstrating that the $(\text{CdSe})_{13}$ assemblies formed sheets. As discussed in the next section, however, one- and two-dimensional wide-angle XRD peaks can be difficult to distinguish, and so the interpretation of **Figure 6.7b** may be more complex than previously suggested.

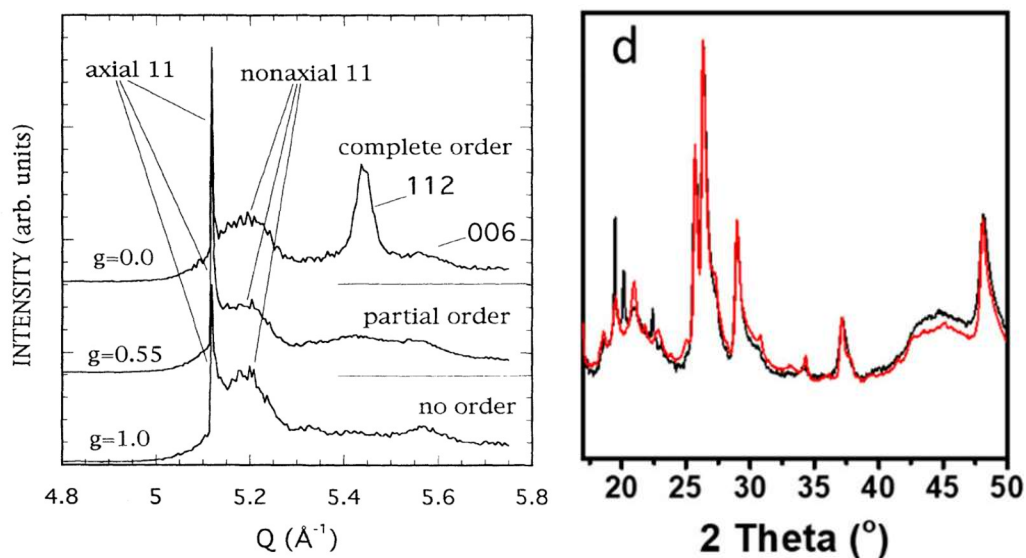


Figure 6.7. Examples of asymmetrical lineshapes with heavy large-angle tails. (a) Simulated diffraction patterns in multiwalled carbon nanotubes. Reproduced from figure 10 of reference 82 by permission of the American Physical Society. (b) Powder diffraction data from semiconductor cluster ($\text{Cd}_{13}\text{Se}_{13}$) aggregates. Reproduced from figure 2 of reference 71 by permission of the American Chemical Society.

6.3.2. Peak shape origin

The peculiar peak geometries are found in a powder diffraction experiment, which collects the diffracted intensity averaged over all spherical angles with a fixed radius. The peak shape indicates that as the sphere of integration in reciprocal space grows, it rises quickly as it first contacts the Bragg rod (or “plane”), then falls off more gradually since the rod or “plane” remains within the sphere of integration. The origin of a lineshape in a powder diffraction pattern may be understood straightforwardly beginning with the shape of the lattice nodes in reciprocal space.¹⁴ A molecular wire has effectively an extremely small crystal size in the axes perpendicular to the wire, and thus the diffracted intensity in these directions in reciprocal space is very diffuse. Conversely, the crystal size along the wire axis is very

large and so the intensity is very sharp. Thus, a molecular wire in reciprocal space consists of a series of stacked parallel planes (**Figure 6.7a**). Similarly, for a two-dimensional sheet the crystal sizes in the two axes in the sheet are very large while the size is vanishing perpendicular to it, so the intensity is distributed as cylinders, or Bragg rods, perpendicular to the lattice in reciprocal space (**Figure 6.7b**).

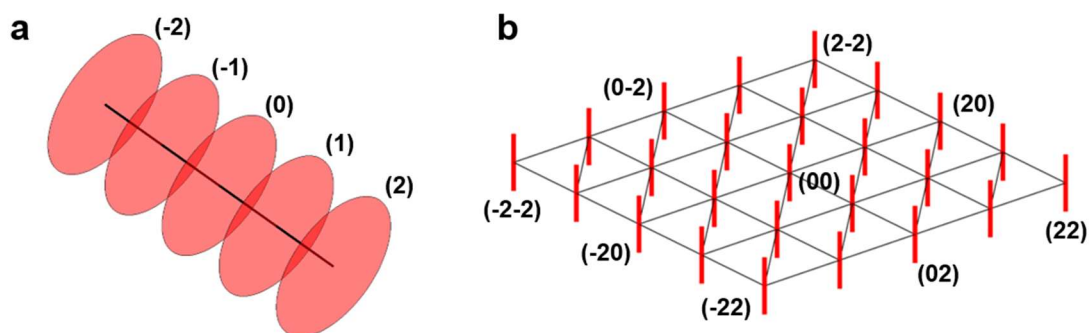


Figure 6.8. Intensity distributions for one- and two-dimensional crystals in reciprocal space. (a) nanowire: intensity is spread into disks (red) perpendicular to the axis of the rod (black line). (b) nanosheet: intensity is distributed along Bragg rods (red bars) perpendicular to the lattice of the sheet (black lines). The Miller indices of some reflections are indicated.

To show that this corresponds to an asymmetric lineshape in the powder pattern, the averaging of intensity in spherical coordinates is performed directly. As a crude and purely illustrative example, let the intensity I at a particular point (q_1, q_2, q_3) in reciprocal space around the reflection at position (h, k, l) take a three-dimensional Gaussian form,

$$I(q_1, q_2, q_3) = \sqrt{\frac{4 \ln 2}{\pi}} \frac{1}{\sigma_1 \sigma_2 \sigma_3} \exp \left(-4 \ln 2 \left\{ \frac{(q_1 - h)^2}{\sigma_1^2} + \frac{(q_2 - k)^2}{\sigma_2^2} + \frac{(q_3 - l)^2}{\sigma_3^2} \right\} \right) \quad (6.3)$$

Where $(\sigma_1, \sigma_2, \sigma_3)$ are the peak widths (full width half maximum, FWHM) in each direction. The Cartesian coordinates (q_1, q_2, q_3) are calculated by transformation of the points (Q, θ, φ) . Q in this case stands in for the radial coordinate. The integration of **Equation 6.3** over all angles θ and φ gives the intensity of the reflection:

$$I(Q) = \int_0^{2\pi} \int_0^\pi I(Q, \theta, \varphi) Q^2 \sin \theta \, d\theta d\varphi \quad (6.4)$$

To demonstrate the effect of crystal shape, the relative values of $\sigma_1, \sigma_2,$ and σ_3 are adjusted. Curves generated by numerical integration are shown in **Figure 6.8**.

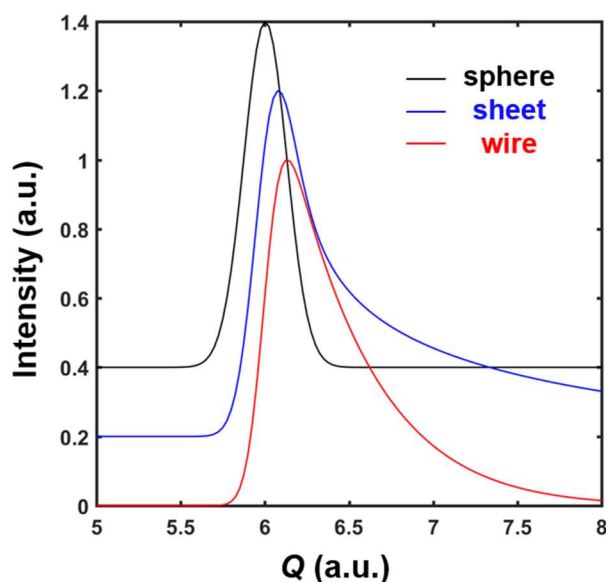


Figure 6.9. Powder diffraction line shapes for nanostructures of varying dimensionality. The spherically averaged intensity of a single reflection at location $(hkl) = (600)$ ($Q_{600} = 6$ a.u.) is determined by numerical integration of **Equations 6.3** and **6.4**. Curves are normalized to their maximum height and offset for clarity. For a sphere, the widths of the Gaussian components $\sigma_1 = \sigma_2 = \sigma_3 = 0.3$; for a sheet, $\sigma_1 = \sigma_2 = 0.25$ and $\sigma_3 = 10$; for a wire, $\sigma_1 = 0.2$ and $\sigma_2 = \sigma_3 = 4$.

It can be seen that the powder line shapes are qualitatively different for nanostructures with varying dimensionality. In spherical particles with all peak widths equal, the reflection takes a symmetric Gaussian shape centered exactly on the reciprocal lattice node as expected for a “normal” powder diffraction line. In a nanosheet with Bragg rods ($\sigma_3 \gg \sigma_1$ and σ_2) the line maximum is observed to be displaced from the spherical-particle peak center, and the line remains heavy-tailed at larger angles. In the case of nanowires (σ_3 and $\sigma_2 \gg \sigma_1$), the line remains asymmetric, but falls off more rapidly at large angles (relative to the peak maximum) compared to peaks from nanosheets. It is seen in section 6.3.3 that this peak shape is qualitatively observed in simulated diffraction patterns from chains of molecules. In principle, **Equation 6.4** represents a peak function which could actually be used for fitting diffraction data. At present the numerical routines used for preparing **Figure 6.8** are too slow for this purpose since the integral is evaluated directly instead of being approximated with a simpler function of a few parameters.

6.3.3. Toy model of powder diffraction in nanowires and molecular aggregates

A more physical model of the system suggested by **Equation 6.3** consists of a linear chain of molecules with well-defined intermolecular orientations. As a very simple starting point, fictitious molecular aggregates were built by stacking benzene (C_6H_6) molecules parallel to each other (**Figure 6.9a,c**). An intermolecular spacing of 3.8 Å was chosen somewhat arbitrarily based on a simulation of the benzene sandwich dimer.⁹¹ The structure factor $S(Q)$ was determined from the Debye scattering equation using the same program as in **Chapter 4.A.3**. Atomic coordinates for C_6H_6 and other molecules were obtained from the repository of sample structures for the molecular visualization program *IQMol*, available at <http://iqmol.org/>. To form chains, a series of consecutive displacement vectors \mathbf{x}_i was generated by selecting the next vector \mathbf{x}_{i+1}

from a uniformly distributed conical surface centered on \mathbf{x}_i with apex angle θ_{\max} . A random point on this surface gives an angle of flexure θ_{flex} and an angle of rotation φ_{rot} . \mathbf{x}_{i+1} is produced by tilting a copy of \mathbf{x}_i by θ_{flex} then rotating it by φ_{rot} , both about the original \mathbf{x}_i . The atomic coordinates for the molecular aggregate then are created by rotating a copy XYZ_i of the monomer (benzene) to align with \mathbf{x}_{i+1} , followed by translation along that vector to give the next unit XYZ_{i+1} . The length of \mathbf{x}_i can also be perturbed according to a normal distribution to create a chain with correlated spacing disorder.

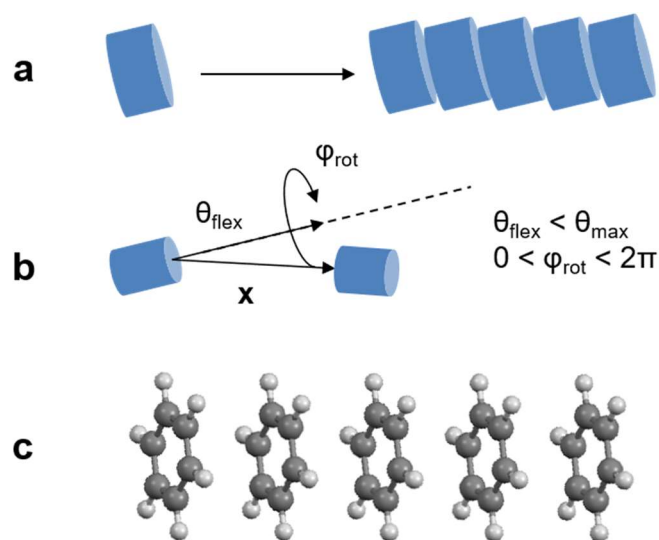


Figure 6.10. Assembly of a toy model of a molecular aggregate. (a) Schematic of a chain prepared by stacking a starting molecule. (b) Parameters used in generating the chain by rotating a molecule to align it to the displacement vector followed by translation. (c) Example of a perfectly aligned pentamer of benzene molecules.

First, diffraction patterns for aggregates with an increasing number of C_6H_6 subunits were calculated. No disorder was incorporated, so that aggregates consist of a truncated perfect lattice of molecules. To exaggerate the high-angle features, the

reduced Q -weighted structure factors $F(Q)$ for these chains are shown in **Figure 6.11**. $F(Q)$ for a single benzene molecule is nearly featureless due to the small size of the structure. As monomer subunits are added, peaks appear at multiples of 1.65 \AA^{-1} , or fractions of the intermolecular spacing. These peaks can be indexed (h) as (1), (2), etc. in one-dimensional reciprocal space. For short chains, these peaks are symmetric, but for longer chains the shape converges to sharp and asymmetric shapes similar to those observed in **Figure 6.7**. The toy model also reproduces the nonaxial peak **Figure 6.7a** at slightly larger angles relative to the principal (h) reflections. For the case of the (1) reflection, the nonaxial peak is centered at about 2.45 \AA^{-1} .

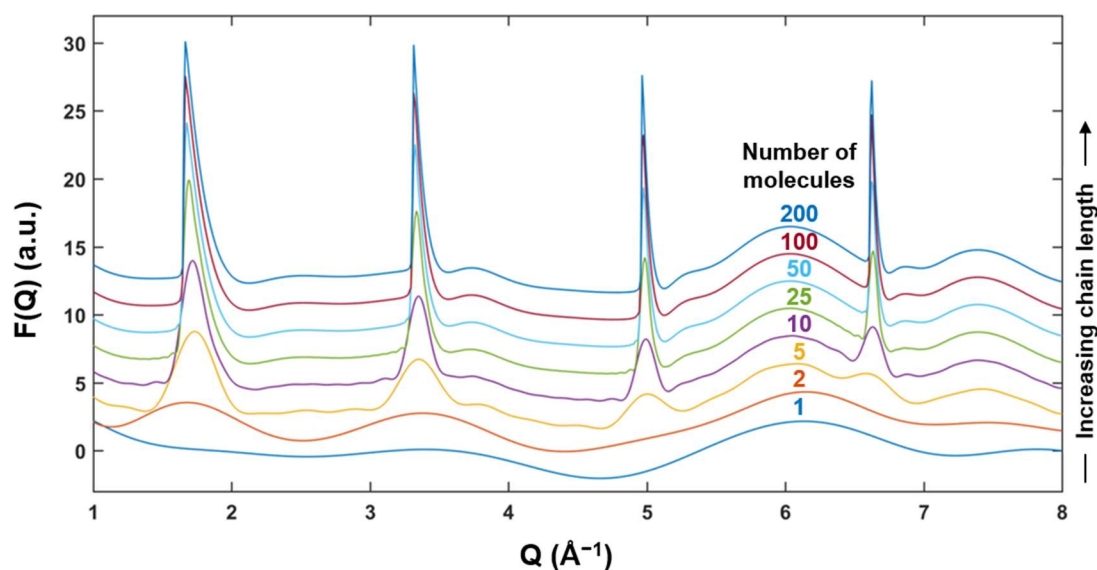


Figure 6.11. Simulated reduced structure factors for molecular chains with different numbers of stacked benzene molecules.

For a more complete analysis, the real-space pair distribution function $G(r)$ is calculated from $F(Q)$ by means of **Equation 6.2**. The resulting curves are shown in **Figure 6.12**. Although $G(r)$ is ideally a non-negative-valued histogram, truncation artifacts as a function of Q_{\min} introduce the sloped or rippling baselines seen here.¹⁵

The curves have also been smoothed using a Gaussian with a width of 0.4 Å to damp truncation artifacts resulting from the finite value of Q_{\max} . The histogram of atomic distances for the benzene molecule contains no values larger than 4.98 Å or smaller than 1.09 Å (the C-H bond length), so $G(r)$ does not have peaks outside this range for the lowest curve. As molecules are added to the chain, replicas of this monomer histogram appear at successive intervals of the intermolecular spacing of 3.8 Å. For a dimer, the first peak corresponding to intermolecular atomic distances occurs at the same r , 3.8 Å, and the largest- r peak is at about 6.3 Å, a difference of 2.5 Å. In comparison, the difference between the longest and smallest distance for a monomer is 3.89 Å. For geometric reasons, the replicas thus become narrower in real space with increasing r and the interatomic distances become less well-resolved.

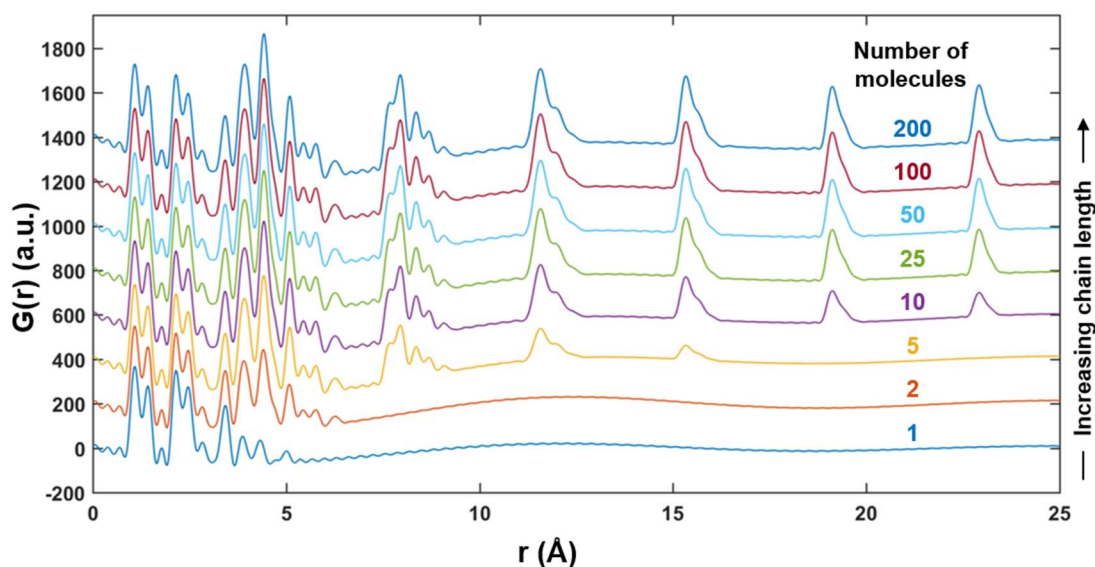


Figure 6.12. Smoothed pair distribution functions for molecular chains from transformation of the reduced structure factors.

Because the different parts of the PDF for each molecule are separable, it is possible that future structure determinations for molecular aggregates could use the

already-known geometry of the monomer as a starting point, and the intermolecular correlations could then be described by appropriately refining chain parameters such as those in **Figure 6.10**. The effects of various kinds of disorder on the scattering pattern are illustrated in **Figure 6.13**. For all types, it was necessary to average the scattering patterns from multiple perturbed structures, where atomic coordinates for a new chain were generated for each structure.

In one kind of disorder, the intermolecular vector is allowed to deviate from its previous direction by an angle, θ_{flex} , up to a value θ_{max} . **Figure 6.13a** shows that increasing θ_{max} , thereby making the chain more flexible, has the effect of greatly reducing the intensities of the (h) reflections at high indices and, for very flexible chains, substantially broadening the peaks. Interestingly, for the most flexible chains (top) the asymmetry of the peak changes to being heavy-tailed at smaller diffraction angles. As a result, the apparent number of peaks related to an inter-monomer spacing in a diffraction pattern, as well as their shape, can be taken as a measurement of the relative flexibility of the chains. One problem is that θ_{max} is not an easily measured physical quantity. However, the statistics of such flexible chains have been extensively studied as constrained random walks, which are of great importance in fields such as polymer physics and biophysics.⁹² An important quantity in random-walk chains is the persistence length ξ , which is roughly a measure of the length over which the chain can be treated as a rigid rod. It can be shown for some polymer models that the mean product of an intermolecular vector, \mathbf{x}_j , generated by the procedure above and the starting vector, \mathbf{x}_i , decays exponentially with the number of iterations or links, N , going from r_i to r_j :

$$C(N) = \langle \mathbf{x}_i \cdot \mathbf{x}_j \rangle = \exp\left(-\frac{NL}{\xi}\right) \quad (6.5)$$

The correlation function $C(N)$ can be determined from the procedure in **Figure 6.10** by averaging the results of the dot product for sufficiently long chains over many random trials. L is the inter-monomer distance, so ξ / L is the persistence number of links. Analyzing the chains used to generate the results of **Figure 6.13a**, the persistence length of the benzene aggregates with intermolecular spacing of 3.8 Å ranges from only 2.3 nm for $\theta_{\max} = 45^\circ$ to 50 nm for $\theta_{\max} = 10^\circ$. Obviously, ξ diverges as θ_{\max} becomes small; for a θ_{\max} of 1° , $\xi \approx 5 \mu\text{m}$, approaching macroscopic dimensions. For comparison, the persistence length of DNA under a similar random-walk model is about 50 nm, and for simple polymers such as polyethylene it is on the order of 1 nm.⁹² For a more refined peak shape model and well-behaved system, ξ may be useful for determining the flexibility of molecular or cluster aggregates.

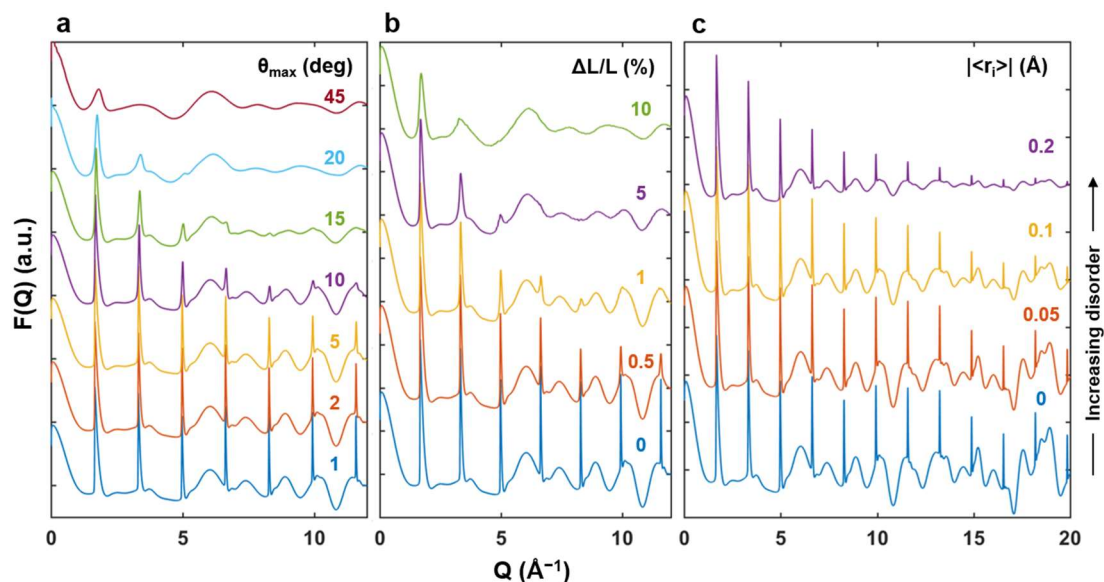


Figure 6.13. Effects of disorder types on reduced structure factors for flexural, spacing, and isotropic thermal disorder (a, b, and c, respectively) of benzene aggregates. In (a-b), the patterns were calculated using 100 monomers; in (c), 50 monomers were used. for (c), $|\langle r_i \rangle|$ is the root mean square atomic displacement. Each pattern is the average of the Debye scattering calculation for 25 different chains.

Figure 6.13b shows the results of another important kind of disorder: agitation of the intermolecular distances in the aggregate, resulting in correlated⁹³ spacing disorder. During chain generation, the intermolecular distance vector \mathbf{x}_i at each step was randomly modified according to a Gaussian distribution. The standard deviation ΔL of the mean intermolecular spacing, $L = 3.8 \text{ \AA}$, for the agitated chains ranges from 0.019 \AA (0.5%) to 0.38 \AA (10%). It is observed that even apparently small displacements of 1% substantially reduce the intensity of (h) reflections at larger angles and broaden all peaks. Because deviations from the mean intermolecular spacing propagate along the chain, this spacing disorder results in increasingly broad peaks in $G(r)$ at larger interatomic distances (not shown). Due to the weakness of intermolecular interactions, random thermal displacements tend to be much larger. Single-crystal diffraction measurements have reported isotropic mean square displacements up to 0.3 \AA for atoms in molecular crystals, and it has been demonstrated that nearly all of this displacement should be taken up by disorder in the position and orientation of the entire molecule.^{94,95} Although these measurements assume uncorrelated motion, if these values were translated to the interspacing disorder considered here, they could pose significant difficulties for distinguishing the important (1), (2), etc. peaks. In the case of the $\text{Cd}_{37}\text{S}_{20}$ MSCs that spurred this investigation, HRTEM showed significant flexibility of the columnar mesophase and irregular gaps between clusters on the nm scale,⁶⁸ in agreement with the observation that adding mesophase correlations did not greatly improve the fit to the PDF during determination of the single-cluster structure.⁶⁷

The impact on the diffraction pattern of the uncorrelated disorder that occurs during thermal agitation, which gives rise to a Debye-Waller factor reducing the magnitude of the atomic form factor for large Q ,¹⁴ is less severe. **Figure 6.13c** illustrates the changes in the diffraction pattern. Here, atomic coordinates for a perfect

chain of 50 benzene molecules were randomly perturbed from their original positions according to a Gaussian distribution, as applies for a harmonic oscillator. $\langle r_i \rangle$ gives the standard deviation of the lengths of these displacements, the directions of which are uniformly distributed on a sphere. Even for displacements of up to 0.2 Å, the amplitudes of (*h*) peaks are attenuated much less rapidly than for similar correlated displacements in **Figure 6.13b**.

An analysis of the impact of different types of disorder on the expected diffraction patterns from the toy model of benzene aggregates has shown that chain flexure, intermolecular spacing disorder, and isotropic thermal agitation can have significant impacts on the observed diffracted intensities, especially of the important asymmetric (*h*) peaks. It may be possible to use changes in these peak shapes to derive information about the aggregate flexibility. If the dependence of the peak parameters on *Q* is generally different for flexure and spacing disorder, they could be separated. Peak symmetry is not affected by thermal displacements, but does change for large correlated displacements. However, the overall effect of all types of disorder is to reduce greatly the amplitude of $F(Q)$ at large values of *Q*. Because the x-ray form factor already diminishes quite rapidly at large scattering angles,⁹⁶ the decay in the molecular correlations further reduces the intensity and thus degrades the overall resolution during structure determination.

6.3.4. Limitations of the toy model and suggested experiments

One limitation of the analysis of an asymmetrical peak shape for one-dimensional nanostructures should be mentioned. Because peak asymmetry is not generally reported in the literature for high-aspect-ratio semiconductor nanoparticles such as nanowires, it is important to know on what length scale perpendicular to the wire or aggregate axis peak asymmetry might be expected. Therefore, patterns for

aggregates of successively larger molecules were simulated. These molecules were “circular” polycyclic aromatic hydrocarbons produced by adding hexagons to each edge of the preceding molecule: benzene (C_6H_6), coronene ($C_{24}H_{12}$), circumcoronene ($C_{54}H_{18}$), $C_{96}H_{24}$, and $C_{150}H_{30}$. Aggregates of 50 molecules with no disorder were constructed in the same fashion as in section 6.3.3 with an intermolecular spacing of 3.4 Å. Depictions of some of these molecules along with the aggregate structure factors are shown in **Figure 6.14**. Disappointingly, it is seen that the asymmetry of the characteristic (h) Bragg peaks decreases rapidly as the width of the aggregate is increased. For circumcoronene, at an approximate diameter of 1.4 nm (**Figure 6.14a**, at right), the reflections are nearly symmetrical (**Figure 6.14b**, center). Some other changes to $F(Q)$ are apparent. The “nonaxial” diffraction peaks move closer to the principal (h) reflection and additional peaks appear. Additionally, as the effective crystallite size becomes non-negligible in directions perpendicular to the chain axis the corresponding reflections become significant, as seen from the two broad peaks at 2.9 and 3.4 Å for $C_{150}H_{30}$. Hence, it is likely that analysis of the asymmetry of the Bragg reflections for one-dimensional chains will require them to be extremely thin. For thicker nanowires, however, it becomes more feasible to apply approaches based on powder diffraction in bulk-like crystals such as Rietveld refinement.

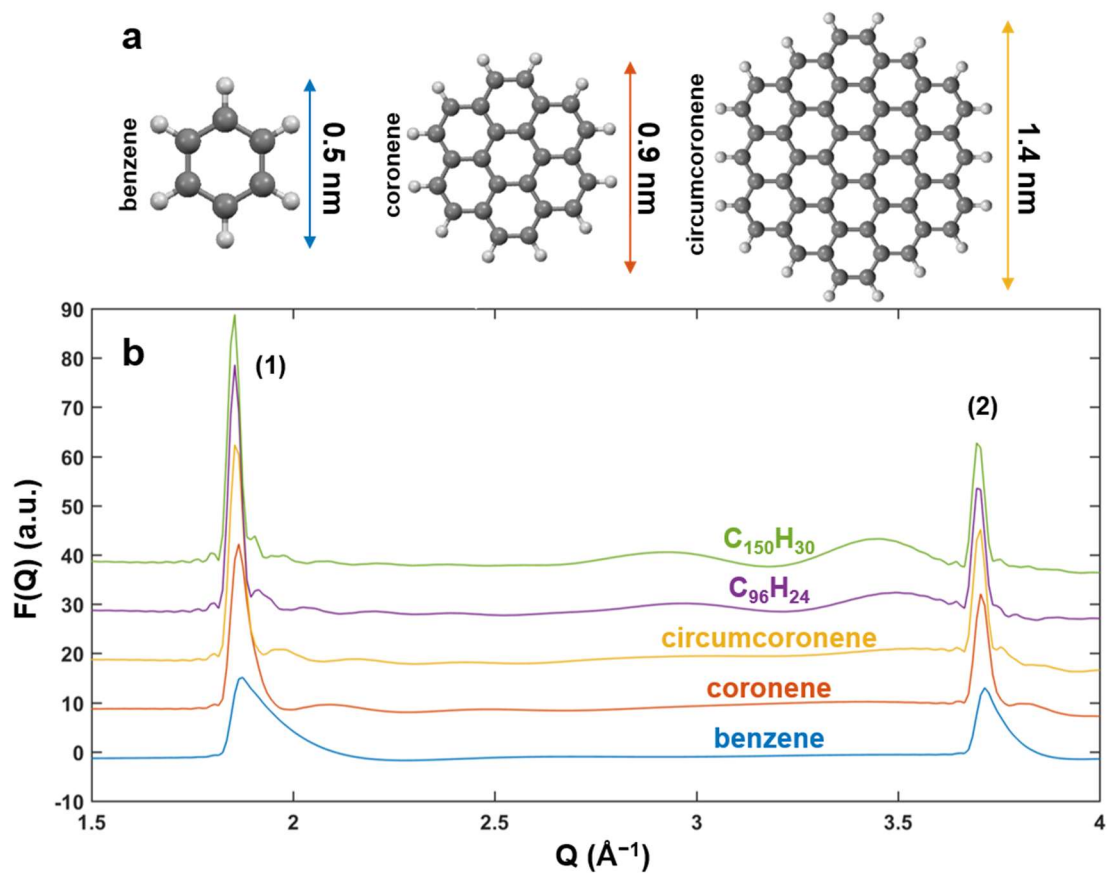


Figure 6.14. Structures of some flat polycyclic aromatic hydrocarbons (a) and reduced structure factors for their aggregates (b). One-dimensional Miller indices are indicated in parentheses. Each aggregate consists of 50 monomers.

Though the work is incomplete at present, some guidelines for interpretation of diffraction patterns from complex mesophase structures, particularly columnar or linear polymeric structures, can be understood, and these rules were presented here. However, experimental data are badly needed to assess to what extent these rules are practically applicable for real systems. Some experiments which could be useful in determining intermolecular configurations for rod-like or wire-like molecular or cluster aggregates are now mentioned.

A number of metal-containing carboxylate, thiolate, or amine complexes, termed metallomesogens, are known to form liquid crystals and have been studied by XRD.⁹⁷ Lamellar structures are commonly reported, but many such metallomesogens form columnar phases. Such materials have been suggested for future applications as one-dimensional conductors, tunable dyes, and nonlinear optical materials. An example of a columnar metallomesogen is shown in **Figure 6.15**; Cu²⁺ carboxylates (Cu(COOR)₂, R = alkyl group), among others, adopt a structure consisting of metal carboxylate “lantern” monomers with a formula Cu₂O₈. Each unit is offset perpendicular to the column axis, so that each metal atom adopts an overall octahedral coordination with one metal-metal bond and five metal-oxygen bonds. The structure of **Figure 6.15** was determined by use of extended X-ray absorption fine structure (EXAFS). EXAFS contains structural information in oscillations of the absorption coefficient of a material at photon energies above (a few hundred eV) that of an absorption edge. These oscillations arise from interference between the wavefunctions of photoelectrons ejected by X-ray absorption and photoelectrons back-scattered from nearby atoms, changing the transition dipole moment and thus the absorption coefficient as a function of X-ray energy.⁹⁸ The oscillations are Fourier-transformed to produce a real-space radial distribution function similar to that derived from the X-ray total scattering pattern. While very powerful, EXAFS suffers from an intrinsic limitation in that the derived radial distribution function decays very rapidly in real space, so that it only probes interatomic distances out to no more than 5 Å in practice. The probability for multiple-scattering events from distant atomic sites is very small, leading to a limited resolution in reciprocal space. EXAFS is also restricted to probing the local environment around the specific element in question, while all atoms in the sample contribute to XRD. An X-ray diffraction analysis of columnar mesophases like those in **Figure 6.15** would be able to determine with better resolution the rigidity of

the column and the conformations of the dimers, which will be important in establishing structure-property relationships for the wide range of mesophases based on different ligands and metals⁹⁷ that have been prepared thus far.

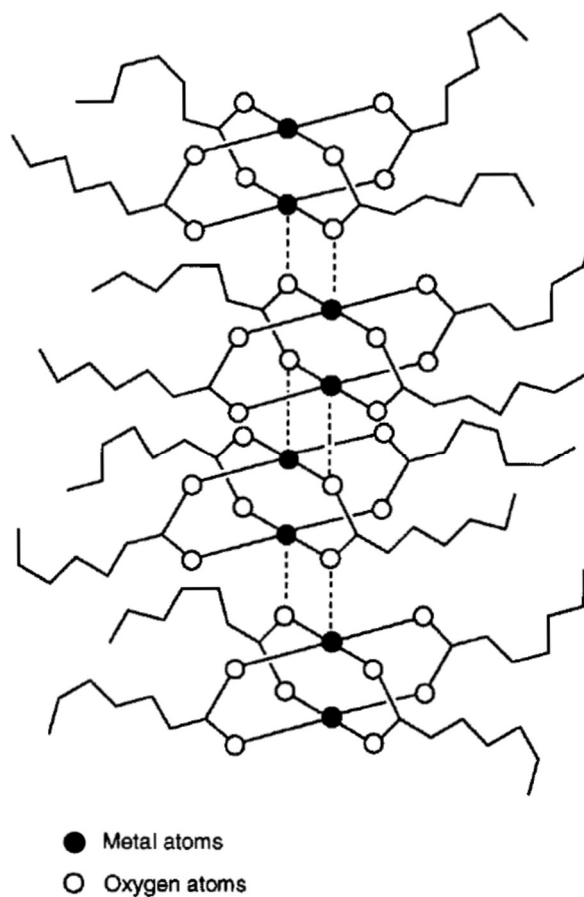


Figure 6.15. Example of a one-dimensional “aggregate” structure in a metal-containing columnar liquid crystal with staggered M_2O_8 centers. Reproduced from figure 8-12 of reference 97 by permission of John Wiley and Sons.

Other systems that have proved to be of enduring interest for electronic and optical applications are molecular dyes and inorganic molecular wires. For the first case, ionic dyes such as 1,1'-diethyl-2,2'-cyanine chloride (pseudocyanine chloride, PIC, with the formula $C_{23}H_{23}N_2^+Cl^-$) form pi-stacked chains in concentrated or high-

ionic-strength solutions.^{99, 100} The PIC molecule and one proposed structure for an aggregate¹⁰¹ are shown in **Figure 6.16**. Such dye aggregates, termed J- or H-aggregates depending on their connectivity,¹⁰² are thought to adopt complex conformations in the solution state which differ from the molecular packing derived from crystallographic experiments in the solid state.¹⁰¹ Despite examinations e.g. by microscopy^{103, 104} and by optical and theoretical methods,¹⁰⁵⁻¹⁰⁷ the actual nearest-neighbor intermolecular correlations still lack direct confirmation.

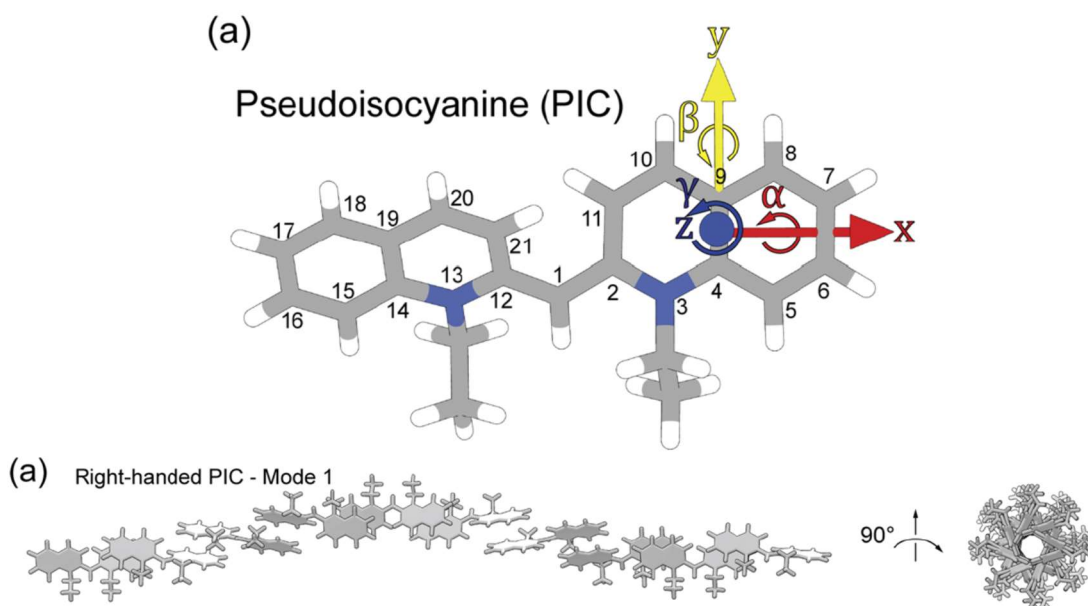


Figure 6.16. Example of an aggregate-forming dye, pseudoisocyanine (PIC). Top: molecular structure of a monomer showing nonplanarity. Bottom: one possible mode of aggregation showing pi-stacking of PIC molecules into a right-handed helix. Reproduced from figures 2a and 3a of reference 101 by permission of AIP Publishing.

At modern synchrotron sources, flux is sufficient to be able to detect aggregates and nanoparticles at very low concentrations by subtracting a solvent background.^{108, 109} The use of a dilute solution will be necessary to minimize

contributions from the structuring of the solvent, as mentioned in **Chapter 4.A.2**. Applying the analysis of the preceding section directly could be used in a first approximation to derive a correlation length, which for dye aggregates is an important parameter owing to its poorly-characterized relationship to the delocalization length¹¹⁰ of excitonic states along the length of the chain. With more sophisticated analysis, the true intermolecular conformation might be confirmed, which will serve as an important check against calculations of the optical properties of aggregates as a function of their structure. The analysis will be equally applicable to inorganic molecular wires such as LiMo_3Se_3 ,¹¹¹⁻¹¹³ and, as previously mentioned, CNTs.⁸² All of these one-dimensional nanomaterials have long been suggested to have great promise for sensors, composites, and molecule-scale electronics. What has been missing in previous investigations is a methodology for deriving important mesoscale parameters based on direct interrogation of the structure in a wide variety of environments, including those in which well-separated wires and aggregates are truly one-dimensional.

6.A. REFERENCES

1. Fenton, J. L.; Steimle, B. C.; Schaak, R. E., Tunable Intraparticle Frameworks for Creating Complex Heterostructured Nanoparticle Libraries. *Science* **2018**, 360, 513-517.
2. Son, D. H.; Hughes, S. M.; Yin, Y.; Paul Alivisatos, A., Cation Exchange Reactions in Ionic Nanocrystals. *Science* **2004**, 306, 1009-1012.
3. Ha, D.-H.; Caldwell, A. H.; Ward, M. J.; Honrao, S.; Mathew, K.; Hovden, R.; Koker, M. K. A.; Muller, D. A.; Hennig, R. G.; Robinson, R. D., Solid–Solid Phase Transformations Induced through Cation Exchange and Strain in 2D Heterostructured Copper Sulfide Nanocrystals. *Nano Letters* **2014**, 14, 7090-7099.
4. Dachraoui, M.; Vedel, J., Improvement of Cuprous Sulphide Stoichiometry by Electrochemical and Chemical Methods. *Solar Cells* **1987**, 22, 187-194.
5. Dennler, G.; Chmielowski, R.; Jacob, S.; Capet, F.; Roussel, P.; Zastrow, S.; Nielsch, K.; Opahle, I.; Madsen, G. K. H., Are Binary Copper Sulfides/Selenides Really New and Promising Thermoelectric Materials? *Advanced Energy Materials* **2014**, 4, 1301581.
6. Pfisterer, F., The Wet-Topotaxial Process of Junction Formation and Surface Treatments of Cu₂S–CdS Thin-Film Solar Cells. *Thin Solid Films* **2003**, 431-432, 470-476.
7. Xie, Y.; Riedinger, A.; Prato, M.; Casu, A.; Genovese, A.; Guardia, P.; Sottini, S.; Sangregorio, C.; Miszta, K.; Ghosh, S.; Pellegrino, T.; Manna, L., Copper Sulfide Nanocrystals with Tunable Composition by Reduction of Covellite Nanocrystals with Cu⁺ Ions. *Journal of the American Chemical Society* **2013**, 135, 17630-17637.
8. Dorfs, D.; Härtling, T.; Miszta, K.; Bigall, N. C.; Kim, M. R.; Genovese, A.; Falqui, A.; Povia, M.; Manna, L., Reversible Tunability of the Near-Infrared Valence

Band Plasmon Resonance in Cu_{2-x}Se Nanocrystals. *Journal of the American Chemical Society* **2011**, 133, 11175-11180.

9. Kriegel, I.; Jiang, C.; Rodríguez-Fernández, J.; Schaller, R. D.; Talapin, D. V.; Como, E. d.; Feldmann, J., Tuning the Excitonic and Plasmonic Properties of Copper Chalcogenide Nanocrystals. *Journal of the American Chemical Society* **2012**, 134, 1583-1590.

10. Groiss, H.; Hesser, G.; Heiss, W.; Schäffler, F.; Leitsmann, R.; Bechstedt, F.; Koike, K.; Yano, M., Coherent {001} Interfaces between Rocksalt and Zinc-Blende Crystal Structures. *Physical Review B* **2009**, 79, 235331.

11. Shaw, S.; Colaux, J. L.; Hay, J. L.; Peiris, F. C.; Cademartiri, L., Building Materials from Colloidal Nanocrystal Arrays: Evolution of Structure, Composition, and Mechanical Properties upon the Removal of Ligands by O_2 Plasma. *Advanced Materials* **2016**, 28, 8900-8905.

12. Shaw, S.; Tian, X.; Silva, T. F.; Bobbitt, J. M.; Naab, F.; Rodrigues, C. L.; Smith, E. A.; Cademartiri, L., Selective Removal of Ligands from Colloidal Nanocrystal Assemblies with Non-Oxidizing He Plasmas. *Chemistry of Materials* **2018**, 30, 5961–5967.

13. Egami, T.; Billinge, S. J. L., *Underneath the Bragg Peaks: Structural Analysis of Complex Materials*. Elsevier: Oxford, 2003.

14. Guinier, A., *X-Ray Diffraction in Crystals, Imperfect Crystals, and Amorphous Bodies*. Dover: Mineola, New York, 1994.

15. Farrow, C. L.; Billinge, S. J. L., Relationship between the Atomic Pair Distribution Function and Small-Angle Scattering: Implications for Modeling of Nanoparticles. *Acta Crystallographica A* **2009**, 65, 232-239.

16. Petkov, V.; Jeong, I.-K.; Chung, J. S.; Thorpe, M. F.; Kycia, S.; Billinge, S. J. L., High Real-Space Resolution Measurement of the Local Structure of Ga_xIn_xAs Using X-Ray Diffraction. *Physical Review Letters* **1999**, 83, 4089-4092.
17. Dinnebier, R. E.; Billinge, S. J. L., *Powder Diffraction: Theory and Practice*. Royal Society of Chemistry: Cambridge, UK, 2008.
18. Thimsen, E.; Peng, Q.; Martinson, A. B. F.; Pellin, M. J.; Elam, J. W., Ion Exchange in Ultrathin Films of Cu₂S and ZnS under Atomic Layer Deposition Conditions. *Chemistry of Materials* **2011**, 23, 4411–4413.
19. Dasgupta, N. P.; Meng, X.; Elam, J. W.; Martinson, A. B. F., Atomic Layer Deposition of Metal Sulfide Materials. *Accounts of Chemical Research* **2015**, 48, 341-348.
20. Chupas, P. J.; Chapman, K. W.; Kurtz, C.; Hanson, J. C.; Lee, P. L.; Grey, C. P., A Versatile Sample-Environment Cell for Non-Ambient X-Ray Scattering Experiments. *Journal of Applied Crystallography* **2008**, 41, 822-824.
21. Zhang, H.; Solomon, L. V.; Ha, D.-H.; Honrao, S.; Hennig, R. G.; Robinson, R. D., (NH₄)₂S, a Highly Reactive Molecular Precursor for Low Temperature Anion Exchange Reactions in Nanoparticles. *Dalton Transactions* **2013**, 42, 12596-12599.
22. Gorlin, Y.; Jaramillo, T. F., Investigation of Surface Oxidation Processes on Manganese Oxide Electrocatalysts using Electrochemical Methods and ex situ X-ray Photoelectron Spectroscopy. *Journal of The Electrochemical Society* **2012**, 159, H782-H786
23. Zhu, H.; Zhang, S.; Huang, Y.-X.; Wu, L.; Sun, S., Monodisperse M_xFe_{3-x}O₄ (M = Fe, Cu, Co, Mn) Nanoparticles and Their Electrocatalysis for Oxygen Reduction Reaction. *Nano Letters* **2013**, 13, 2947-2951.

24. Yu, T.; Moon, J.; Park, J.; Park, Y. I.; Na, H. B.; Kim, B. H.; Song, I. C.; Moon, W. K.; Hyeon, T., Various-Shaped Uniform Mn₃O₄ Nanocrystals Synthesized at Low Temperature in Air Atmosphere. *Chemistry of Materials* **2009**, 21, 2272-2279.
25. Haynes, W. M.; Bruno, T. J.; Lide, D. R., *CRC Handbook of Chemistry and Physics, 96th edition*. CRC Press: Boca Raton, FL, 2015.
26. Yin, Y.; Rioux, R. M.; Erdonmez, C. K.; Hughes, S.; Somorjai, G. A.; Alivisatos, A. P., Formation of Hollow Nanocrystals through the Nanoscale Kirkendall Effect. *Science* **2004**, 304, 711-714.
27. Thomson, J. W.; Nagashima, K.; Macdonald, P. M.; Ozin, G. A., From Sulfur–Amine Solutions to Metal Sulfide Nanocrystals: Peering into the Oleylamine–Sulfur Black Box. *Journal of the American Chemical Society* **2011**, 133, 5036-5041.
28. Suntivich, J.; Hong, W. T.; Lee, Y.-L.; Rondinell, J. M.; Yang, W.; Goodenough, J. B.; Dabrowski, B.; Freeland, J. W.; Shao-Horn, Y., Estimating Hybridization of Transition Metal and Oxygen States in Perovskites from O K-edge X-ray Absorption Spectroscopy. *Journal of Physical Chemistry C* **2014**, 118, 1856-1863.
29. Ha, D.-H.; Moreau, L. M.; Honrao, S.; Hennig, R. G.; Robinson, R. D., The Oxidation of Cobalt Nanoparticles into Kirkendall-Hollowed CoO and Co₃O₄: The Diffusion Mechanisms and Atomic Structural Transformations. *Journal of Physical Chemistry C* **2013**, 117, 14303-14312.
30. Bettermann, G.; Krause, W.; Riess, G.; Hofmann, T., Phosphorus Compounds, Inorganic. In *Ullmann's Encyclopedia of Industrial Chemistry*, Elvers, B., Ed. John Wiley and Sons: New York, 2000.

31. Langner, B. E., Selenium and Selenium Compounds. In *Ullmann's Encyclopedia of Industrial Chemistry*, Elvers, B., Ed. John Wiley and Sons: New York, 2000.
32. Suntivich, J.; Gasteiger, H. A.; Yabuuchi, N.; Shao-Horn, Y., Electrocatalytic Measurement Methodology of Oxide Catalysts Using a Thin-Film Rotating Disk Electrode. *Journal of the Electrochemical Society* **2010**, 157, 81263-81268.
33. Bard, A. J.; Faulkner, L. R., *Electrochemical Methods: Fundamentals and Applications*. 2nd ed.; Wiley: New York, 2000.
34. McBreen, J., The Electrochemistry of β -MnO₂ and γ -MnO₂ in Alkaline Electrolyte. *Electrochimica Acta* **1975**, 20, 221-225.
35. Kuo, D.-Y.; Kawasaki, J. K.; Nelson, J. N.; Kloppenburg, J.; Hautier, G.; Shen, K. M.; Schlom, D. G.; Suntivich, J., Influence of Surface Adsorption on the Oxygen Evolution Reaction on IrO₂(110). *Journal of the American Chemical Society* **2017**, 139, 3473–3479.
36. McCrum, I. T.; Janik, M. J., pH and Alkali Cation Effects on the Pt Cyclic Voltammogram Explained Using Density Functional Theory. *Journal of Physical Chemistry C* **2016**, 120, 457–471.
37. Llorente, V. B.; Dzhagan, V. M.; Gaponik, N.; Iglesias, R. A.; Zahn, D. R. T.; Lesnyak, V., Electrochemical Tuning of Localized Surface Plasmon Resonance in Copper Chalcogenide Nanocrystals. *The Journal of Physical Chemistry C* **2017**, 121, 18244-18253.
38. Yao, Y. Reaction Mechanism and Size-Dependent Electrochemical Properties Study of Cu_{2-x}S Versus Li. M.S. Thesis, Cornell University, 2018.
39. Potter, R., An Electrochemical Investigation of the System Copper-Sulfur. *Economic Geology* **1977**, 72, 1524-1542.

40. Asami, K.; Nishi, H.; Tatsuma, T., Electrochemical Redox-Based Tuning of Near Infrared Localized Plasmons of CuS Nanoplates. *Nanoscale* **2016**, 6, 14092-14096.
41. Coughlan, C.; Ibáñez, M.; Dobrozhan, O.; Singh, A.; Cabot, A.; Ryan, K. M., Compound Copper Chalcogenide Nanocrystals. *Chemical Reviews* **2017**, 117, 5865-6109.
42. Kumar, V.; Kröger, F. A., Self-Diffusion and the Defect Structure of Cadmium Sulfide. *Journal of Solid State Chemistry* **1971**, 3, 387-400.
43. Stevenson, D. A., Diffusion in the Chalcogenides of Zn, Cd, and Pb. In *Atomic Diffusion in Semiconductors*, Shaw, D., Ed. Plenum Publishing Company: New York, 1973.
44. Mehrer, H., *Diffusion in Solids*. Springer: Heidelberg, 2007.
45. Shewmon, P. G., *Diffusion in Solids*. 2nd ed.; Minerals, Metals, & Materials Society: Warrendale, Pa., 1989.
46. Yang, Y.; Chen, C.-C.; Scott, M. C.; Ophus, C.; Xu, R.; Pryor, A.; Wu, L.; Sun, F.; Theis, W.; Zhou, J.; Eisenbach, M.; Kent, P. R. C.; Sabirianov, R. F.; Zeng, H.; Ercius, P.; Miao, J., Deciphering Chemical Order/Disorder and Material Properties at the Single-Atom Level. *Nature* **2017**, 542, 75-79.
47. Muller, D. A.; Nakagawa, N.; Ohtomo, A.; Grazul, J. L.; Hwang, H. Y., Atomic-Scale Imaging of Nanoengineered Oxygen Vacancy Profiles in SrTiO₃. *Nature* **2004**, 430, 657–661.
48. Kim, H.; Zhang, J. Y.; Raghavan, S.; Stemmer, S., Direct Observation of Sr Vacancies in SrTiO₃ by Quantitative Scanning Transmission Electron Microscopy. *Physical Review X* **2016**, 6, 041063.
49. Ishikawa, R.; Mishra, R.; Lupini, A. R.; Findlay, S. D.; Taniguchi, T.; Pantelides, S. T.; Pennycook, S. J., Direct Observation of Dopant Atom Diffusion in a

Bulk Semiconductor Crystal Enhanced by a Large Size Mismatch. *Physical Review Letters* **2014**, 113, 155501.

50. Gunawan, A. A.; Mkhoyan, K. A.; Wills, A. W.; Thomas, M. G.; Norris, D. J., Imaging “Invisible” Dopant Atoms in Semiconductor Nanocrystals. *Nano Letters* **2011**, 11, 5553–5557.

51. Peters, J. L.; van den Bos, K. H. W.; Van Aert, S.; Goris, B.; Bals, S.; Vanmaekelbergh, D., Ligand-Induced Shape Transformation of PbSe Nanocrystals. *Chemistry of Materials* **2017**, 29, 4122-4128.

52. Yalcin, A. O.; Fan, Z.; Goris, B.; Li, W.-F.; Koster, R. S.; Fang, C.-M.; Blaaderen, A. v.; Casavola, M.; Tichelaar, F. D.; Bals, S.; Tendeloo, G. V.; Vlugt, T. J. H.; Vanmaekelbergh, D.; Zandbergen, H. W.; Huis, M. A. v., Atomic Resolution Monitoring of Cation Exchange in CdSe-PbSe Heteronanocrystals during Epitaxial Solid–Solid–Vapor Growth. *Nano Letters* **2014**, 14, 3661–3667.

53. Williams, D. B.; Carter, C. B., *Transmission Electron Microscopy: A Textbook for Materials Science*. 2nd ed.; Springer Science+Business Media: New York, 2009.

54. Zheng, H.; Rivest, J. B.; Miller, T. A.; Sadtler, B.; Lindenberg, A.; Toney, M. F.; Wang, L.-W.; Kisielowski, C.; Alivisatos, A. P., Observation of Transient Structural-Transformation Dynamics in a Cu₂S Nanorod *Science* **2011**, 333, 206-209.

55. Blackburn, J. L.; Chappell, H.; Luther, J. M.; Nozik, A. J.; Johnson, J. C., Correlation between Photooxidation and the Appearance of Raman Scattering Bands in Lead Chalcogenide Quantum Dots. *Journal of Physical Chemistry Letters* **2011**, 2, 599-603.

56. Yu, Y.; Zhang, D.; Kisielowski, C.; Dou, L.; Kornienko, N.; Bekenstein, Y.; Wong, A. B.; Alivisatos, A. P.; Yang, P., Atomic Resolution Imaging of Halide Perovskites. *Nano Letters* **2016**, 16, 7530–7535.

57. Brennan, M. C.; Kuno, M.; Rouvimov, S., Crystal Structure of Individual CsPbBr₃ Perovskite Nanocubes. *Inorganic Chemistry* **2019**, *58*, 1555–1560.
58. Deconihout, B.; Pareige, C.; Pareige, P.; Blavette, D.; Menand, A., Tomographic Atom Probe: New Dimension in Materials Analysis. *Microscopy and Microanalysis* **1999**, *5*, 39–47.
59. Kelly, T. F.; Larson, D. J., Atom Probe Tomography 2012. *Annual Review of Materials Research* **2012**, *42*, 1-31.
60. Gur, I.; Fromer, N. A.; Geier, M. L.; Alivisatos, A. P., Air-Stable All-Inorganic Nanocrystal Solar Cells Processed from Solution. *Science* **2005**, *310*, 462-465.
61. Kinder, E.; Moroz, P.; Diederich, G.; Johnson, A.; Kirsanova, M.; Nemchinov, A.; O'Connor, T.; Roth, D.; Zamkov, M., Fabrication of All-Inorganic Nanocrystal Solids through Matrix Encapsulation of Nanocrystal Arrays. *Journal of the American Chemical Society* **2011**, *133*, 20488–20499.
62. Moroz, P.; Liyanage, G.; Kholmicheva, N. N.; Yakunin, S.; Rijal, U.; Uprety, P.; Bastola, E.; Mellott, B.; Subedi, K.; Sun, L.; Kovalenko, M. V.; Zamkov, M., Infrared Emitting PbS Nanocrystal Solids through Matrix Encapsulation. *Chemistry of Materials* **2014**, *26*, 4256–4264.
63. Sharma, R.; Sawvel, A. M.; Barton, B.; Dong, A.; Buonsanti, R.; Llodes, A.; Schaible, E.; Axnanda, S.; Liu, Z.; Urban, J. J.; Nordlund, D.; Kisielowski, C.; Milliron, D. J., Nanocrystal Superlattice Embedded within an Inorganic Semiconducting Matrix by in Situ Ligand Exchange: Fabrication and Morphology. *Chemistry of Materials* **2015**, *27*, 2755–2758.
64. Perea, D. E.; Liu, J.; Bartrand, J.; Dicken, Q.; Thevuthasan, S. T.; Browning, N. D.; Evans, J. E., Atom Probe Tomographic Mapping Directly Reveals the Atomic Distribution of Phosphorus in Resin Embedded Ferritin. *Scientific Reports* **2016**, *6*, 1-9.

65. Prosa, T. J.; Larson, D. J., Modern Focused-Ion-Beam-Based Site-Specific Specimen Preparation for Atom Probe Tomography. *Microscopy and Microanalysis* **2017**, *23*, 194–209.
66. Kim, S.-H.; Kang, P. W.; Park, O. O.; Seol, J.-B.; Ahn, J.-P.; Lee, J. Y.; Choi, P.-P., A New Method for Mapping the Three-Dimensional Atomic Distribution within Nanoparticles by Atom Probe Tomography (APT). *Ultramicroscopy* **2018**, *190*, 30-38.
67. Williamson, C. B.; Nevers, D. R.; Nelson, A.; Hadar, I.; Banin, U.; Hanrath, T.; Robinson, R. D., Chemically Reversible Isomerization of Inorganic Clusters. *Science* **2019**, *363*, 731-735.
68. Nevers, D. R.; Williamson, C. B.; Savitzky, B. H.; Hadar, I.; Banin, U.; Kourkoutis, L. F.; Hanrath, T.; Robinson, R. D., Mesophase Formation Stabilizes High-purity Magic-sized Clusters. *Journal of the American Chemical Society* **2018**, *140*, 3652–3662.
69. Kudera, S.; Zanella, M.; Giannini, C.; Rizzo, A.; Li, Y.; Gigli, G.; Cingolani, R.; Ciccarella, G.; Spahl, W.; Parak, W. J.; Manna, L., Sequential Growth of Magic-Size CdSe Nanocrystals. *Advanced Materials* **2007**, *19*, 548-552.
70. Wang, Y.; Liu, Y. H.; Zhang, Y.; Wang, F.; Kowalski, P. J.; Rohrs, H. W.; Loomis, R. A.; Gross, M. L.; Buhro, W. E., Isolation of the Magic-Size CdSe Nanoclusters [(CdSe)₁₃(n-octylamine)₁₃] and [(CdSe)₁₃(oleylamine)₁₃]. *Angewandte Chemie International Edition* **2012**, *51*, 6154-6157.
71. Hsieh, T.-E.; Yang, T.-w.; Hsieh, C.-y.; Huang, S.-j.; Yeh, Y.-q.; Chen, C.-H.; Li, E. Y.; Liu, Y.-H., Unraveling the Structure of Magic-Size (CdSe)₁₃ Cluster Pairs. *Chemistry of Materials* **2018**, *30*, 5468-5477.
72. Riehle, F. S.; Bienert, R.; Thomann, R.; Urban, G. A.; Krüger, M., Blue Luminescence and Superstructures from Magic Size Clusters of CdSe. *Nano Letters* **2009**, *9*, 514-518.

73. Nevers, D. R.; Williamson, C. B.; Hanrath, T.; Robinson, R. D., Surface Chemistry of Cadmium Sulfide Magic-Sized Clusters: A Window into Ligand-Nanoparticle Interactions. *Chemical Communications* **2017**, 53, 2866-2869.
74. Kasuya, A.; Sivamohan, R.; Barnakov, Y. A.; Dmitruk, I. M.; Nirasawa, T.; Romanyuk, V. R.; Kumar, V.; Mamykin, S. V.; Tohji, K.; Jeyadevan, B.; Shinoda, K.; Kudo, T.; Terasaki, O.; Liu, Z.; Belosludov, R. V.; Sundararajan, V.; Kawazoe, Y., Ultra-Stable Nanoparticles of CdSe Revealed from Mass Spectrometry. *Nature Materials* **2004**, 3, 99-102.
75. Beecher, A. N.; Yang, X.; Palmer, J. H.; LaGrassa, A. L.; Juhas, P.; Billinge, S. J. L.; Owen, J. S., Atomic Structures and Gram Scale Synthesis of Three Tetrahedral Quantum Dots. *Journal of the American Chemical Society* **2014**, 136, 10645-10653.
76. Martin, T. P., Shells of Atoms. *Physics Reports* **1996**, 273, 199-241.
77. Baletto, F.; Ferrando, R.; Fortunelli, A.; Montalenti, F.; Mottet, C., Crossover Among Structural Motifs in Transition and Noble-Metal Clusters. *Journal of Chemical Physics* **2002**, 116, 3856-3863.
78. Kroto, H. W.; Heath, J. R.; O'Brien, S. C.; Curl, R. F.; Smalley, R. E., C₆₀: Buckminsterfullerene. *Nature* **1985**, 318, 162-163.
79. Yu, Q.; Liu, C.-Y., Study of Magic-Size-Cluster Mediated Formation of CdS Nanocrystals: Properties of the Magic-Size Clusters and Mechanism Implication. *Journal of Physical Chemistry C* **2009**, 113, 12766-12771.
80. Friedfeld, M. R.; Stein, J. L.; Cossairt, B. M., Main-Group-Semiconductor Cluster Molecules as Synthetic Intermediates to Nanostructures. *Inorganic Chemistry* **2017**, 56, 8689-8697.
81. Zhang, J.; Hao, X.; Rowell, N.; Kreouzis, T.; Han, S.; Fan, H.; Zhang, C.; Hu, C.; Zhang, M.; Yu, K., Individual Pathways in the Formation of Magic-Size Clusters

- and Conventional Quantum Dots. *Journal of Physical Chemistry Letters* **2018**, *9*, 3660-3666.
82. Reznik, D.; Olk, C. H.; Neumann, D. A.; Copley, J. R. D., X-Ray Powder Diffraction from Carbon Nanotubes and Nanoparticles. *Physical Review B* **1995**, *52*, 116-124.
83. Saito, Y.; Yoshikawa, T.; Bandow, S.; Tomita, M.; Hayashi, T., Interlayer Spacings in Carbon Nanotubes. *Physical Review B* **1993**, *48*, 1907-1909.
84. Warren, B. E., X-Ray Diffraction in Random Layer Lattices. *Physical Review* **1941**, *59*, 693-698.
85. Warren, B. E., X-Ray Diffraction Study of Carbon Black. *Journal of Chemical Physics* **1934**, *2*, 551-555.
86. Woznica, N.; Hawelek, L.; Fischer, H. E.; Bobrinetskiy, I.; Burian, A., The Atomic Scale Structure of Graphene Powder Studied by Neutron and X-ray Diffraction. *Journal of Applied Crystallography* **2015**, *48*, 1429-1436.
87. Zhou, O.; Fleming, R. M.; Murphy, D. W.; Chen, C. H.; Haddon, R. C.; Ramirez, A. P.; Glarum, S. H., Defects in Carbon Nanostructures. *Science* **1994**, *263*, 1744-1747.
88. Shi, H.; Reimers, J. N.; Dahn, J. R., Structure-Refinement Program for Disordered Carbons. *Journal of Applied Crystallography* **1993**, *26*, 827-836.
89. Bernal, J. D., The Structure of Graphite. *Proceedings of the Royal Society A: Mathematical, Physical and Engineering Sciences* **1924**, *106*, 749-773.
90. Trucano, P.; Chen, R., Structure of Graphite by Neutron Diffraction. *Nature* **1975**, *258*, 136-137.
91. Pitoňák, M.; Neogrady, P.; Řezáč, J.; Jurečka, P.; Urban, M.; Hobza, P., Benzene Dimer: High-Level Wave Function and Density Functional Theory Calculations. *Journal of Chemical Theory and Computation* **2008**, *4*, 1829-1834.

92. Rubinstein, M.; Colby, R. H., *Polymer Physics*. Oxford University Press: Oxford, 2003.
93. Jeong, I.-k.; Proffen, T.; Mohiuddin-Jacobs, F.; Billinge, S. J. L., Measuring Correlated Atomic Motion Using X-ray Diffraction. *Journal of Physical Chemistry A* **1999**, 103, 921-924.
94. Schomaker, V.; Trueblood, K. N., On the Rigid-Body Motion of Molecules in Crystals. *Acta Crystallographica* **1968**, B24, 63-76.
95. Dunitz, J. D.; Maverick, E. F.; Trueblood, K. N., Atomic Motions in Molecular Crystals from Diffraction Measurements. *Angewandte Chemie International Edition* **1988**, 27, 880-895.
96. Brown, P. J.; Fox, A. G.; Maslen, E. N.; O'Keefe, M. A.; Willis, B. T. M., Intensity of Diffracted Intensities. In *International Tables for Crystallography, Vol. C: Mathematical, Physical and Chemical Tables*, Prince, E., Ed. John Wiley and Sons: Weinheim, 2006.
97. Barberá, J., X-Ray Studies of Metallomesogens. In *Metallomesogens: Synthesis, Properties, and Applications*, Serrano, J. L., Ed. Wiley-VCH Verlag GmbH: Weinheim, 1995.
98. Calvin, S., *XAFS for Everyone*. CRC Press: Boca Raton, 2013.
99. Scheibe, G., Über die Veränderlichkeit der Absorptionsspektren in Lösungen und die Nebenvalenzen als ihre Ursache. *Angewandte Chemie International Edition* **1937**, 50, 212-219.
100. Jelley, E. E., Molecular, Nematic and Crystal States of 1:1'-Diethyl- ψ -Cyanine Chloride. *Nature* **1937**, 631, 631-632.
101. Bricker, W. P.; Banal, J. L.; Stone, M. B.; Bathe, M., Molecular Model of J-Aggregated Pseudoisocyanine Fibers. *Journal of Chemical Physics* **2018**, 149, 024905.

102. Würthner, F.; Kaiser, T. E.; Saha-Möller, C. R., J-Aggregates: From Serendipitous Discovery to Supramolecular Engineering of Functional Dye Materials. *Angewandte Chemie International Edition* **2011**, 50, 3376-3410.
103. von Berlepsch, H.; Böttcher, C.; Dähne, L., Structure of J-Aggregates of Pseudoisocyanine Dye in Aqueous Solution. *Journal of Physical Chemistry B* **2000**, 104, 8792-8799.
104. Kitahama, Y.; Kimura, Y.; Takazawa, K., Study of Internal Structure of meso-Tetrakis (4-Sulfonatophenyl) Porphine J-Aggregates in Solution by Fluorescence Microscope Imaging in a Magnetic Field. *Langmuir* **2006**, 22, 7600-7604.
105. Walczak, P. B.; Eisfeld, A.; Briggs, J. S., Exchange Narrowing of the J Band of Molecular Dye Aggregates. *Journal of Chemical Physics* **2008**, 128, 044505.
106. Ohno, O.; Kaizu, Y.; Kobayashi, H., J-Aggregate Formation of a Water-Soluble Porphyrin in Acidic Aqueous Media. *Journal of Chemical Physics* **1993**, 99, 4128-4139.
107. Spano, F. C.; Silva, C., H- and J-Aggregate Behavior in Polymeric Semiconductors. *Annual Review of Physical Chemistry* **2014**, 65, 477-500.
108. Zobel, M.; Neder, R. B.; Kimber, S. A. J., Universal Solvent Restructuring Induced by Colloidal Nanoparticles. *Science* **2015**, 347, 201-204.
109. Terban, M. W.; Johnson, M.; Di Michiel, M.; Billinge, S. J. L., Detection and Characterization of Nanoparticles in Suspension at Low Concentrations Using the X-ray Total Scattering Pair Distribution Function Technique. *Nanoscale* **2015**, 7, 5480-5487.
110. Spano, F. C., The Spectral Signatures of Frenkel Polarons in H- and J-Aggregates. *Accounts of Chemical Research* **2010**, 43, 429-439.

111. Tarascon, J. M.; DiSalvo, F. J.; Chen, C. H.; Carroll, P. J.; Walsh, M.; Rupp, L., First Example of Monodispersed $(\text{Mo}_3\text{Se}_3)_\infty^1$ Clusters. *Journal of Solid State Chemistry* **1985**, 58, 290-300.
112. Mihailovic, D., Inorganic Molecular Wires: Physical and Functional Properties of Transition Metal Chalco-Halide Polymers. *Progress in Materials Science* **2009**, 54, 309-350.
113. DiSalvo, F. J., Solid-State Chemistry: A Rediscovered Chemical Frontier. *Science* **1990**, 247, 649-655.